

DISS. ETH No. 20251

# **Synthesis, Characterization and Tribiochemical Behavior of Polyphosphate Glasses**

A dissertation submitted to:

ETH ZURICH

for the degree of:

Doctor of Sciences

presented by:

**MAURA CROBU**

Diploma in Chemical Engineering

University of Cagliari, Italy

Born on August 2, 1982

Citizen of Italy

Accepted on the recommendation of:

Prof. Dr. Nicholas D. Spencer, examiner

Prof. Dr. Antonella Rossi, co-examiner

Prof. Dr. Markus Niederberger, co-examiner

Prof. Dr. Richard K. Brow, co-examiner

2012



For my parents



*Bisogna opporre al pessimismo dell'intelligenza  
l'ottimismo della volontà.*

A. Gramsci



# Abstract

The formation of glass-like poly(thio)phosphate glasses of different chain-lengths under tribological conditions is considered to be the key factor for the useful antiwear properties of phosphorus-based engine-oil antiwear additives. Among several techniques applied to investigating the structure, composition and thickness of these films, nano-indentation measurements have shown that the mechanical properties vary with the chemical composition and the morphological structure. The antiwear surface protection mechanism is, therefore, a combination of the chemical and mechanical properties of the tribofilms. Understanding the mechanical and tribochemical properties of such glasses turns out to be a key step for inferring their underlying mechanisms of action. However, so far no analytical technique has been able to identify the composition unambiguously or to determine the polyphosphate chain-length in the tribological films formed on the sliding surfaces, mainly due to the lack of well-defined polyphosphate glass samples.

In the first part of this thesis zinc, iron and mixed zinc and iron bulk phosphate glasses with different chain lengths were synthesized. The samples were characterized by means of X-ray diffraction (XRD), micro-elemental analysis, Fourier-transform infrared spectroscopy (FT-IR), X-ray photoelectron spectroscopy (XPS), and, for the first time, with time-of-flight secondary ion mass spectroscopy (ToF-SIMS).

The Vickers' hardness and reduced Young's modulus measured by micro-indentation and nano-indentation were found to decrease with increasing chain length for both zinc- and iron- polyphosphates. Iron polyphosphates were found to be harder than zinc polyphosphates with the same chain length.

Several parameters in the XPS spectra of tribofilms are found to be sensitive to the chain length: the integrated intensity ratio of the bridging (P-O-P) and non-bridging (P=O and P-O-M) oxygen peaks used for fitting the oxygen 1s signal, the shift of the P2p<sub>3/2</sub> signal, the modified Auger parameter and the P3s signal in the valence-band region. Supported by the investigation of pure and well-characterized compounds, a more robust method based on a two-dimensional plot of the BO/NBO ratio versus the binding-energy difference of Zn3s- P2p<sub>3/2</sub> could be achieved for the identification of the chain length of zinc polyphosphates. For the first time also ToF-SIMS is proposed as a suitable technique for the identification of polyphosphate glasses of different chain lengths. The discrimination is achieved by comparing the intensity of the relevant ToF-SIMS peaks. Principal-component analysis was used, in

order to identify the peaks whose intensity is sensitive to the chain length. XPS and ToF-SIMS data were correlated using a partial-least-square regression.

In the second part of the thesis, the tribological tests on the polyphosphate discs were carried out using steel and quartz balls as counterparts in a poly- $\alpha$ -olefin (PAO) bath at room temperature. The coefficient of friction and the wear rate measured in the case of zinc-containing polyphosphates were lower than those of iron polyphosphates and were found to decrease with decreasing chain length. The composition of the contact area in the wear track of the discs and of the balls was monitored by small-area and imaging X-ray photoelectron spectroscopy (i-XPS). The XPS analysis showed that the composition of the short-chain-length polyphosphates remained unchanged after tribological stress. The long-chain-length polyphosphates are depolymerized in the wear track as a consequence of the tribochemical reaction. Pressure and shear stress control the depolymerization of the glass, but the counterpart material was also found to influence this reaction: iron oxide from the steel balls reacts with the polyphosphates and promotes their depolymerization.

XPS analyses of the steel balls after the mechanical tests on polyphosphate discs showed the formation of a glassy phosphate transfer film in the contact area, reducing friction and wear of the steel ball. For zinc polyphosphates, the transfer film is well adherent and compact, and in the case of iron phosphates the glass transferred from the disc to the ball during the test is accumulating towards the border rather than adhering to the contact area. This corresponds to a higher wear of the ball. The formation of an adhesive transfer film explains the low values of the coefficient of friction and of the wear rates of the steel ball, with best results for zinc polyphosphates. These findings suggest that a third-body mechanism is governing the wear in the steel-versus-polyphosphate tribopair.

These results allow a better understanding of the antiwear efficiency of ZnDTP additives. The tribological stress leads to depolymerization reactions and the formation of short-chain-length polyphosphates, which are harder and thus more wear-resistant. The presence of iron oxide (steel ball) promotes this depolymerization and might also assist good adhesion of the tribofilm to the steel substrate. Ashless P-based additives (without Zn) provide a less effective antiwear resistance because their tribofilms only contain iron polyphosphates. In this work it was shown that iron polyphosphates do not form adhesive transfer films on the steel ball, in contrast to zinc-bearing glasses. The presence of zinc in the polyphosphate network is thus crucial for the antiwear efficiency of the tribofilms.



# Riassunto

La formazione di strati sottili costituiti da vetri poli(tio)fosfati a diversa lunghezza di catena è considerata il fattore chiave per l'acquisizione di ottime proprietà antiusura da parte degli additivi per applicazioni motoristiche a base di fosforo. Tra le numerose tecniche utilizzate per lo studio di struttura, composizione e spessore di questi strati sottili, misure di nano-penetrazione hanno mostrato che le loro proprietà meccaniche variano con la composizione e la morfologia. Il meccanismo grazie al quale le superfici sono protette dall'usura, dipende, pertanto, dalle proprietà chimiche e meccaniche dei film tribologici. Lo studio delle proprietà meccaniche e tribo-chimiche di questi vetri è il passo fondamentale per capirne il meccanismo d'azione. Sino ad ora, tuttavia, principalmente a causa della mancanza delle sostanze pure di riferimento, nessuna tecnica analitica è stata in grado di identificare in maniera non ambigua la lunghezza di catena dei polifosfati nei film tribologici formati all'interfaccia tra le due superfici in moto relativo.

Nella prima parte della tesi, sono stati sintetizzati i polifosfati di zinco, ferro e i misti di zinco e ferro con diverse lunghezze di catena. La caratterizzazione dei campioni è stata eseguita tramite diffrazione a raggi X (XRD), analisi micro-elementare, spettroscopia infrarossa a trasformata di Fourier (FT-IR), spettroscopia fotoelettronica a raggi X (XPS) e spettroscopia di massa a tempo di volo (ToF-SIMS).

La durezza Vickers e il modulo di Young ridotto, misurati con il durimetro e il nano-durimetro, diminuiscono all'aumentare della lunghezza di catena per entrambi i polifosfati di zinco e ferro. A parità di lunghezza di catena i polifosfati di ferro sono più duri di quelli di zinco.

Sono stati individuati molti parametri sensibili alla lunghezza di catena negli spettri XPS dei film tribologici: il rapporto tra le intensità dei segnali dell'ossigeno a ponte (P-O-P) e non a ponte (P=O e P-O-M), lo spostamento del segnale  $P2p_{3/2}$ , del parametro Auger modificato e del segnale P 3s nella banda di valenza. Grazie allo studio sistematico delle sostanze pure di riferimento, è stato sviluppato un metodo di identificazione della lunghezza di catena dei polifosfati di zinco molto affidabile (o efficace) basato su un grafico bidimensionale dove in ascissa si trova il rapporto di intensità tra i segnali dell'ossigeno a ponte e quelli non a ponte, ed in ordinata la differenza tra le energie di legame dello Zn 3s e del P  $2p_{3/2}$ . Per la prima volta anche il ToF-SIMS è stato proposto come tecnica analitica per l'identificazione della lunghezza di catena dei polifosfati. Dal confronto delle intensità dei picchi rilevanti

negli spettri ToF-SIMS è possibile distinguere tra diverse lunghezze di catena. L'analisi delle componenti principali è stata utilizzata per individuare i picchi la cui intensità è sensibile alla lunghezza di catena mentre si è fatto ricorso all'analisi di regressione ai minimi quadrati parziali per stabilire se esiste una relazione tra i valori misurati con l'XPS con quelli ottenuti dal ToF-SIMS.

Nella seconda parte della tesi sono state eseguite le prove tribologiche utilizzando dischi di polifosfato e palline di acciaio e quarzo come controparti in un bagno di poli-alfa-olefine a temperatura ambiente. Il coefficiente di attrito ed il tasso di usura misurati sui dischi di polifosfato di zinco sono più bassi di quelli ottenuti sui dischi di polifosfato di ferro. Inoltre, i dischi di polifosfato di zinco a catena corta mostravano attrito e usura più bassi rispetto a quelli a catena lunga. La composizione dell'area di contatto sulla traccia di usura sui dischi è stata monitorata tramite XPS. I risultati mostrano che la composizione dei polifosfati a catena corta rimane invariata dopo le prove tribologiche. I polifosfati a catena lunga, invece, sono depolimerizzati nella pista di usura conseguentemente alla reazione tribo-chimica. Sono la pressione e lo stress di taglio ad attivare la depolimerizzazione del vetro, ma anche la composizione della controparte influenza la reazione: l'ossido di ferro reagisce con i polifosfati e promuove la polimerizzazione.

L'analisi XPS delle palline d'acciaio dopo i test tribologici sui dischi di polifosfato ha mostrato che un film di trasferimento di polifosfato è presente nell'area di contatto e ha l'effetto di ridurre l'attrito e l'usura delle medesime. Nel caso dei polifosfati di zinco il film di trasferimento è ben aderente e compatto, mentre nel caso dei polifosfati di ferro il vetro trasferito dal disco alla pallina durante la prova si accumula sul bordo anziché aderire all'area di contatto. Di conseguenza l'usura della pallina è maggiore in questo caso. La formazione di un film di trasferimento aderente al substrato spiega i bassi valori del coefficiente di attrito e del tasso di usura della pallina d'acciaio nel caso dei polifosfati di zinco. Questi risultati suggeriscono che l'usura nella coppia acciaio su polifosfato avvenga secondo un meccanismo che coinvolge un 'terzo corpo': lo strato di polifosfato trasferito dal disco alla sfera.

Questi risultati consentono una migliore comprensione del meccanismo grazie al quale il dialchil-ditiofosfato di zinco (ZnDTP) è un efficace additivo antiusura. Lo stress tribologico provoca la reazione di depolimerizzazione dei vetri conducendo alla formazione di polifosfati a catena corta che sono più duri e quindi più resistenti all'usura. La presenza di ossido di ferro (sulla superficie delle palline di acciaio) facilita la depolimerizzazione e potrebbe anche conferire una buona adesione del film tribologico all'acciaio. Additivi contenenti fosforo ma non zinco sembrano possedere una resistenza all'usura meno efficace verosimilmente dovuta alla formazione di film tribologici composti da soli polifosfati di ferro che non aderiscono alle palline di

acciaio. La presenza di zinco nel polifosfato di ferro appare dunque essenziale per garantire l'efficienza del film antiusura.



# Table of contents

<b>Abstract</b>	v
<b>Riassunto</b>	vii
<b>Table of contents</b>	xi
<b>1 Introduction</b>	<b>1</b>
1.1 Objectives of the thesis	2
1.2 Outline of the thesis	3
<b>2 State of the art</b>	<b>7</b>
2.1 Principles of tribology	7
2.1.1 Friction	7
2.1.2 Wear	8
2.1.3 Lubrication	9
2.1.4 Theory of the third body	10
2.2 Tribochemistry	11
2.2.1 Lubricant additives	11
2.2.2 The tribochemical nature of antiwear films	11
2.3 P-based antiwear additives: ZnDTPs and ashless additives	12
2.3.1 ZnDTP reactions in solution	12
2.3.2 ZnDTP thermal and tribo-film formation and composition	12
2.3.3 Mechanical Properties and antiwear mechanism of ZnDTP tribofilms	15
2.3.4 “Ashless” additives directly derived from ZnDTP	16
2.4 Polyphosphate glasses	17
2.4.1 Composition and structure	18
2.4.2 Surface analysis	20
2.4.3 Mechanical properties	21
2.5 Surface-analytical techniques in tribology	22
2.5.1 XPS and the challenges of tribochemistry	22
2.5.2 ToF-SIMS: a rapidly developing technique	23
2.6 Summary	25
<b>3 Experimental</b>	<b>33</b>
3.1 Materials	33
3.1.1 Tribopairs	33
3.1.2 Lubricant oil	34

3.1.3	List of materials and suppliers	34
3.2	<i>Synthesis of the glasses</i>	35
3.2.1	Synthesis	35
3.2.2	Mechanical polishing	37
3.3	<i>Bulk characterization</i>	38
3.3.1	X-ray Diffraction (XRD)	38
3.3.2	Infrared spectroscopy	38
3.3.3	Microelemental analysis	38
3.3.4	Microindentation	38
3.3.5	Nanoindentation	39
3.3.6	Atomic Force Microscopy (AFM)	39
3.3.7	Density	39
3.4	<i>Tribological experiments</i>	39
3.4.1	CETR tribometer	39
3.4.2	Constant load tribological experiments	40
3.4.3	Optical microscopy	41
3.4.4	Data processing	41
3.5	<i>X-ray photoelectron spectroscopy</i>	41
3.5.1	PHI Quantera SXM	41
3.5.2	VG Theta Probe	44
3.5.3	Data processing	44
3.5.4	Quantitative Analysis	45
3.6	<i>Time-of-Flight Secondary Ion Mass Spectroscopy</i>	46
3.6.1	ToF.SIMS <sup>5</sup>	46
3.6.2	Data Processing	47
3.6.3	Principal Component Analysis (PCA)	48
<b>4</b>	<b>Bulk characterization of polyphosphate glasses</b>	<b>51</b>
4.1	<i>Physico-chemical characterization of polyphosphate glasses</i>	51
4.1.1	XRD	51
4.1.2	Microelemental analysis	52
4.1.3	Fourier-Transformed Infrared Spectroscopy	54
4.1.4	Density	58
4.2	<i>Mechanical properties</i>	59
4.2.1	Microindentation	59
4.2.2	Nanoindentation	60
4.3	<i>Discussion</i>	62
4.4	<i>Summary</i>	66
<b>5</b>	<b>Surface analysis of zinc, iron and mixed zinc and iron polyphosphate glasses</b>	<b>69</b>
5.1	<i>XPS analysis</i>	69

5.1.1	Survey spectra	69
5.1.2	Zinc polyphosphate glasses	70
5.1.3	Iron polyphosphate glasses	73
5.1.4	Mixed iron/zinc polyphosphate glasses	77
5.1.5	Quantitative analysis	79
5.2	<i>ToF-SIMS analysis</i>	83
5.2.1	Positive-mode ToF-SIMS spectra	83
5.2.2	Zinc polyphosphates	84
5.2.3	Iron polyphosphates	85
5.2.4	Mixed zinc and iron polyphosphates	87
5.3	<i>Discussion</i>	88
5.3.1	Chemical state of O, P and Zn and Fe in polyphosphate glasses	88
5.3.2	XPS quantitative analysis of polyphosphates	92
5.3.3	Surface characterization of polyphosphates by ToF-SIMS	94
5.3.4	Effect of primary ions on ToF-SIMS spectra of polyphosphate glasses	96
5.4	<i>Summary</i>	97
<b>6</b>	<b>Chain-length-identification strategy in polyphosphate glasses by means of XPS and ToF-SIMS</b>	<b>101</b>
6.1	<i>Chain-length-identification strategy in polyph. glasses by means of XPS</i>	101
6.1.1	The bridging/non bridging (BO/NBO) ratio	101
6.1.2	Other parameters for the chain-length identification	104
6.1	<i>ToF SIMS</i>	108
6.1.1	Chain-length identification by ToF-SIMS: PCA analysis	108
6.1.2	Determining the polyphosphate chain length from ToF-SIMS data	111
6.2	<i>Summary</i>	113
<b>7</b>	<b>Tribochemical properties of zinc polyphosphate glasses</b>	<b>117</b>
7.1	<i>Steel-versus-zinc metaphosphate tribopair: the establishment of a protocol for the assessment of the tribochemical properties of polyphosphate glasses</i>	118
7.1.1	Tribological tests	118
7.1.2	Steel-versus-zinc metaphosphate tribopair: friction and wear	118
7.1.3	Steel-versus-zinc-metaphosphate tribopair: XPS analysis of the balls	123
7.1.4	Steel-versus-zinc metaphosphate tribopair: XPS analysis of the discs	126
7.2	<i>Effect of the chain-length and of the counterpart material on the tribochemistry of bulk zinc polyphosphate glasses</i>	127
7.2.1	Steel-versus-zinc-polyphosphate tribopair: tribological tests	127
7.2.2	Steel-versus-polyphosphate tribopair: XPS analysis of the polyphosphate disc	129
7.2.3	Steel-versus-zinc-polyphosphate tribopair: XPS analysis of the steel ball	132
7.3	<i>Quartz-versus-zinc polyphosphate tribopair</i>	135

7.3.1	Quartz-versus-zinc polyphosphate tribopair: tribological tests	135
7.3.2	Quartz-versus-zinc polyphosphate tribo-pair: XPS analysis of the polyphosphate disc	136
7.3.3	Quartz-versus-zinc-polyphosphate tribo-pair: XPS analysis of the quartz balls	137
7.4	<i>The tribochemical reaction of depolymerization at the steel-versus-zinc-metaphosphate interface</i>	139
7.4.1	Steel-versus-zinc-metaphosphate tribopair: composition of the transfer film	139
7.4.2	Steel-versus-zinc-metaphosphate tribopair: composition of the wear track on the disc	140
7.4.3	Proposed reaction at the ball/disc interface	141
7.5	<i>Effect of chain-length and role of iron on the tribochemical reaction of depolymerization of zinc polyphosphate glasses</i>	141
7.5.1	Reaction of depolymerization: effect of chain-length	142
7.5.2	Role of iron in the tribochemical reaction of zinc polyphosphate glasses	143
7.6	<i>Summary</i>	147
<b>8</b>	<b>Tribochemistry of iron and mixed zinc/iron polyphosphate glasses</b>	<b>149</b>
8.1	<i>Steel-versus-iron-polyphosphate tribopair</i>	149
8.1.1	Steel-versus-iron-poly0.33 tribopair: friction and wear	149
8.1.2	Steel-versus-iron poly0.33 tribopair: XPS analysis of the steel ball	150
8.1.3	Steel-versus-iron-poly0.33 tribopair: XPS analysis of the glass discs	153
8.2	<i>Steel-versus-mixed-zinc-and-iron polyphosphates</i>	155
8.2.1	Steel-versus-mixed-zinc-and-iron-polyphosphates tribopair: friction and wear	155
8.2.2	Steel-versus-mixed zinc and iron polyphosphates tribopair: XPS analysis of the steel ball	158
8.2.3	Steel-versus-mixed-zinc-and-iron-polyphosphates tribopair: XPS analysis of the glass discs	163
8.3	<i>Effect of the counter-ion on the friction, wear and tribochemical behavior of polyphosphate glasses</i>	166
8.4	<i>Summary</i>	167
<b>9</b>	<b>Polyphosphate glasses as model compounds for tribofilms</b>	<b>169</b>
9.1	<i>Bulk polyphosphate glasses as models for ZnDTP tribofilms: advantages and disadvantages</i>	169
9.2	<i>Influence of tribochemical reaction on the tribofilm formation and composition</i>	171
9.3	<i>Antiwear mechanism of polyphosphate tribofilms</i>	173
9.4	<i>Effect of the cation in the tribochemistry of polyphosphate glasses; ashless thiophosphates and interaction of ZnDTP with other additives</i>	175
9.5	<i>Characteristics of a functional tribofilm</i>	177



---

<b>10</b>	<b>Conclusions and Outlook</b>	<b>183</b>
	10.1 Conclusions	183
	10.2 Outlook	185
	<b>Appendix</b>	<b>187</b>
	<i>Appendix A XPS</i>	188
	A.1 Linearity of the binding energy scale of the XP-spectrometers	188
	A.2 Sensitivity factors	190
	A.3 Survey spectra	193
	A.4 Reference Phosphate compounds	195
	<i>Appendix B Processing of tribological data</i>	199
	<i>Appendix C TOF-SIMS</i>	200
	C.1 Reference compounds	200
	C.2 Spectra acquired with Bi <sub>1</sub> <sup>+</sup> primary ions	201
	C.1 Comparison between normalization methods	203
	C.2 Peak list	204
	<b>Curriculum vitae</b>	207
	<b>Acknowledgements</b>	211



# 1 Introduction

Reduction of costs, in terms of energy consumption and maintenance, and improvements in safety are increasingly important issues for the development of modern engineered systems in transportation, chemical, biomedical, mechanical and aerospace industries. Lubricants are normally used to reduce friction and wear between two sliding or rolling surfaces. Scientific research is being increasingly applied to respond to the more stringent performance requirements of modern engines. There is an increasing interest in the development of new lubricant additives that are able to improve lubricant performance. Lubricant additives are molecules able to adsorb/react at the sliding interfaces, providing low-shear-strength protective films that are able to minimize energy consumption by reducing friction and/or preventing the damage of components as a consequence of wear. In most cases, additives that act as friction modifiers have little antiwear action, while protective films formed by antiwear additives can also lead to an increase in friction. The choice of an oil formulation is therefore the consequence of a compromise between these two requirements. This choice has been further complicated in the last 20 years by the increasingly strict environmental regulations that limit the use of metals, phosphorus and sulfur content in the lubricants, partly because of their intrinsic toxicity, and partly because they are poisonous for downstream catalytic converters.

One of the most successful and long-lived classes of lubricant additives are the zinc dialkyldithiophosphates (ZnDTPs), known for their antioxidant, corrosion inhibition, and antiwear properties [1; 2]. The uniqueness of ZnDTP lies in its ability to form thin glassy reaction layers at the sliding interface that, thanks to their ability to become thicker and harder where the contact pressure is higher and to adapt to almost every stress condition, are very effective in preventing wear [1; 3-5]. ZnDTP has been extensively employed in almost all engine-oil formulations but its use is now likely to become limited because its degradation products are rich in Zn, P and S. A possible alternative has been found in ashless thiophosphates, although the wear-protection performance of these new molecules is still not comparable with that of ZnDTP [6-9].

The surface chemistry of ZnDTP tribofilms has been extensively investigated, but there are still open questions concerning the chemical mechanism of formation of the tribofilm and the kinetics of its formation, removal and replenishment. It is generally accepted that ZnDTP tribofilms present a solid, pad-like, structure consisting mainly of glassy zinc phosphates with the presence of sulfide species; iron oxide is present in the layer beneath the surface, and an organic layer is detectable on

the top [10]. It has been observed that the friction force correlates with thickness and composition (chain length) of the antiwear film. A similar structure has also been observed in the tribofilms generated by ashless thiophosphates [8; 11].

Despite the impressive amount of research, which employed all modern surface investigation tools in order to understand the antiwear mechanism of ZnDTP, numerous questions still remain open, as will be pointed out more in detail in Chapter 2.

## 1.1 Objectives of the thesis

In order to design new molecules that are as effective as ZnDTP but with reduced Zn, P and S content, as required by the most recent environmental regulations, a better understanding of the correlation between the tribochemical reactions of film formation and the friction processes is necessary.

The aim of this work is to gain a better understanding of the protection mechanism of the tribofilms formed in the presence of ZnDTP or other phosphorus-based additives. In order to get a new perspective on the topic after more than 70 years of research on ZnDTP, it is necessary to approach the problem with a different strategy. While it is commonly accepted that the antiwear effectiveness of ZDTP is correlated with its ability to form a thick polyphosphate film, very little is known about the mechanical and tribological properties of bulk polyphosphate glasses. Bulk polyphosphates are good candidates to be used as model systems of ZnDTP tribofilms. Pursuing this idea, the following four goals were defined:

- *Synthesis and characterization of zinc, iron and mixed zinc/iron polyphosphates.* Polyphosphate glasses of different compositions and in the form of discs can be obtained by melting stoichiometric mixtures of  $P_2O_5$  and metal oxides, as was already demonstrated in a feasibility study carried out by R. Pinna [12]. One of the advantages of using a model system, rather than a real tribofilm, is that the chemical composition can be tuned and well characterized. The application of surface-analytical techniques (X-ray photoelectron spectroscopy, XPS; time-of-flight secondary ion mass spectrometry, ToF-SIMS) is key, when investigating tribochemical reactions in tribological systems. Far more information can be obtained by means of these techniques if reference spectra, acquired on a well-characterized compounds, are available. Moreover, tribological systems represent very complex analytical problems, and therefore the development of a strategy to discriminate the different compounds present on the basis of reference spectra could become a very valuable analytical tool.

- *Tribological and mechanical characterization of the glasses; dependence on the composition and the chain-length.* One of the open questions about ZDTP tribofilms is whether the tribofilm antiwear efficiency benefits from the presence of short- or long-chain-length polyphosphates. It has been observed that the tribofilms formed in the presence of ashless phosphate-based additives, mainly composed of iron polyphosphates, are not as efficient as ZnDTP tribofilms. The chain-length and composition of polyphosphate glasses can be tuned by changing the metal oxide content during the synthesis. Therefore, once a protocol for carrying out mechanical and tribological tests on polyphosphate glasses has been defined, the effect of chain-length and composition on the mechanical and tribological properties can be clarified.
- *Effect of the sliding process on the chemical composition: tribochemical reactions.* ZnDTP tribofilms on steel have a layered structure: at the bottom a short-chain-length polyphosphate layer is present, intergrown with the iron oxide film. The outermost layer is thinner and formed by long-chain-length poly(thio)phosphates also containing sulphides and oxides. [10; 13; 14]. Another unsolved problem in the field is the origin of the gradient of composition in the tribofilms and the role potentially played in its antiwear mechanism. Using surface-analytical techniques, the chemical changes caused by the sliding process on the polyphosphate glasses can be followed and the tribochemical reactions involved identified.
- *New insights into the antiwear mechanism of phosphorus-based additives.* The use of model systems might suffer from a few disadvantages due to the fact that the conclusions drawn on the model system might not directly apply to a real, more complex system such as a tribofilm. A careful and critical comparison of the two systems is outlined, in order to use all the new pieces of information and fit them into the incomplete puzzle of the antiwear mechanism of ZnDTP. Our group has a long experience in the investigation of ZnDTP and ashless additives that will become important in this last, most important, step [9; 15-17]

## 1.2 Outline of the thesis

This work naturally divides itself into two main branches. The first part concerns the synthesis and characterization of the polyphosphates. Here, a strategy for the chain-length identification by means of surface-analysis techniques is developed. In the second part, the tribological behavior of the glasses is investigated and the analytical strategy developed in the first part is applied to identify the tribochemical reactions involved. Finally the relevance of those results on the broader and more

complicated problem of the antiwear effectiveness of P-based additives will be discussed.

The outline of the thesis is schematically summarized in Figure 1.1.

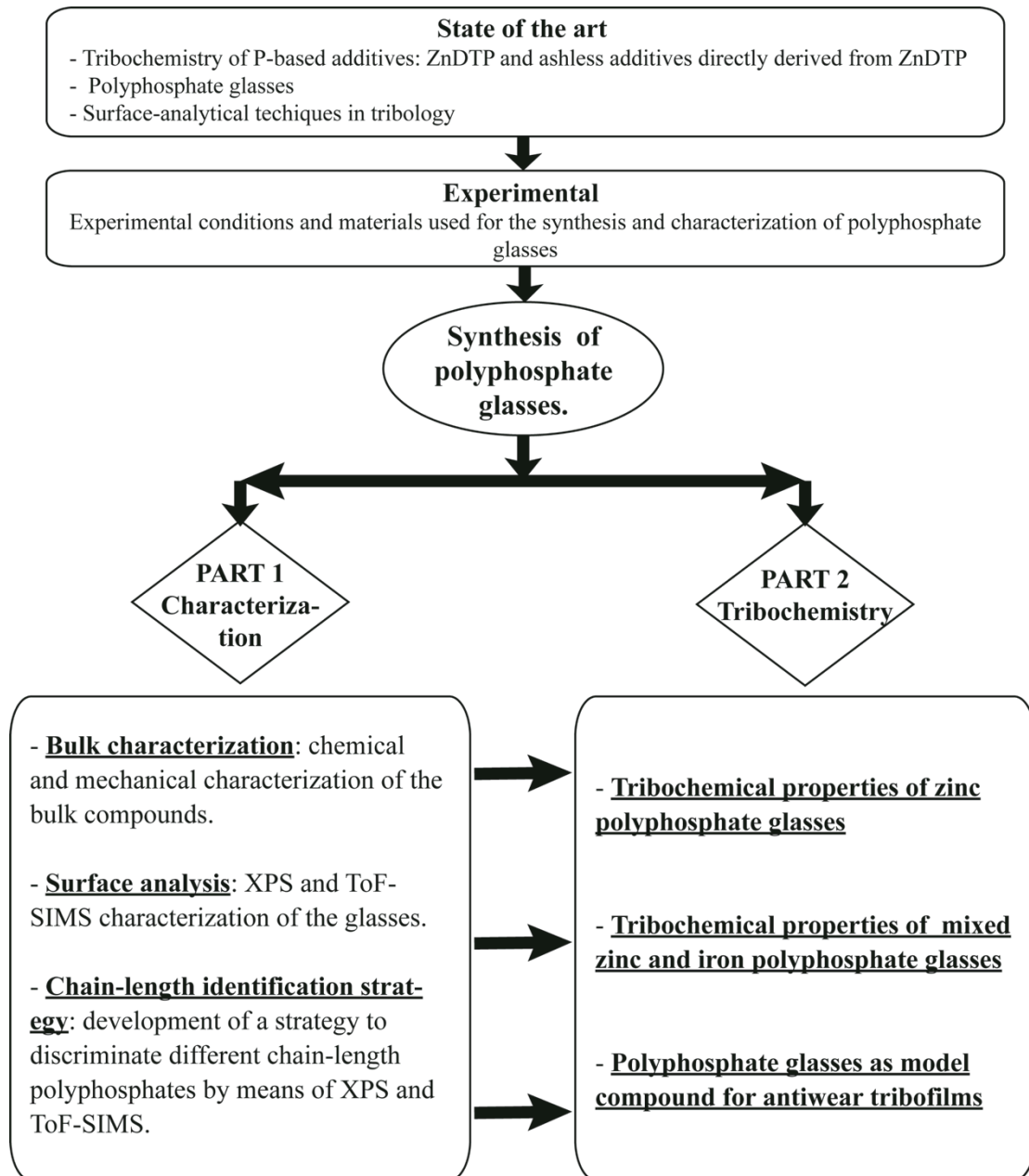


Figure 1.1: Outline of the thesis

## References

- [1] Spikes H.: The History and Mechanisms of ZDDP. *Tribol. Lett.* 17, 469-489 (2004).
- [2] Gellman A., and Spencer N.: Surface chemistry in tribology. *Proceedings of the Institution of Mechanical Engineers, Part J: Journal of Engineering Tribology* 216, 443-461 (2002).
- [3] Minfray C., Le Mogne T., Lubrecht A. A., and Martin J. M.: Experimental simulation of chemical reactions between ZDDP tribofilms and steel surfaces during friction processes. *Tribol. Lett.* 21, 67-78 (2006).
- [4] Eglin M., Rossi A., and Spencer N. D.: X-ray photoelectron spectroscopy analysis of tribostressed samples in the presence of ZnDTP: a combinatorial approach. *Tribol. Lett.* 15, 199-209 (2003).
- [5] Bec S., Tonck A., Georges J. M., Coy R. C., Bell J. C., and Roper G. W.: Relationship between mechanical properties and structures of zinc dithiophosphate anti-wear films. *Proc. R. Soc. London A* 455, 4181-4203 (1999).
- [6] Hugh Spikes: Low- and zero-sulphated ash, phosphorus and sulphur anti-wear additives for engine oils. *Lubricat. Sci.* 20, 103-136 (2008).
- [7] Najman M. N., Kasrai M., Bancroft G. M., Frazer B. H., and Stasio G. D.: The Correlation of Microchemical Properties to Antiwear (AW) Performance in Ashless Thiophosphate Oil Additives. *Tribol. Lett.* 17, 811-822 (2004).
- [8] Heuberger R., Rossi A., and Spencer N. D.: Reactivity of alkylated phosphorothionates with steel: a tribological and surface-analytical study. *Lubricat. Sci.* 20, 79-102 (2008).
- [9] Mangolini F., *Reactivity of Environmentally Compatible Lubricant Additives: an In Situ and Ex Situ Investigation*, PhD Thesis No. 19677, ETH Zürich, Zürich, 2011.
- [10] Heuberger R., Rossi A., and Spencer N. D.: XPS study of the influence of temperature on ZnDTP tribofilm composition. *Tribol. Lett.* 25, 185-196 (2007).
- [11] Mangolini F., Rossi A., and Spencer N. D.: Chemical Reactivity of Triphenyl Phosphorothionate (TPPT) with Iron: An ATR/FT-IR and XPS Investigation. *J. Phys. Chem. C* 115, 1339-1354 (2011).
- [12] Pinna R., *Synthesis and characterization of Zn and Fe polyphosphates glasses*, Master Thesis, University of Cagliari, Cagliari, 2001/2002.
- [13] Yin Z., Kasrai M., Fuller M., Bancroft G. M., Fyfe K., and Tan K. H.: Application of soft X-ray absorption spectroscopy in chemical characterization of antiwear films generated by ZDDP Part I: the effects of physical parameters. *Wear* 202, 172-191 (1997).
- [14] Martin J. M., Grossiord C., Le Mogne T., Bec S., and Tonck A.: The two-layer structure of ZnDTP tribofilms: Part I: AES, XPS and XANES analyses. *Tribol. Int.* 34, 523-530 (2001).
- [15] Eglin M., *Development of a combinatorial approach to lubricant additive characterization*, PhD Thesis No. 15054, ETH Zurich, Zürich, 2003, pp. 226.
- [16] Piras F. M., Rossi A., and Spencer N. D.: Combined in situ (ATR FT-IR) and ex situ (XPS) study of the ZnDTP-iron surface interaction. *Tribol. Lett.* 15, 181-191 (2003).
- [17] Heuberger R. C., *Combinatorial Study of the Tribochemistry of Anti-Wear Lubricant Additives LSST*, ETH, Zürich, 2007, pp. 226.





## 2 State of the art

A review of the literature relevant to this project is presented in this chapter.

The basic concepts of friction and wear and tribochemistry have been summarized in Sections 2.1 and 2.2. Section 2.3 reviews the results of more than 70 years of research on the tribochemistry of P-based additives, focusing especially on the properties of the tribofilms and their antiwear action.

There are no previous works on the tribochemistry of bulk polyphosphate glasses, but, by virtue of the numerous technological applications, their structure and properties have been already investigated as described in Section 2.4. Finally the relevance of surface-analytical techniques, with a particular attention to XPS and ToF-SIMS, is discussed in Section 2.5

### 2.1 Principles of tribology

Tribology is the science and technology of interacting surfaces in relative motion". The term "Tribology" (derived from the Greek word "τριβοσ" meaning "rubbing") embraces the study of friction, wear and lubrication, as well as the interactions between solids, liquids and gases when in presence of a mechanical stress [1].

#### 2.1.1 Friction

Friction is defined as the resistance to relative motion of two adjacent bodies. Friction is experienced in everyday life when driving a car, playing a bowed instrument or simply walking [2; 3]. Some empirical laws of frictions, the so-called Amontons' laws, have been known since antiquity. The first law states that the friction force,  $F$ , is proportional to the normal load,  $L$ :

**Equation 2.1**

$$F = \mu L$$

where  $\mu$  is the coefficient of friction, still widely used today to characterize the friction behavior of materials.

The second law states that the friction force is independent of the apparent area of contact. Leonardo da Vinci, in the late 15<sup>th</sup> century, was the first to make these observations, which were then rediscovered by Gillaume Amontons in 1699 [1].

Friction, although apparently described by simple laws, is a very complex process. Surfaces that appear flat on the macroscopic scale, are normally bumpy on the microscopic scale. When approaching two rough surfaces together, the actual contact takes place only between asperities. The real contact area is therefore far smaller than the apparent contact area. Even at very small loads, the contact pressure at the asperities reaches the yield stress and plastic strain takes place until the area of contact is sufficient to support the load. Friction is, then, a typical stochastic process that can be described as a collection of single-asperity interactions [4]. Virtually every sliding condition produces a different level of friction.

Our understanding of the friction mechanism is mostly limited to simple models. When one surface is sliding over another there are at least two factors that contribute to the energy losses generated during friction: adhesion and deformation [5].

### 2.1.2 *Wear*

Wear can be defined as the phenomenon of material removal from a surface while interacting with a second surface [3]. The loss of material can decrease the durability and reliability of engineered systems such as gears, bearings or engines, and therefore the reduction and control of wear are fundamental for technological innovation.

As with friction, wear is also a very complicated phenomenon. Different mechanisms can be identified, giving rise to different types of wear, and usually more than one wear mechanism at a time can be identified in every tribosystem. The most common types are listed in the following and summarized in Figure 2.1:

- Adhesive wear, resulting from the shear of the friction junctions [5].
- Abrasive wear, caused by the presence of hard particles or protuberances at the interface [5].
- Delamination or fatigue wear, generated after repeated friction cycles [3].
- Chemical wear, which takes place in presence of corrosive media because the tribochemical reaction at the contact interface is accelerated [3].

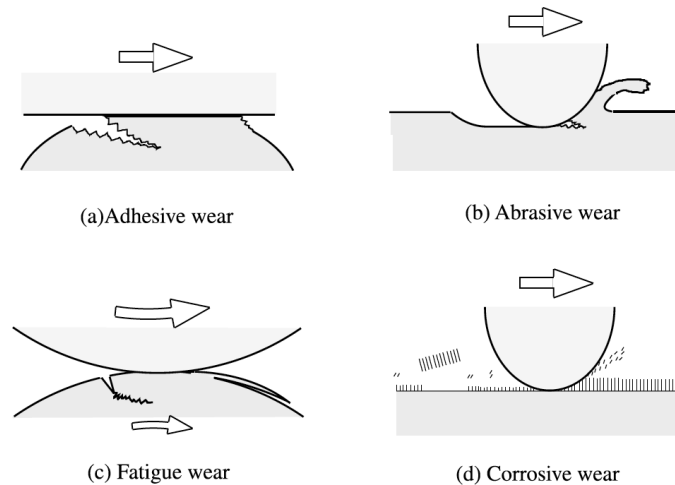


**Figure 2.1: Schematic images of four representative wear modes [3]**

### 2.1.3 Lubrication

Lubricants are used to control friction and minimize wear in a variety of tribological applications. The friction force between two rubbing surfaces in the presence of a lubricant depends mainly on its viscosity  $\eta$ , the sliding velocity  $v$ , and on the normal load. For high velocities and low loads a thick layer of lubricant separates the sliding surfaces resulting in a low coefficient of friction (hydrodynamic lubrication, Figure 2.2).

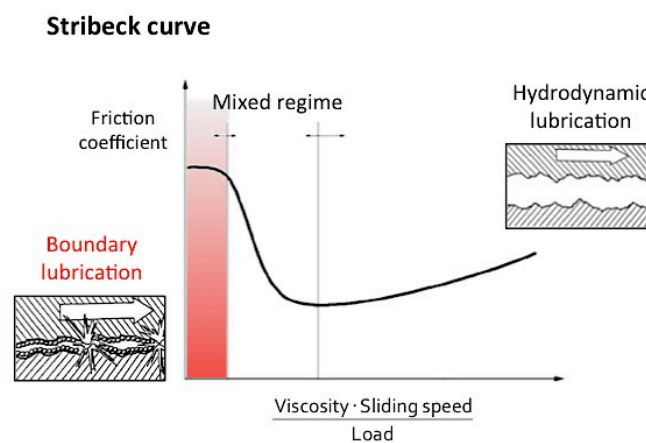


**Figure 2.2: Stribeck curve**

At increasing loads and lower speeds the fluid-film thickness decreases until the distance between the two surfaces becomes too small and their asperities come into contact. In the mixed regime the lubricant film still supports part of the load but the contact between the asperities causes higher friction and wear. Finally, the lubricant film is squeezed out from the contact area and solid-solid contact occurs (boundary lubrication regime, Figure 2.2) [2; 4; 5].

### 2.1.4 Theory of the third body

In an attempt to create a unified approach to wear and friction, Maurice Godet in the 1970's introduced the concept of the third body. Third bodies can be defined as a zone between the two first bodies, enclosed by frontiers close to the surface, which mark a change in composition or structure from the bulk material [6]. Similar to a fluid, the solid third body transmits the load, participates in the velocity accommodation mechanism and separates the first bodies [7; 8].

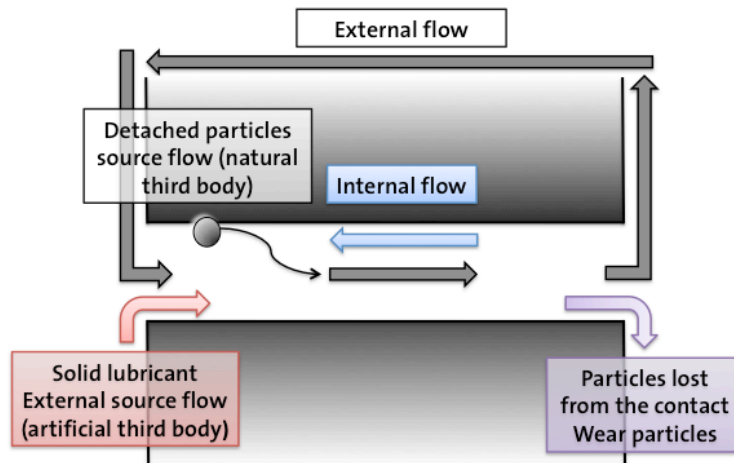


**Figure 2.3: tribological circuit (adapted from [9])**

The sliding process can be described as a closed system, in which the moving interfaces cause some particles to detach; some of those particles stay in the contact, some others are recirculated in the contact, and only a few of them are lost as wear particles (Figure 2.3) [9; 10]. The particles trapped in the contact can participate in withstanding the load and accommodating the difference in velocity (Figure 2.4) [8; 11; 12]. A material is likely to produce an effective third body when it is capable of forming particles that can later be compacted and which adhere well to both its bulk and the counter-face material [6; 13; 14].

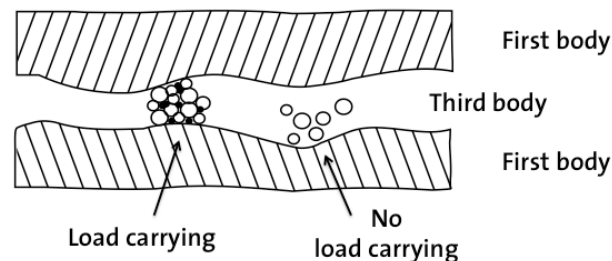


**Figure 2.4: schematic of a sliding contact with formation of wear (adapted from [9])**

Tribochemical films constitute one of the many kinds of 'third bodies' that facilitate sliding at moving interfaces. Understanding the properties of the third bodies

generated during sliding is fundamental if we wish to design long-lasting tribomaterials [13].

## 2.2 Tribochemistry

Tribochemistry concerns the reactions occurring between lubricant and surfaces. This branch of tribology is an interdisciplinary field, in which both physical and chemical phenomena are interacting synergistically. The experimentally observed influence of friction on the chemical reactions is the acceleration of reactions known as ‘tribochemical reactions’ [15].

### 2.2.1 Lubricant additives

The development of modern engine and transmission technologies would have been impossible without advanced lubricant additives chemistry and formulations. Lubricants for industrial applications, such as internal combustion engines, contain a large variety of additives [16]. The most common package of additives used in oil formulations contains anti-wear and extreme-pressure (EP) lubrication additives, oxidation inhibitors, corrosion inhibitors, detergents, dispersants, viscosity improvers, pour-point depressants and foam inhibitors [2].

Anti-wear additives and friction modifiers are probably the most important of all the additives used in oil formulations [2].

### 2.2.2 The tribochemical nature of antiwear films

Zinc dialkyldithiophosphates (ZnDTP’s) are the most commonly used antiwear additives in engine and other industrial lubricants by virtue of their antiwear, corrosion inhibition and antioxidant properties [17]. Like other phosphorus-based additives they are able to react at the surface under tribological conditions to form a protective layer, the “*tribofilm*” (Figure 2.5), which is able to prevent further wear or scuffing [18]. Numerous studies have shown that these tribofilms are mainly composed of zinc and iron glassy poly(thio)phosphates [17; 19-21].

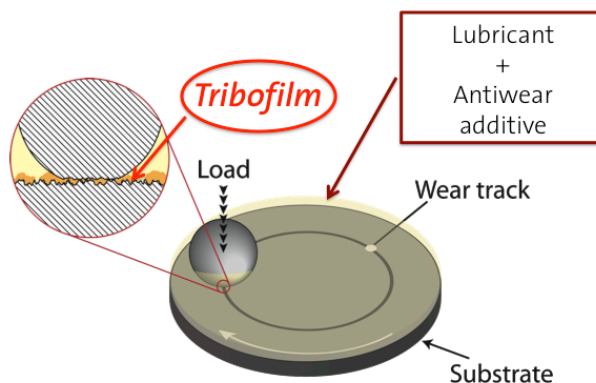


Figure 2.5: Tribofilm formation

ZnDTP and its degradation products, while also being toxic *per se*, can decrease the activity of downstream catalytic converters [17], thereby putting the vehicle out of environmental compliance. These implications led to the need to develop new, “ashless”, or metal-free lubricants [22]. The state of the art of the tribochemistry of ZnDTPs and ashless phosphorus-based additives can be found in the following sections.

### 2.3 P-based antiwear additives: ZnDTPs and ashless additives

#### 2.3.1 ZnDTP reactions in solution

A simplified schematic of zinc dialkyldithiophosphate (ZnDTP) general formula is represented in Figure 2.6.

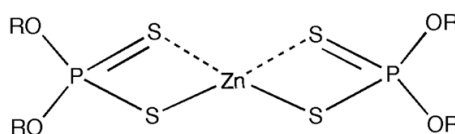


**Figure 2.7: General formula of ZnDTP (the R group can be an alkyl- or aryl-dithiophosphate)**

The decomposition of this molecule in oil solution can take place following two main mechanisms: oxidation [23] and thermal decomposition [24].

The oxidative decomposition mechanism renders ZnDTP a highly effective oxidation inhibitor. ZnDTP was found to decompose hydroperoxides and peroxy-radicals, thereby interrupting the peroxide oxidation cycle [17]. The numerous chemical reactions that might be involved in the process have been summarized by Willermet in [23]. It is commonly accepted that the decomposition products of ZnDTP formed by this route are no longer able to produce effective antiwear tribofilms [17].

At temperatures between 130 and 230°C a completely different decomposition mechanisms takes place. Organothiophosphates, in general, are strong alkylating agents. The migration of an alkyl group from the oxygen to the sulfur atom in the ZnDTP molecule, caused by an initial nucleophilic attack, has been observed by many authors [25-27]. The RS group is then very easily displaced by the attack of a phosphoryl group, leading to the formation of poly(thio)phosphates [17; 25].

#### 2.3.2 ZnDTP thermal and tribo-film formation and composition

Thermal films are the result of the immersion of a metallic sample in a ZnDTP heated solution for a certain time, as opposed to tribofilms, which are formed under tribological conditions when combining heat and mechanical stress. The ZnDTP molecules are degraded on a metal surface at much lower temperatures than those necessary for their degradation in solution [28]. The full mechanism of film formation

is still not clear, but it has been shown that ZnDTP adsorbs on the metal surface via the P=S sulfur atom [17]. At temperatures above 80°C the adsorbed molecules decompose thanks to the presence of metal that acts as a catalyst [17; 29]. Thermal films, like tribofilms, are mainly constituted of polyphosphates, but with a higher zinc content than the corresponding tribofilms [30]. Longer-chain-length polyphosphates are formed at higher temperatures. Sulfate and sulfide species are sometimes also detected in the thermal films, but the composition of the film is depleted in S in comparison with the oil solution [28]. These thermally formed films also show resistance to rubbing [17; 29].

It is clear that different mechanisms are involved in the formation of thermal films and tribofilms. As previously mentioned, at room temperature, ZnDTP molecules only interact weakly with the steel surface, but under sliding conditions the additive is able to react and form a thin tribofilm, about 5 nm in thickness [20]. Moreover, a direct proportionality between the rate of growth and the product of sliding distance and rubbing time has been found [31], proving that the formation of the tribofilm is promoted by the tribological stress.

On the tribological films formed at room temperature, phosphates, no polyphosphates, and some sulfides and organosulfur species have been found. An increase in the growth rate of phosphates was observed with increasing applied loads [20]. At higher temperatures with tribological stress the formation of longer polyphosphates and thicker films (about 3.5 nm at 180°C [32]) is observed, while the application of higher loads resulted in shorter poly(thio)phosphate chain lengths and to an increase in the film thickness [32; 33] (about 6nm at 150°C and 10N [33]).

The final thickness of the tribofilm is a consequence of an equilibrium between the wear rate and the reaction kinetics of film formation, and therefore it is influenced by all experimental conditions [34]. ZnDTP's ability to change its properties according to experimental conditions has certainly contributed to its successful use as an antiwear additive, but it can also explain the apparent disagreement in the literature on the exact thickness, structure and chemistry of the films. Gellman and Spencer [18] represented the general structure of a tribofilm formed on steel in presence of ZnDTP in the following scheme:

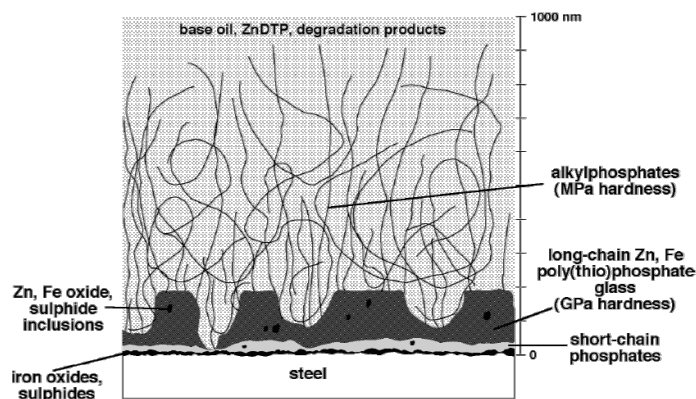


**Figure 2.8: Structure of a tribofilm formed on steel in the presence of ZnDTP [18]**

Underneath a viscous layer, which may easily be removed by solvent washing, a film consisting of amorphous zinc and/or iron polyphosphates is formed [18; 20; 21; 35; 36]. This tribofilm is presumed to have a layered structure: at the bottom a short-chain-length polyphosphate layer should be present, intergrown with the iron oxide film. The top layer is thinner and comprises long-chain-length polyphosphates. This model was substantiated by many experimental investigations [32; 37; 38]. Since it is unlikely that there is a clear interface between the different layers, but rather a gradual transition [18], ZnDTP tribofilms are often described as containing a gradient in composition.

The mechanism of formation of such a polyphosphate layer is still unclear. Numerous pathways for the decomposition of ZnDTPs have been identified [23] and the different mechanisms proposed agree with the fact that physisorption and thermo/oxidative degradation are the first two steps of the process [39]. Different theories as to how the long-chain-length polyphosphates are formed after the decomposition of ZnDTP have been formulated:

- The products of the thermo/oxidative degradation are phosphates that subsequently form polyphosphates by condensation [23].
- The products of the thermo/oxidative degradation are long chain-length polyphosphates, which depolymerize in the presence of iron cations [28; 37].

The experimental results shows that shorter polyphosphate chains are present in the tribological scars rather than in the non-contact regions, and that higher loads give rise to shorter chain-lengths [32; 40]. However, the origin of different chain-length polyphosphates in the tribofilms and the role potentially played in the antiwear mechanism is still under debate.



### 2.3.3 *Mechanical Properties and antiwear mechanism of ZnDTP tribofilms*

The thickness of a tribofilm ranges from a few nm to several hundreds of nm. They exhibit a complex pad-like structure, high roughness and heterogeneous composition. An appropriate mechanical characterization of such films is technically very difficult and, in practice, nanoindentation is the only tool available for these investigations.

A hardness of 1.5 GPa was measured by Aktary [41] on the thermal films, while the tribofilm showed values between 3 and 5 GPa. A similar range of values was also measured by Bec, who was the first to observe that the mechanical properties of the tribofilms change with different applied conditions, in particular the hardness was found to be always similar to the load applied during the test [35]. This ability to accommodate to conditions led to ZnDTP tribofilms being dubbed ‘smart’ materials.

Using nanometer-scale chemical and mechanical characterization methods, Nicholls attempted a first correlation between the chain-length and the mechanical properties of polyphosphates, proposing that the long-chain polyphosphates could enhance the tribofilm’s antiwear behaviour because of their higher mechanical properties in comparison to short-chain polyphosphates [42]. This interpretation was based on the observation that the reduced modulus  $E^*$  measured on the larger pads, containing longer chain-length polyphosphates, was much higher than the modulus measured in the valleys, in which only short chain-length polyphosphates were found.

In fact, there is no agreement on the influence of the composition and chain length on the mechanical properties of the film. For example, it is still not clear if the tribofilm antiwear efficiency benefits from the presence of short or long chain-length polyphosphates. Martin, in 1999, was the first to propose that the reaction between long chain-length polyphosphates and iron oxide, energetically favorable on the basis of the principle of hard and soft acids and bases (HSAB) [43], could also play a role in the antiwear mechanism [44]. According to his hypothesis the long chain-length polyphosphates could limit wear by “digesting” the abrasive iron oxide particles, forming zinc oxide and shorter-chain-length mixed iron/zinc phosphates [19; 38; 45]. It is also believed that the presence of mixed iron/zinc phosphates at the bottom of the tribofilm could promote the adhesion of the tribofilm itself to the steel substrate [19]. While there is still not clear experimental evidence of this mechanism, the most commonly accepted model for the antiwear resistance of ZnDTP is that the polyphosphate film acts as a sacrificial mechanical barrier [17]. The wear would take place in the phosphate layer and be continuously replenished by the reaction of ZnDTP present the solution. When the wear conditions become more severe and the phosphate layer is disrupted, the ability of ZnDTP to produce sulfides confers to the additives its extreme-pressure (EP) antiwear action [17; 46]. However experiments

have shown that, in the mild-wear regime, the tribofilms resist tribological stress and wear only very slowly when the ZnDTP solution is replaced with base oil [31].

The study of model systems of ZDTP tribofilms, such as polyphosphates, has been considered in order to reduce the complexity of real systems. Gauvin tested the behavior of pure zinc orthophosphate powder as an antiwear additive. Under boundary-lubrication conditions, the orthophosphate formed an adherent film on the steel substrate. This film was found to reduce wear [47].

#### 2.3.4 “Ashless” additives directly derived from ZnDTP

“The future of ZnDTP has become very uncertain” was written by Spikes in an eloquent editorial that opened a special issue of *Lubrication Science* published in 2008, dedicated to “ashless” (metal-free) additives [48]. The degradation products of ZnDTP, metal salts, sulphur and phosphorus oxides, are able to poison the activity of downstream catalytic converters and thus the permitted level of these harmful components in modern lubricant specifications is becoming lower and lower [22]. For these reasons there is great interest in identifying new additives that, while being environmentally friendly, are still able to replace the antioxidant and antiwear action of ZnDTPs.

The success of ZnDTP has led researchers to investigate the ashless equivalents obtained by substituting zinc with an organic group (for example mono- and di-thiophosphates), but also more generally, molecules containing sulfur and phosphorus (organosulfur compounds, phosphate esters, etc) [22].

Ashless additives have been an important research topic at the ETH Laboratory for Surface Science and Technology (LSST). F.M. Piras studied in detail the surface reactivity of tributyl thiophosphate (TBT) using in-situ ATR-FT-IR and ex-situ XPS [49]. R. Heuberger studied the reactivity of alkylated phosphorothionates. He tested the tribological performance in comparison with the pure PAO and the ZnDTP. The tribological behavior of the additives investigated was not comparable with that of ZnDTP. The films formed in the presence of phosphorothionates were thinner than those formed from ZnDTP and contained half of the phosphorus and one fourth of the sulphur. Moreover, the predominant sulphur species were sulphates rather than the sulphides typical of ZnDTP tribofilms. The chain length of the iron phosphate in the tribofilms was longer at higher temperatures, but still not comparable with the long chains formed by ZnDTP. A study of the thermal reactivity of these molecules in oil solution has been carried out at LSST by F. Mangolini [50] and he showed that phosphorothionates (see Figure 2.9) do not possess comparable antioxidant properties to ZnDTP [51].

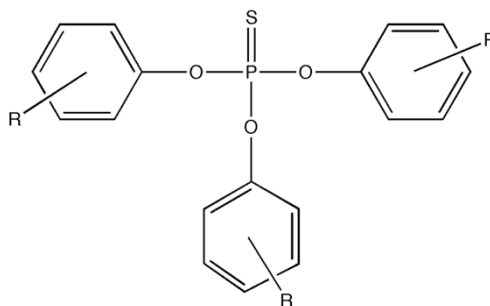


**Figure 2.9: Chemical structure of triphenyl phosphorothionates (TPPTs), in which the alkyl chain R is H (TPPT), t-butyl (b-TPPT) or p-nonyl (TPPT)**

The reactivity of the molecules, both in solution and on steel, turned out to be strongly dependent on the architecture of the molecule. The thermal films formed in the presence of phosphorothionates showed a much lower resistance to wear than ZnDTP thermal films [51].

It is clear that understanding the reasons for these differences could facilitate research into the replacement of ZnDTP.

#### 2.4 Polyphosphate glasses

Research on polyphosphate glasses has been recently stimulated by the wide range of technical uses of these compounds. The materials are good candidates for various optical applications, such as optical waveguides and high-power lasers. They have been considered as materials for nuclear-waste immobilization and, thanks to their very high thermal-expansion coefficient, as materials for hermetic seals. Phosphate-based glasses have unique dissolution properties in aqueous fluids: The P-O-P linkages present in the glass networks can be hydrolyzed [52], which results in poor water durability, therefore limiting potential practical uses of these materials. On the other hand, this poor chemical durability to hydrolysis renders these compounds useful as bioactive functional materials in applications such as hard- and soft-tissue engineering and controlled-release glasses [53]. The introduction of dopants can also be used for tuning their biocompatibility [54], their biological functionalities [53], and for improving their chemical durability [55].

Polyphosphate glasses have also been found to be responsible for the good antiwear properties of phosphorus-based engine-oil additives. As already described in the previous section (paragraph 2.1), these additives are able to react at the interface between two sliding surfaces to form a reaction film—the so-called tribofilm. In the field of tribology, the hope of understanding the antiwear mechanism of phosphorus-based additives has led to renewed interest in investigating the mechanical and tribochemical properties of zinc and iron polyphosphates [47; 56].

### 2.4.1 Composition and structure

Polyphosphates are formed by repeated condensation of tetrahedral  $\text{PO}_4$  groups, which, by linking through covalent bridging oxygen atoms, can share their corners with similar tetrahedra. The tetrahedra can be classified by the number of bridging (P-O-P) oxygens per tetrahedron ( $Q^i$  terminology, see Figure 2.10), while a common way to classify the networks of phosphate glasses is to take into account the oxygen to phosphorus ratio. Depending on the  $[\text{O}]/[\text{P}]$  ratio, the number of tetrahedral linkages through bridging oxygen atoms changes and a wide range of compositions and structures is possible [57; 58].

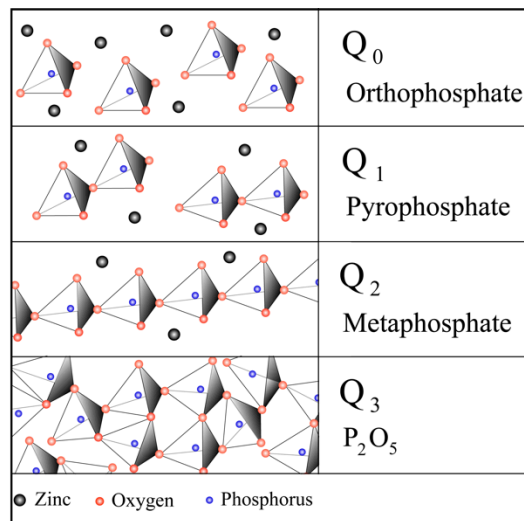


**Figure 2.10: Terminology for different composition and structures in zinc polyphosphate glasses**

Vitreous  $\text{P}_2\text{O}_5$  is formed by a cross-linked network of  $Q^3$  tetrahedra. Each tetrahedron is linked to three other tetrahedra and to a terminal oxygen  $\text{P}=\text{O}$ . When a modifying oxide is added to  $\text{P}_2\text{O}_5$  the network is depolymerised and the concentrations of  $Q^i$  tetrahedra are then dependent on the glass composition (fig 3)[59].

Considering a binary  $x\text{R}_2\text{O} (1-x) \text{P}_2\text{O}_5$ , it can be classified as follows:

- Ultraphosphate glasses ( $0 \leq x \leq 0.5$ ;  $2.5 \leq [\text{O}]/[\text{P}] \leq 3.0$ )
- Metaphosphate glasses ( $x=0.50$ ;  $[\text{O}]/[\text{P}]=3$ )
- Polyphosphate glasses ( $x > 0.50$ ;  $[\text{O}]/[\text{P}] > 3$ )
- Pyrophosphates ( $x=0.67$ ;  $[\text{O}]/[\text{P}]=3.5$ )
- Orthophosphates ( $x=0.75$ ;  $[\text{O}]/[\text{P}]=4$ )

Since they contain P atoms in the fully oxidized state, the condensed phosphates are reasonably stable to chemical attack. However the P-O-P linkages can be easily broken by hydrolysis, resulting in poor water durability [52].

Van Wazer in 1958 [60] described metaphosphates and polyphosphates as structures based on polyphosphate anions with an average chain length given by:

**Equation 2.2**

$$n_{av} = 2(1-x)/(2x-1)$$

The results obtained with zinc polyphosphate glasses showed that  $n_{av}$  can be computed directly from the glass composition when the presence of ring anions can be neglected [61]. Near the metaphosphate composition, long-chain structures are mainly present, while cross-linked chains and rings, typical of the ultraphosphate region, disappear [62; 63]. At higher concentrations of ZnO, a depolymerization of the phosphate network is observed and the long chains are transformed into trimers, dimers and monomers as the composition approaches orthophosphate [62; 63]. From detailed  $^{31}\text{P}$  MAS-NMR studies, it has been shown that the glasses near the pyrophosphate composition undergo a disproportionation reaction (**Figure 2.11**): while the overall  $n_{av}$  stays unchanged, the concentration of  $Q^2$  and  $Q^0$  tetrahedra is higher than predicted [59; 64]. This increased structural complexity might contribute to increasing the compositional range for zinc polyphosphate glass formation. High-performance liquid chromatography (HPLC) has also been used to determine the distributions of phosphate-anion chains and rings and thus to provide detailed structural information [61-63].

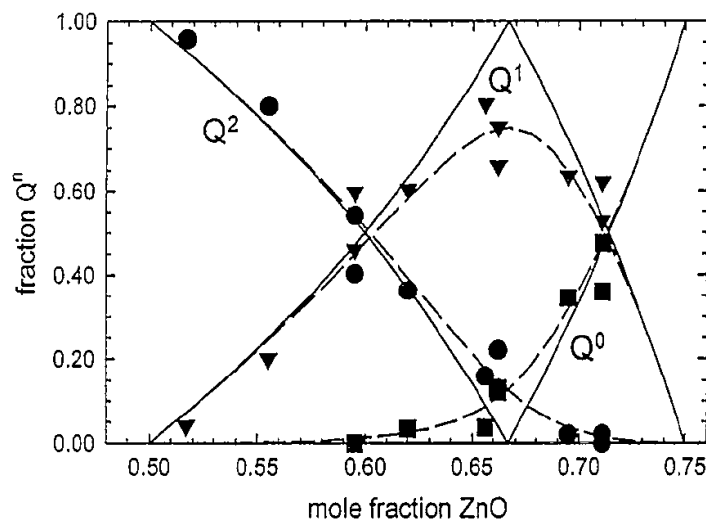


**Figure 2.11: The effect of composition on the  $Q^i$  distributions determined by  $^{31}\text{P}$  MAS-NMR (closed symbols) [59]**

The possibility of synthesizing zinc polyphosphate glasses over a wide compositional range is the main reason why they have often been chosen, among many other different binary phosphate glasses, for detailed structural studies. Zinc phosphate glasses show a discontinuity in the composition-property dependence of refractive index, mass density and glass transition temperature ( $T_g$ ) in the transition from ultra- to polyphosphate composition [65; 66]. It has been observed, for example,

that the  $T_g$  values go through a minimum between metaphosphate and pyrophosphate composition. A change in coordination of the  $Zn^{2+}$  cation from 4 to 6 at the metaphosphate composition has been hypothesized for explaining this anomalous behavior. However, this theory has not so far been supported by any experimental evidence. On the contrary, the Zn coordination number, studied by means of neutron and x-ray diffraction (XRD) [66; 68-71], was found to be nearly constant with the composition at an average value of 4 [65; 66; 68-71]. The origin of the anomaly has rather to be found in a change of the short- and medium-range ordering of  $PO_4$  and  $ZnO_4$  tetrahedra [59; 64-66]. The value of the zinc coordination is nevertheless lower when compared to its crystalline form: the presence of long chains, in fact, constitutes a sterical inhibition to the reorganization of the glasses, resulting in a more open structure and a larger molar volume [59].

The short- and medium-range order of polyphosphate glasses is also affected by the cation field strength. The phosphate chains are linked between them through the bonds between the terminal oxygens and the modifying cations. Raman spectroscopy [59; 72] and infrared spectroscopy (IR) [72-80] have been commonly employed for studying the structure of polyphosphates and they have shown that the modifier M-O bond becomes increasingly covalent as the field strength of the modifier increases, resulting in more rigid networks [58]. The nature of the modifier, M-O-P, bonds will then affect the properties of the glass, i.e., glass transition temperature, much more than the P-O-P bonds [58].

About twenty years ago it was discovered that the addition of iron phosphate to sodium or other phosphate glasses dramatically increases their chemical durability. Iron containing polyphosphate glasses possess both  $Fe^{2+}$  and  $Fe^{3+}$  ions, even when the starting batch includes only  $Fe_2O_3$  [55; 81; 82]. Both ions occupy octahedral coordination sites, but  $Fe^{3+}$  can occupy two sites, both octahedral, with different levels of disorder and distortion [55; 83]. Changes in the glass properties with the replacement of P-O-P bonds with P-O-Fe bonds results from the ability of  $Fe^{3+}$  to strengthen the phosphate chains and also from the shortening of the average chain-length [84].

#### 2.4.2 Surface analysis

XPS analysis of phosphate glasses was first performed in the 1970s. It was observed that the O1s signal could be curve-fitted with two components: the first component could be assigned to the bridging P-O-P oxygen atoms (BO), while the second component included two kinds of terminal oxygen atoms, P=O and P-O-M. Since the chemical shift between these latter two signals, i.e. P=O and P-O-M, is small and, therefore, they cannot be distinguished by any XP-spectrometer, a single peak, labeled as non-bridging oxygen (NBO), is usually used in XPS curve-fitting procedures [85; 86]. Moreover some diffraction studies [58] together with *ab initio*

molecular-orbital calculations suggest that there is no P=O bond but that the electrons are delocalized over each non-bridging oxygen [58]. The identification of the chain length in polyphosphate glasses, including some binary zinc phosphates [61; 87; 88], on the basis of the BO-to-NBO ratio has been extensively reported in the literature [20; 21; 32; 33; 49; 84; 89-92]. Previous studies have also shown that the P 2p binding energy is dependent on the metal oxide content of the glass [91]. The XPS analysis of some Fe-containing glasses allowed not only the quantification of the average chain-length of the glasses, but also the determination of the average oxidation state [84].

A limitation to the surface analysis of polyphosphate glasses is that they are not inert to ion-beam sputtering. Ion-beam sputtering is used as excitation source in SIMS and often used in XPS for obtaining ‘sputter-cleaned’ surfaces or depth profiles. Phosphate glasses have been shown to exhibit preferential sputtering of phosphorus under low-energy ion bombardment, resulting in a depolymerization of the glasses [93]

#### 2.4.3 Mechanical properties

Polyphosphate glasses are characterized by poor mechanical properties when compared to silicate glasses, which limits their practical applications [94-96]. Recently it has been observed that the structural strength of these glasses is increasing with the degree of connectivity, as for other oxide systems [81; 94; 95]. Moreover, their structural strength is not only governed by the energy of the chemical bonds forming the phosphate chains, but also by the ionic interactions between the chains, which are determined by the field strength of the modifier ions [94].

A model for calculating the elastic modulus from the total bonding energy per unit volume of glass [97] has been proposed. The total bonding energy,  $U_m$ , can be calculated as a function of the dissociation energy,  $G_i$  and of the mole fraction,  $X_i$ , of the  $i$ th oxide:

$$U_m = V_t \sum_i G_i X_i$$

**Equation 2.3**

$V_t$  is the atomic packing density of the glass defined as the ratio between the sum of the volumes of all the atoms involved in one mole of the glass,  $v$ , and the molar volume of the glass:

$$V_t = \frac{\rho}{M} \sum_i v_i X_i$$

**Equation 2.4**

$\rho$  is the density and  $M$  the molecular mass of the glass [54; 94; 98]. Values for  $G_i$  and  $\nu_i$  can be found in [97; 99] for many of the most common oxides.

Baikova et.al. investigated four systems of phosphate glasses and found that there is a linear dependence of the Young's modulus on the total bonding energy per unit volume of the glass [94; 97]. Therefore it is possible to estimate changes in the Young's modulus with changes in composition. In general the presence of di- and trivalent rather than monovalent oxides will increase the Young's modulus and the mechanical strength of the glasses [95].

## 2.5 Surface-analytical techniques in tribology

The tribofilms formed on tribostressed surfaces in the presence of antiwear additives generally have a thickness ranging from 10 to 200 nm and a heterogeneous composition in both vertical and lateral directions. In order to follow and identify the tribochemical reactions taking place at the surface, it is necessary to gain information about the elements in the film, their chemical state and their distribution in space. X-ray absorption near-edge spectroscopy (XANES) is a powerful technique that provided many of the results reviewed in Section 2.2. XANES provides a sampling depth of 5 nm in total electron yield (TEY) and 60 nm in fluorescent field (FY), with a lateral resolution of 500 nm [37]. Zinc and iron are detected, but only with some difficulty. Another limitation of this technique is that requires the access to a synchrotron radiation source. X-ray photoelectron spectroscopy (XPS), in contrast, is an easily accessible technique that can be used to reconstruct the quantitative distribution of the elements and their chemical states, with a depth resolution in the nm range [100-102]. Auger Electron Spectroscopy (AES) can achieve a lateral resolution in the nanometer range, but its application in tribology [38] has been limited because it fails to provide information on the molecular level and problems can arise if the films are not conductive. Excellent lateral resolution—a few hundreds of nm—and a depth resolution in the monolayer range, make ToF-SIMS a good additional candidate to investigate tribofilms.

### 2.5.1 XPS and the challenges of tribochemistry

X-ray photoelectron spectroscopy (XPS) has been already extensively applied to tribology in order to investigate the surface chemistry of mechanically stressed samples [20; 21; 32; 33; 51]. Imaging XPS (i-XPS) and angle resolved XPS (AR-XPS) have been used to determine the composition of thermal films and tribofilms, spatially and in-depth, respectively [32; 33; 103; 104].

Chain-length identification by means of XPS normally relies on the BO/NBO ratio, as described in Section 2.4.2. However, the quantification of the BO/NBO ratio turns out to be easily affected by the presence of contaminants or other compounds,



such as iron oxides and hydroxides for example. Another practical limitation is the dramatic change induced in the glass surface composition by ion-beam sputtering, commonly used to obtain contamination-free surfaces for XPS analysis or to perform sputtering depth profiles [93]. Previous studies have also shown that the P 2p binding energy is dependent on the metal oxide content of the glass [91], but a systematic study on pure zinc and iron polyphosphates to serve as reference compounds has not existed until now.

Complementary information to that provided by the core-electron photo-electronic signals could also be obtained by investigating the valence-band region and the Auger signals. The valence-band region allows chemical information to be obtained that cannot be identified from the core levels [105]. A few studies have already shown that the XPS valence band could be used to distinguish oxides from phosphate compounds and also differentiate between different phosphates [106]. Another powerful tool that can gain important chemical information is the Auger parameter and its representation in the so-called Wagner plot [107]. The use of such an approach could make it possible to identify chemical states unequivocally and learn about the local chemical environment of core-ionized atoms [108-110].

### 2.5.2 ToF-SIMS: a rapidly developing technique

ToF-SIMS can provide complementary information to XPS, thanks to its monolayer surface sensitivity combined with excellent lateral resolution (on the order of 100 nm). ToF-SIMS imaging of elements (Zn, Fe, Ca, P, S) and low-mass ions ( $\text{PO}$ ,  $\text{PO}_2$ ,  $\text{PO}_3$ ) has been already successfully applied to tribological samples [45; 111-113]. In Figure 2.12, from the work of Rossi et al. [112], the ToF-SIMS image of a wear track formed on steel in the presence of ZnDTP is reported.

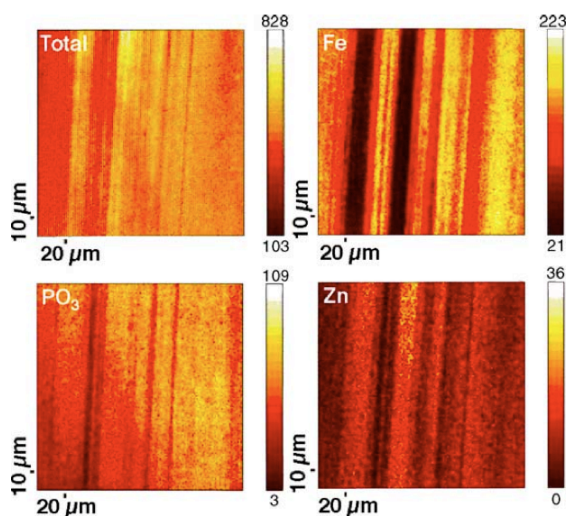
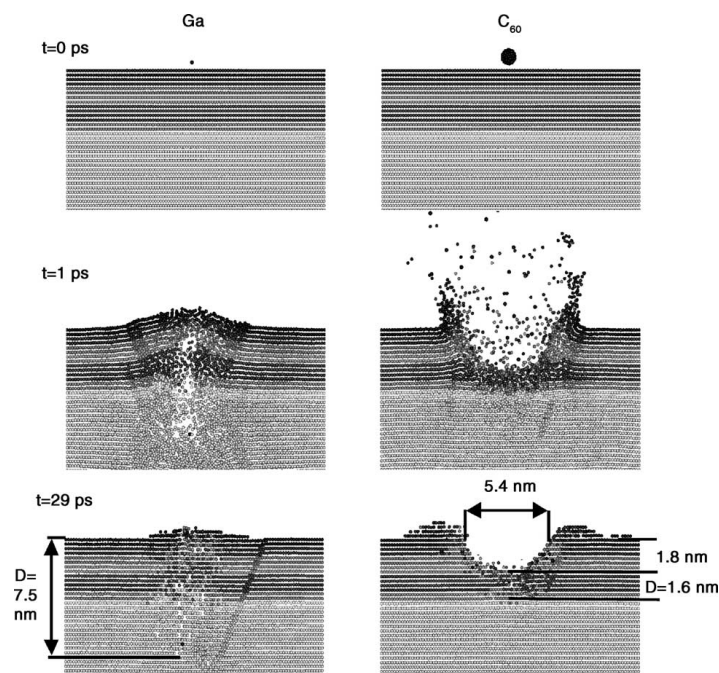


Figure 2.12: Wear track formed on a steel disc in presence of ZnDTP [112]

Murase also investigated adsorption and reaction of phosphate-type lubricant additives (zinc and sulfur free) on ferrous materials by ToF-SIMS [114].

The capabilities of such a technique have not been pushed to the limits in tribology so far. The recent introduction of polyatomic primary ion sources has been found to improve the yield of secondary ions [115]. The use of cluster projectiles, in fact, improves the ion-formation efficiency, allowing the detection of high-mass molecular fragments with good signal-to-noise ratio [116].

Moreover it has been observed that the related surface damage is significantly lower than that arising from monoatomic projectiles, because the deposition of collision energy is closer to the surface [115; 117]. The physics of the phenomena are still under investigation but the first molecular-dynamics results already gave a good representation of it: while monoatomic projectiles cause the ejection of a small number of particles and they cause the damage of several nm of the material, polyatomic projectiles cause the ejection of many more particles but the damage is limited to the first one or two monolayers (see Figure 2.13 from Postawa [117]). The use of cluster primary ions improves the sensitivity of the technique, allowing the static limit to be overcome and broadening the possible applications of ToF-SIMS to many analytical systems, especially polymers, organic and biological samples.



**Figure 2.13: Results of the molecular dynamics simulation of the impact of two different projectiles: monoatomic Ga and polyatomic C<sub>60</sub> [117]**

This approach has been applied to the identification of different calcium phosphate phases of six biologically interesting calcium phosphate phases [118; 119]. Chusuei was able to distinguish between the different samples using the relative PO<sub>3</sub><sup>-</sup>

$/\text{PO}_2^-$  secondary ions (SI) ratios in conjunction with the XPS quantitative analysis [118]. Later Lu carried out a principal component analysis (PCA) of the ToF-SIMS data, which led the author to the conclusion that a discrimination between the phases can be achieved by comparing the corrected intensities of few characteristic ions, such as  $\text{PO}_3^-$ ,  $\text{O}^-$ ,  $\text{Ca}^+$ ,  $\text{PO}_2$  and  $\text{OH}^-$  [119].

ToF-SIMS spectra contain such an enormous amount of information that their interpretation can become daunting. The use of multivariate analysis (MVA) as a help to data interpretation is becoming more and more common in the SIMS community and the number of experimental studies showing successful practical applications of MVA to complex sets of data is exponentially increasing [120]. Thanks to its fast development, the increasing importance of ToF-SIMS in many technical applications can be undoubtedly foreseen.

## 2.6 Summary

The complex topic of ZnDTP and ashless thiophosphate tribochemistry has been reviewed in this chapter. There are still numerous open questions on the formation of the tribofilms, their composition, mechanical properties and antiwear mechanism. Some of these questions are summarized in the following:

- Many analytical techniques have been employed in an attempt to determine the chain length of polyphosphate glasses in the tribofilms. A systematic analytical study of the pure compounds for the validation of the analytical method is not available for any of these surface-analytical techniques. Even for XPS, the most used approach, the use of the BO/NBO ratio alone is not robust enough when applied to complex tribofilms. Is there a strategy that can allow reliable chain-length determination from XPS spectra?
- Recent new technical developments have made ToF-SIMS a very appealing technique, thanks also to its capability of providing monolayer information depth and high spatial resolution. Is it possible to use ToF-SIMS alone or in combination with other techniques, in order to discriminate between different chain-length polyphosphates?
- Many points in the mechanism of formation of ZnDTP tribofilms are still controversial. What is the difference between thermal and tribofilms and what is the role played by tribochemical reactions? What is the role of sulfur, metallic iron and temperature in the mechanism of film formation?

- Why are long-chain-length polyphosphates found only at the outermost layer of the tribofilm?
- Does the tribofilm functionally benefit from the presence of long or short chain-length polyphosphates?
- Is the iron oxide reacting with the polyphosphates in the tribofilm? And what is the effect of this reaction on the antiwear properties?
- How are pressure and shear stress affecting the composition and mechanical properties of the tribofilm?
- Is there a difference between the mechanical and/or tribochemical properties of long and short chain-length polyphosphates? And between zinc and iron polyphosphates? And their mixtures?
- What is the difference between the tribofilms formed in the presence of ZnDTP and those formed in the presence of ashless thiophosphates? Why do ashless thiophosphates not possess a similar effective antiwear action to ZnDTP?

The study of bulk polyphosphate glasses described in the following chapters (see Outline in Figure 1.1) will provide answers to some of these questions, as well as new insights into the tribochemistry of antiwear additives, but new questions will also be added to the list.

The synthesis of polyphosphate glasses as pure compounds will also provide the possibility to develop robust analytical methods to reliably determine the polyphosphate chain-length by XPS and, for the first time, by ToF-SIMS.

## ***References***

- [1] Hutchings I. M.: *Tribology, Friction and Wear of Engineering Materials*, London (1992).
- [2] Stachowiak G. W., and Batchelor A. W.: *Engineering tribology*, Elsevier, Amsterdam (1993).
- [3] *Modern Tribology Handbook*, CRC Press LLC, Boca Raton (2001).
- [4] Myshkin N. K., Kim C. K., and Petrokovets M. I.: *Introduction to tribology*, Cheong Moon Gak, Seoul (1997).
- [5] Glaeser W. A.: *Characterization of tribological materials*, Manning Publications Co., Stoneham (1993).

- [6] Godet M.: Extrapolation in tribology. *Wear* 77, 29-44 (1982).
- [7] Iordanoff I., Berthier Y., Descartes S., and Heshmat H.: A Review of Recent Approaches for Modeling Solid Third Bodies. *Journal of Tribology* 124, 725-735 (2002).
- [8] Descartes S., and Berthier Y.: Rheology and flows of solid third bodies: background and application to an MoS<sub>1.6</sub> coating. *Wear* 252, 546-556 (2002).
- [9] Berthier Y.: Maurice Godet's Third Body. in: Dowson, D., Taylor, C. M., Childs, T. H. C., Dalmaz, G., Berthier, Y., Flamand, L., M., G. J., and Lubrecht, A. A., (Eds.), *Tribology Series*, Elsevier, 1996, pp. 21-30.
- [10] Singer I. L., Le Mogne T., Donnet C., and Martin J. M.: Third body formation and friction reduction on Mo/SiC sliding in reactive gases. in: Dowson, D., Taylor, C. M., Childs, T. H. C., Dalmaz, G., Berthier, Y., Flamand, L., M., G. J., and Lubrecht, A. A., (Eds.), *Tribology Series*, Elsevier, 1996, pp. 79-90.
- [11] Ludema K. C.: Third Bodies: Perspectives on Modeling in Lubricated Contacts, in close fitting contacts, Etc: Following on the Concepts of Dr. Maurice Godet. in: Dowson, D., Taylor, C. M., Childs, T. H. C., Dalmaz, G., Berthier, Y., Flamand, L., M., G. J., and Lubrecht, A. A., (Eds.), *Tribology Series*, Elsevier, 1996, pp. 3-19.
- [12] Hou K., Kalousek J., and Magel E.: Rheological model of solid layer in rolling contact. *Wear* 211, 134-140 (1997).
- [13] Singer I. L.: How Third-Body Processes Affect Friction and Wear. *MRS Bull.*, 37-40 (1998).
- [14] Singer I. L.: Mechanics and chemistry of solids in sliding contact. *Langmuir* 12, 4486-4491 (1996).
- [15] Pawlak Z.: Preface. in: Zenon, P., (Ed.), *Tribology and Interface Engineering Series*, Elsevier, 2003, pp. v-vii.
- [16] Chapter 2 Lubrication chemistry. in: Zenon, P., (Ed.), *Tribology and Interface Engineering Series*, Elsevier, 2003, pp. 11-66.
- [17] Spikes H.: The History and Mechanisms of ZDDP. *Tribol. Lett.* 17, 469-489 (2004).
- [18] Gellman A., and Spencer N.: Surface chemistry in tribology. *Proceedings of the Institution of Mechanical Engineers, Part J: Journal of Engineering Tribology* 216, 443-461 (2002).
- [19] Minfray C., Le Mogne T., Martin J.-M., Onodera T., Nara S., Takahashi S., Tsuboi H., Koyama M., Endou A., Takaba H., Kubo M., Del Carpio C. A., and Miyamoto A.: Experimental and Molecular Dynamics Simulations of Tribochemical Reactions with ZDDP: Zinc Phosphate-Iron Oxide Reaction. *Tribol. Trans.* 51, 589 - 601 (2008).
- [20] Eglin M., Rossi A., and Spencer N. D.: X-ray photoelectron spectroscopy analysis of tribostressed samples in the presence of ZnDTP: a combinatorial approach. *Tribol. Lett.* 15, 199-209 (2003).
- [21] Piras F. M., Rossi A., and Spencer N. D.: Combined in situ (ATR FT-IR) and ex situ (XPS) study of the ZnDTP-iron surface interaction. *Tribol. Lett.* 15, 181-191 (2003).
- [22] Hugh Spikes: Low- and zero-sulphated ash, phosphorus and sulphur anti-wear additives for engine oils. *Lubricat. Sci.* 20, 103-136 (2008).
- [23] Willermet P. A., Dailey D. P., Carter R. O., Schmitz P. J., and Zhu W.: Mechanism of Formation of Antiwear Films from Zinc Dialkyldithiophosphates. *Tribol. Int.* 28, 177-187 (1995).
- [24] Dickert J. J., and Rowe C. N.: Thermal decomposition of metal O,O-dialkyl phosphorodithioates. *J. Org Chem.* 32, 647-653 (1967).
- [25] Hilgetag G., and Teichman.H: Alkylating Properties of Alkyl Thiophosphates. *Angew. Chem. Int. Ed.* 4, 914 (1965).

- [26] Coy R. C., and Jones R. B.: The thermal-degradation and EP performance of zinc dialkyldithiophosphate additives in white oil. *Asle Transactions* 24, 77-90 (1981).
- [27] Jones R. B., and Coy R. C.: The chemistry of the thermal-degradation of zinc dialkyldithiophosphate additives. *Asle Transactions* 24, 91-97 (1981).
- [28] Fuller M., Yin Z., Kasrai M., Bancroft G. M., Yamaguchi E. S., Ryason P. R., Willermet P. A., and Tan K. H.: Chemical characterization of tribochemical and thermal films generated from neutral and basic ZDDPs using X-ray absorption spectroscopy. *Tribol. Int.* 30, 305-315 (1997).
- [29] Nicholls M. A., Do T., Norton P. R., Kasrai M., and Bancroft G. M.: Review of the lubrication of metallic surfaces by zinc dialkyl-dithiophosphates. *Tribol. Int.* 38, 15-39 (2005).
- [30] Hershberger J., Ajayi O. O., and Fenske G. R.: Zinc content of ZDDP films formed thermally and mechanically. *Tribol. Int.* 38, 299-303 (2005).
- [31] Fujita H., and Spikes H. A.: The formation of zinc dithiophosphate antiwear films. *PROC. INST. MECH. ENG. J.* 218, 265-277 (2004).
- [32] Heuberger R., Rossi A., and Spencer N. D.: XPS study of the influence of temperature on ZnDTP tribofilm composition. *Tribol. Lett.* 25, 185-196 (2007).
- [33] Heuberger R., Rossi A., and Spencer N. D.: Pressure Dependence of ZnDTP Tribochemical Film Formation: A Combinatorial Approach. *Tribol. Lett.* 28, 209-222 (2007).
- [34] Suominen Fuller M. L., Rodriguez Fernandez L., Massoumi G. R., Lennard W. N., Kasrai M., and Bancroft G. M.: The use of X-ray absorption spectroscopy for monitoring the thickness of antiwear films from ZDDP. *Tribol. Lett.* 8, 187-192 (2000).
- [35] Bec S., Tonck A., Georges J. M., Coy R. C., Bell J. C., and Roper G. W.: Relationship between mechanical properties and structures of zinc dithiophosphate anti-wear films. *Proc. R. Soc. London A* 455, 4181-4203 (1999).
- [36] Martin J. M., Belin M., Mansot J. L., Dexpert H., and Lagarde P.: Friction-Induced Amorphization with ZDDP, an EXAFS Study. *A S L E Transactions* 29, 523-531 (1986).
- [37] Yin Z., Kasrai M., Fuller M., Bancroft G. M., Fyfe K., and Tan K. H.: Application of soft X-ray absorption spectroscopy in chemical characterization of antiwear films generated by ZDDP Part I: the effects of physical parameters. *Wear* 202, 172-191 (1997).
- [38] Martin J. M., Grossiord C., Le Mogne T., Bec S., and Tonck A.: The two-layer structure of Zndtp tribofilms: Part I: AES, XPS and XANES analyses. *Tribol. Int.* 34, 523-530 (2001).
- [39] Nicholls M. A., Do T., Norton P. R., Bancroft G. M., Kasrai M., Capehart T. W., Cheng Y. T., and Perry T.: Chemical and mechanical properties of ZDDP antiwear films on steel and thermal spray coatings studied by XANES spectroscopy and nanoindentation techniques. *Tribol. Lett.* 15, 241-248 (2003).
- [40] Canning G. W., Suominen Fuller M. L., Bancroft G. M., Kasrai M., Cutler J. N., De Stasio G., and Gilbert B.: Spectromicroscopy of tribological films from engine oil additives. Part I. Films from ZDDP's. *Tribol. Lett.* 6, 159-169 (1999).
- [41] Aktary M., McDermott M. T., and McAlpine G. A.: Morphology and nanomechanical properties of ZDDP antiwear films as a function of tribological contact time. *Tribol. Lett.* 12, 155-162 (2002).
- [42] Nicholls M. A., Bancroft G. M., Norton P. R., Kasrai M., De Stasio G., Frazer B. H., and Wiese L. M.: Chemomechanical properties of antiwear films using X-ray absorption microscopy and nanoindentation techniques. *Tribol. Lett.* 17, 245-259 (2004).

- [43] Pearson R. G.: Chemical hardness Wiley, New York (1997).
- [44] Martin J.: Antiwear mechanisms of zinc dithiophosphate: a chemical hardness approach. *Tribol. Lett.* 6, 1-8 (1999).
- [45] Minfray C., Martin J. M., Esnouf C., Le Mogne T., Kersting R., and Hagenhoff B.: A multi-technique approach of tribofilm characterization. *Thin Solid Films*, 272-277 (2004).
- [46] Minfray C., Le Mogne T., Lubrecht A. A., and Martin J. M.: Experimental simulation of chemical reactions between ZDDP tribofilms and steel surfaces during friction processes. *Tribol. Lett.* 21, 67-78 (2006).
- [47] Gauvin M., Dassenoy F., Belin M., Minfray C., Guerret-Piecourt C., Bec S., Martin J. M., Montagnac G., and Reynard B.: Boundary lubrication by pure crystalline zinc orthophosphate powder in oil. *Tribol. Lett.* 31, 139-148 (2008).
- [48] Hugh A. Spikes: Beyond ZDDP. *Lubricat. Sci.* 20, 77-78 (2008).
- [49] Rossi A., Piras F. M., Kim D., Gellman A. J., and Spencer N. D.: Surface reactivity of tributyl thiophosphate: effects of temperature and mechanical stress. *Tribol. Lett.* 23, 197-208 (2006).
- [50] Mangolini F., Rossi A., and Spencer N.: Reactivity of Triphenyl Phosphorothionate in Lubricant Oil Solution. *Tribol. Lett.* 35, 31-43 (2009).
- [51] Mangolini F., Reactivity of Environmentally Compatible Lubricant Additives: an In Situ and Ex Situ Investigation, PhD Thesis No. 19677, ETH Zürich, Zürich, 2011.
- [52] Takebe H., Baba Y., and Kuwabara M.: Dissolution behavior of ZnO-P<sub>2</sub>O<sub>5</sub> glasses in water. *J. Non-Cryst. Solids* 352, 3088-3094 (2006).
- [53] Abou Neel E. A., Pickup D. M., Valappil S. P., Newport R. J., and Knowles J. C.: Bioactive functional materials: a perspective on phosphate-based glasses. *J. Materials Chem.* 19, 690-701 (2009).
- [54] Muresan D., Dragan Bularda M., Popa C., Baia L., and Simon S.: Structural and biological investigation of phosphate glasses with silver. *Biophysics, Environmental Physics*, 232-237 (2004).
- [55] Marasinghe G. K., Karabulut M., Ray C. S., Day D. E., Shumsky M. G., Yelon W. B., Booth C. H., Allen P. G., and Shuh D. K.: Structural features of iron phosphate glasses. *J. Non-Cryst. Solids* 222, 144-152 (1997).
- [56] Crobu M., Rossi A., Mangolini F., and Spencer N. D.: Tribochemistry of Bulk Zinc Metaphosphate Glasses. *Tribol. Lett.* 39, 121-134 (2010).
- [57] Corbridge: Phosphorus. An Outline of its Chemistry, Biochemistry and Technology, Amsterdam (1990).
- [58] Brow R. K.: Review: the structure of simple phosphate glasses. *J. Non-Cryst. Solids* 263-264, 1-28 (2000).
- [59] Brow R. K., Tallant D. R., Myers S. T., and Phifer C. C.: The Short-Range Structure of Zinc Polyphosphate Glass. *J. Non-Cryst. Solids* 191, 45-55 (1995).
- [60] Van Wazer J. R.: Phosphorus and its compounds, New York (1958).
- [61] Sales B. C., Otaigbe J. U., Beall G. H., Boatner L. A., and Ramey J. O.: Structure of zinc polyphosphate glasses. *J. Non-Cryst. Solids* 226, 287-293 (1998).
- [62] Wiench J. W., Tischendorf B., Otaigbe J. U., and Pruski M.: Structure of zinc polyphosphate glasses studied by two-dimensional solid and liquid state NMR. *J. Mol. Struct.* 602, 145-157 (2002).
- [63] Tischendorf B., Otaigbe J. U., Wiench J. W., Pruski M., and Sales B. C.: A study of short and intermediate range order in zinc phosphate glasses. *J. Non-Cryst. Solids* 282, 147-158 (2001).
- [64] Walter G., Goerigk G., and Rüssel C.: The structure of phosphate glass evidenced by small angle X-ray scattering. *J. Non-Cryst. Solids* 352, 4051-4061 (2006).

- [65] Walter G., Hoppe U., Vogel J., Carl G., and Hartmann P.: The structure of zinc polyphosphate glass studied by diffraction methods and  $^{31}\text{P}$  NMR. *J. Non-Cryst. Solids*, 252-262 (2004).
- [66] Hoppe U., Walter G., Carl G., Neufeind J., and Hannon A. C.: Structure of zinc phosphate glasses probed by neutron and X-ray diffraction of high resolving power and by reverse Monte Carlo simulations. *J. Non-Cryst. Solids* 351, 1020-1031 (2005).
- [67] Brow R. K., Click C. A., and Alam T. M.: Modifier coordination and phosphate glass networks. *J. Non-Cryst. Solids*, 9-16 (2000).
- [68] Musinu A., and Piccaluga G.: An X-ray diffraction study of the short-range order around Ni(II), Zn(II) and Cu(II) in pyrophosphate glasses. *J. Non-Cryst. Solids* 192-193, 32-35 (1995).
- [69] Musinu A., Piccaluga G., Pinna G., Narducci D., and Pizzini S.: Short-range order of Zn and Cu in metaphosphate glasses by X-ray diffraction. *J. Non-Cryst. Solids* 111, 221-227 (1989).
- [70] Bionducci M., Licheri G., Musinu A., Navarra G., Piccaluga G., and Pinna G.: The structure of a Zn(II) metaphosphate glass .1. The cation coordination by a combination of X-ray and neutron diffraction, EXAFS and X-ray anomalous scattering. *J. Phys. Sci.* 51, 1209-1215 (1996).
- [71] Lai A., Musinu A., Piccaluga G., and Puligheddu S.: Structural evolution in zinc and lead phosphate glasses by x-ray diffraction and P MAS NMR spectroscopy. *Phys. Chem. Glasses* 38, 173-178 (1997).
- [72] Meyer K.: Characterization of the structure of binary zinc ultraphosphate glasses by infrared and Raman spectroscopy. *J. Non-Cryst. Solids* 209, 227-239 (1997).
- [73] Efimov A. M.: IR fundamental spectra and structure of pyrophosphate glasses along the  $2\text{ZnO} \cdot \text{P}_2\text{O}_5 - 2\text{Me}(2)\text{O} \cdot \text{P}_2\text{O}_5$  (Me being Na and Li). *J. Non-Cryst. Solids* 209, 209-226 (1997).
- [74] Le Saout G., Fayon F., Bessada C., Simon P., Blin A., and Vaills Y.: A multispectroscopic study of  $\text{PbO}_x\text{ZnO}_{0.6-x}(\text{P}_2\text{O}_5)_{0.4}$  glasses. *J. Non-Cryst. Solids* 293, 657-662 (2001).
- [75] Bartholomew R. F.: Structure and properties of silver phosphate glasses -- Infrared and visible spectra. *J. Non-Cryst. Solids* 7, 221-235 (1972).
- [76] Rulmont A., Cahay R., Liegeoisduyckaerts M., and Tarte P.: Vibrational Spectroscopy of Phosphates - Some General Correlations between Structure and Spectra. *European Journal of Solid State and Inorganic Chemistry* 28, 207-219 (1991).
- [77] Termine J. D., and Lundy D. R.: Vibrational-spectra of some phosphate salts amorphous to X-ray-diffraction. *Calcified Tissue Research* 15, 55-70 (1974).
- [78] Dayanand C., Bhikshamaiah G., Tyagaraju V. J., Salagram M., and Krishna Murthy A. S. R.: Structural investigations of phosphate glasses: a detailed infrared study of the  $x(\text{PbO})-(1-x)\text{P}_2\text{O}_5$  vitreous system. *J. Mater. Sci.* 31, 1945-1967 (1996).
- [79] Schwarz J., Ticha H., Tichy L., and Mertens R.: Physical properties of  $\text{PbO-ZnO-P}_2\text{O}_5$  glasses - I. Infrared and Raman spectra. *Journal of Optoelectronics and Advanced Materials* 6, 737-746 (2004).
- [80] Velli L. L., Varsamis C. P. E., Kamitsos E. I., Moncke D., and Ehrt D.: Structural investigation of metaphosphate glasses. *Phys. Chem. Glasses* 46, 178-181 (2005).
- [81] Reis S. T., Karabulut M., and Day D. E.: Chemical durability and structure of zinc-iron phosphate glasses. *J. Non-Cryst. Solids* 292, 150-157 (2001).
- [82] Armelao L., Bettinelli M., Rizzi G. A., and Russo U.: X-Ray photoelectron and Mossbauer spectroscopies of a binary iron phosphate glass. *J. Materials Chem.* 1, 805-808 (1991).



- [83] Concas G., Congiu F., Manca E., Muntoni C., and Pinna G.: Mössbauer spectroscopic investigation of some iron-containing sodium phosphate glasses. *J. Non-Cryst. Solids*, 175-178 (1995).
- [84] Brow R. K., and Arens C. M.: An XPS study of iron phosphate glasses. *Phys. Chem. Glasses* 35, 132-199 (1993).
- [85] Bruckner R., Chun H. U., Goretzki H., and Sammet M.: XPS measurements and structural aspects of silicate and phosphate-glasses. *J. Non-Cryst. Solids* 42, 49-60 (1980).
- [86] Gresch R., Müller-Warmuth W., and Dutz H.: X-ray photoelectron spectroscopy of sodium phosphate glasses. *J. Non-Cryst. Solids* 34, 127-136 (1979).
- [87] Brow R. K.: An XPS study of oxygen bonding in zinc phosphate and zinc borophosphate glasses. *J. Non-Cryst. Solids* 194, 267-273 (1996).
- [88] Onyiriuka E. C.: Zinc phosphate glass surfaces studied by XPS. *J. Non-Cryst. Solids*, 268-273 (1993).
- [89] Chowdary B. V. R., Tan K. L., Chia W. T., and Gopalakrishnan R.: X-ray photoelectron spectroscopic studies of molybdenum phosphate glassy sistem. *J. Non-Cryst. Solids*, 95-102 (1990).
- [90] Smets B. M. J., and Krol D. M.: Group III ions in sodium silicate glass. Part 1. X-ray photoelectron spectroscopy study *Phys. Chem. Glasses* 25, 113-118 (1984).
- [91] Liu H. S., Chin T. S., and Yung S. W.: FTIR and XPS studies of low-melting PbO-ZnO-P<sub>2</sub>O<sub>5</sub> glasses. *Mater. Chem. Phys.* 50, 1-10 (1997).
- [92] Shih P. Y., Yung S. W., and Chin T. S.: FTIR and XPS studies of P<sub>2</sub>O<sub>5</sub>-Na<sub>2</sub>O-CuO glasses. *J. Non-Cryst. Solids* 244, 211-222 (1999).
- [93] Brow R. K.: Ion beam effects on the composition and structure of glass surfaces. *J. Vac. Sci. Technol.* 7, 1673-1676 (1989).
- [94] Baikova L. G., Pukh V. P., Fedorov Y. K., Sinani A. B., Tikhonova L. V., and Kireenko M. F.: Mechanical properties of phosphate glasses as a function of the total bonding energy per unit volume of glass. *Glass Phys. Chem.* 34, 126-131 (2008).
- [95] Kurkjian C. R.: Mechanical properties of phosphate glasses. *J. Non-Cryst. Solids* 263-264, 207-212 (2000).
- [96] Karabulut M., Melnik E., Stefan R., Marasinghe G. K., Ray C. S., Kurkjian C. R., and Day D. E.: Mechanical and structural properties of phosphate glasses. *J. Non-Cryst. Solids* 288, 8-17 (2001).
- [97] Makishima A., and Mackenzie J. D.: Direct calculation of Young's modulus of glass. *J. Non-Cryst. Solids* 12, 35-45 (1973).
- [98] Sun K.-H.: Fundamental condition of glass formation. *Journal of the American Ceramic Society* 30, 277-281 (1947).
- [99] Appen A. A., Glushkova V. B., and Kayalova S. S.: Calculation of Bonding Energy in Oxides. *Izv. Akad. Nauk SSSR, Neorg. Mater.* 30, 277-281 (1965).
- [100] Rossi A., and Elsener B.: XPS analysis of passive films on the amorphous alloy Fe<sub>70</sub>Cr<sub>10</sub>P<sub>13</sub>C<sub>7</sub> - Effect of the applied potential. *Surf. Interface Anal.* 18, 499-504 (1992).
- [101] Scorciapino M. A., Navarra G., Elsener B., and Rossi A.: Nondestructive Surface Depth Profiles from Angle-Resolved X-ray Photoelectron Spectroscopy Data Using the Maximum Entropy Method. I. A New Protocol. *J. Phys. Chem. C* 113, 21328-21337 (2009).
- [102] Olla N., Elsener and Rossi: Nondestructive in-depth composition profile of oxy-hydroxide nanolayers on iron surfaces from ARXPS measurement. *Surf. Interface Anal.* 38, 964-974 (2006).

- [103] Eglin M., Rossi A., and Spencer N. D.: A combinatorial approach to elucidating tribochemical mechanisms. *Tribol. Lett.* 15, 193-198 (2003).
- [104] Mangolini F., Rossi A., and Spencer N. D.: Chemical Reactivity of Triphenyl Phosphorothionate (TPPT) with Iron: An ATR/FT-IR and XPS Investigation. *J. Phys. Chem. C* 115, 1339-1354 (2011).
- [105] Briggs D.: XPS: Basic Principles, Spectral Features and Qualitative Analysis. in: Briggs, D., and Grant, J. T., (Eds.), *Surface Analysis by Auger and X-ray Photoelectron Spectroscopy*, IMPublications, Trowbridge, 2003.
- [106] Gaskell K. J., Smith M. M., and Sherwood P. M. A.: Valence band x-ray photoelectron spectroscopic studies of phosphorus oxides and phosphates. *Journal of Vacuum Science & Technology A: Vacuum, Surfaces, and Films* 22, 1331-1336 (2004).
- [107] Wagner C. D., and Joshi A.: The Auger Parameter, Its Utility and Advantages - a Review. *J. Electron. Spectrosc.* 47, 283-313 (1988).
- [108] Moretti G.: Auger parameter and Wagner plot in the characterization of chemical states by X-ray photoelectron spectroscopy: a review. *J. Electron. Spectrosc.*, 95-144 (1998).
- [109] Moretti G.: Auger parameter and Wagner plot in the characterization of chemical states: initial and final state effects. *J. Electron. Spectrosc.*, 365-370 (1995).
- [110] Satta M., and Moretti G.: Auger parameters and Wagner plots. *J. Electron. Spectrosc.* 178-179, 123-127 (2010).
- [111] Smith G. C., and Bell J. C.: Multi-technique surface analytical studies of automotive anti-wear films. *Appl. Surf. Sci.*, 222-227 (1999).
- [112] Rossi A., Eglin M., Piras F. M., Matsumoto K., and Spencer N. D.: Surface analytical studies of surface-additive interactions, by means of in situ and combinatorial approaches. *Wear* 256, 578-584 (2004).
- [113] Minfray C., Martin J. M., De Barros M. I., Le Mogne T., Kersting R., and Hagenhoff B.: Chemistry of ZDDP tribofilm by ToF-SIMS. *Tribol. Lett.* 17, 351-357 (2004).
- [114] Murase A., and Ohmori T.: ToF-SIMS analysis of phosphate-type lubricant additives adsorbed on friction surfaces of ferrous materials. *Surf. Interface Anal.* 31, 93-98 (2001).
- [115] Wucher A.: Molecular secondary ion formation under cluster bombardment: A fundamental review. *Appl. Surf. Sci.* 252, 6482-6489 (2006).
- [116] Hagenhoff B., Pfitzer K., Tallarek E., Kock R., and Kersting R.: Polyatomic primary ion bombardment of organic materials: experiences in routine analysis. *Appl. Surf. Sci.* 231-232, 196-200 (2004).
- [117] Postawa Z.: Sputtering simulations of organic overlayers on metal substrates by monoatomic and clusters projectiles. *Appl. Surf. Sci.* 231-232, 22-28 (2004).
- [118] Chusuei C. C., Goodman D. W., Van Stipdonk M. J., Justes D. R., and Schweikert E. A.: Calcium phosphate phase identification using XPS and time-of-flight cluster SIMS. *Anal. Chem.* 71, 149-153 (1999).
- [119] Lu H. B., Campbell C. T., Graham D. J., and Ratner B. D.: Surface characterization of hydroxyapatite and related calcium phosphates by XPS and TOF-SIMS. *Anal. Chem.* 72, 2886-2894 (2000).
- [120] Vickerman J. C.: Multivariate Data Analysis Techniques in Surface Analysis. in: Vickerman, J. C., (Ed.), *Surface Analysis - the Principal Techniques*, 1997, pp. 564-612.

### 3 Experimental

The first part of this chapter describes the materials and lubricants used for the tribological tests (Section 3.1), and the materials and the protocols used for the synthesis and mechanical polishing of polyphosphate glasses (Section 3.2). In the second part of the chapter the experimental conditions for all the techniques used in this work have been reported. This part is organized in four sections: section 3.3 concerns the techniques used to characterize the bulk glasses (X-ray diffraction (XRD), Fourier transform infrared spectroscopy (FT-IR), microelemental analysis, micro- and nanoindentation, and atomic force microscopy (AFM)), section 3.4 describes the protocol used for the tribological experiments, while sections 3.5 and 3.6 concern the surface-analytical techniques (X-ray photoelectron spectroscopy (XPS) and time-of-flight secondary ion mass spectrometry (ToF-SIMS)) used to characterize the samples before and after the tribological tests. The principles of the techniques are not described in this chapter. An outline of recent developments and applications to tribological systems of XPS and ToF-SIMS can be found in Chapter 2.

#### 3.1 Materials

##### 3.1.1 Tribopairs

The tribological tests were performed by rubbing steel and quartz balls with a diameter of 6 mm against polyphosphate discs of different compositions. Steel discs have also been tested for comparison.

The polyphosphate discs used for the tribological tests in this thesis were synthesized as described in the following section 3.2.

The steel discs and balls were made of 100Cr6 steel (AISI 52100, DIN 1.3505), ordinarily used as bearing material; its composition is reported in Table 3.1. The measured hardness was found to be  $775 \pm 6$  HV10 [1; 2]. The roughness of the steel balls was characterized by means of a white-light profilometer (Sensofar PLu Neox, Sensofar-Tech SL., Terrassa, Spain) and was found to be  $0.277 \pm 0.003$   $\mu\text{m}$ .

**Table 3.1: Composition of 100Cr6 (wt.%)**

<i>C</i>	<i>Cr</i>	<i>Mn</i>	<i>S</i>	<i>P</i>	<i>Si</i>
0.95-1.10	1.35-1.85	0.25-0.45	< 0.025	< 0.025	0.15-0.35

The quartz balls were made of optical fused quartz (Spectrosil® 2000) composed of SiO<sub>2</sub> for  $\geq 99.999$  wt.%; the hardness was ca. 1050-1300 Kg/m<sup>2</sup> (Vickers DPH), provided by Saint-Gobain Quartz PLC.

### 3.1.2 Lubricant oil

Lubricated, rather than dry conditions were chosen for the tribological tests, so as to resemble the rheological and heat-transfer properties of a metal-metal lubricated contact. A commercial poly- $\alpha$ -olefin oil (PAO, Durasyn 166) with a density of 830 Kg/m<sup>3</sup> and a viscosity of 43 mPa·s at 275K was used in this thesis as base oil (See Figure 3.1 for the structure of the molecule)

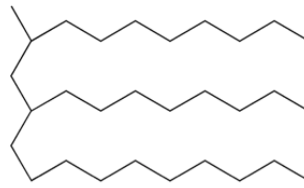


**Figure 3.1: Structure of polyalphaolefin base oil**

### 3.1.3 List of materials and suppliers

The suppliers for all the materials used in this project are listed in the following table:

**Table 3.2: List of materials and suppliers**

<i>Materials</i>	<i>Suppliers</i>	<i>Remarks</i>
100Cr6 discs	CSEM SA, Neuchatel, Switzerland	-
100Cr6 balls	Hydrel GmbH, Romanshorn, Switzerland	6 mm
Quartz balls	Quick-Ohm Küpper & Co GmbH, Wuppertal, Germany	6 mm
PAO	Tunap Industrie GmbH & Co., Mississauga, Canada	-
<i>Materials for the synthesis</i>		
Ammonium dihydrogen phosphate	Acros Organics, Geel, Belgium	99.9% extra pure
Zinc oxide	Alfa Aesar, Karlsruhe, Germany	99.9%
Iron(III) oxide	Sigma-Aldrich	Puriss p.a.
Crucibles	Metoxit AG, Thayngen, Switzerland	High-density alumina
Furnace (RHF 16/3)	Carbolite®, Hope Valley, UK	-
Oven (FD23)	BINDER GmbH, Tuttlingen, Germany	-
<i>Solvents</i>		
Ethanol	Scharlab S.L., Sentmentat, Spain	Analytical grade ACS
Acetone	Sigma-Aldrich	Puriss p.a.
Isopropanol	Sigma-Aldrich	Puriss p.a..
Toluene	Sigma-Aldrich	Puriss p.a.
Cyclohexane	Sigma-Aldrich	≥ 99.5%.
<i>Reference compounds</i>		
Calcium phosphate	Sigma-Aldrich	Pure
<i>Grinding and polishing supplies</i>		
Grinding papers	Struers GmbH, Birmensdorf, Switzerland	Grit 320, 600, 1200, 2400
Polishing cloths (DP-Plus, DP-Nap)	Struers GmbH, Birmensdorf, Switzerland	-
Diamond paste (DP-Paste, P)	Struers GmbH, Birmensdorf, Switzerland	3, 1, and 1/4 μm

## 3.2 Synthesis of the glasses

### 3.2.1 Synthesis

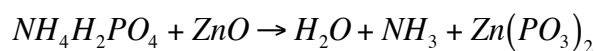
Different composition polyphosphates (see Table 3.3) were synthesized starting from stoichiometric mixtures of ammonium dihydrogen phosphate, zinc oxide, and iron oxide.

**Table 3.3: Batch composition of all polyphosphate compositions synthesized in this work**

<i>Zinc polyphosphates</i>				
<i>Given name</i>	<i>Formula</i>	<i>[O]/[P]</i>	<i>[M]*/[P]</i>	<i>Stoichiometry (at.%)</i>
Zinc metaphosphate	0.5(ZnO)·0.5(P <sub>2</sub> O <sub>5</sub> )	3	0.5	[Zn]=11.11; [P]=22.22; [O]= 66.67
Zinc poly <sub>0.67</sub>	0.57(ZnO)·0.43(P <sub>2</sub> O <sub>5</sub> )	3.167	0.667	[Zn]=13.79; [P]=20.69; [O]= 65.52
Zinc pyrophosphate	0.67(ZnO)·0.33(P <sub>2</sub> O <sub>5</sub> )	3.5	1	[Zn]=18.18; [P]=18.18; [O]= 63.64
Zinc orthophosphate	0.75(ZnO)·0.25(P <sub>2</sub> O <sub>5</sub> )	4	1.5	[Zn]=23.08; [P]=15.38; [O]= 61.54
<i>Iron polyphosphates</i>				
<i>Given name</i>	<i>Formula</i>	<i>[O]/[P]</i>	<i>[M]*/[P]</i>	<i>Stoichiometry (at.%)</i>
Iron poly <sub>0.33</sub>	0.25(Fe <sub>2</sub> O <sub>3</sub> )·0.75(P <sub>2</sub> O <sub>5</sub> )	3	0.333	[Fe]=7.69; [P]=23.08; [O]= 69.23
Iron poly <sub>0.5</sub>	0.33(Fe <sub>2</sub> O <sub>3</sub> )·0.67(P <sub>2</sub> O <sub>5</sub> )	3.167	0.5	[Fe]=9.64; [P]=21.69; [O]= 68.67
Iron poly <sub>0.67</sub>	0.40(Fe <sub>2</sub> O <sub>3</sub> )·0.60(P <sub>2</sub> O <sub>5</sub> )	3.5	0.667	[Fe]=12.90; [P]=19.35; [O]= 67.64
Iron poly <sub>1</sub>	0.5(Fe <sub>2</sub> O <sub>3</sub> )·0.5(P <sub>2</sub> O <sub>5</sub> )	4	1	[Fe]=16.67; [P]=16.67; [O]= 66.67
<i>Mixed iron and zinc polyphosphates</i>				
<i>Given name</i>	<i>Formula</i>	<i>[O]/[P]</i>	<i>[M]*/[P]</i>	<i>Stoichiometry (at.%)</i>
Zinc25 iron75 poly <sub>0.5</sub>	0.40(ZnO)· 0.07(Fe <sub>2</sub> O <sub>3</sub> )·0.53(P <sub>2</sub> O <sub>5</sub> )	3	0.5	[Zn]=2.41; [Fe]=7.23; [P]=19.28; [O]= 71.08
Zinc50 iron50 poly <sub>0.5</sub>	0.20(ZnO)· 0.14(Fe <sub>2</sub> O <sub>3</sub> )·0.57(P <sub>2</sub> O <sub>5</sub> )	3	0.5	[Zn]=5.40; [Fe]=5.40; [P]=21.63; [O]= 67.57
Zinc75 iron25 poly <sub>0.5</sub>	0.15(ZnO)· 0.23(Fe <sub>2</sub> O <sub>3</sub> )·0.62(P <sub>2</sub> O <sub>5</sub> )	3	0.5	[Zn]=8.22; [Fe]=2.74; [P]=21.92; [O]= 67.12

[M]\* is the total content including by summing zinc and iron contents

The reaction for zinc metaphosphate is described in the following as an example:

**Equation 3.1**

The reagents in powder form were melted in alumina crucibles at temperatures ranging between 1473-1573 K and then quenched in a copper tray that had been previously cooled to 253 K. Different temperatures and heating times were used, depending on the composition and they have been described in detail in Table 3.4.

**Table 3.4: Heating parameters for the synthesis of polyphosphate glasses**

<i>Zinc polyphosphates</i>			
<i>Composition</i>	<i>Heating rate (K/min)</i>	<i>Temperature set point (K)</i>	<i>Dwelling time (hrs)</i>
Zinc metaphosphate	2	1473	2
Zinc polyphosphate <sub>0.6</sub>	2	1473	2
Zinc pyrophosphate	2	1473	2
Zinc orthophosphate	2	1473	2
<i>Iron polyphosphates</i>			
<i>Composition</i>	<i>Heating rate (K/min)</i>	<i>Temperature set point (K)</i>	<i>Dwelling time (hrs)</i>
Iron poly <sub>0.33</sub>	1.8	1523	4
Iron poly <sub>0.5</sub>	1.8	1523	4
Iron poly <sub>0.67</sub>	1.8	1573	4
Iron poly <sub>1</sub>	1.8	1573	4
<i>Mixed iron and zinc polyphosphates</i>			
<i>Composition</i>	<i>Heating rate (K/min)</i>	<i>Temperature set point (K)</i>	<i>Dwelling time (hrs)</i>
Zinc25 iron75 poly <sub>0.5</sub>	1.8	1473	4
Zinc50 iron50 poly <sub>0.5</sub>	1.8	1473	4
Zinc75 iron25 poly <sub>0.5</sub>	1.8	1523	4

The zinc polyphosphate samples were clear and transparent, while the iron and mixed zinc and iron phosphate were black and reflective; they were all obtained in the shape of round discs of 2-3 cm of diameter and 3-4 mm in thickness with the only exception for zinc orthophosphate and iron poly<sub>1</sub>, which could be obtained in amorphous state only in small fragments (less than 1mm thick and 1 cm wide). After quenching, the samples were annealed at 623 K for 8 hrs, in order to reduce internal stresses.

### 3.2.2 Mechanical polishing

Prior to the mechanical and tribological tests, the samples were mechanically polished. Grinding was performed using grit 320, 600, 1200 and 2400 silicon carbide paper. The polishing was then carried out using 3 and 1 μm diamond paste on polishing cloths. Ethanol was always used as a polishing lubricant, in order to remove the heat produced by friction and to reduce chemical changes at the surface. The surface roughness (Ra) was measured by atomic force microscopy (AFM) and found to be 4.0±0.2nm. The samples were then kept in an ultrasonic bath in ethanol for ten minutes prior to the tests.

### 3.3 Bulk characterization

#### 3.3.1 X-ray Diffraction (XRD)

X-ray diffraction (XRD) was used in order to ascertain that the samples were amorphous. The analyses were performed using a powder diffractometer STOE STADI P (STOE & Cie GmbH, Darmstadt, Germany), equipped with an image-plate detector and a Cu K $\alpha$  X-ray source.

#### 3.3.2 Infrared spectroscopy

Transmission FT-IR spectra were acquired with a Nicolet™ 5700 Fourier-transform infrared spectrometer (Thermo Electron Corporation, Madison, WI, USA). The experimental conditions are listed in Table 3.5. The glasses were ground together with dried KBr and pressed into a pellet. The spectra were processed with OMNIC™ software (V7.2, Thermo Electron Corporation, Madison, WI, USA). A single-beam spectrum of a bare KBr pellet was acquired before each measurement as a background spectrum.

**Table 3.5: Transmission FT-IR experimental conditions**

<i>Detector</i>	DGTS/KBr
<i>Resolution</i>	2 cm <sup>-1</sup>
<i>Number of Scans</i>	64
<i>Scan Velocity</i>	0.6329 cm/s
<i>Acquisition Time</i>	136 s
<i>Gain Control</i>	1

#### 3.3.3 Microelemental analysis

The microelemental analysis for oxygen was carried out by means of a RO-478 (Leco Corporation, St. Joseph, MI, USA). The phosphorus content was determined by the molybdovanadate method after microwave digestion and subsequent leaching (2 x 50 min) in concentrated sulfuric acid and perchloric acid at 483 and 508 K.

#### 3.3.4 Microindentation

The microindentation tests were carried out using a micro Vickers hardness tester (MTX- $\alpha$ , Wolpert) at different loads (0.1, 0.3, 0.5 and 1 N). Ten indentations were performed on each sample per load. The hardness was calculated using the length of the two diagonals of the indentation, which were measured with the help of a light microscope.



### 3.3.5 Nanoindentation

The measurements were performed using a TriboIndenter (Hysitron Inc., USA) with a standard Berkovich tip in load-controlled mode. A force of 600 mN was applied in a loading time of 20 s, held for 2 s and unloaded in 20 s. Ten indentations were performed on each sample. The mechanical properties, hardness  $H$  and reduced Young's modulus  $E_r$ , were calculated using the unloading segment according to the Oliver–Pharr method [3].

### 3.3.6 Atomic Force Microscopy (AFM)

AFM TappingMode™ (Dimension 3000, Digital Instruments, Santa Barbara, CA, USA) was used to measure the roughness of the surface. A cantilever (OMLC-AC160-TS-R3, Olympus Micro Cantilevers, Japan) with a normal spring constant of around 26.1 N/m and resonant frequency of around 300kHz was used. The roughness analysis was done using the NanoscopeV5 software.

### 3.3.7 Density

The density of the samples was determined by immersion in isopropanol at room temperature by means of Archimedes' method. The uncertainty was calculated to be  $\pm 0.1 \text{ g/cm}^3$

## 3.4 Tribological experiments

### 3.4.1 CETR tribometer

The tribological tests were carried out by means of a CETR UMT-2 tribometer (see Figure 3.2, Center for Tribology, Campbell CA, USA) with a ball-on-disk set-up. The experiments were performed in rotational motion with pure sliding contact.

The ball holder is mounted on a carriage that allows both vertical and lateral movement. A rotational drive moves the disc, which is mounted inside a cup filled with base oil. The ball is pressed onto the disc by a spring (the spring constant has been measured according to [4]); a two-dimensional load cell, mounted in between the carriage and the ball holder, allows both normal load and friction force to be measured. The load cell has a maximum load of 20N and a resolution of 1 mN in the two axes. During the experiment, the computer continuously moves the carriage up and down, in order to maintain the desired load. The friction force, the load, the position of the carriage ( $x$ ,  $z$  and rotation) and the time can be recorded during the experiment.

In order to have homogeneous conditions in all the parts of the disc, a planarity check was performed prior to each experiment. The  $z$ -values of the carriage as a function of the rotation were recorded while sliding a stylus onto the disc with 200 mN normal load for two turns. If a variation higher of  $\pm 10\mu\text{m}$  was observed, the

planarity could be adjusted by placing aluminum shims between the disc holder and the rotational drive.

The calibration of the load cell was performed using standard weights.

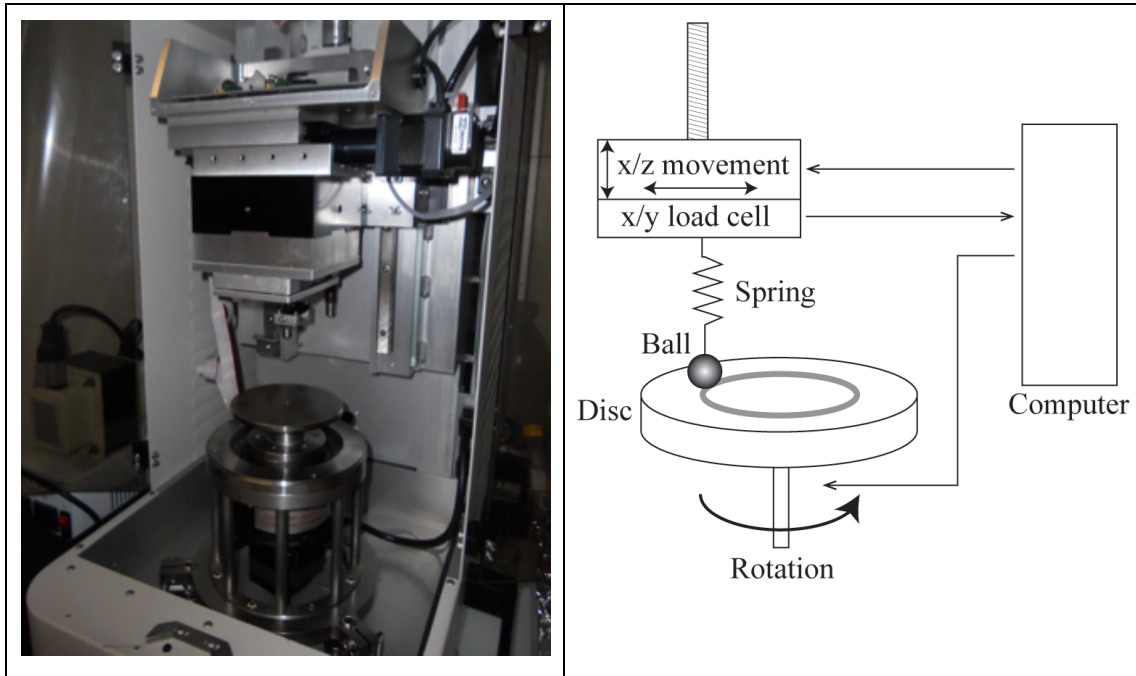


**Figure 3.2: CETR UMT-2 tribometer: picture and schematic**

### 3.4.2 Constant load tribological experiments

For the first time in this work, polyphosphate glasses have been used as discs for tribological tests, and therefore, first of all it is necessary to define a reproducible protocol for such tests. The challenges to overcome were at least three: the brittleness of the glass, the irregular and uncontrollable shape of the samples, the reactivity of the compounds and, as a consequence, the surface contamination. After a first phase during which different experimental protocols were tried, a procedure that allows the repeatable and reproducible production of glasses was established. The casting method was improved, in order to obtain thicker samples that are not easily broken. The surface was flattened using a mechanical polishing procedure as described in section 3.2.2. In order to avoid contamination, all the polishing was made by hand and just on one side of the sample. Having an irregular contact between the bottom of the sample and the sample-holder would result in an uneven distribution of the forces when a normal load is applied and, possibly, to brittle fracture. This problem was solved using a thin layer of plasticine between the sample and the metal underneath.

The tests were performed at room temperature in pure polyalphaolefin at two different loads, 5 and 7 N, with a constant sliding speed of 30 mm/min.

In the first tests the running-in was performed on a 100Cr6 steel disc at 10N and 300mm/min for 2hrs in the presence of pure PAO, in order to achieve a

conformal and reproducible flat on the ball. Four concentric wear tracks, separated from each other by 0.75 mm, were obtained on each disc. In this first set of experiments on zinc metaphosphate, it was observed that the formation of a glassy transfer film on the ball during the first test was influencing the results obtained in the following tests on the same disc (see Chapter 7). In order to have reproducible and comparable results, the protocol was changed and all the tests were performed using a new ball (without running-in) at the beginning of each test.

Before the XPS analysis, balls and discs were cleaned in an ultrasonic bath for 10 min in n-hexane and gently wiped with a tissue paper.

The tribostressed balls and discs were also examined with the aid of a light microscope.

### 3.4.3 *Optical microscopy*

Optical microscopy images were taken using an AX10 Imager M1m (Carl Zeiss, Oberkochen, Germany) with objectives from 5 X to 40 X and equipped with a CCD camera.

### 3.4.4 *Data processing*

The friction force, the load, and the position of the carriage (x, z and rotation) are recorded as a function of time in a data-file saved at the end of each experiment. An ASCII-file can be exported for further processing using the CETR Viewer program. Matlab R20011a software (The MathWorks, Inc., Natick, MA, USA) was used for reading and processing the data. For investigating the dependence of the COF on the sliding time/distance, an average COF (with standard deviation) was obtained for each sliding turn and plotted as a function of the sliding distance. From all the data acquired during each test, an average coefficient of friction ( $COF_{av}$ ) was also calculated, together with its standard deviation. At the beginning of the tests some running-in effects could be observed, while the second part of the curve was characterized by a COF that was constant with time. A second averaged COF was, therefore, calculated by averaging all the data obtained after the first 2000 turns. This parameter has been defined in this work as COF at steady state ( $COF_{SS}$ ) and has been used to more easily compare the tribological behavior of different tribopairs.

An example of a Matlab routine for data reduction can be found in the Appendix B.

## 3.5 **X-ray photoelectron spectroscopy**

### 3.5.1 *PHI Quantera SXM*

The XPS analyses were performed by means of a PHI Quantera SXM spectrometer (ULVAC-PHI, Chanhassen, MN, USA) equipped with an AlK $\alpha$

monochromatic source whose beam size ranges from 5 to 200  $\mu\text{m}$ . The Gauze input lenses collect the photoelectrons at an emission angle of  $45^\circ$  and direct them through the high-resolution spherical capacitor analyzer to the 32-channel detector system. The angle between the analyzer axis and the X-ray source is  $45^\circ$ . The spectrometer is also equipped with a low-voltage argon ion gun and an electron neutralizer for charge compensation (Figure 3.3).

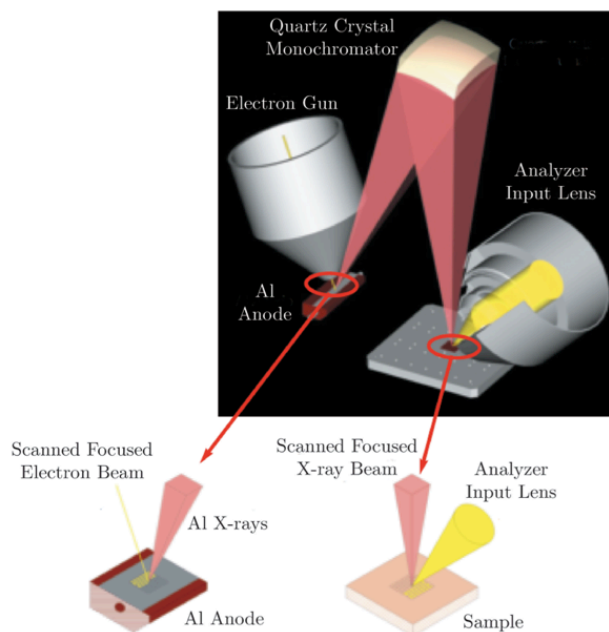


**Figure 3.3: Schematic of the PHI Quantera SXM [5]**

The calibration was performed using sputter-cleaned gold, silver and copper as reference materials, according to ISO15472:2001 (Appendix A.1). The accuracy was found to be  $\pm 0.1$  eV. All the experiments were run at residual pressures below  $5 \times 10^{-7}$  Pa. Binding energy values are reported in this work as means over three or more independent measurements with their corresponding standard deviations.

Survey spectra were acquired in fixed analyzer transmission (FAT) mode setting a pass-energy (PE) of 280 eV. The acquisition parameters for the high-resolution spectra were chosen according to the different samples requirements. The zinc polyphosphates were not susceptible to sample degradation, therefore the high-resolution spectra were collected with a PE of 26 eV and a step size of 0.05 eV for their characterization (Chapter 5); the step size increased to 0.10 eV when analyzing the tribological samples (Chapter 7). A pass energy of 69 eV and a step size of 0.125 eV was instead used in the case of iron-containing polyphosphates, in order to minimize the acquisition time and, therefore, the sample degradation. A complete list of the analysis conditions can be found in Table 3.6. The full width at half maximum of the peak height, FWHM, of the silver  $\text{Ag}3d_{5/2}$  signal was 0.6 eV at PE of 26 eV and 0.7 at 69 eV.

**Table 3.6: X-ray photoelectron spectroscopy (XPS) acquisition parameters for the high-resolution XP-spectra collected with the PHI Quantera SXM**

<i>Zinc polyphosphates</i>					
<i>Element</i>	<i>Acquisition lower end [eV]</i>	<i>Acquisition width [eV]</i>	<i>No. of sweeps</i>	<i>Pass energy [eV]</i>	<i>Step size [eV]</i>
<i>O 1s</i>	525	16	9	26	0.05/0.1*
<i>P 2p, Zn 3s</i>	126	20	27	26	0.05/0.1*
<i>Zn 2p</i>	1015	16	9	26	0.05/0.1*
<i>Zn LMM</i>	480	35	12	26	0.05/0.1*
<i>Valence band</i>	-5	40	27	26	0.05/0.1*
<i>C 1s</i>	277	18	27	26	0.05/0.1*
<i>Iron polyphosphates</i>					
<i>Element</i>	<i>Acquisition lower end [eV]</i>	<i>Acquisition width [eV]</i>	<i>No. of sweeps</i>	<i>Pass energy [eV]</i>	<i>Step size [eV]</i>
<i>Fe 2p</i>	702	20	12	69	0.125
<i>Fe 3s</i>	82	20	27	69	0.125
<i>O 1s</i>	525	16	9	69	0.125
<i>P 2p</i>	126	16	12	69	0.125
<i>Valence band</i>	-5	40	27	69	0.125
<i>C 1s</i>	278	20	27	69	0.125
<i>Fe 2p</i>	702	40	27	69	0.125
<i>Mixed zinc and iron polyphosphates</i>					
<i>Element</i>	<i>Acquisition lower end [eV]</i>	<i>Acquisition width [eV]</i>	<i>No. of sweeps</i>	<i>Pass energy [eV]</i>	<i>Step size [eV]</i>
<i>Fe 2p</i>	702	20	27	69	0.125
<i>Fe 3s</i>	82	20	64	69	0.125
<i>O 1s</i>	525	16	9	69	0.125
<i>P 2p, Zn 3s</i>	126	20	27	69	0.125
<i>Zn 2p</i>	1015	16	27	69	0.125
<i>Zn LMM</i>	480	35	27	69	0.125
<i>Valence band</i>	-5	40	27	69	0.125
<i>C 1s</i>	278	20	27	69	0.125
<i>Fe 2p</i>	702	40	27	69	0.125

\* A step size of 0.05 was chosen for the characterization of the homogeneous samples after synthesis, while a value of 0.10 was chosen for the tribological samples.

The beam diameters used were 100  $\mu\text{m}$  and 20  $\mu\text{m}$ , depending on the size of the feature analyzed. X-ray excited secondary electron images (SXI) were used in order to determine the topography and, thus, to be able to collect small-area XPS spectra from the features present on the sample.

Imaging-XPS (i-XPS) was performed with a beam size of 20  $\mu\text{m}$  and a PE of 140 eV in snapshot mode; under these conditions the spectra were acquired over a BE range of 15.5 eV. The full width at half-maximum of the peak height, FWHM, of the silver  $\text{Ag}3d_{5/2}$  signal for the pass energy of 140 eV was 1.0 eV. The area of the maps was 600 x 600  $\mu\text{m}^2$  and required 1-2 hours of acquisition per map. Maps of the carbon signal, C1s, were acquired in order to exclude the possibility of sample charging.

### 3.5.2 *VG Theta Probe*

The angle-resolved (AR) XPS analysis were performed using the VG Theta Probe (Thermo Fisher Scientific, East Grinstead, UK) spectrometer is equipped with an Al/Mg  $K\alpha$  twin source as well as with a monochromatic  $\text{Al}K\alpha$  source with beam diameter varying between 15 and 400  $\mu\text{m}$ . The acquisition of AR-XPS spectra on this spectrometer is advantageous thanks to the combination of a radian lens with a two-dimensional detector equipped with 112 energy channels and 96 angular channels that allows the simultaneous acquisition of angle-resolved spectra with an emission angle ranging from 23 to 83°. The source-to-analyser angle is 67.38° for the average emission angle of 53°. A low-energy electron/ion flood gun is also available for charge compensation. The spectra were acquired in angle-resolved mode (16 emission angles) using the monochromatic  $\text{Al}K\alpha$  source with a beam size of 400  $\mu\text{m}$  (power of 100 W) in the constant-analyzer-energy (CAE) mode. A PE of 100 eV and a step size of 0.1 eV (FWHM for silver  $\text{Ag}3d_{5/2} = 0.84$  eV) were used.

### 3.5.3 *Data processing*

The spectra were processed using CasaXPS software (version 2.3.15, Casa Software Ltd, Wilmslow, Cheshire, UK). The background subtraction was performed using the Shirley-Sherwood iterative method. After background subtraction, the peaks were fitted using the product of Gaussian and Lorentzian functions. When necessary a tail function was added, in order to account for the asymmetry of signal. The fitting parameters reported in Table 3.7 (full width at half maximum, FWHM, and Gaussian to Lorentzian ratio) have been obtained from the synthesized polyphosphates (Chapter 5).

**Table 3.7: Peak-fitting parameters for polyphosphate glasses**

<i>Element</i>	<i>Assignment</i>	<i>BE [eV]</i>	<i>FWHM [eV]</i>	<i>Fitting parameters</i>
<i>P 2p<sub>3/2</sub></i>	Phosphate	134.0 – 134.8	1.5 - 1.7	GL(30)
<i>P 2p<sub>1/2</sub></i>	Phosphate	134.9 – 135.7	1.5 - 1.7	GL(30)
<i>O 1s</i>	Non bridging oxygen	531.8 – 532.4	1.6 – 1.8	GL(30)
	Bridging oxygen	533.2 – 534.1	1.6 – 1.8	GL(30)
<i>Zn 2p<sub>3/2</sub></i>	Phosphate	1022.6 – 1023.1	1.6 – 1.8	GL(65)
<i>Zn 3s</i>	Phosphate	140.9 – 141.1	2.0 – 2.2	GL(60)
<i>ZnL<sub>3</sub>M<sub>4,5</sub>M<sub>4,5</sub></i>	<sup>1</sup> G	500.3 – 500.8	2.5 – 2.8	GL(30)
	<sup>3</sup> F	503.5 – 504.0	2.5 – 2.8	GL(30)
<i>Fe 2p<sub>3/2</sub></i>	Fe(II) phosphate	712.2 – 712.6	1.5 - 1.7	GL(60)T(0.8)
	Fe(II) phosphate satellite	Fe(II) + 6	2.6 – 2.9	GL(45)
	Fe(III) phosphate	713.7 – 714.1	1.5 - 1.7	GL(60)T(0.8)
	Fe(x-ray degradation) phosphate	709.8 – 710.2	1.5 - 1.7	GL(60)T(2)
	Fe(x-ray degradation) satellite	Fe (x-ray deg.) + 5.5	2 - 4	GL(45)
<i>C 1s</i>	Aliphatic	285.0	1.4 – 1.6	GL(30)
	C-O	286.6 – 286.9	1.4 – 1.6	GL(30)
	C=O	288.7 -288.9	1.4 – 1.6	GL(30)

The maps were processed using Multi-Pak<sup>TM</sup> software (version 8.1c, ULVAC-PHI, Chanhassen, MN, USA). These maps show the spatial distribution of the intensity of the selected element. For each pixel a complete spectrum was acquired, the calculated intensity of each spectrum corresponding to the color in the map. If more than one chemical state was present, the spectrum could be fitted using different functions for each chemical state. The chemical-state maps were reconstructed using a linear-least-squares routine [6].

### 3.5.4 Quantitative Analysis

The quantitative analysis was carried out using the first-principles method valid for homogeneous samples [7]. The area of the peaks assigned to each component is proportional to the atomic concentration, after correcting for the sensitivity factor, calculated as follows:

$$s_A = \sigma_A(h\nu) \cdot \Lambda_{MA} \cdot L_A(\gamma) \cdot T(E_A)$$

**Equation 3.2**

where  $\sigma$  is the Scofield photoionization cross-section [8],  $L_A$  describes the anisotropy of the photoemission, calculated according to [9], and  $T$  is the analyzer transmission function. The analyzer transmission function is can be calculated as in the following [ref]:

**Equation 3.3**

$$T(KE) = \left( \frac{a^2}{a^2 + RR^2} \right)^b$$

RR is the retard ratio, i.e. the ratio between the kinetic energy, KE, and the chosen pass energy, PE (KE/PE), while  $a$  and  $b$  are derived by fitting the log/log plot of the normalized intensity divided by the pass energy versus the retard ratio. The peaks considered here were Cu2p<sub>3/2</sub>, Cu3p and CuLMM collected at different pass-energy values. For Quantera SXM (ULVAC – PHI),  $a$  and  $b$  were respectively 43.299 and 0.193 when a beam size of 20 and 100  $\mu\text{m}$  was used. For the Theta-Probe the values of  $a$  and  $b$  were calculated for each emission angle and are reported in Table 3.8.

**Table 3.8: Transmission function parameters,  $a$  and  $b$ , as a function of the emission angle acquired at 400 $\mu\text{m}$  beam size for the Theta Probe spectrometer**

<i>Emission angle</i>	24.88	28.63	32.38	36.13	39.88	43.63	47.38	51.13	54.88	58.63	62.38	66.13
<i>a</i>	17.57	16.73	13.33	10.91	11.48	12.51	13.95	15.84	19.02	20.77	22.34	22.24
<i>b</i>	0.389	0.427	0.363	0.323	0.363	0.387	0.411	0.414	0.461	0.466	0.532	0.489

The inelastic mean free path,  $\Lambda$ , was calculated using the TPP-2M formula [10] as a function of the material characteristics. The parameters used in this work are summarized in the Appendix A.3.

### 3.6 Time-of-Flight Secondary Ion Mass Spectroscopy

#### 3.6.1 ToF-SIMS<sup>5</sup>

Time-of-flight secondary ion mass spectra (ToF-SIMS) were recorded using a ToF-SIMS<sup>5</sup> system (ION-TOF GmbH, Münster, Germany) equipped with a reflectron ToF analyzer, a pulsed bismuth primary-ion-beam source (acceleration voltage: 25 keV, pulsed ion current: 0.3 pA) and a low-energy flood gun (acceleration voltage: 20 eV) for charge compensation. The pulse length determines the mass resolution and mass accuracy: in order to maximize intensity the continuous beam is divided into ion ‘packages’ that are then deflected of 90° by a high-voltage pulse by a technique known as ‘bunching’. In this work, the beam alignment was set to bunched mode and optimized for high mass resolution.



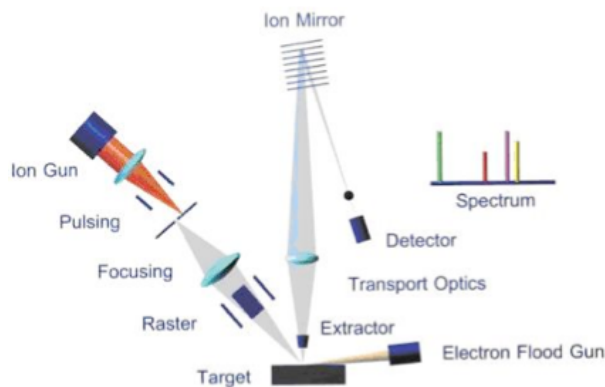


**Figure 3.4: Schematic of the ToF-SIMS<sup>5</sup> (ION-TOF)**

Each sample was analyzed using  $\text{Bi}_3^{++}$  primary ions with a pulsed primary-ion current of 0.3 pA and an ion dose of  $1 \times 10^{12}$  ions  $\text{cm}^{-2}$ , which is well below the static limit for SIMS of  $1 \times 10^{13}$  ions  $\text{cm}^{-2}$  [11].

Both negative and positive spectra were acquired with an analyzed area of  $200 \mu\text{m} \times 200 \mu\text{m}$  for all experiments in a mass range from  $m/z=0$  to 800.

### 3.6.2 Data Processing

The spectra were processed using IonSpec software (ION-TOF GmbH, Münster, Germany).

Normalization is a common preprocessing method in multivariate analysis of SIMS data, which consists of scaling the data by a constant for each sample. This constant could be the intensity of a specific peak, the sum of the intensities of specific peaks or the total intensity of each sample. Normalization preserves the shape of the spectra and is used with the assumption that chemical variances are described only by the relative changes in ion intensities. This method is able to eliminate, or at least attenuate, systematic differences in the absolute intensities caused by topography, sample charging, changes in primary ion dose, possible contamination due to sample preparation and other effects [7]. For these reasons in this work the intensity of each peak was normalized by the total intensity.

The calibration has been performed using minimum 5 different peaks of certain attribution distributed over the  $m/z$  scale from 0 to 300 for all samples in both negative and positive mode (see details in Table 3.9).

**Table 3.9: Fragments used for the calibration of the m/z scale in both positive and negative mode**

<i>Zinc polyphosphates</i>		<i>Iron polyphosphates</i>		<i>Mixed zinc and iron polyphosphates</i>	
<i>Ion</i>	<i>Nominal mass</i>	<i>Ion</i>	<i>Nominal mass</i>	<i>Ion</i>	<i>Nominal mass</i>
C <sup>-</sup>	12	C <sup>-</sup>	12	C <sup>-</sup>	12
CH <sub>2</sub> <sup>-</sup>	14	CH <sub>2</sub> <sup>-</sup>	14	CH <sub>2</sub> <sup>-</sup>	14
F <sup>-</sup>	19	FeO <sup>-</sup>	72	F <sup>-</sup>	19
PO <sup>-</sup>	47	PO <sub>4</sub> <sup>-</sup>	95	FeO <sup>-</sup>	72
ZnO <sup>-</sup>	79	FePO <sub>2</sub> <sup>-</sup>	119	ZnO <sup>-</sup>	78
ZnP <sub>2</sub> O <sub>7</sub> <sup>-</sup>	238	Fe <sub>2</sub> P <sub>3</sub> O <sub>8</sub> <sup>-</sup>	333	ZnP <sub>2</sub> O <sub>7</sub> <sup>-</sup>	238
C <sup>+</sup>	12	C <sup>+</sup>	12	C <sup>+</sup>	12
CH <sub>3</sub> <sup>+</sup>	15	CH <sub>3</sub> <sup>+</sup>	15	CH <sub>3</sub> <sup>+</sup>	15
Al <sup>+</sup>	27	Al <sup>+</sup>	27	Al <sup>+</sup>	27
Zn <sup>+</sup>	64	Fe <sup>+</sup>	56	Fe <sup>+</sup>	56
C <sub>7</sub> H <sub>7</sub> <sup>+</sup>	91	C <sub>7</sub> H <sub>7</sub> <sup>+</sup>	91	Zn <sup>+</sup>	64
				C <sub>7</sub> H <sub>7</sub> <sup>+</sup>	91

### 3.6.3 Principal Component Analysis (PCA)

Principal component analysis (PCA) is a multivariate-analysis (MVA) technique with the aim of reducing matrices of data to their lowest dimensionality. The data are organized in matrices formed by  $p$  variables ( $X_1, X_2, \dots, X_p$ ), in this case the normalized areas of the peaks, and transformed in combination of these to produce indices  $Z_1, Z_2, \dots, Z_p$ . The  $Z_i$  are called principal components and they are ordered so that the first indices display the largest amount of variation within the data. The PCA is successful when able to capture the most variance with the first few principal components. This is possible only when the original variables are highly correlated within them; when this is not the case, the PCA is not able to reduce the data dimensionality, but it will still give the valuable information that no correlation is present within the data set [12; 13].

PCA was applied to the ToF-SIMS data obtained in this work in order to find correlations within the spectra of the different composition polyphosphates under investigation. Using the procedure described in the previous paragraph (3.6.2) a list of selected peaks of interest was found and, after careful calibration of all samples, the normalized intensities for each peak for each sample were obtained.

The first step for PCA is organizing the data in the data matrix  $S$  as described in Table 3.10.

**Table 3.10: The form of data for the principal component analysis**

<i>Peak</i>	<i>Sample<sub>1</sub></i>	<i>Sample<sub>2</sub></i>	...	<i>Sample<sub>p</sub></i>
1	S <sub>11</sub>	S <sub>12</sub>	...	S <sub>1p</sub>
2	S <sub>21</sub>	S <sub>22</sub>	...	S <sub>2p</sub>
...	...	...	...	...
n	S <sub>n1</sub>	S <sub>n2</sub>	...	S <sub>np</sub>

The PCA then consists in calculating the eigenvectors of the sample covariance matrix  $C$  (Equation 3.4).

$$C = S'S$$

**Equation 3.4**

The eigenvectors are calculated as follows:

$$Cz_i = \lambda_i z_i$$

**Equation 3.5**

where  $z_i$  is the eigenvector and  $\lambda_i$  the corresponding eigenvalue. The coefficients of the  $i^{\text{th}}$  principal component are given by  $z_i$  and its variance by  $\lambda_i$ . Therefore, while  $Z$  is the loading matrix, the scores matrix is then calculated as:

$$T = SZ$$

**Equation 3.6**

All the components that only account for a small variation of the data can be discarded and the first most significant  $n$  components will be sufficient to describe all the variation present in the data. Now that the matrixes  $T$  and  $Z$  only contain  $n$  factors, the data can be finally approximated by:

$$S = Z'T + E$$

**Equation 3.7**

where  $E$  is the residual value.

The PCA calculations reported in this work have been performed using the NB toolbox (NESAC/BIO MVA Toolbox [14]). The toolbox runs on Matlab and contains a set of Matlab GUIs that can be used to run MVA of ToF-SIMS data.

## *References*

- [1] Mangolini F., Reactivity of Environmentally Compatible Lubricant Additives: an In Situ and Ex Situ Investigation, PhD Thesis No. 19677, ETH Zürich, Zürich, 2011.
- [2] Sessini V., Contact Characteristics of Iron/steel Surfaces During the Running-in Process, Bachelor Thesis, Università degli Studi di Cagliari, 2008.
- [3] Pharr G. M., and Oliver W. C.: Measurement Of Thin-Film Mechanical-Properties Using Nanoindentation. *MRS Bull.* 17, 28-33 (1992).
- [4] Eglin M., Development of a combinatorial approach to lubricant additive characterization, PhD Thesis No. 15054, ETH Zurich, Zürich, 2003, pp. 226.
- [5] Physical Electronics, PHI Quantera - Scanning X-ray Microprobe, technical specifications, Chanhassen, MN, USA (2004).
- [6] CasaXPS Manual 2.3.15, Casa Software Ltd).
- [7] Seah M. P.: Quantification of AES and XPS, in *Practical Surface Analysis*, John Wiley & Sons (1990).
- [8] Scofield J. H.: Hartree-Slater Subshell Photoionization Cross-Sections at 1254 and 1487eV. *J. Electron. Spectrosc.* 8, 129-137 (1976).
- [9] Reilman R. F., Msezane A., and Manson S. T.: Relative Intensities in Photoelectron-Spectroscopy of Atoms and Molecules. *J. Electron. Spectrosc.* 8, 389-394 (1976).
- [10] Tanuma S., Powell C. J., and Penn D. R.: Calculations of electron inelastic mean free paths. V. Data for 14 organic compounds over the 50-2000 eV range. *Surf. Interface Anal.* 21, 165-176 (1994).
- [11] Van Vaeck L., Adriaens A., and Gijbels R.: Static secondary ion mass spectrometry (S-SIMS) Part 1: methodology and structural interpretation. *Mass Spectrometry Reviews* 18, 1-47 (1999).
- [12] Manly B. F. J.: *Multivariate statistical method: a primer*, Chapman & Hall, London (1986).
- [13] Vickerman J. C.: *Multivariate Data Analysis Techniques in Surface Analysis*. in: Vickerman, J. C., *Surface Analysis - the Principal Techniques*, 1997, pp. 564-612.
- [14] Graham D., <http://mvsa.nb.uw.edu>.

## 4 Bulk characterization of polyphosphate glasses

This chapter is divided into two main parts. Section 4.1 concerns the physico-chemical characterization of the glasses (X-ray diffraction, elemental analysis, infrared spectroscopy and density) while the second section, 4.2, describes the mechanical properties of the samples and reports the results of measurements of micro- and nano-indentation.

The microelemental analyses presented in this chapter were performed by Mr. M. Schneider from the Laboratory of Organic Chemistry, ETH Zürich. The IR spectra of the zinc polyphosphates and part of the iron polyphosphates were measured by Dr. F. Mangolini (LSST, ETH-Zürich) who collaborated on the interpretation of the spectra as well. The nanoindentation was carried out by Dr. D. Courty (Nanometallurgy, ETH-Zürich). All remaining experiments were performed by me with the support and supervision of Prof. A. Rossi and Prof. N.D. Spencer; this is the case for all subsequent chapters when not differently specified.

### 4.1 Physico-chemical characterization of polyphosphate glasses

#### 4.1.1 XRD

The phosphate glasses synthesized in this work were obtained in the shape of round discs, 2-3 cm in diameter and 3-4 mm in thickness. The zinc phosphates were clear and transparent while the iron and mixed phosphates appeared black and highly reflective.

The absence of any peak in XRD (Figure 4.1) confirmed the amorphous state of the samples. The first discontinuity in the spectrum is due to a filter used as protection for the detector. Obtaining glassy samples became more difficult with increasing metal oxide content. In order to obtain glassy zinc oxide and iron poly<sub>1</sub> the cooling rate was increased by decreasing the thickness of the samples: only very thin and small glassy samples (less than 1cm x 1 mm) could be obtained for these compositions.

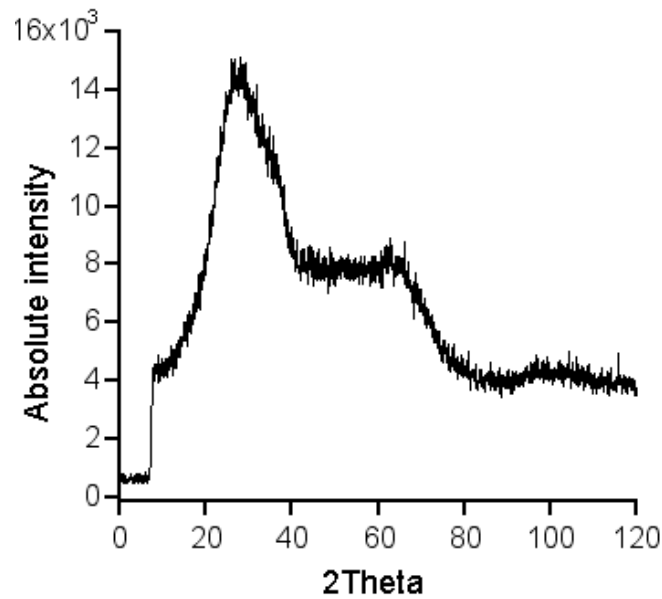


**Figure 4.1: X-ray diffraction spectrum of an amorphous zinc metaphosphate sample [1]**

#### *4.1.2 Microelemental analysis*

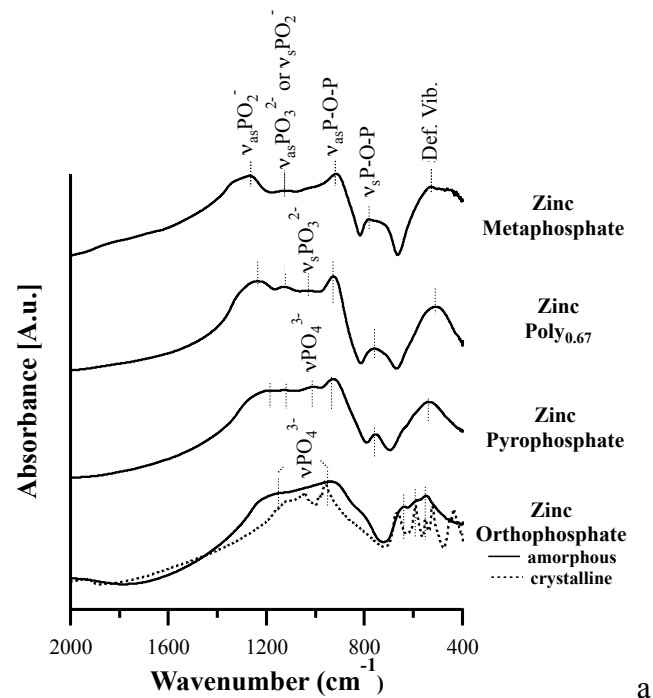
The phosphorus content of all samples was determined by micro-elemental analysis and is reported in Table 4.1. The measured P content for the zinc polyphosphate samples is compared with the batch composition (Table 4.1): there is excellent agreement with expected P content for all glasses.

The comparison is not possible in the case of iron-containing polyphosphates: it is known that when iron-containing polyphosphates are synthesized in air the resulting glass will contain both iron(II) and iron(III), even if only  $\text{Fe}_2\text{O}_3$  was used in the synthesis, therefore the oxygen content in the final composition will be different from that of the batch [2].

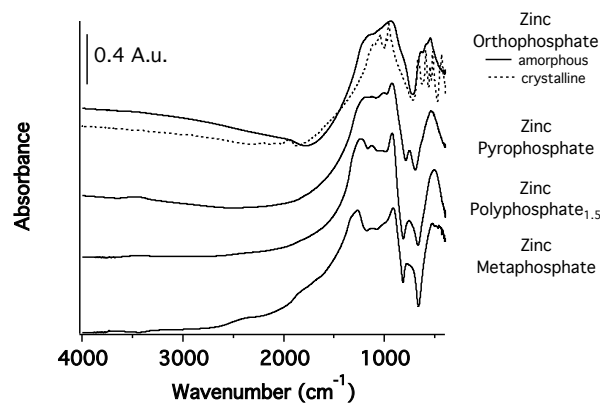
**Table 4.1: Results of the micro-elemental analysis compared with the composition of zinc polyphosphates calculated for the batch**

<i>Zinc polyphosphates</i>				
	<i>Zinc Orthophosphate</i>	<i>Zinc Pyrophosphate</i>	<i>Zinc Poly<sub>0.67</sub></i>	<i>Zinc metaphosphate</i>
<i>Elemental analysis</i>	[P]=16.1±0.5 wt.%	[P]=20.3±0.5 wt.%	[P]=24.8±0.5 wt.%	[P]=27.6±0.5 wt.%
<i>Calculated composition</i>	[P]=15 wt.%; [O]=33 wt.%; [Zn]=50.8 wt.%	[P]=20.3 wt.%; [O]=36.8 wt.%; [Zn]=42.3 wt.%	[P]=24.7 wt.%; [O]=40.5 wt.%; [Zn]=34.8 wt.%	[P]=27.9 wt.%; [O]=43.0 wt.%; [Zn]=29.3 wt.%
<i>Iron polyphosphates</i>				
	<i>Iron poly<sub>1</sub></i>	<i>Iron poly<sub>0.67</sub></i>	<i>Iron poly<sub>0.5</sub></i>	<i>Iron poly<sub>0.33</sub></i>
<i>Elemental analysis</i>	[P]=20.5±0.5 wt.%	[P]=24.7±0.5 wt.%	[P]=26.0±0.5 wt.%	[P]=27.9±0.5 wt.%
<i>Mixed iron and zinc polyphosphates</i>				
	<i>Zinc75 iron25 poly<sub>0.5</sub></i>	<i>Zinc50 iron50 poly<sub>0.5</sub></i>	<i>Zinc25 iron75 poly<sub>0.5</sub></i>	
<i>Elemental analysis</i>	[P]=26.4±0.5 wt.%	[P]=26.1±0.5 wt.%	[P]=26.5±0.5 wt.%	

## 4.1.3 Fourier-Transformed Infrared Spectroscopy



a



b

**Figure 4.2: Transmission FT-IR spectra of zinc polyphosphate glasses with different compositions. The FT-IR spectrum of crystalline zinc orthophosphate is shown for comparison [1]**

The transmission FT-IR spectra of the zinc phosphate glasses synthesized in the present work are shown in Figure 4.2. The IR peaks and the assigned functional groups are listed in Table 4.2.

As reported in the literature, in the case of phosphate glasses with different compositions [3-12], the vibrational spectra of amorphous zinc phosphates are characterized by broad absorption bands in the fingerprint region ( $2000\text{-}400\text{ cm}^{-1}$ ). The absence of water in the glasses synthesized in the present work is supported by the detection of no bands between  $3600\text{ and }3400\text{ cm}^{-1}$ , where the O-H stretching vibration of  $\text{H}_2\text{O}$  would be expected [13; 14] (Figure 4.2b).



In the case of zinc metaphosphate, the asymmetric envelope between 1350 and 1200  $\text{cm}^{-1}$  (maximum at 1271  $\text{cm}^{-1}$ ) can be assigned to the  $\nu_{as}(PO_2^-)$  of  $Q_2$  units and to the  $\nu(P=O)$  of  $Q_3$  units [7; 8; 12]. A contribution to this complex envelope can also originate from the characteristic  $\nu_s(PO_2^-)$  of  $Q_2$  units, which is usually found as a weak shoulder at ca. 1160  $\text{cm}^{-1}$  [7; 8]. The infrared spectra of metaphosphate glasses are usually characterized by a strong band between 820 and 1050  $\text{cm}^{-1}$ , which is assigned to the  $\nu_{as}(P-O-P)$  of  $Q_2$  units in chain- and ring-type formation [8]. The presence of a peak at 917  $\text{cm}^{-1}$  suggests that the tetrahedral units are predominantly arranged in a chain-like structure. The other two bands at 784 and 526  $\text{cm}^{-1}$  detected in the FT-IR spectrum of glassy zinc metaphosphate can be assigned to the  $\nu_s(P-O-P)$  of  $Q_2$  units and to the P-O bending mode, respectively [7; 8; 12].

The absorption bands appearing in the transmission FT-IR spectrum of zinc metaphosphate were also detected in the spectrum of zinc poly<sub>0.67</sub>, but the peaks exhibited a slight shift (Table 4.2). Moreover, an intense peak was found at 1134  $\text{cm}^{-1}$  and can be assigned to the characteristic stretching vibration of  $Q_1$  units, i.e.  $\nu_{as}(PO_3^{2-})$ .

In the case of glassy zinc pyrophosphate, a complex envelope was also detected in the FT-IR spectrum. The presence of  $Q_1$  units resulted in the appearance of strong absorption bands at 1122  $\text{cm}^{-1}$ , assigned to  $\nu_{as}(PO_3^{2-})$ , at 932  $\text{cm}^{-1}$ , assigned to  $\nu_{as}(P-O-P)$ , and at 757  $\text{cm}^{-1}$ , assigned to  $\nu_s(P-O-P)$ . Weak peaks at 1188  $\text{cm}^{-1}$ , assigned to the  $\nu_{as}(PO_2^-)$  of  $Q_2$  units, and at 1012  $\text{cm}^{-1}$ , assigned to the  $\nu(PO_4^{3-})$  of  $Q_0$  units, were also detected.

**Table 4.2: IR frequencies ( $\text{cm}^{-1}$ ) and functional groups for the transmission FT-IR spectra of zinc phosphate glasses with different composition**

<b>Zinc polyphosphate glasses</b>				
<b>Frequency (<math>\text{cm}^{-1}</math>)</b>				<b>Functional Group</b>
<b>Zinc metaphosphate</b>	<b>Zinc poly<sub>0.67</sub></b>	<b>Zinc pyrophosphate</b>	<b>Zinc orthophosphate</b>	
			551	
526	514	548	586	$\delta P-O$
			640	
784	759	757		$\nu_s P-O-P$
917	929	932		$\nu_{as} P-O-P$
		1012	946	$\nu PO_4^{3-}$
			1151 sh	
	1039			$\nu_s PO_3^{2-}$
1136	1134	1122		$\nu_{as} PO_3^{2-}$ and/or $\nu_s PO_2^-$
1271	1238	1188		$\nu_{as} PO_2^-$
<b>Iron polyphosphate glasses</b>				
<b>Frequency (<math>\text{cm}^{-1}</math>)</b>				<b>Functional Group</b>
<b>Iron poly<sub>0.33</sub></b>	<b>Iron poly<sub>0.5</sub></b>	<b>Iron poly<sub>0.67</sub></b>	<b>Iron poly<sub>01</sub></b>	
			563	
486	507	515	588	$\delta P-O$
			636	
776	763	757		$\nu_s P-O-P$
924	930	926		$\nu_{as} P-O-P$
			1020	
			1090	$\nu PO_4^{3-}$
1063	1160	1070		$\nu_{as} PO_3^{2-}$ and/or $\nu_s PO_2^-$
1229		1298		$\nu_{as} PO_2^-$
<b>Mixed zinc and iron polyphosphate glasses</b>				
<b>Frequency (<math>\text{cm}^{-1}</math>)</b>				<b>Functional Group</b>
<b>Zinc75 iron25 poly<sub>0.5</sub></b>	<b>Zinc50 iron50 poly<sub>0.5</sub></b>	<b>Zinc25 iron75 poly<sub>0.5</sub></b>		
499	501	507		$\delta P-O$
764	762	764		$\nu_s P-O-P$
922	928	924		$\nu_{as} P-O-P$
1121				$\nu_{as} PO_3^{2-}$ and/or $\nu_s PO_2^-$
1250	1217	1186		$\nu_{as} PO_2^-$

As for zinc orthophosphate, the FT-IR spectrum of both the amorphous and the crystalline compound is shown in Figure 4.2 for comparison. Compared to the FT-IR spectrum of crystalline zinc orthophosphate, which is characterized by several peaks appearing as a consequence of the change in symmetry induced by the distortion of the tetrahedral orthophosphate anion [15; 16], a broad peak with maximum at  $946\text{ cm}^{-1}$  and a shoulder at higher wavenumbers was detected in the FT-IR spectrum of the amorphous compound, in agreement with the literature [15; 16].

The iron polyphosphates (Figure 4.3) and the mixed zinc and iron polyphosphates (Figure 4.4) show analogous peaks. Zinc metaphosphate and iron  $\text{poly}_{0.5}$  are also provided in Figure 4.4 for comparison: going from zinc to iron polyphosphates a broadening of the peaks can be observed but the absorption bands are essentially the same observed for the zinc metaphosphate.

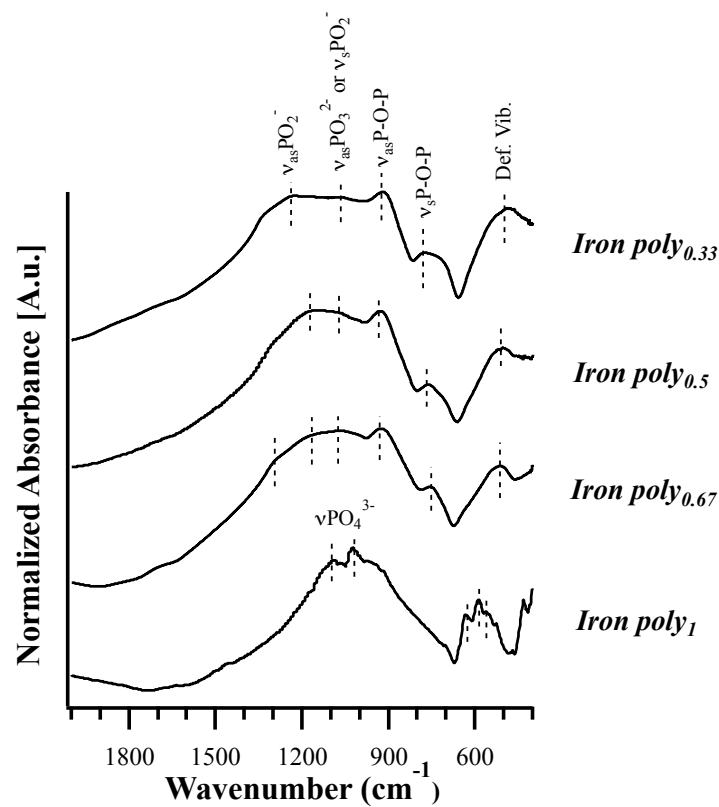


**Figure 4.3: Transmission FT-IR spectra of iron polyphosphate glasses with different compositions**

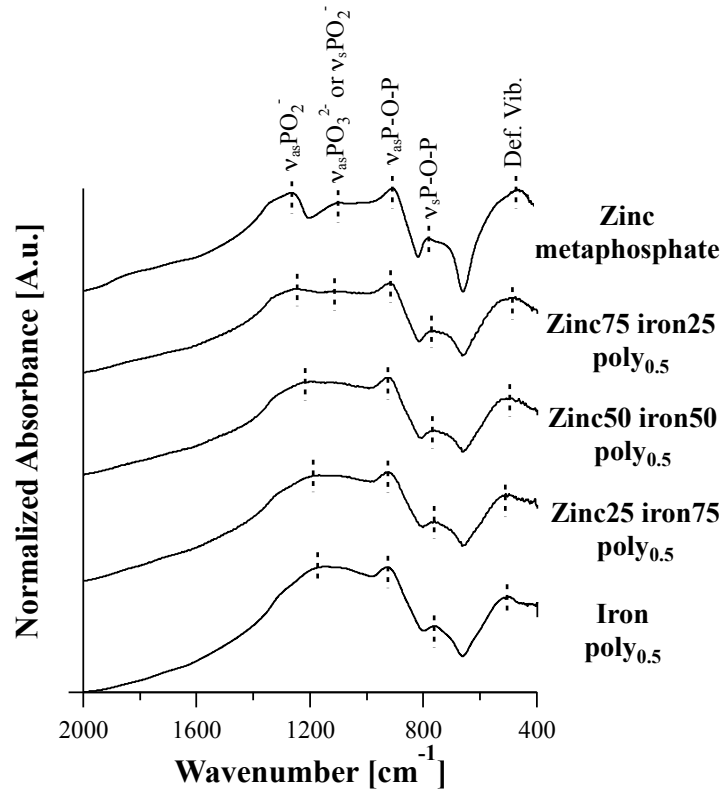


**Figure 4.4: Transmission FT-IR spectra of mixed zinc and iron polyphosphate glasses with different compositions**

#### 4.1.4 Density

The measured densities for all compositions are depicted in Figure 4.5 as a function of composition. The measured values vary from the  $2.8 \text{ g/cm}^3$  of iron  $\text{poly}_{0.33}$  and  $\text{poly}_{0.5}$  to  $4.0 \text{ g/cm}^3$  for zinc orthophosphate.

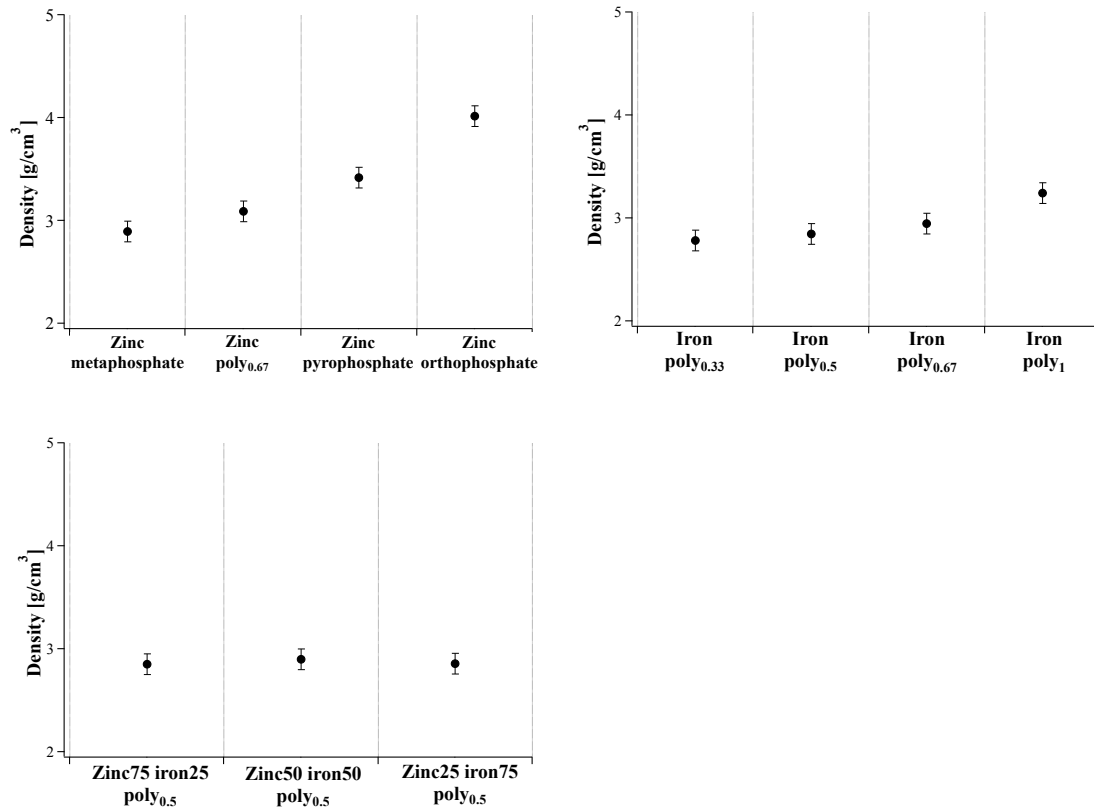


**Figure 4.5: Measured density values for different composition polyphosphates**

## 4.2 Mechanical properties

### 4.2.1 Microindentation

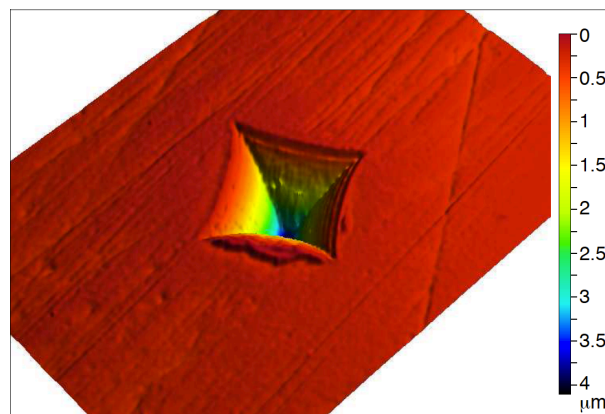


**Figure 4.6: 3-D topography following microindentation on zinc metaphosphate obtained by white-light profilometry**

The Vickers' hardness of the mechanically polished samples as a function of load was measured by means of microindentation. It was possible to use loads up to 1 Kgf without causing brittle fracture of the polyphosphates surfaces. In Figure 4.6 the

3-D topography of a zinc metaphosphate sample following indentation is reported as an example.

The measured values range from 2.5 to 4 GPa and a comparison between zinc and iron polyphosphates can be found in the graph of Figure 4.7. In the case of zinc the sequence is found to be zinc metaphosphate < poly<sub>0.5</sub> < pyrophosphate. An analogous trend is detected for iron, even if the differences are less pronounced. Iron polyphosphates in general are harder than zinc polyphosphates and, upon increasing the metal content of the glasses, the hardness increases.

A trend towards higher hardness can also be observed with increasing applied load; this trend is more pronounced for the long-chain-length samples and tends to disappear with increasing metal oxide content.

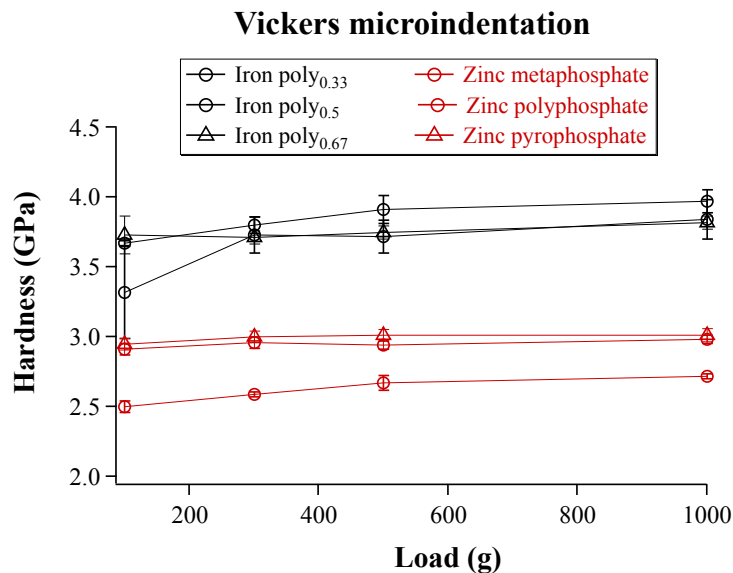


**Figure 4.7: Vickers hardness as a function of the microindentation applied load on zinc and iron polyphosphates**

#### 4.2.2 Nanoindentation

Microindentation could not be used for all samples: the short-chain-length samples (zinc orthophosphate and iron poly<sub>1</sub>) were too small and brittle. For this reason these compositions were also excluded from the tribological tests (see Chapter 7 and 8). Nevertheless, nanoindentation could be applied to all of them: hardness and elastic modulus can be estimated from the un-loading segment of the force-displacement curve, e.g. zinc metaphosphate in Figure 4.8, using the Oliver-Pharr method [17].

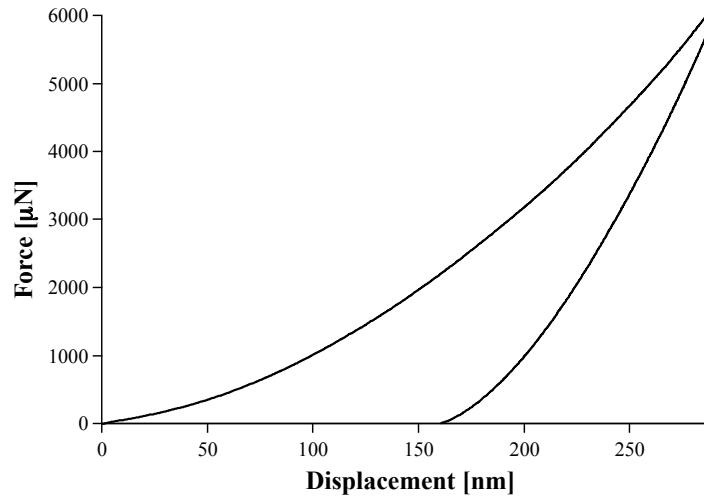


**Figure 4.8: Typical force-displacement curve for a nanoindentation measurement on zinc metaphosphate**

The values of hardness and reduced modulus are plotted in Figure 4.9. The reduced modulus,  $E_r$ , is correlated to the elastic modulus,  $E$ , and the Poisson's ratio,  $\nu$ , of both sample and indenter:

**Equation 4.1**

$$\frac{1}{E_r} = \frac{1 - \nu^2}{E} + \frac{1 - \nu_i^2}{E_i}$$

The values of hardness and reduced modulus measured on the different polyphosphates under investigation are summarized in Figure 4.9.

The mechanical properties of the surface and cross-section of a series of samples were compared and no anisotropy was observed in the mechanical properties [18].

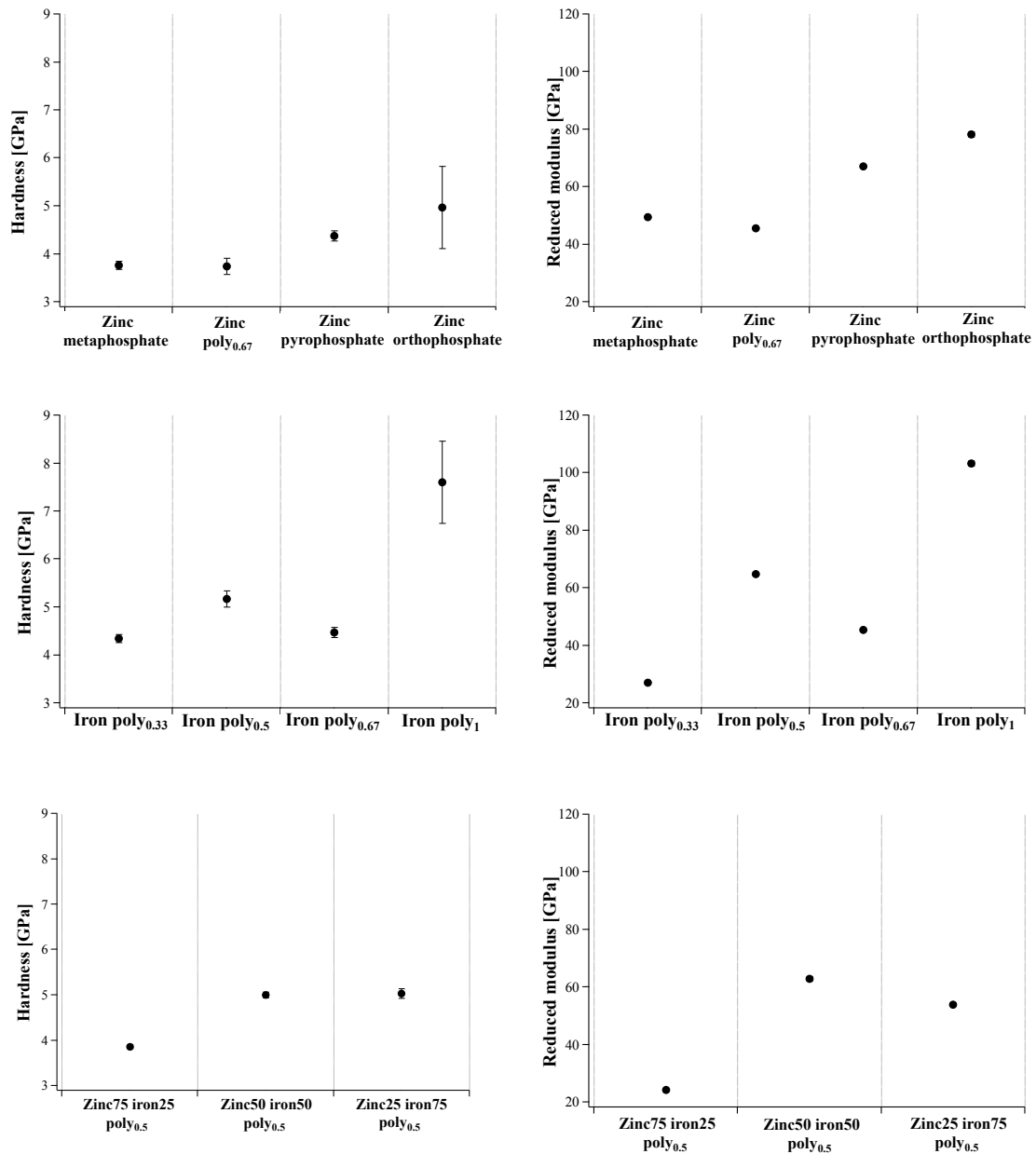


**Figure 4.9: Hardness and reduced modulus obtained from nanoindentation measurements on different compositions of polyphosphates**

### 4.3 Discussion

The results of the XRD analysis and of the micro-elemental analysis demonstrated that the synthesized glasses had the expected composition (Table 4.1) and structure (i.e. amorphous).

The FT-IR spectra (Figure 4.2) of zinc metaphosphate showed the characteristic peaks of glasses with metaphosphate composition, in agreement with previous studies concerning binary amorphous phosphates [7; 8; 12]. Moreover, the absence of any strong absorption band in the region between 1050 and 1150  $\text{cm}^{-1}$ ,



where the characteristic stretching vibration of  $Q_1$  units (i.e.  $\nu_{as}(PO_3^{2-})$ ) occurs, indicates that the phosphate tetrahedral structure did not undergo any disproportionation reaction ( $Q_2 \rightarrow Q_3 + Q_1$ ), as reported in [12].

Moving from zinc metaphosphate to pyrophosphate, the blue shift and red shift of, respectively, the asymmetric and symmetric P-O-P stretching vibrations observed as the amount of ZnO in the phosphate glass increases (Table 4.2), is in agreement with the literature [19]. However, the structures of glasses, whose composition is close to that of pyrophosphate, are known to contain, besides  $Q_1$  units, a certain amount of  $Q_0$  and  $Q_2$  units, which are the products of the disproportionation reaction of  $Q_1$  units ( $Q_1 \rightarrow Q_2 + Q_0$ ) [5]. As a consequence of this, the characteristic absorption bands of  $Q_2$  and  $Q_0$  units might contribute to the complex envelopes appearing in the FT-IR spectra of glassy pyrophosphates. The detection of weak peaks, which can be assigned to the  $\nu_{as}(PO_2^-)$  of  $Q_2$  units and to the  $\nu(PO_4^{3-})$  of  $Q_0$  units, clearly indicates that the pyrophosphate structure comprised orthophosphate anions as well as polymeric phosphate chains, suggesting that the pyrophosphate groups indeed underwent a disproportionation reaction.

With the addition of iron instead of zinc, Figure 4.4, the absorption bands, already broad due to the amorphous state of the samples, become broader but peaks analogous to the zinc metaphosphate composition are observed. This is probably due to the presence of more than one oxidation state of iron that results in a highly disordered short-range order. In the region between 1050 and 1250  $cm^{-1}$  a complex envelope constituted by the vibrations of  $Q_2$  units is present. With increasing iron oxide content, a blue shift of the symmetric P-O-P stretching vibration and a red shift of the asymmetric P-O-P is observed, in analogy with zinc polyphosphates (Figure 4.3 and Table 4.2)

The density of polyphosphate glasses (Figure 4.5) has been experimentally determined and published for many different compositions and the values obtained in this work are in good agreement with the literature [20-22]. The graphs in Figure 4.5 show a trend toward higher density values with increasing metal oxide content for both zinc and iron polyphosphates, in agreement with the literature [20-22]. No changes in the density are observed in the case of mixed polyphosphates where the total metal content is constant with different zinc-to-iron ratios.

It has been shown that some properties of the glass, such as the refractive index [22], are highly correlated with the molar volume, MV, defined as the molecular weight divided by the density. The values of MV for the polyphosphates under investigation are reported in Table 4.3. A decrease of the molar volume with

the increase of the iron content is observed. In the mixed polyphosphates the MV decreases with increasing zinc to iron oxide ratio, while the density remains constant.

**Table 4.3: Values of molecular weight (calculated using the batch composition), density and molar volume for all polyphosphates under investigation**

<i>Zinc polyphosphates</i>				
<i>Given name</i>	<i>Formula</i>	<i>Molecular Weight</i>	<i>Density <math>\rho</math> [g/cm<sup>3</sup>]</i>	<i>Molar Volume</i>
Zinc metaphosphate	0.5(ZnO)·0.5(P <sub>2</sub> O <sub>5</sub> )	112	2.9±0.1	39
Zinc poly <sub>0.67</sub>	0.57(ZnO)·0.43(P <sub>2</sub> O <sub>5</sub> )	107	3.1±0.1	35
Zinc pyrophosphate	0.67(ZnO)·0.33(P <sub>2</sub> O <sub>5</sub> )	101	3.4±0.1	30
Zinc orthophosphate	0.75(ZnO)·0.25(P <sub>2</sub> O <sub>5</sub> )	97	4.0±0.1	24
<i>Iron polyphosphates</i>				
<i>Given name</i>	<i>Formula</i>	<i>Molecular Weight</i>	<i>Density <math>\rho</math> [g/cm<sup>3</sup>]</i>	<i>Molar Volume</i>
Iron poly <sub>0.33</sub>	0.25(Fe <sub>2</sub> O <sub>3</sub> )·0.75(P <sub>2</sub> O <sub>5</sub> )	146	2.8±0.1	53
Iron poly <sub>0.5</sub>	0.33(Fe <sub>2</sub> O <sub>3</sub> )·0.67(P <sub>2</sub> O <sub>5</sub> )	148	2.8±0.1	52
Iron poly <sub>0.67</sub>	0.40(Fe <sub>2</sub> O <sub>3</sub> )·0.60(P <sub>2</sub> O <sub>5</sub> )	149	2.9±0.1	51
Iron poly <sub>1</sub>	0.5(Fe <sub>2</sub> O <sub>3</sub> )·0.5(P <sub>2</sub> O <sub>5</sub> )	151	3.2±0.1	47
<i>Mixed iron and zinc polyphosphates</i>				
<i>Given name</i>	<i>Formula</i>	<i>Molecular Weight</i>	<i>Density <math>\rho</math> [g/cm<sup>3</sup>]</i>	<i>Molar Volume</i>
Zinc25 iron75 poly <sub>0.5</sub>	0.40(ZnO)·0.07(Fe <sub>2</sub> O <sub>3</sub> )·0.53(P <sub>2</sub> O <sub>5</sub> )	137	2.9±0.1	48
Zinc50 iron50 poly <sub>0.5</sub>	0.20(ZnO)·0.14(Fe <sub>2</sub> O <sub>3</sub> )·0.57(P <sub>2</sub> O <sub>5</sub> )	127	2.9±0.1	44
Zinc75 iron25 poly <sub>0.5</sub>	0.15(ZnO)·0.23(Fe <sub>2</sub> O <sub>3</sub> )·0.62(P <sub>2</sub> O <sub>5</sub> )	119	2.9±0.1	42

Only few experimental works on the mechanical properties of polyphosphate glasses are available in the literature [23-27].

The results presented in paragraph 4.2.1 and 4.2.2 are only the final results of an extended study that allowed the optimization of the synthesis protocol. In the master project of M. Süess [18] a first characterization of the glasses can be found: the polyphosphates showed higher values of hardness with increasing oxide content and an increase in the measured hardness with the applied load. The glasses also showed the presence of some small gas bubbles preferably located at the surface of the samples. The roughness caused by the presence of the bubbles did not disappear even after mechanical polishing, influencing the results of the mechanical and tribological tests. The problem was solved by decreasing the heating rate during the

synthesis (see Chapter 3, Table 3.4), therefore increasing the time available for the gas bubbles, produced by the chemical reaction, to diffuse away from the polyphosphate melt. None of the samples used in this chapter and the following contained any gas bubbles.

The results of the microindentation tests on the new samples show the same trends with composition but with higher absolute values (around 2 GPa difference) compared to the samples with bubbles. Conversely, the nanoindentation results were comparable for the two sets of samples because the volume of sample involved in this test is small enough not to be influenced by the presence of the gas bubbles.

A higher value of the measured hardness with higher indentation load is always observed in the microindentation results, especially for the samples with lower metal oxide content. This phenomenon is commonly referred to as reversed indentation size effect (RISE) and it is rather poorly understood [28]. Sangwal [29] offered an explanation that applies to most materials. Materials showing RISE do not exhibit resistance or undergo elastic recovery but they release the indentation stress away from the indentation site by relaxation, leading to larger indentation areas, and therefore lower hardness at low loads [18; 29]. It can be hypothesized that polyphosphate glasses have the ability to collapse free volume and to densify their structures by plastic deformation. At lower loads, free volume can be collapsed rather easily causing a rather low hardness. While increasing the load, a layer of collapsed, densified material builds up around the indentation pyramid. The densified glass presents more resistance towards further indentation; hence the hardness increases with higher indentation loads. This could also explain why the RISE effect is stronger when the metal oxide content is lower: those same samples are characterized by low density (Table 4.3) and a long-chain-length structure (Paragraph 4.3). It is reasonable to hypothesize that the presence of long phosphate chains is inhibiting the formation of a close-packed, high-density solid, and therefore the glass will have a lower resistance towards indentation and a higher possibility to deform its structure. It is clear that the density of the glass is influencing its mechanical properties.

The values of hardness obtained by nanoindentation (Figure 4.9) are comparable to those obtained by microindentation (Figure 4.7). Iron polyphosphates show higher hardness and for both zinc and iron polyphosphates the hardness increases with increasing metal oxide content. The reduced modulus follows the same trend.

Recently it has been observed that the structural strength of these glasses is increasing with the degree of connectivity in the glass [25; 26; 30; 31]. Baikova et.al. investigated a four series of phosphate glasses and found that there is a linear dependence of the Young's modulus on the total bonding energy per unit volume of the glass (see also Chapter 2) [25; 32]. The total bonding energy,  $U_m$ , is calculated

using the atomic packing density of the glass and the dissociation energies of the oxides that can be found in [32]. If we calculate  $U_m$  for zinc metaphosphate and zinc pyrophosphate we obtain 3.4 and 3.9 kcal/cm<sup>3</sup>, therefore we can predict an increase in the Young modulus value when going from long to short chain-lengths.

An increase of the density of the material would result in an increase of  $U_m$  in the predictive formula in agreement with our previous hypotheses based on the microindentation results. A similar change in the mechanical properties with the atomic packing density has been already observed in silicate glasses [33].

The mechanical properties play an important role in the friction and wear behavior of a material therefore these results will be discussed again together with the tribological results in Chapter 9.

#### **4.4 Summary**

X-ray-amorphous polyphosphate glasses with different compositions have been described in this chapter. It was shown that polyphosphates with high-phosphorus content are characterized by long, linear phosphate chains; these chains become shorter with increasing metal oxide content. Their hardness (HV) was found to be in the range between 2 and 5 GPa. Iron polyphosphates showed higher hardness values compared to zinc metaphosphate. Both iron and zinc long-chain-length polyphosphates exhibited lower hardness than the short-chain-length compositions. The reduced elastic modulus showed a similar trend with composition.

## References

- [1] Crobu M., Rossi A., Mangolini F., and Spencer N. D.: Tribochemistry of Bulk Zinc Metaphosphate Glasses. *Tribol. Lett.* 39, 121-134 (2010).
- [2] Armelao L., Bettinelli M., Rizzi G. A., and Russo U.: X-Ray photoelectron and Mossbauer spectroscopies of a binary iron phosphate glass. *J. Materials Chem.* 1, 805-808 (1991).
- [3] Bartholomew R. F.: Structure and properties of silver phosphate glasses - Infrared and visible spectra. *J. Non-Cryst. Solids* 7, 221-235 (1972).
- [4] Dayanand C., Bhikshamaiah G., Tyagaraju V. J., Salagram M., and Krishna Murthy A. S. R.: Structural investigations of phosphate glasses: a detailed infrared study of the  $x(\text{PbO})-(1-x) \text{P}_2\text{O}_5$  vitreous system. *J. Mater. Sci.* 31, 1945-1967 (1996).
- [5] Efimov A. M.: IR fundamental spectra and structure of pyrophosphate glasses along the  $2\text{ZnO} \cdot \text{P}_2\text{O}_5 - 2\text{Me}(2)\text{O} \cdot \text{P}_2\text{O}_5$  (Me being Na and Li). *J. Non-Cryst. Solids* 209, 209-226 (1997).
- [6] Liu H. S., Chin T. S., and Yung S. W.: FTIR and XPS studies of low-melting  $\text{PbO-ZnO-P}_2\text{O}_5$  glasses. *Mater. Chem. Phys.* 50, 1-10 (1997).
- [7] Meyer K.: Characterization of the structure of binary zinc ultraphosphate glasses by infrared and Raman spectroscopy. *J. Non-Cryst. Solids* 209, 227-239 (1997).
- [8] Rulmont A., Cahay R., Liegeoisduyckaerts M., and Tarte P.: Vibrational Spectroscopy of Phosphates - Some General Correlations between Structure and Spectra. *European Journal of Solid State and Inorganic Chemistry* 28, 207-219 (1991).
- [9] Schwarz J., Ticha H., Tichy L., and Mertens R.: Physical properties of  $\text{PbO-ZnO-P}_2\text{O}_5$  glasses - I. Infrared and Raman spectra. *Journal of Optoelectronics and Advanced Materials* 6, 737-746 (2004).
- [10] Shih P. Y.: Properties and FTIR spectra of lead phosphate glasses for nuclear waste immobilization. *Mater. Chem. Phys.* 80, 299-304 (2003).
- [11] Termine J. D., and Lundy D. R.: Vibrational-spectra of some phosphate salts amorphous to X-ray-diffraction. *Calcified Tissue Research* 15, 55-70 (1974).
- [12] Velli L. L., Varsamis C. P. E., Kamitsos E. I., Moncke D., and Ehrt D.: Structural investigation of metaphosphate glasses. *Phys. Chem. Glasses* 46, 178-181 (2005).
- [13] Colthup N. B., Daly L. H., and Wiberley S. E.: *Introduction to Infrared and Raman Spectroscopy*, Academic Press (1990).
- [14] Socrates G.: *Infrared and Raman Characteristic Group Frequencies*, John Wiley & Sons, Chichester (2001).
- [15] Chen W. S., Monroe E. A., Condrate R. A., and Guo Y. M.: An investigation of the hardening process for several phosphate glass-containing cements. *Journal of Materials Science-Materials in Medicine* 4, 111-116 (1993).
- [16] Crisp S., Oneill I. K., Prosser H. J., Stuart B., and Wilson A. D.: Infrared spectroscopic studies on development of crystallinity in dental zinc phosphate cements. *J. Dent. Res.* 57, 245-254 (1978).
- [17] Pharr G. M., and Oliver W. C.: Measurement Of Thin-Film Mechanical-Properties Using Nanoindentation. *MRS Bull.* 17, 28-33 (1992).
- [18] Süess M., The influence of the phosphorus to zinc ration on chemical and mechanical properties of zinc phosphate glasses, Master project - ETH Zürich, 2009.
- [19] Karabulut M., Metwalli E., Day D. E., and Brow R. K.: Mossbauer and IR investigations of iron ultraphosphate glasses. *J. Non-Cryst. Solids* 328, 199-206 (2003).

- [20] Walter G., Goerigk G., and Russel C.: The structure of phosphate glass evidenced by small angle X-ray scattering. *J. Non-Cryst. Solids* 352, 4051-4061 (2006).
- [21] Brow R. K.: Review: the structure of simple phosphate glasses. *J. Non-Cryst. Solids* 263-264, 1-28 (2000).
- [22] Brow R. K., Tallant D. R., Myers S. T., and Phifer C. C.: The Short-Range Structure of Zinc Polyphosphate Glass. *J. Non-Cryst. Solids* 191, 45-55 (1995).
- [23] Wang K., Russel C., and Liu C. S.: Preparation, mechanical properties and corrosion behaviors of oriented Ca(PO<sub>3</sub>)<sub>2</sub> glass-ceramics. *Mater. Chem. Phys.* 111, 106-113 (2008).
- [24] Sunnegardh-Gronberg K., Peutzfeldt A., and van Dijken J. W. V.: Hardness and in vitro wear of a novel ceramic restorative cement. *European Journal of Oral Sciences* 110, 175-178 (2002).
- [25] Baikova L. G., Pukh V. P., Fedorov Y. K., Sinani A. B., Tikhonova L. V., and Kireenko M. F.: Mechanical properties of phosphate glasses as a function of the total bonding energy per unit volume of glass. *Glass Phys. Chem.* 34, 126-131 (2008).
- [26] Kurkjian C. R.: Mechanical properties of phosphate glasses. *J. Non-Cryst. Solids* 263-264, 207-212 (2000).
- [27] Karabulut M., Melnik E., Stefan R., Marasinghe G. K., Ray C. S., Kurkjian C. R., and Day D. E.: Mechanical and structural properties of phosphate glasses. *J. Non-Cryst. Solids* 288, 8-17 (2001).
- [28] Mukhopadhyay N. K., and Paufler P.: Micro- and nanoindentation techniques for mechanical characterisation of materials. *International Materials Reviews* 51, 209-245 (2006).
- [29] Sangwal K.: On the reverse indentation size effect and microhardness measurement of solids. *Mater. Chem. Phys.* 63, 145-152 (2000).
- [30] Pawlak Z., Yarlagaadda P. K. D. V., Frost R., and Hargreaves D.: The mechanical characteristics of phosphate glasses under high temperature and friction-induced cross-linking processes. *Journal of Achievements in Materials and Manufacturing Engineering* 37, 458-465 (2009).
- [31] Reis S. T., Karabulut M., and Day D. E.: Chemical durability and structure of zinc-iron phosphate glasses. *J. Non-Cryst. Solids* 292, 150-157 (2001).
- [32] Makishima A., and Mackenzie J. D.: Direct calculation of Young's modulus of glass. *J. Non-Cryst. Solids* 12, 35-45 (1973).
- [33] Greaves G. N., Greer A. L., Lakes R. S., and Rouxel T.: Poisson's ratio and modern materials. *Nature Materials* 10, 823-837 (2011).

## 5 Surface analysis of zinc, iron and mixed zinc/iron polyphosphate glasses

The surface chemistry of amorphous zinc, iron and mixed zinc/iron polyphosphates of different compositions has been investigated by means of X-ray photoelectron spectroscopy (Section 5.1) and time-of-flight secondary-ion mass spectroscopy (Section 5.2). The XPS results allowed the identification of the chemical state of the elements, and information on the short-range structure of the glasses could also be obtained using, for example, the intensity ratio of the bridging (P-O-P) and non-bridging (P=O and P-O-M) oxygen peaks (Section 5.3.1). The averaged composition of the glasses is also provided (Section 5.3.2). The ToF-SIMS spectra showed that the fragmentation patterns of the different polyphosphates appeared to be analogous for all compositions (Section 5.2), while the different chain-length polyphosphates could be discriminated by comparing the normalized intensities of selected characteristic phosphate fragments (Section 5.3.3). Finally, the effect of different primary ions on the ToF-SIMS fragmentation patterns is discussed (Section 5.3.4).

The XPS and ToF-SIMS analysis of zinc polyphosphates has been published in [1] and the preliminary ToF-SIMS results of iron polyphosphates in [2].

### 5.1 XPS analysis

The phosphate samples were analyzed by XPS immediately after the annealing step in order to avoid any source of contamination.

#### 5.1.1 Survey spectra

Typical survey spectra for a zinc<sub>25</sub> iron<sub>75</sub> poly<sub>0.5</sub>, a zinc metaphosphate and an iron poly<sub>0.33</sub> sample are reported in Figure 5.1. Similar spectra were obtained for all the glass compositions investigated in the present work (see Appendix A.4). The main signals in the spectrum belong to the glass constituents (P, O, Zn, Fe). Minor contamination by carbon, arising from the ambient exposure of the samples before analysis, and aluminum, due to the crucibles used for the synthesis, was always observed. The intensity of the carbon 1s peak was always lower than 4% of that of the oxygen 1s signal.

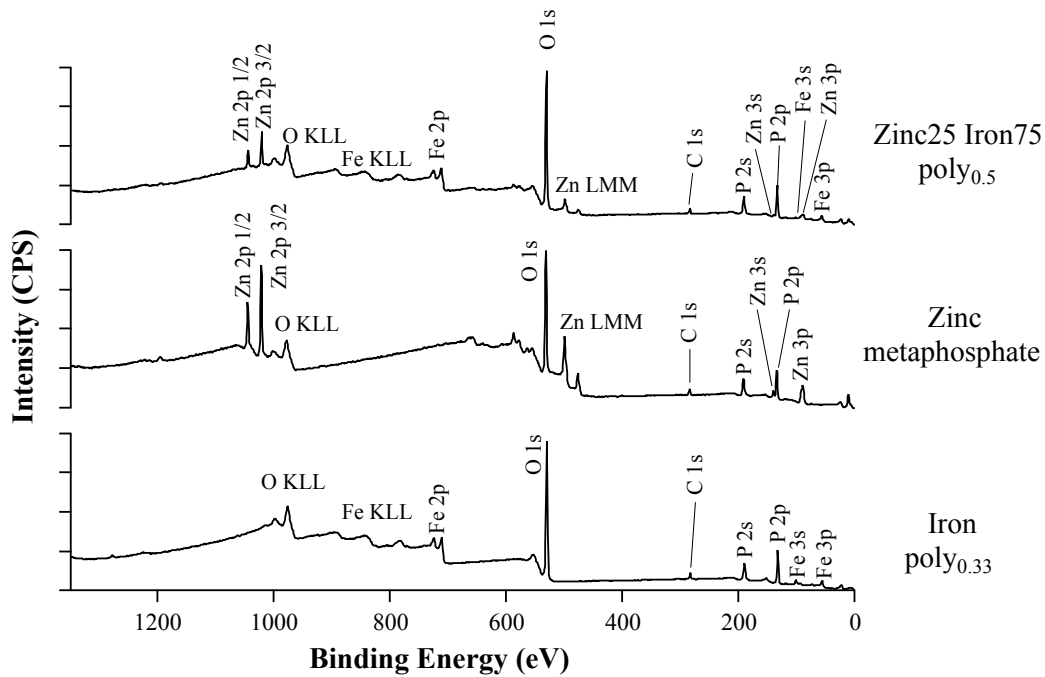


**Figure 5.1: Survey spectra of zinc25 iron75 poly<sub>0.5</sub>, zinc metaphosphate and iron poly<sub>0.33</sub>**

### 5.1.2 Zinc polyphosphate glasses

In Figure 5.2, the high-resolution spectra for the four samples of different composition under investigation are depicted. Moving from the top spectrum to the bottom one in each graph, the ZnO content increases, i.e. the chain-length decreases. The phosphorus peak was fitted with a doublet due to the spin-orbit coupling. The component at lower BE, assigned to the P 2p<sub>3/2</sub>, and one at higher BE was assigned to the P 2p<sub>1/2</sub>. The Zn 3s signal was acquired in the same BE range as that of the P 2p signal: it is immediately evident that the between P 2p/Zn 3s area ratio is changing with the composition of the glass. Moreover, while the Zn 3s does not shift by changing the glass composition (141.0 eV), the P 2p<sub>3/2</sub> signal changes gradually from 134.1<sub>0</sub> eV to 134.7<sub>5</sub> eV moving from the orthophosphate to the metaphosphate composition. The binding-energy difference between the P 2p<sub>3/2</sub> and the P 2p<sub>1/2</sub> signal was not constrained and the mean value was found to be 0.90 ± 0.05 eV. In agreement with the different photoionization probabilities predicted by Scofield the Zn 2p<sub>3/2</sub> signal was much more intense than the Zn 3s signal, its position was also constant at 1223.0 ± 0.1 eV. The intensities of both Zn 3s and Zn 2p<sub>3/2</sub> peaks decrease upon going from ortho- to metaphosphate in agreement with the calculated stoichiometry.



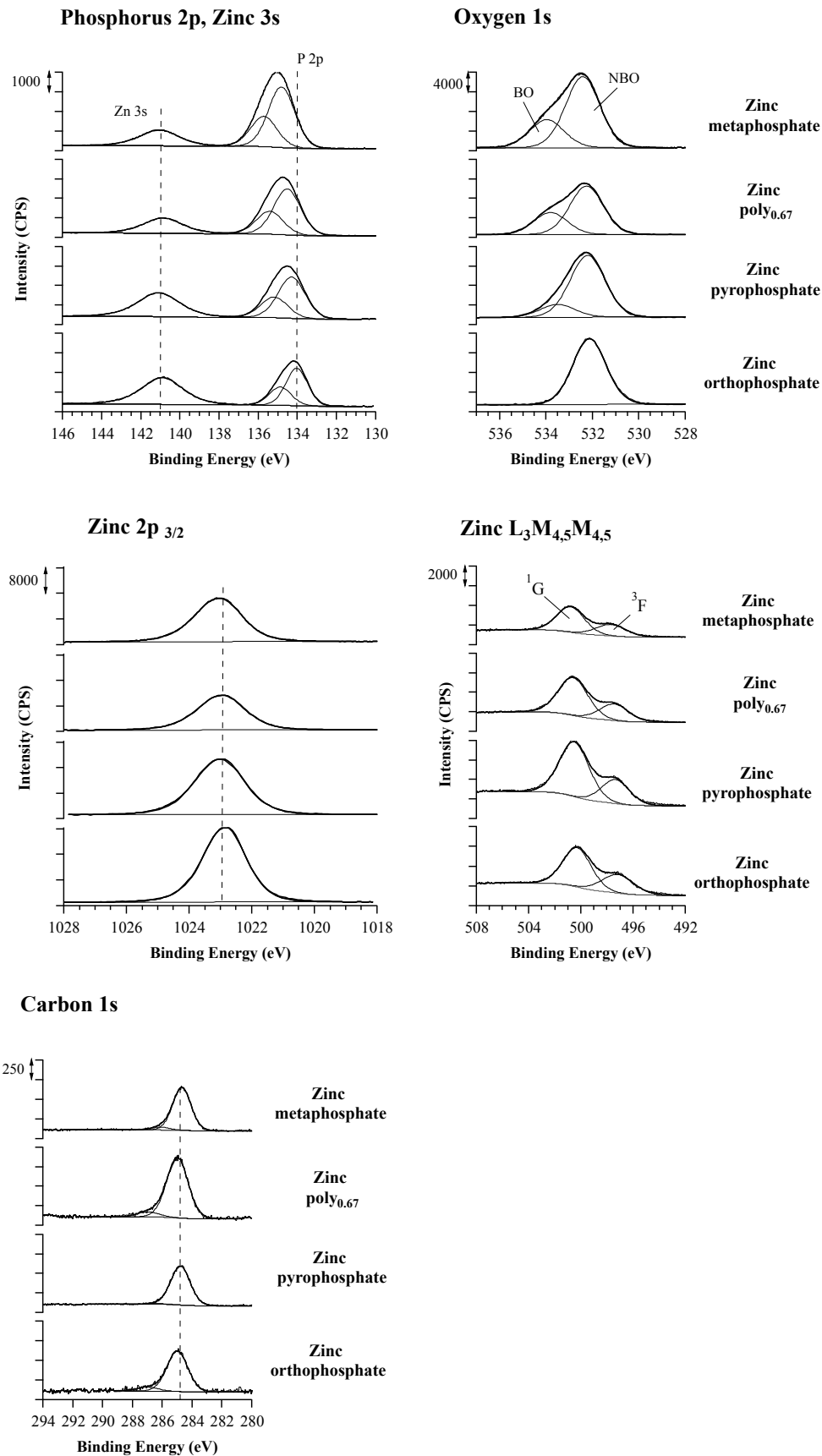


**Figure 5.2: Phosphorus P 2p, zinc Zn 3s, oxygen O 1s, zinc Zn 2p<sub>3/2</sub>, zinc Zn L<sub>3</sub>M<sub>4,5</sub>M<sub>4,5</sub> and carbon C 1s high-resolution XPS spectra for zinc metaphosphate, zinc poly<sub>0.67</sub>, zinc pyrophosphate and zinc orthophosphate**

**Table 5.1: XPS peak binding energies of zinc polyphosphate glasses**

	<i>Zinc orthophosphate</i>	<i>Zinc pyrophosphate</i>	<i>Zinc poly<sub>0.67</sub></i>	<i>Zinc metaphosphate</i>
<i>O 1s - NBO [eV]</i>	532.2 <sub>0</sub> ±0.1 <sub>1</sub>	532.26±0.04	532.28±0.05	532.40±0.09
<i>O 1s - BO [eV]</i>	-	533.69±0.08	533.7 <sub>1</sub> ±0.1 <sub>2</sub>	534.0 <sub>7</sub> ±0.1 <sub>0</sub>
<i>P 2p<sub>3/2</sub> [eV]</i>	134.10±0.09	134.35±0.08	134.49±0.05	134.75±0.08
<i>Zn 2p<sub>3/2</sub> [eV]</i>	1022.94±0.09	1023.10±0.04	1023.01±0.04	1023.0 <sub>4</sub> ±0.1 <sub>0</sub>
<i>Zn 3s [eV]</i>	140.96±0.07	141.0 <sub>5</sub> ±0.1 <sub>3</sub>	140.94±0.07	141.02±0.09
<i>ZnL<sub>3</sub>M<sub>4,5</sub>M<sub>4,5</sub> [eV]</i>	500.31±0.05	500.56±0.08	500.61±0.09	500.7 <sub>7</sub> ±0.1 <sub>4</sub>
<i>The maximum error for the binding energy values was found to be ±0.1 eV for all signals.</i>				
<i>P 2p<sub>1/2</sub>-P 2p<sub>3/2</sub> BE difference</i>	0.90±0.02	0.90±0.02	0.91±0.02	0.86±0.04
<i>BO/NBO Intensity ratio</i>	-	0.20±0.05	0.37±0.05	0.48±0.02
<i>Zinc Modified Auger Parameter, α' [eV]</i>	2009.23±0.09	2009.1 <sub>4</sub> ±0.1 <sub>0</sub>	2009.00±0.09	2008.8 <sub>7</sub> ±0.1 <sub>7</sub>
<i>ZnL<sub>3</sub>M<sub>4,5</sub>M<sub>4,5</sub><sup>1</sup>G<sup>-3</sup>F BE difference</i>	3.19±0.03	3.16±0.03	3.18±0.01	3.13±0.02

The use of a subscript indicates that the digits are given only to avoid loss of information.

The possibility of distinguishing phosphate glasses of different chain lengths by XPS is known to be based on the calculation of the ratio between the bridging oxygen (BO) and non-bridging oxygen (NBO) peaks, used for fitting the O 1s signal. This procedure has been extensively reported in the literature in the case of both silicate and phosphate glasses [3-11]. In the present work, the oxygen 1s signal was fitted with two peaks: the NBO component was found at 532.3±0.1 eV for all samples, while the position of the BO turned out to be slightly dependent on the composition. In order to have an insight into the influence of the ZnO content on the position of the bridging-oxygen peak, the distance between the two peaks was calculated ( $\Delta E_{BO/NBO}$ ). The value of  $\Delta E_{BO/NBO}$  was found to be 1.4<sub>3</sub> eV for zinc pyrophosphate and 1.6<sub>7</sub> eV for zinc metaphosphate.

However, the most evident difference between the four spectra was the BO/NBO area ratio; this value was found to decrease from 0.48±0.02 for zinc metaphosphate to 0.20±0.05 for the zinc pyrophosphate. In the orthophosphate spectra, the BO signal was not detected.

Previous publications [12] reported for ZnO that the Zn  $L_3M_{4,5}M_{4,5}$  region consists of three different final states, but in the spectra of this work only two signals could be resolved, the  $^1G$  and the  $^3F$ . The position of the most intense peak of the Auger Zn  $L_3M_{4,5}M_{4,5}$ , the  $^1G$  signal, was found to shift from 500.7<sub>7</sub> eV for zinc metaphosphate to 500.3<sub>1</sub> eV for zinc orthophosphate. The  $^3F$  signal was found at a distance of 3.2 eV in the binding-energy scale. The modified Auger parameter,  $\alpha'$ , was calculated by adding the BE of the Zn  $2p_{3/2}$  to the KE of the Zn  $L_3M_{4,5}M_{4,5}$   $^1G$  and found to shift from 2008.9 $\pm$  0.1 for zinc metaphosphate to 2009.2 $\pm$  0.1 eV for the orthophosphate.

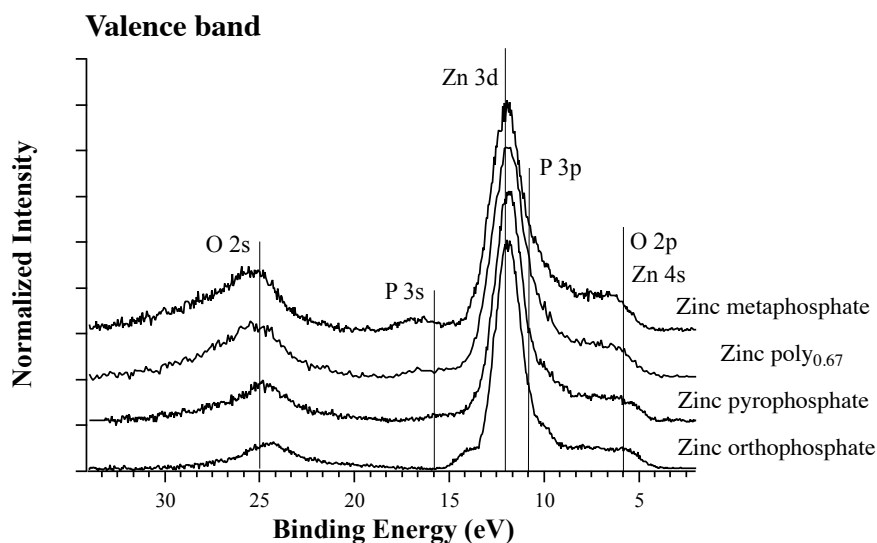


**Figure 5.3: Valence-band high-resolution XPS spectra after background subtraction, for zinc metaphosphate, zinc polyphosphate 1.5, zinc pyrophosphate and zinc orthophosphate**

The valence-band region is reported in Figure 5.3 and appears to be dominated by a very intense Zn 3d peak at ~12.5 eV; the Zn 4s and O 2p signals are contributing to the peak found at ~6 eV [13]. As previously observed in sodium polyphosphate glasses [14], the O 2s shows a broad signal at ~25eV, while P 3s and P 3p should appear at 14 and 11 eV. The peak at lower BE cannot be clearly resolved from the Zn 3d signal whereas the P 3s peak is clearly observed and its position shifts towards high BEs for the samples with longer chain-length.

### 5.1.3 Iron polyphosphate glasses

Iron-containing polyphosphates are not inert to X-ray radiation. A component at BE of 710 eV appears in the Fe 2p signal as a consequence of X-ray-induced degradation and increases with the acquisition time (Figure 5.4). This peak, observed also by [15; 16] on commercial crystalline phosphates, cannot be attributed to iron oxide because the oxygen spectrum remains unchanged and no signal can be detected at 530 eV.

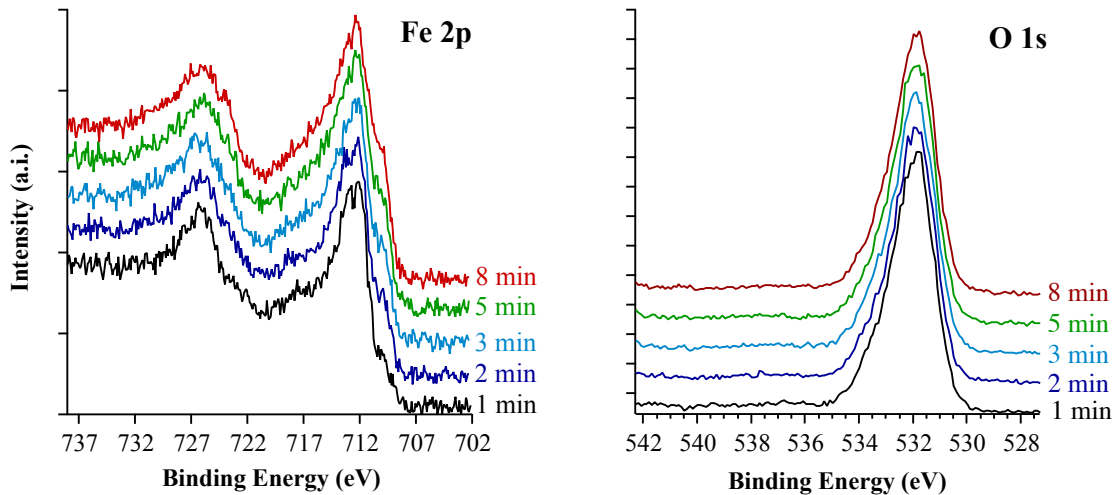


**Figure 5.4: Degradation kinetics of Fe 2p and O 1s signals for iron poly<sub>0.33</sub>**

In order to minimize the degradation, all the spectra of iron-containing polyphosphates were acquired setting a pass energy of 69 eV and a step size of 0.125 eV (see Paragraph 3.5.1). The Fe 2p<sub>3/2</sub> region was always acquired as first region. The use of a larger beam size could have further reduced the degradation and the time required for the analysis, but it was decided to use the same acquisition conditions for characterizing both the glasses after the synthesis and the tribologically stressed samples described in the second part of this work (Chapter 8); the size of the scars under investigation would not have allowed the use of a larger beam size.

In Figure 5.5, the P2p, O1s, Fe2p<sub>2/3</sub> and the valence-band high-resolution spectra of the iron polyphosphate with different compositions are represented. Moving from the top spectrum to the bottom one in each graph, the iron content increases, while the intensity of the phosphorus peak is decreasing.

The oxygen 1s and phosphorus 2p signals were curve fitted with the same parameters used for zinc polyphosphates (paragraph 5.1.2) and the position of the maximum is provided in Table 5.2. The BO/NBO was found to vary from 0.59±0.05 for iron poly<sub>0.33</sub> to 0.16±0.01 for iron poly<sub>1</sub>. Also the P 2p<sub>3/2</sub> BE was found to shift from 134.13±0.06 for iron poly<sub>0.33</sub> to 133.78±0.1<sub>0</sub> for iron poly<sub>1</sub>.

In the valence-band region, the two phosphorus peaks, P 3s and P 3p could be identified and the distance between the peaks is seen to decrease with increasing iron content (Table 5.2).

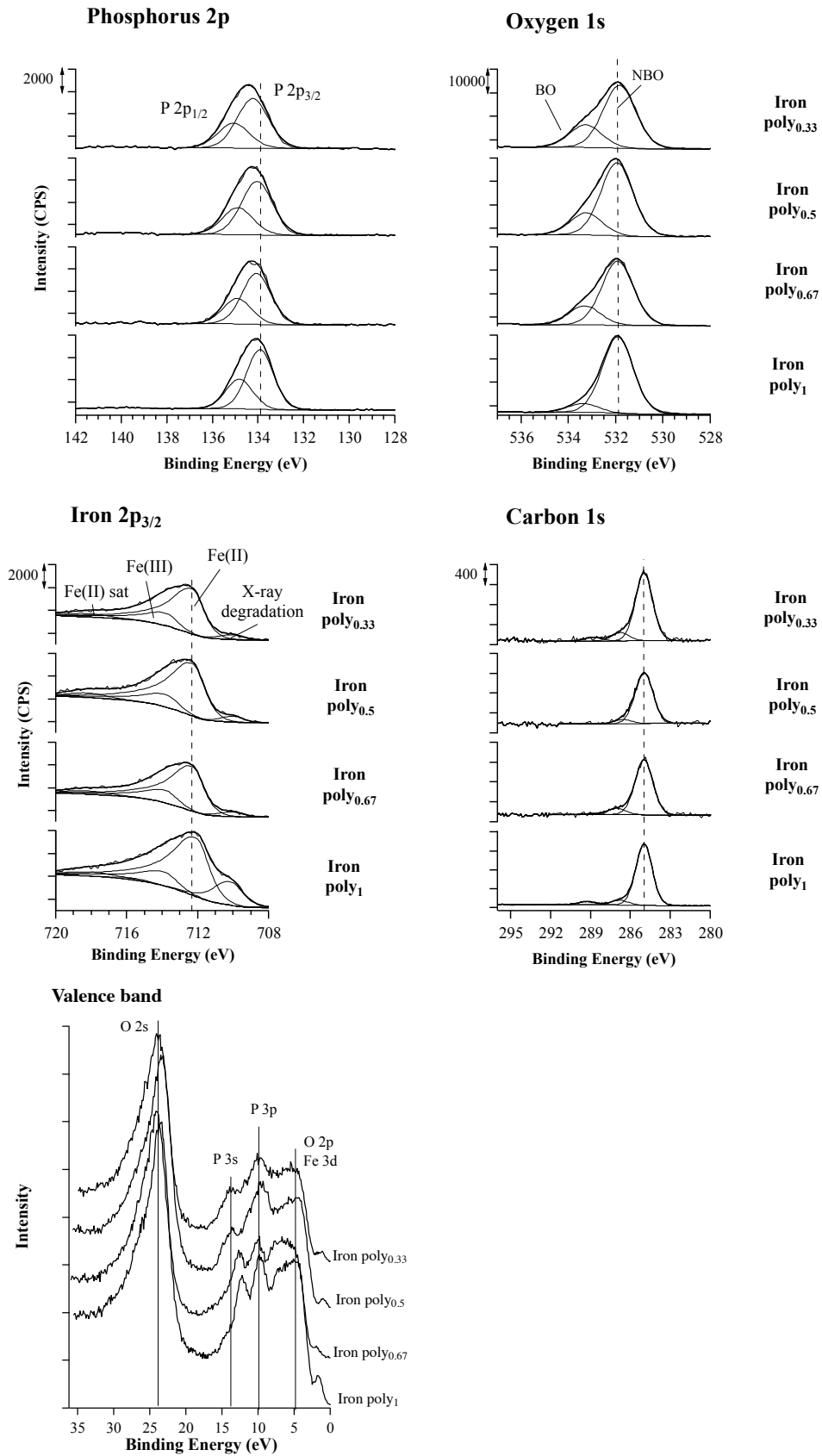


**Figure 5.5: Phosphorus P 2p, oxygen O 1s iron Fe 2p<sub>3/2</sub>, valence band region and carbon C 1s high-resolution XPS spectra for iron poly<sub>0.67</sub>, iron poly<sub>0.5</sub>, iron poly<sub>0.33</sub> and iron poly<sub>1</sub>**

**Table 5.2: XPS peak binding energies of iron polyphosphate glasses**

	<i>Iron poly<sub>1</sub></i>	<i>Iron poly<sub>0.67</sub></i>	<i>Iron poly<sub>0.5</sub></i>	<i>Iron poly<sub>0.33</sub></i>
<b><i>O 1s - NBO [eV]</i></b>	531.7 <sub>7</sub> ±0.1 <sub>1</sub>	531.88±0.07	531.91±0.04	531.84±0.07
<b><i>O 1s - BO [eV]</i></b>	533.27±0.09	533.24±0.07	533.21±0.04	533.27±0.06
<b><i>P 2p<sub>3/2</sub> [eV]</i></b>	133.7 <sub>8</sub> ±0.1 <sub>0</sub>	134.02±0.07	134.06±0.02	134.13±0.06
<b><i>Fe(II) 2p<sub>3/2</sub> [eV]</i></b>	712.09±0.04	712.26±0.04	712.27±0.06	712.32±0.03
<b><i>Fe(III) 2p<sub>3/2</sub> [eV]</i></b>	714.02±0.06	713.77±0.02	713.76±0.10	713.90±0.05
<b><i>P 2p<sub>1/2</sub>-P 2p<sub>3/2</sub> BE difference</i></b>	0.92±0.01	0.94±0.01	0.96±0.03	0.92±0.04
<b><i>BO/NBO Intensity ratio</i></b>	0.16±0.01	0.46±0.03	0.52±0.06	0.59±0.05
<b><i>Fe(III)/Fe(II) Intensity ratio</i></b>	0.16±0.01	0.24±0.02	0.22±0.04	0.21±0.03

The use of a subscript indicates that the digits are given only to avoid loss of information.

The shape of the iron phosphate peaks is clearly asymmetric, therefore a tail component was added to the Gaussian/Lorentzian shape (see Paragraph 3.5.2 and Table 3.7). The Fe2p<sub>3/2</sub> peak was fitted with three components, one at 712.3±0.1eV, assigned to iron phosphate with valence II, one at 713.8±0.1eV, assigned to iron phosphate with valence III and one at 710±0.1eV, assigned to the component originating from the x-ray induced degradation (Table 5.2). A satellite peaks was also added to the curve-fitting function of the Fe(II) phosphate peak and the Fe degradation peak. The first satellite, associated to the Fe(II) phosphate peak, was constrained at 6 eV of distance towards higher binding energies, while the second satellite peak was associated to the degradation peak (which we supposed also originated from a Fe with a valence of II) at 5.5 eV of distance. The area of both peaks was constrained as 8% of the main peak. These fitting parameters were based on those reported for iron oxides by Olla and Fantauzzi [17; 18].

The chain length of the samples in this case could not be directly calculated from the metal content because iron is present in two different oxidation states and the quantitative ratio between Fe(III) and Fe(II) in the glass cannot be controlled by the synthesis conditions. Nonetheless it can be observed that the P 2p peak is shifting towards higher BEs and the BO/NBO ratio is decreasing with increasing iron content (Table 5.2), indicating that the average chain length of iron polyphosphates is decreasing with the iron content as in the case of zinc polyphosphates. The intensity

ratio between Fe(III) and Fe(II) components can be calculated from the XPS data and was found to be rather constant at 0.2.

#### 5.1.4 *Mixed iron/zinc polyphosphate glasses*

The polyphosphates containing both zinc and iron were also susceptible to X-ray degradation. Therefore, the spectra reported in Figure 5.6 were recorded with the same experimental conditions used for the iron polyphosphates in order to minimize the analysis time.

The zinc content is increasing, moving from the top to the bottom and, as a consequence, the intensities of Zn 3s, Zn 2p<sub>3/2</sub> and Fe 2p<sub>3/2</sub> signals are varying accordingly.

The curve-fittings of P 2p, Zn 3s, O 1s, Zn 2p<sub>3/2</sub> and Fe 2p<sub>3/2</sub> were the same as extensively described in the previous paragraphs (5.1.2 and 5.1.3) and the obtained results are reported in Table 5.3.

The metal-to-phosphorus ratio is 0.5 for all the compositions investigated in this paragraph, but the measured BO/NBO intensity ratio is increasing with decreasing the iron content. Therefore the substitution of zinc oxide with iron oxide leads to a shortening of the average chain-length of the glasses, also substantiated by a shift in the P 2p<sub>3/2</sub> BE.

The measured Fe(III) to Fe(II) ratio is 0.2, as for the iron polyphosphates.

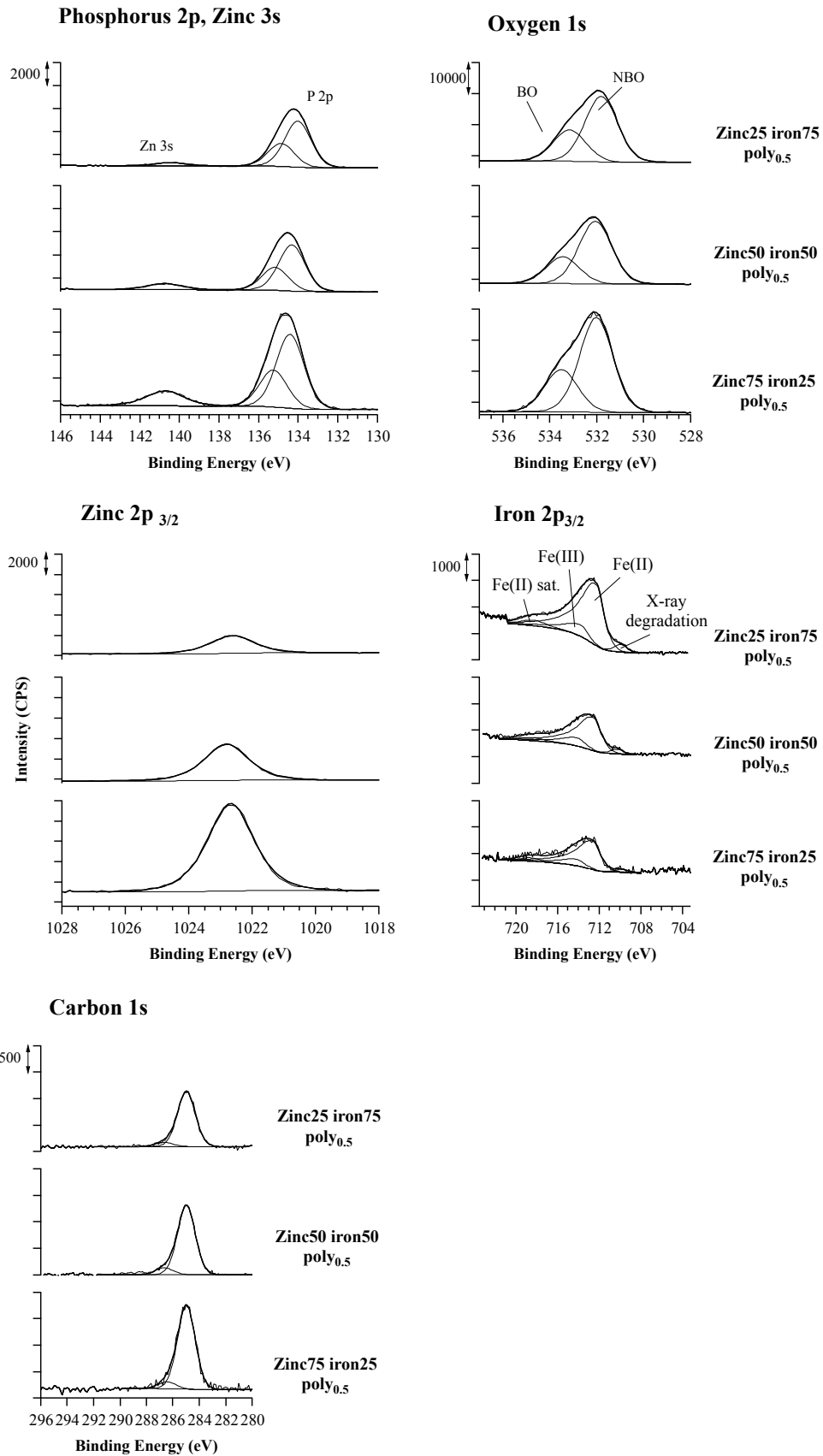


**Figure 5.6:** Phosphorus P 2p, zinc Zn 3s, oxygen O 1s, zinc Zn 2p<sub>3/2</sub>, iron Fe 2p<sub>3/2</sub>, and carbon C 1s high-resolution XPS spectra for zinc25 iron75 poly<sub>0.5</sub>, zinc50 iron50 poly<sub>0.5</sub> and zinc75 iron25 poly<sub>0.5</sub>



**Table 5.3: XPS peak binding energies of mixed iron and zinc polyphosphate glasses**

	<i>Zinc25 iron75 poly<sub>0.5</sub></i>	<i>Zinc50 iron50 poly<sub>0.5</sub></i>	<i>Zinc75 iron25 poly<sub>0.5</sub></i>
<i>O 1s - NBO [eV]</i>	531.84±0.05	532.08±0.01	532.01±0.02
<i>O 1s - BO [eV]</i>	533.2 <sub>7</sub> ±0.1 <sub>1</sub>	533.47±0.01	533.51±0.02
<i>P 2p<sub>3/2</sub> [eV]</i>	134.10±0.08	134.32±0.01	134.38±0.03
<i>Zn 2p<sub>3/2</sub> [eV]</i>	1022.66±0.02	1022.81±0.01	1022.67±0.02
<i>Zn 3s [eV]</i>	140.53±0.06	140.76±0.02	140.68±0.04
<i>Fe(II) 2p<sub>3/2</sub> [eV]</i>	712.30±0.07	712.61±0.03	712.5 <sub>2</sub> ±0.1 <sub>1</sub>
<i>Fe(III) 2p<sub>3/2</sub> [eV]</i>	713.80±0.07	714.11±0.03	714.0 <sub>2</sub> ±0.1 <sub>1</sub>
<i>P 2p<sub>1/2</sub>-P 2p<sub>3/2</sub> BE difference</i>	0.92±0.02	0.90±0.02	0.91±0.04
<i>BO/NBO Intensity ratio</i>	0.4 <sub>1</sub> ±0.1 <sub>1</sub>	0.42±0.01	0.50±0.01
<i>Fe(III)/Fe(II) Intensity ratio</i>	0.22±0.03	0.22±0.02	0.23±0.05

The use of a subscript indicates that the digits are given only to avoid loss of information.

### 5.1.5 Quantitative analysis

In Table 5.4 the results of the XPS quantitative analysis for all the samples under investigation in this chapter are reported.

In the case of zinc polyphosphates the composition obtained by XPS, are in agreement with the batch and measured (see chapter 4, table 4.1) values with a relative uncertainty always lower than 12%, calculated as the deviation from the expected value for the less abundant element. The results were similar using both the Zn 2p and Zn 3s signal for the calculation. The corrected ratio between Zn 3s and Zn 2p is equal to 1. This result substantiates the assumption that the quantitative analysis is not affected by the presence of carbon on the glass surfaces, which thus can be considered negligible. The values reported in Table 5.4 were calculated considering the Zn 2p<sub>3/2</sub> signal; this is much more intense than the Zn 3s peak, which exhibits a higher signal/noise ratio.

However, a closer look at the results reported Table 5.4 reveals the presence of a systematic error in the composition calculated by XPS: the measured phosphorus content is always higher than that obtained by elemental analysis.

**Table 5.4: Results of the XPS quantitative analysis in comparison with the composition of the samples under investigation calculated from the batch composition**

	<i>Zinc orthophosphate</i>	<i>Zinc pyrophosphate</i>	<i>Zinc poly<sub>0.67</sub></i>	<i>Zinc metaphosphate</i>
<i>XPS</i>	[P]=16 wt.%; [O]=29 wt.%; [Zn]=55 wt.%	[P]=23 wt.%; [O]=36 wt.%; [Zn]=41 wt.%	[P]=29 wt.%; [O]=40 wt.%; [Zn]=31 wt.%	[P]=33 wt.%; [O]=41 wt.%; [Zn]=26 wt.%
<i>Batch composition</i>	[P]=15 wt.%; [O]=33 wt.%; [Zn]=50.8 wt.%	[P]=20.3 wt.%; [O]=36.8 wt.%; [Zn]=42.3 wt.%	[P]=24.7 wt.%; [O]=40.5 wt.%; [Zn]=34.8 wt.%	[P]=27.9 wt.%; [O]=43.0 wt.%; [Zn]=29.3 wt.%
	<i>Iron poly<sub>1</sub></i>	<i>Iron poly<sub>0.67</sub></i>	<i>Iron poly<sub>0.5</sub></i>	<i>Iron poly<sub>0.33</sub></i>
<i>XPS</i>	[Fe] / [P] = 0.45	[Fe] / [P] = 0.27	[Fe] / [P] = 0.25	[[Fe] / [P] = 0.21
<i>Batch composition</i>	[Fe] / [P] = 1.00	[Fe] / [P] = 0.67	[Fe] / [P] = 0.50	[Fe] / [P] = 0.33
	<i>Zinc25 iron75 poly<sub>0.5</sub></i>	<i>Zinc50 iron50 poly<sub>0.5</sub></i>	<i>Zinc75 iron25 poly<sub>0.5</sub></i>	
<i>XPS</i>	[M] / [P] = 0.34 [Zn] / [Fe] = 0.48	[M] / [P] = 0.35 [Zn] / [Fe] = 1.58	[M] / [P] = 0.5 [Zn] / [Fe] = 4.20	
<i>Batch composition</i>	[M] / [P] = 0.5 [Zn] / [Fe] = 0.33	[M] / [P] = 0.5 [Zn] / [Fe] = 1	[M] / [P] = 0.5 [Zn] / [Fe] = 3	

For all the iron-containing glasses, iron polyphosphates and mixed zinc and iron polyphosphates, the oxygen content in the iron-containing polyphosphates depends upon the Fe(II)/Fe(III) ratio and upon the structure of the glass. Therefore, the intensity ratio between the corrected intensities of iron and phosphorus [Fe] / [P] obtained from the XPS data have been compared to their ratios in the bulk compositions (Table 5.4). For the mixed zinc and iron polyphosphates, instead, the ratio between the total metal content (zinc plus iron) and the phosphorus content [M] / [P] has been calculated together with the ratio between zinc and iron content [Zn] / [Fe]. It is immediately evident that also for the iron-containing polyphosphates the phosphorus content is always higher than the expected value. The errors are much higher compared to zinc polyphosphate because the measured iron content is always lower than that of the bulk; this is particularly evident in the mixed polyphosphates, where the [M] / [P], which is constant in the batch composition, seems to increase with zinc content (Table 5.4).

These results led us to hypothesize a difference in composition between bulk and surface of the sample. During the cooling of the sample, a gradient in its composition might occur and in order to confirm or revoke this hypothesis, not only the surfaces but also their cross-sections were analyzed, together with the pulverized materials or glasses. Cross-sectioning allows XPS analysis in a plane perpendicular to the interface under study, so that differences in the composition might be revealed in that plane. The calculated composition for zinc metaphosphate, reported in Table 5.5, revealed that the samples had a homogeneous composition: identical results were obtained analyzing the other samples' cross-sections and their surfaces. Only a slight difference in the oxygen content was noticed for the pulverized samples, as expected since they were crushed in air.

**Table 5.5: XPS quantitative analysis results for zinc metaphosphate after different sample preparations**

	<i>Zinc metaphosph. after quenching</i>	<i>Zinc metaphosph. freshly cleaved cross section</i>	<i>Zinc metaphosph. Pulverized*</i>	<i>Zinc metaphosph. mechanically polished</i>
<i>[P]**</i>	33 wt.%	33 wt.%	31 wt.%	31 wt.%
<i>[O]**</i>	41 wt.%	41 wt.%	42 wt.%	43 wt.%
<i>[Zn]**</i>	26 wt.%	26 wt.%	27 wt.%	26 wt.%
<i>BO/NBO Intensity ratio</i>	0.48±0.02	0.47±0.05	0.39±0.05	0.39±0.05
<i>P/Zn Intensity ratio</i>	2.8±0.6	2.6±0.2	2.5±0.2	2.4±0.2
<i>P-Zn [eV] BE difference</i>	6.19±0.06	6.2±0.1	6.3±0.1	6.3±0.1

\*The sample was pulverized in air and pressed into a pellet prior to the XPS analysis

\*\* The maximum relative error in the XPS quantitative analysis is 12%.

Analogous results were obtained with iron-containing polyphosphates. The composition of the samples remains unchanged but the average chain-length is slightly shortened as an effect of mechanical stress in the pulverized and mechanical polished samples.

Another source of inhomogeneity of composition could be the degradation of the surface due to hydrolysis. Despite the efforts made in order to minimize the exposure to air, some water could adsorb on the surface and cause depolymerization of the glass and the formation of a compositional gradient. Angular-resolved (AR) XPS was performed, showing that the surface of the samples after quenching is

homogeneous within the experimental error. The results obtained on zinc metaphosphate are reported as an example in Figure 5.7 and Figure 5.8.

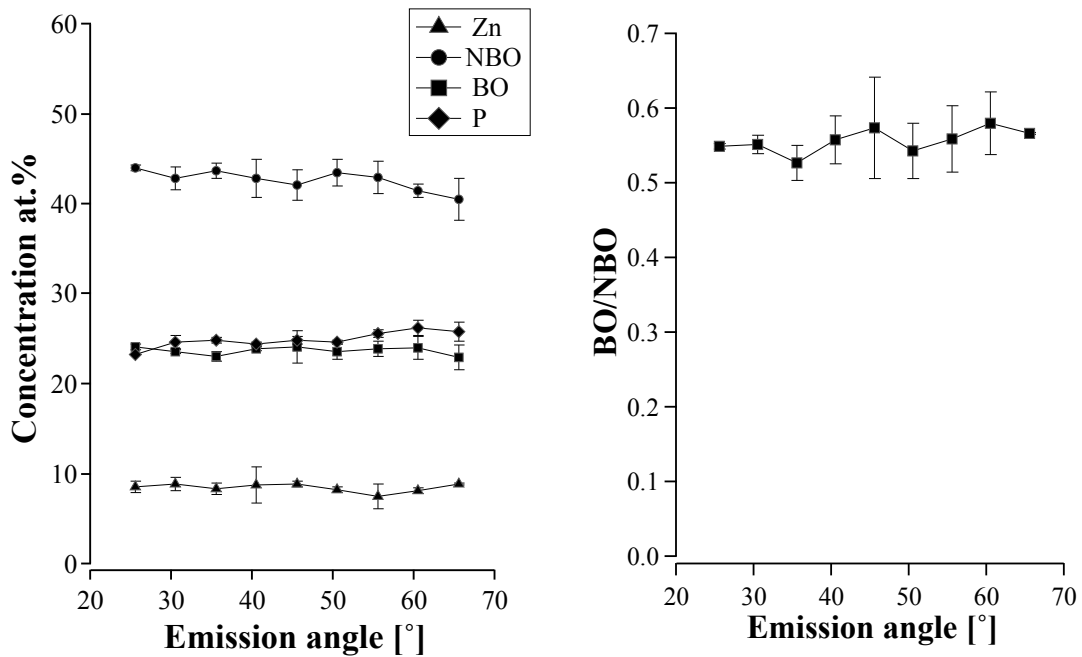


Figure 5.7: AR-XPS results for zinc metaphosphate after quenching

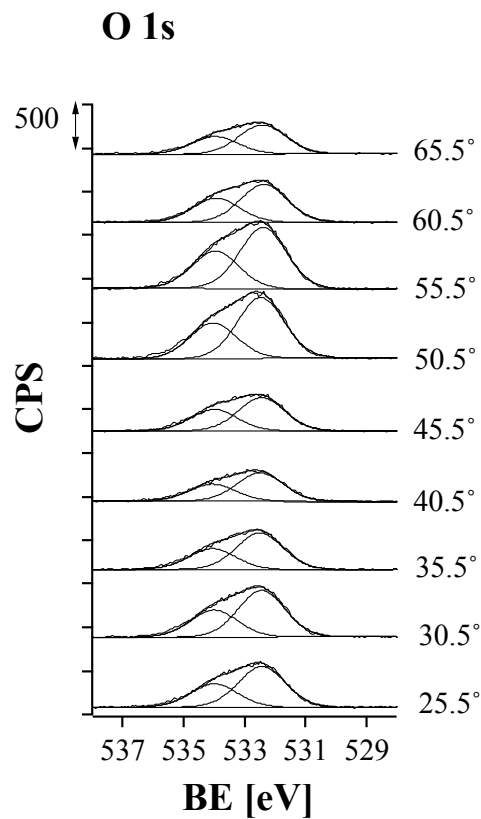


Figure 5.8: AR-XPS O1s spectra for zinc metaphosphate after quenching

## 5.2 ToF-SIMS analysis

The sample-preparation procedure followed for the XPS analysis was not ideal for ToF-SIMS experiments. The surface of the samples after quenching was not planar, which resulted in poor sample-charging compensation and, in general, in a low mass resolution. Moreover, the presence of some small copper particles from the copper tray used for the quenching could be detected on the surface and dramatically affected the spectra, increasing their complexity. In order to improve the quality of the spectra, the samples were mechanically polished prior to ToF-SIMS analysis (see Chapter 3). A mass-resolution ( $m/\Delta m$ ) higher than 7000 was always achieved in the polished samples, while the rough surface of the fractured zinc orthophosphate allowed only a resolution of around 6000. The spectra of the samples after quenching were also acquired: they exhibited a mass resolution lower than 5000 but it was possible to observe the same phosphate fragments and the same trends described here for the mechanically polished samples. The comparison of the polished samples with the non-polished ones, for both negative and positive polarity spectra, helped in identifying the peaks resulting from the mechanical polishing. Those peaks were mostly organic and did not interfere with the inorganic peaks characteristic of the phosphate glasses.

The influence of the sample-preparation procedure was investigated by XPS in the previous section (see Paragraph 5.1.5).

### 5.2.1 Positive-mode ToF-SIMS spectra

The positive-mode ToF-SIMS spectra of zinc metaphosphate and iron poly<sub>0.33</sub> are reported in Figure 5.9 as an example. Analogous spectra were obtained for all investigated samples.

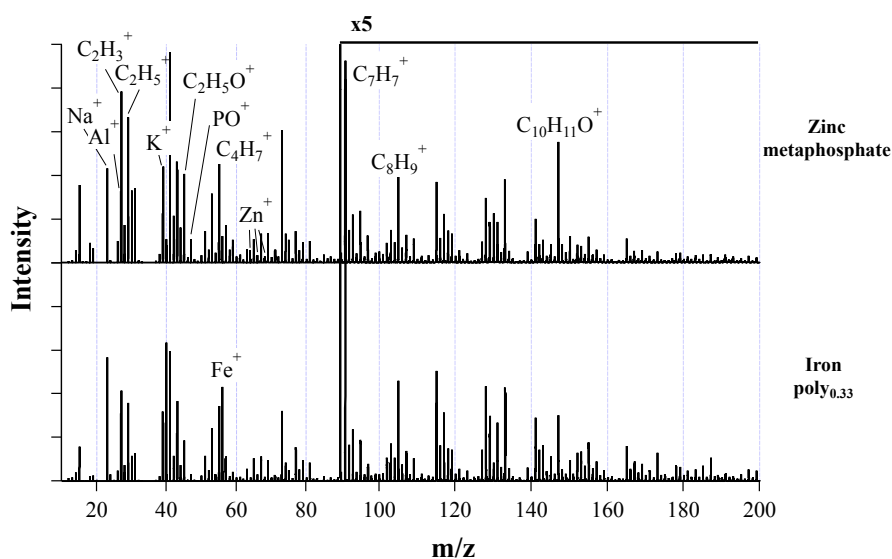


Figure 5.9: Positive-ion spectra in the mass range 10-200 amu of zinc metaphosphate and iron poly<sub>0.33</sub>

All positive-mode spectra (Figure 5.9) show the presence of aluminum, in agreement with the XPS results. The polished samples also indicated slight sodium and potassium contamination. The remaining elements detected in the spectra were phosphorus, iron, zinc and its isotopes. The most intense peaks could be attributed to organic fragments, usually very intense in the positive-mode spectra. Some typical phosphate fragments ( $\text{PO}^+$ ,  $\text{PO}_3^+$ ) were also detected, but the sensitivity for those peaks was found to be much higher in the negative mode.

### 5.2.2 Zinc polyphosphates

The negative-ion spectra of the four zinc polyphosphates in a mass range from 10 to 400 amu are shown in Figure 5.10. The most intense peaks were assigned to the phosphate fragments  $\text{PO}^-$ ,  $\text{PO}_2^-$ ,  $\text{PO}_3^-$ ,  $\text{PO}_4^-$ . At higher masses a typical pattern for the zinc phosphates could be identified, i.e. fragments containing up to four phosphorus atoms with a periodicity of  $\text{PO}_2$ :  $\text{ZnPO}_3^-$ ,  $\text{ZnPO}_4^-$ ;  $\text{ZnP}_2\text{O}_6^-$ ,  $\text{ZnP}_2\text{O}_7^-$ ;  $\text{ZnP}_3\text{O}_8^-$ ,  $\text{ZnP}_3\text{O}_9^-$ ,  $\text{ZnP}_5\text{O}_9^-$ ,  $\text{ZnP}_5\text{O}_9^-$ ,  $\text{ZnP}_5\text{O}_9^-$ ,  $\text{ZnP}_5\text{O}_9^-$ . This pattern characterizes the spectra of all the glasses under investigation, but the relative intensities of these peaks were found to be dependent on the composition. The long-chain-length zinc metaphosphate shows higher intensity for all the phosphate-related peaks listed above, especially at high masses ( $\text{ZnP}_2\text{O}_7^-$ ,  $\text{ZnP}_3\text{O}_9^-$ ,  $\text{ZnP}_5\text{O}_9^-$ ,  $\text{ZnP}_5\text{O}_9^-$ ). The spectrum of zinc orthophosphate presents additional peaks that can be attributed to zinc oxide and hydroxide:  $\text{ZnO}^-$ ,  $\text{ZnOH}^-$ ,  $\text{ZnO}_2^-$ ,  $\text{ZnO}_2\text{H}^-$  and their isotopes.

In the case of Zn-containing ions, all the corresponding isotopes were always detected. Only the most intense three ( $^{64}\text{Zn}$ ,  $^{66}\text{Zn}$ ,  $^{68}\text{Zn}$ ) are, however, indicated in Figure 5.1. At masses higher than 300 amu, the isotope patterns of the different polyphosphate peaks become increasingly superimposed. The pattern that appears between 360 and 370 amu, for example, could be the result of the superimposition of two or more peaks:  $\text{ZnP}_7\text{O}_5^-$ ,  $\text{ZnP}_3\text{O}_9^-$ ,  $\text{ZnP}_5\text{O}_9^-$  or  $\text{ZnP}_3\text{P}_2\text{O}_7^-$ . Going towards masses higher than 600 amu, the pattern turns into an uninterrupted series of peaks.

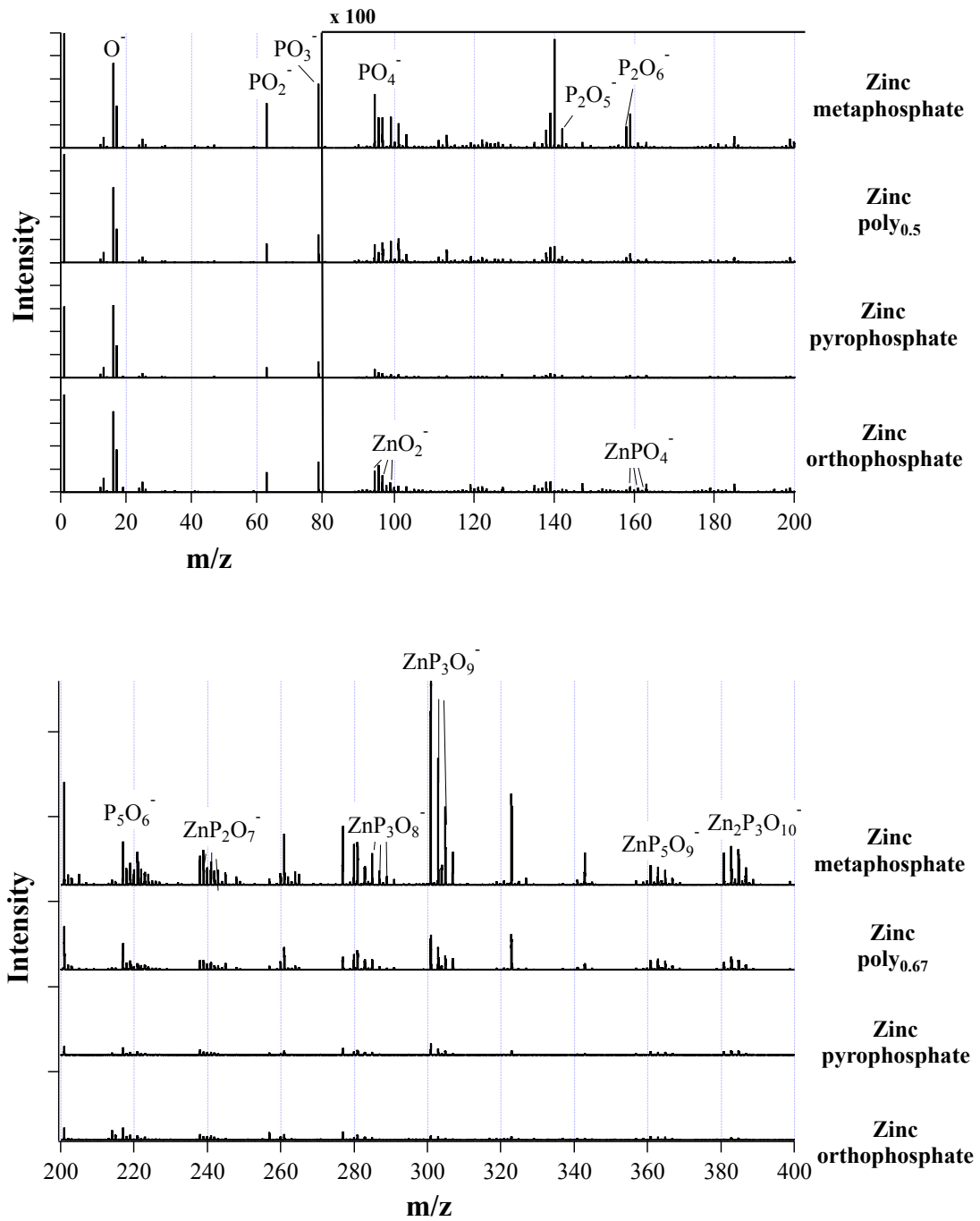


Figure 5.10: Negative-ion spectra in the mass range 10-200 amu (upper) and 200-400 amu (below) of zinc metaphosphate, zinc poly<sub>0.67</sub>, zinc pyrophosphate and zinc orthophosphate

### 5.2.3 Iron polyphosphates

In Figure 5.11 the negative mode spectra of iron polyphosphates are reported.

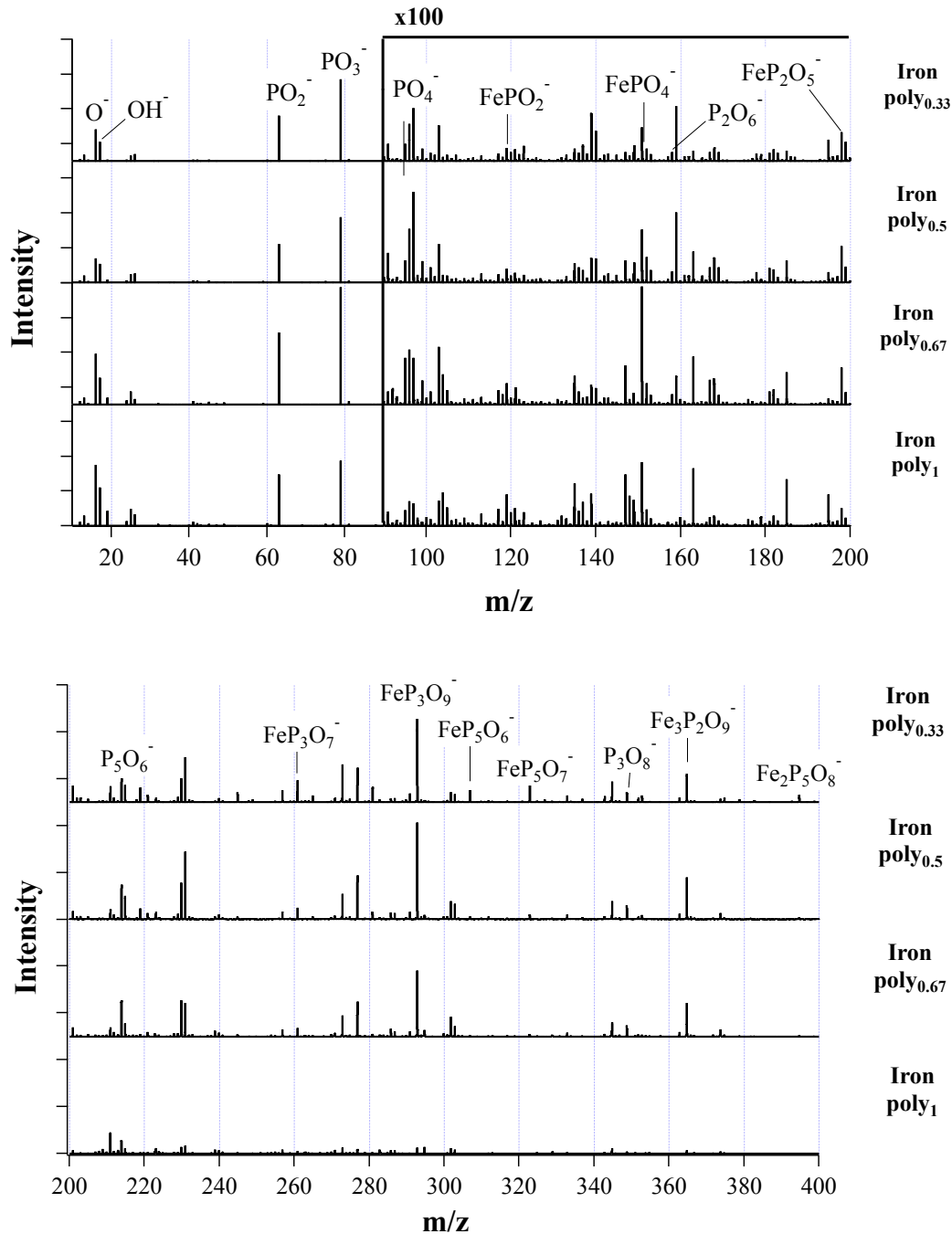


Figure 5.11: Negative-ion spectra in the mass range 10-200 amu (upper) and 200-400 amu (below) of iron  $\text{poly}_{0.33}$ , iron  $\text{poly}_{0.5}$ , iron  $\text{poly}_{0.67}$  and iron  $\text{poly}_1$

The phosphate fragmentation pattern dominates the negative-mode spectra of all iron polyphosphates. The most intense peaks in the spectrum, for all compositions, are  $\text{O}^-$ ,  $\text{PO}_2^-$ ,  $\text{PO}_3^-$ ,  $\text{PO}_4^-$ . Iron polyphosphates show higher intensities peaks compared to zinc polyphosphates. The fragmentation pattern of iron polyphosphates is analogous to that of zinc polyphosphates: many polyphosphate fragments with one atom of iron are identified:  $\text{FePO}_2^-$ ,  $\text{FePO}_4^-$ ,  $\text{FeP}_2\text{O}_6^-$ ,  $\text{FeP}_2\text{O}_7^-$ ,  $\text{FeP}_3\text{O}_8^-$ ,  $\text{FeP}_3\text{O}_9^-$ , together with fragments with a higher number of iron atoms:  $\text{Fe}_2\text{P}_3\text{O}_8^-$ ,  $\text{Fe}_2\text{P}_3\text{O}_9^-$ ,



$\text{Fe}_2\text{P}_3\text{O}_{10}^-$ ,  $\text{Fe}_3\text{P}_3\text{O}_9^-$ ,  $\text{Fe}_3\text{P}_3\text{O}_{10}^-$  and  $\text{Fe}_3\text{P}_3\text{O}_{11}$ . The high-mass fragments can be interpreted far more unambiguously than those of the zinc polyphosphates.

Many polyphosphate fragments without metal atoms could also be observed in both zinc and iron polyphosphate spectra, e.g.,  $\text{P}_2\text{O}_5^-$ ,  $\text{P}_2\text{O}_6^-$ ,  $\text{P}_3\text{O}_8^-$ ,  $\text{P}_9\text{O}_{13}^-$ .

The spectra of iron and zinc metaphosphates have been also acquired with the  $\text{Bi}_1^+$  primary ions for comparison (see Appendix C.2). The fragmentation pattern was found to be similar but with different relative intensities. For masses up to 100 amu the intensities of the peaks for the  $\text{Bi}_1^+$  spectra were comparable or slightly higher than those of the  $\text{Bi}_3^{++}$ . In contrast, at higher masses the  $\text{Bi}_3^{++}$  spectra showed intensities one order-of-magnitude higher for both iron and zinc metaphosphates.

#### 5.2.4 Mixed zinc and iron polyphosphates

The fragmentation pattern of mixed polyphosphates, shown in Figure 5.12, is the combination of the patterns characteristic for zinc and iron polyphosphates. Going from the top to the bottom, the zinc-containing fragments become less intense with decreasing zinc content and vice versa for the iron-containing fragments. In the spectra of zinc75 iron25 poly<sub>0.5</sub>, which contain more zinc than iron, the zinc fragments are less intense compared with those of iron. This difference is explained by the fact that iron has only one main isotope ( $^{54}\text{Fe}$ , 92%), while zinc is characterized by 5 stable isotopes, three of them having natural abundances higher than 10% ( $^{64}\text{Zn}$ , 49%;  $^{66}\text{Zn}$ , 28%;  $^{68}\text{Zn}$ , 19%). Probably also for this reason the fragments containing both iron and zinc are detected only with very low intensity:  $\text{ZnFeP}_2\text{O}_7^-$ ,  $\text{ZnFePO}_9^-$ ,  $\text{ZnFeP}_2\text{O}_8^-$ ,  $\text{ZnFeP}_3\text{O}_{10}^-$ .

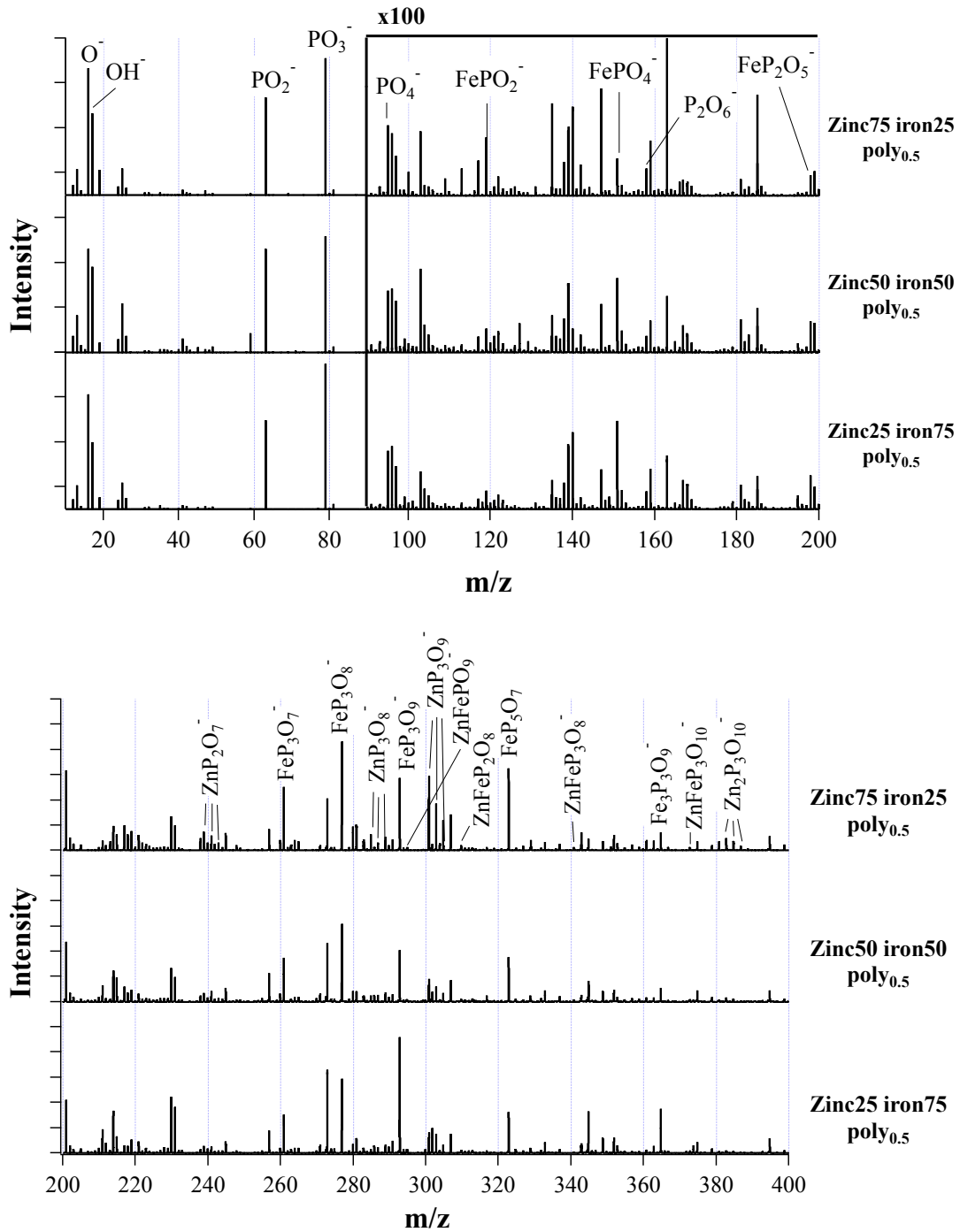


Figure 5.12: Negative-ion spectra in the mass range 10-200 amu (upper) and 200-400 amu (below) of zinc75 iron25 poly<sub>0.5</sub>, zinc50 iron50 poly<sub>0.5</sub> and zinc25 iron75 poly<sub>0.5</sub>

### 5.3 Discussion

#### 5.3.1 Chemical state of O, P and Zn and Fe in polyphosphate glasses

Few XPS data on zinc and iron binary phosphate glasses in the polyphosphate composition region are available in the literature [5; 7; 19; 20]. Since they were all acquired with a non-monochromatic source, a direct comparison with the data in this

work is very difficult. For the iron-containing polyphosphates, the comparison is made even more difficult because the synthesis conditions, such as the temperature and the dwelling time, are heavily affecting the Fe(III)/Fe(II) ratio of the glasses [20]. As a consequence of this, a direct comparison of the literature data with the present work is difficult. The BE values for all elements found in this work (Table 5.1, Table 5.2 and Table 5.3) are in good agreement with those reported in the literature [5; 7; 8].

The previous publications were often focused on investigating the short-range structure of the glasses by studying the oxygen bonding. It is acknowledged that the addition of a modifying oxide leads to progressive de-polymerization of the glass [21-23]. If one defines the glass with the general formula  $x(\text{ZnO}) \cdot (1-x)\text{P}_2\text{O}_5$ , the BO/NBO intensity ratio can be calculated from the following equation [7; 24]:

**Equation 5.1**

$$\text{BO/NBO} = 0.5 \cdot (3-4x)$$

The values calculated from this equation are in good agreement with those measured in this work (Table 5.1). The BEs of both oxygen components slightly move towards lower binding energies when going towards lower chain-length, implying that the effective charge of the oxygen atoms in the  $Q_2$  units is higher than that in  $Q_0$  and  $Q_1$  units. The same was also observed for ternary  $\text{PbO-ZnO-P}_2\text{O}_5$  glasses [8]. The curve-fit of the O 1s XP-spectra with two components, one assigned to the non-bridging oxygen and one to the bridging oxygen, supports the concept that the two different oxygen atoms in the polyphosphate chains ( $\text{P=O}$  and  $\text{P-O-M}$ ) cannot be resolved since they have a difference in the binding energy below the energy resolution here achievable. This finding might be explained by the electronic delocalization on the  $\text{PO}_2^-$  group. The assignment of the FT-IR absorption bands (Chapter 4) has also been performed on the basis of this evidence: the peak was interpreted as a group vibration ( $\nu\text{PO}_2^-$ ) rather than of two single and distinct vibrations ( $\nu\text{P=O}$  and  $\nu\text{P-O}^-$ ) [1].

The BE of the P  $2p_{3/2}$  signal increases when the metal oxide content in the glasses decreases, in agreement with Liu [8]: this shift can be observed in both the zinc and iron polyphosphates (Table 5.1, Table 5.2 and Table 5.3) with decreasing chain-length. Moreover a shift of the P  $2p_{3/2}$  BE towards higher values is observed also in the mixed zinc and iron polyphosphate, where the total metal oxide content is constant, but the substitution of some divalent zinc with trivalent iron leads to a depolymerization of the glass. The chemical shift of  $\text{P}2p_{3/2}$  can be explained by taking into account the fact that the number of  $\text{PO}_2$  units is increasing with chain length, thus increasing the partial positive charge on each phosphorus atom [25].

In Figure 5.13, the BE of the Zn  $2p_{3/2}$  signal and the KE of the Auger Zn  $L_3M_{4,5}M_{4,5} 1G$  signal are plotted in a Wagner plot: the straight lines with slope -1 represents the Auger parameter values ( $\alpha'$ ).

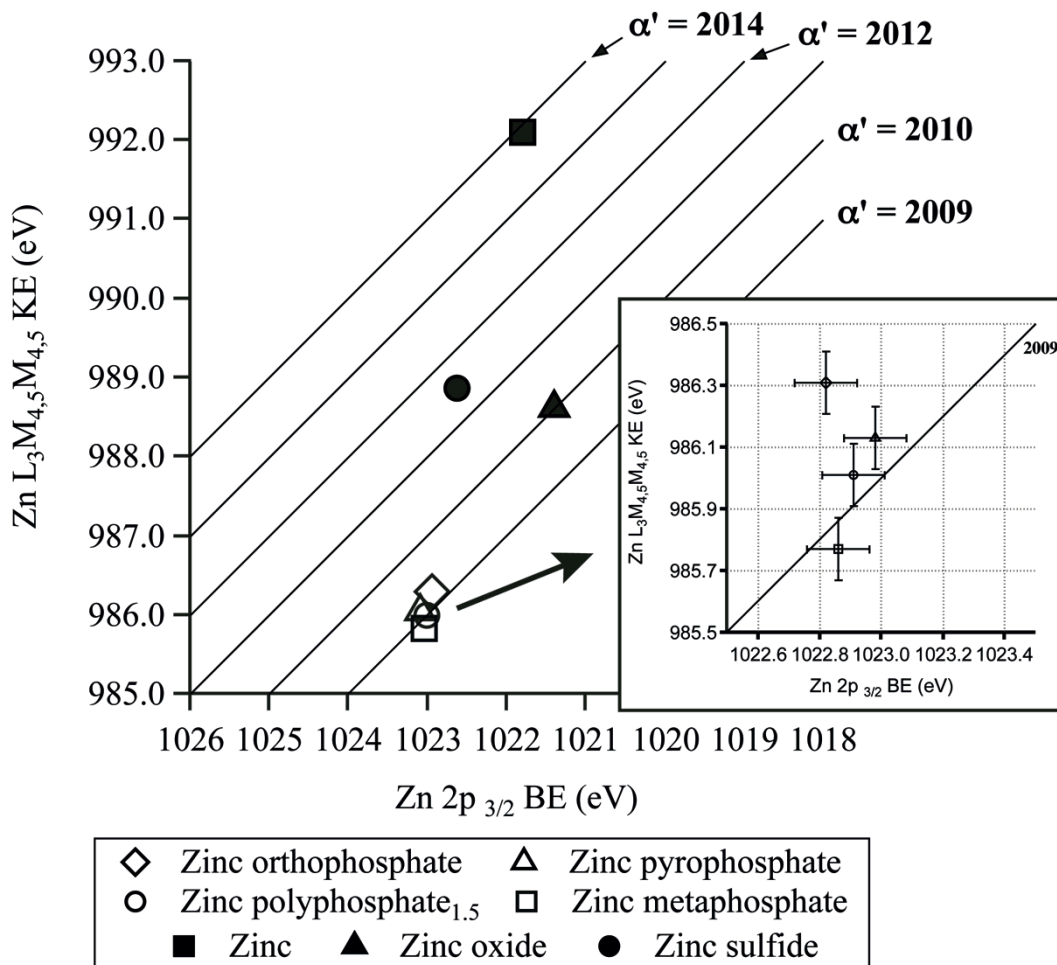


Figure 5.13: Wagner plot of different chain-length polyphosphate in comparison with zinc, zinc oxide and zinc sulfide [1]

In addition to the polyphosphate data, data for metallic zinc, zinc oxide and zinc sulfide are also plotted in Figure 5.13 for comparison. The Wagner plot can be used not only to identify chemical states, but also to investigate the local chemical environment of the core-ionized atoms, thanks to the recent development of theoretical models based on classical electrostatic and quantum chemistry [26; 27]. As extensively studied by Moretti and co-workers [26-28], shifts in the Auger parameter are a direct measurement of the polarization energy. Assuming that the polarization energy is proportional to the square of the charge and that the BE difference between two core levels is a constant, one can write:

$$\Delta\alpha' = 2\Delta R_{ea}$$

Equation 5.2

where  $R_{ea}$  is the extra-atomic relaxation energy—the energy related to the relaxation phenomena taking place outside the ionized atom. Applying this equation to the polyphosphate referred to zinc oxide, we can calculate 2.13 eV for zinc orthophosphate, 2.18 eV for zinc pyrophosphate, 2.25 eV for zinc poly<sub>0.67</sub>, 2.31 eV for zinc metaphosphate. . With an error of  $\pm 0.1$  eV in the BEs, the uncertainty in the estimate of  $R_{ea}$  is  $\pm 0.14$ , and therefore we can only state that there is a trend in the data towards lower values of  $R_{ea}$  with shorter chain-length. These results may indicate that the polyphosphate network becomes more resistant to polarization with increasing chain-length. Moreover, the polyphosphates under investigation appear in the plot in a vertical line, for which the longer the chain length, the lower the Auger parameter. In this situation, the shift in the Auger parameter is correlated to a change in the Madelung potential. The negative shift of  $\alpha'$  going towards longer chain lengths indicates a decrease of the Madelung potential due to the increased covalent character of the compound [27]. With increasing polyphosphate chain length, the electron delocalization on the PO<sub>2</sub> groups also increases, lending stability to the chains but also increasing the positive effective charge on the P atom [25]. This is confirmed by the valence-band region, where the position of the P 3s shifts towards high BEs for the samples with longer chain-length. This result is also consistent with the data for sodium phosphate, where the set of phosphate peaks is even more widely separated for long chain-length samples [14].

It was already known that iron-containing polyphosphate glasses synthesized in air possess both Fe<sup>2+</sup> and Fe<sup>3+</sup> ions, even when the starting batch includes only Fe<sub>2</sub>O<sub>3</sub> [20; 29-31]. The ratio between Fe<sup>3+</sup> and Fe<sup>2+</sup> ions is affected by the synthesis parameters (time and temperature) and the values obtained by XPS were found to be in good agreement with those measured by Mössbauer spectroscopy [19; 20].

To our knowledge there are no publications reporting the X-ray degradation of iron-containing polyphosphates. The degradation peak at 710 eV cannot be attributed to iron oxide, because there is not a corresponding peak in the oxygen spectrum, therefore the peak must arise from iron phosphate, most probably iron (II) with a distorted/changed electronic structure. The degradation rate in Figure 5.14 has been plotted as the variation with time of the ratio of the degradation peak intensity and the total intensity of Fe 2p<sub>3/2</sub>.

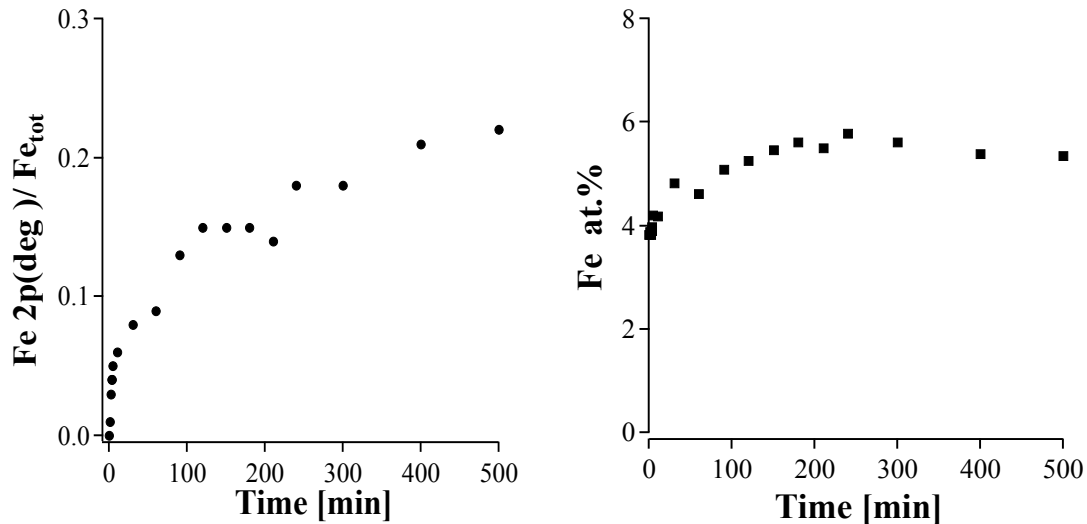


**Figure 5.14: Degradation rate for iron poly<sub>0.33</sub> acquired with a beam size of 100 $\mu$ m, a power of 25W and a PE of 69 eV**

### 5.3.2 XPS quantitative analysis of polyphosphates

To the best of our knowledge, this is the first time that XPS quantitative analysis has been applied to homogeneous polyphosphate glasses. The results (Table 5.4 and Table 5.5) show a systematic error: the phosphorus content calculated applying the first-principle method is always higher than that measured by elemental analysis. However, the results of the analysis on the cross-sections and the pulverized metaphosphate samples (Table 5.4 and Table 5.5) confirmed that the samples had a homogeneous composition. A crystalline commercial calcium phosphate was also analyzed and the XPS quantitative results, similarly, showed an overestimation of the phosphorus content compared to the stoichiometric composition (see Appendix A.5). Similar results were obtained on the same glasses using a different spectrometer [32]. Calcium and mixed zinc and calcium phosphates were also synthesized using the same protocol and showed the same systematic error in the quantitative analysis [33].

The case of iron is even more unexpected: the peak originating from the X-ray degradation is growing in intensity with time but all the other peaks in the Fe 2p spectrum are not decreasing (see Figure 5.14). The change in the electronic structure caused by X-rays corresponds somehow to a change in the sensitivity factor. In Table 5.6 the calculated (using the first-principles method) and experimental relative sensitivity factors referred to the P 2p peak are reported. The experimental values for iron show differences up to 50% of those calculated using the first-principles method.

**Table 5.6: Calculated and experimental relative sensitivity factors referred to the P2p peak**

<i>Peak 1</i>	<i>Peak 2</i>	<i>Compound</i>	$S_1/S_2$ ( <i>Experimental</i> )	$S_1/S_2$ ( <i>First principle method</i> )
O 1s	P 2p	Zinc metaphosphate	1.41	1.75
O 1s	P 2p	Zinc polyphosphate	1.48	1.75
O 1s	P 2p	Zinc pyrophosphate	1.48	1.75
O 1s	P 2p	Zinc orthophosphate	1.55	1.75
Zn 2p	P 2p	Zinc metaphosphate	5.98	7.81
Zn 2p	P 2p	Zinc polyphosphate	5.94	7.87
Zn 2p	P 2p	Zinc pyrophosphate	6.50	7.88
Zn 2p	P 2p	Zinc orthophosphate	6.88	7.89
Zn 3s	P 2p	Zinc metaphosphate	0.48	0.76
Zn 3s	P 2p	Zinc polyphosphate	0.51	0.76
Zn 3s	P 2p	Zinc pyrophosphate	0.58	0.76
Zn 3s	P 2p	Zinc orthophosphate	0.63	0.76
Fe 2p	P 2p	Iron poly <sub>0.33</sub>	3.68	5.74
Fe 2p	P 2p	Iron poly <sub>0.5</sub>	2.92	5.74
Fe 2p	P 2p	Iron poly <sub>0.67</sub>	2.29	5.74
Fe 2p	P 2p	Iron poly <sub>1</sub>	3.70	5.74
Fe 2p	P 2p	Zinc25 iron75 poly <sub>0.5</sub>	3.08	5.74
Fe 2p	P 2p	Zinc50 iron50 poly <sub>0.5</sub>	2.45	5.74
Fe 2p	P 2p	Zinc75 iron25 poly <sub>0.5</sub>	2.63	5.74
Zn 2p	P 2p	Zinc25 iron75 poly <sub>0.5</sub>	7.49	7.0
Zn 2p	P 2p	Zinc50 iron50 poly <sub>0.5</sub>	6.73	7.0
Zn 2p	P 2p	Zinc75 iron25 poly <sub>0.5</sub>	6.39	7.0

The explanations for these results could be different. Shirley's algorithm has been used as background subtraction method for this work [34]: this method has the undoubted advantage of being simple and well established, but it omits the shake-up intensities when calculating the peak areas. In some cases those intensities may also significantly vary with chemical state and such changes would not be taken into account when applying a Shirley background. The use of the Tougaard's background subtraction approach [35] could improve the accuracy of the peak areas but would require an acquisition window about five times larger than average (~100 eV instead of ~20 eV). Errors may also arise from a wrong estimate of the sensitivity factors using the first-principles method. The values of the photoionization cross-sections, for example, have been calculated by Scofield using the Hartree-Slater model, which is inaccurate because of its approximate manner of treating the electron-electron

interactions [36]. Nevertheless, Scofield's cross-sections are still the most accurate values available today [37]. Whatever the source of the error, it is evident that great care should be taken when investigating polyphosphates using quantitative XPS. Experimental sensitivity factors calculated directly from a reference compound should be used whenever possible.

### 5.3.3 *Surface characterization of polyphosphates by ToF-SIMS*

A characteristic 'fingerprint' composed of phosphate fragments was identified in the negative-mode spectra of all the glasses. The absence of contaminant elements in the positive spectra was essential, in order to be able to confirm the assignment of the peaks in the negative spectra. The comparison with the spectra of the samples before mechanical polishing was also used to identify the peaks arising from the solvent used during the polishing step. The overall fragmentation mechanism appears to be the same for iron and zinc polyphosphates. The same fragments are, indeed, observed:  $\text{P}_2\text{O}_6^-$ ,  $\text{P}_3\text{O}_8^-$ ,  $\text{P}_9\text{O}_{13}^-$ , but also  $\text{Fe/ZnPO}_4^-$ ,  $\text{Fe/ZnP}_2\text{O}_6^-$ ,  $\text{Fe/ZnP}_2\text{O}_7^-$ ,  $\text{Fe/ZnP}_3\text{O}_8^-$ ,  $\text{Fe/ZnP}_3\text{O}_9^-$ : a periodicity of  $\text{PO}_2$  characterizes the entire fragmentation pattern. The spectra of the short chain-length polyphosphates, zinc orthophosphate, iron poly<sub>1</sub>, are unequivocally identified by the presence of the fragments related to the zinc/iron oxy-hydroxide. Moreover, the intensity of the phosphorus-containing fragments is lower except for the  $\text{PO}_4$ -containing peaks. In contrast, the iron/zinc polyphosphates with intermediate chain length are characterized by the same fragments and can only be distinguished by taking into account the differences in relative intensities of the phosphate fragments. In Figure 5.15 the normalized intensities of selected fragments for zinc metaphosphate, zinc orthophosphate, iron poly<sub>0.33</sub> and iron poly<sub>1</sub> are shown. The  $\text{PO}_2^-$  and  $\text{PO}_3^-$  fragments have not been considered in this comparison because their intensity was so high that the saturation limit of the analyzer could have been reached. Every normalization method is removing some information from the data, especially in this case where the intensity of every peak is dependent on composition and chain-length of the glass. Nonetheless normalization is necessary in order to remove variations in the data induced by topography, sample charging and experimental conditions [38]. Different normalization methods can be applied to ToF-SIMS data, based on the total intensity, for example, on the sum of selected peaks or on a single selected signal [83]. The choice of the normalization method has to be done taking into account of the characteristics of the system investigated [39]. In this case the intensity of most of the selected polyphosphate peaks are sensitive to the composition of the samples therefore using one of them or their sum would remove the information useful to the goal of the analysis. A correction for the stoichiometry could be used to overcome this problem with the assumption that the intensity varies linearly with the intensity. For these reasons it was chosen to normalize the data by the total intensity of the spectra



because it was less correlated with composition than the other two possible parameters. Other normalization methods, based on the sum of the selected peaks and on the intensity of the P<sup>-</sup> signal corrected by the stoichiometry still showed the same trends in the data but gave less satisfactory results on the multivariate analysis (Appendix C.1).

□

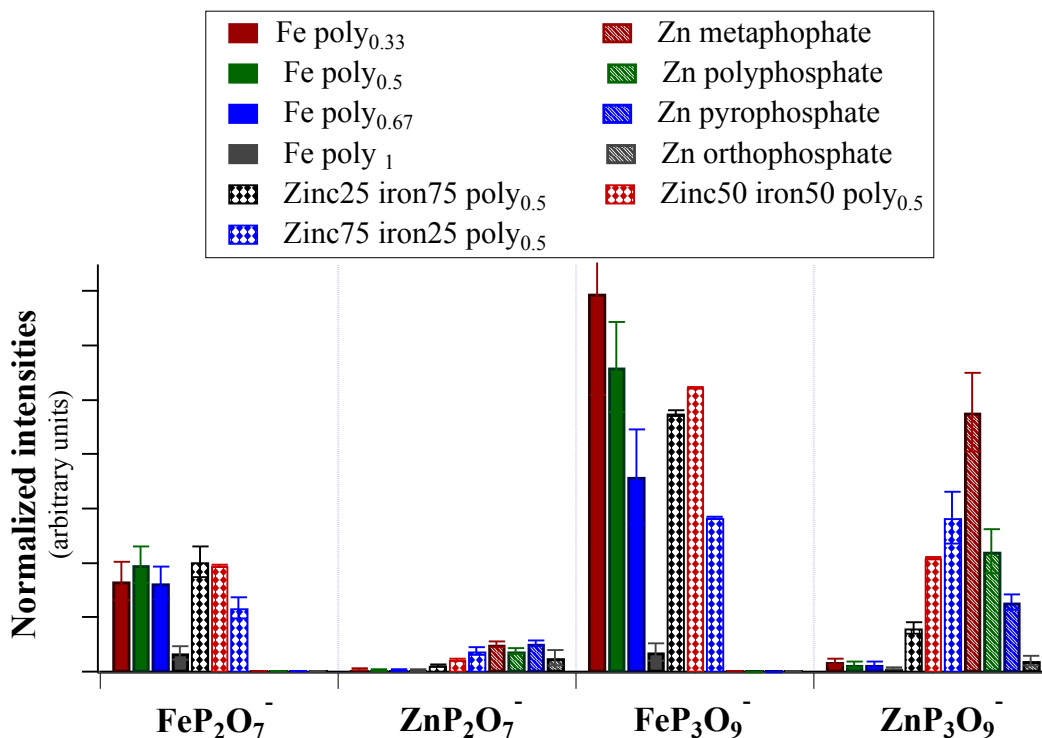


**Figure 5.15: Comparison between the normalized intensities of the characteristic ToF-SIMS signals of zinc metaphosphate and zinc orthophosphate, iron poly<sub>0.33</sub> and iron poly<sub>1</sub>**

All the polyphosphate fragments containing two or more phosphorus atoms have higher intensity in the long-chain polyphosphate samples (see Figure 5.15:  $\text{Fe}/\text{ZnP}_2\text{O}_7^-$ ,  $\text{Fe}/\text{ZnP}_3\text{O}_9^-$ ). The intensity of the zinc- or iron-containing peaks in mixed zinc and iron polyphosphates are not only influenced by the chain-length, but also by the stoichiometry of the compound. The intensity of the zinc-containing samples is therefore clearly increasing with increasing zinc content and increasing chain-length. The iron-containing fragments instead do not show a clear increasing trend with increasing iron content because the chain-length is varying in the opposite direction, therefore resulting in an opposite effect on the intensity of those peaks.

Low-intensity phosphate peaks with 3 or more P atoms are present also in samples such as zinc pyrophosphate, whose structure should be constituted by phosphate dimers (Figure 5.10). In the pyrophosphate composition, as also shown by FT-IR in Chapter 4, the glass undergoes a disproportionation reaction with the consequence that some Q<sub>0</sub> and Q<sub>2</sub> tetrahedra coexist with the Q<sub>1</sub>. This phenomenon is

not detected by the XPS measurements because the calculated BO/NBO intensity ratio provides an averaged chain-length value. However, the ToF-SIMS spectra are certainly affected by the local structure of the samples. Another difference in the case of the XPS measurements is the sample preparation (see paragraph 2.3). The surface of the mechanically polished samples has also been characterized by XPS (see Table 4 for the case of zinc metaphosphate). The BO/NBO decreases from  $0.45 \pm 0.05$  for the sample analyzed after quenching to  $0.39 \pm 0.05$  for the mechanically polished zinc metaphosphate, while the  $Zn3s-P2p_{3/2}$  increases from  $6.19 \pm 0.06$  eV to  $6.3 \pm 0.1$  eV. These results suggest a slight depolymerization, within experimental error, of the glass in comparison with the samples analyzed after the quenching. The same trend can be observed in the samples pulverized in air and indicates that the mechanical stress is inducing changes in the glass composition.

ToF-SIMS has been already employed for differentiating between calcium phosphate phases. In this case selected peaks have been discriminated and used as a fingerprint for identification of the CaP phases [54,55]. These results show for the first time that it is possible to discriminate between different composition polyphosphates; this discrimination appears clearer (higher differences between the intensities with lower error bars) for iron polyphosphates than with zinc polyphosphates. This difference is most likely only due to the presence of many zinc isotopes, as already discussed in the previous section.

The method described here can show some limitations in practical applications, for example, with a mixture of compounds. The stability of the method in the presence of contaminants should also be explored. The use of statistical methods, such as principal-component analysis, could help interpreting such complex spectra.

#### 5.3.4 *Effect of primary ions on ToF-SIMS spectra of polyphosphate glasses*

It has been observed that the use of cluster projectiles improves the ion-formation efficiency for most materials, allowing the detection of high-mass molecular fragments with good signal-to-noise ratio [40]. This phenomenon also applies to polyphosphate glasses, as one can see in Figure 5.16, where the normalized intensities of four polyphosphates obtained with  $Bi_1$  projectiles have been compared to those obtained with  $Bi_3^{++}$  polyatomic projectiles.

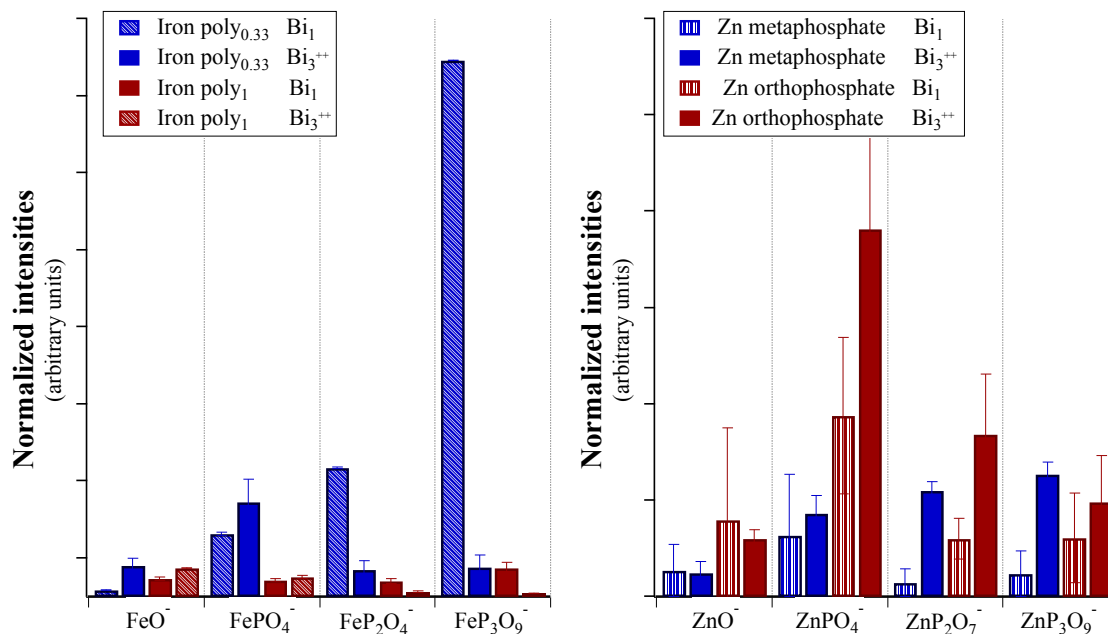


**Figure 5.16: Comparison between the normalized intensities of the characteristic ToF-SIMS signals of zinc metaphosphate, zinc orthophosphate, iron poly<sub>0.33</sub> and iron poly<sub>1</sub> with two different primary ions: Bi<sub>3</sub><sup>++</sup> and Bi<sub>1</sub>**

The results obtained with the Bi<sub>1</sub><sup>+</sup> primary ions showed a similar fragmentation pattern but with intensities one order-of-magnitude lower than for the high-mass molecular peaks. It has to be emphasized that these peaks are found, in the Bi<sub>3</sub><sup>++</sup> spectra, to be diagnostic for discriminating between the different polyphosphate chain-lengths in this investigation. This discrimination is, therefore, possible thanks to the increased sensitivity for high-mass molecular peaks obtained with the use of polyatomic projectiles.

#### 5.4 Summary

In the XPS data, the BO/NBO intensity ratio gives a direct and quantitative measure of the average chain-length of polyphosphate glasses. The chemical shifts of oxygen and phosphorus are suggesting that there is a delocalization of the electrons on the PO<sub>2</sub><sup>-</sup> group. With increasing chain-length, the partial positive charge on phosphorus atoms is increasing, explaining the higher binding energy of the P 2p signal, and the effective negative charge on the oxygen atoms is increasing, leading to a lower binding energy of the O 1s peak. These results are further confirmed by the chemical shift of the P 3s in the valence-band region, and by changes in the extra-atomic relaxation energy, calculated using the modified Auger parameter.

The iron-containing polyphosphates turned out to be susceptible to x-ray degradation. The degradation rate was determined by monitoring the ratio between the Fe(II) phosphates and the Fe(degradation) intensity with increasing acquisition

time. The results of the quantitative analysis obtained using the first-principles method were not always accurate within the samples under investigation; the phosphorus content was systematically overestimated and the iron content underestimated. A list of experimentally derived sensitivity factors was therefore obtained.

ToF-SIMS was also shown to be a powerful method for successfully discriminating polyphosphates of different composition by comparing the corrected intensities of the phosphate fragments. Zinc, iron and mixed zinc/iron polyphosphates show similar fragmentation patterns. Short-chain-length polyphosphates can be differentiated by the presence of peaks attributed to zinc oxide and hydroxide. Polyphosphates of intermediate and long chain-length show the same fragmentation patterns, but the intensity of the phosphate peaks at high masses ( $\text{Zn/FeP}_2\text{O}_7^-$ ,  $\text{Zn/FeP}_3\text{O}_9^-$ ) decreases upon decreasing the chain-length. In this study,  $\text{Bi}_3^{++}$  primary ions are demonstrated to improve the yield of molecular fragments compared to  $\text{Bi}_1$  projectiles, allowing the detection of high-mass fragments and improving the analytical sensitivity of the technique.

## References

- [1] Crobu M., Rossi A., Mangolini F., and Spencer N. D.: Chain-length identification in zinc polyphosphate glasses using Time of flight secondary ion mass spectroscopy and X-ray photoelectron spectroscopy. *Analytical and Bioanalytical Chemistry* (2012).
- [2] Crobu M., Rossi A., and Spencer N. D.: ToF-SIMS of polyphosphate glasses. *Surface & Interface Analysis*, (Submitted).
- [3] Bruckner R., Chun H. U., Goretzki H., and Sammet M.: XPS measurements and structural aspects of silicate and phosphate-glasses. *J. Non-Cryst. Solids* 42, 49-60 (1980).
- [4] Smets B. M. J., and Krol D. M.: Group III ions in sodium silicate glass. Part 1. X-ray photoelectron spectroscopy study *Phys. Chem. Glasses* 25, 113-118 (1984).
- [5] Onyiriuka E. C.: Zinc phosphate glass surfaces studied by XPS. *J. Non-Cryst. Solids*, 268-273 (1993).
- [6] Khawaja E. E., Durrani S. M. A., Aladel F. F., Salim M. A., and Hussain M. S.: X-ray photoelectron-spectroscopy and fourier transform-infrared studies of transition-metal phosphate-glasses. *J. Mater. Sci.* 30, 225-234 (1995).
- [7] Brow R. K.: An XPS study of oxygen bonding in zinc phosphate and zinc borophosphate glasses. *J. Non-Cryst. Solids* 194, 267-273 (1996).
- [8] Liu H. S., Chin T. S., and Yung S. W.: FTIR and XPS studies of low-melting PbO-ZnO- P<sub>2</sub>O<sub>5</sub> glasses. *Mater. Chem. Phys.* 50, 1-10 (1997).
- [9] Shih P. Y., Yung S. W., and Chin T. S.: FTIR and XPS studies of P<sub>2</sub>O<sub>5</sub>-Na<sub>2</sub>O-CuO glasses. *J. Non-Cryst. Solids* 244, 211-222 (1999).
- [10] Salim M. A., Khattak G. D., Fodor P. S., and Wenger L. E.: X-ray photoelectron spectroscopy (XPS) and magnetization studies of iron-vanadium phosphate glasses. *J. Non-Cryst. Solids* 289, 185-195 (2001).
- [11] Flambard A., Videau J. J., Delevoeye L., Cardinal T., Labrugere C., Rivero C. A., Couzi M., and Montagne L.: Structure and nonlinear optical properties of sodium-niobium phosphate glasses. *J. Non-Cryst. Solids* 354, 3540-3547 (2008).
- [12] Antonides E., Janse E. C., and Sawatzky G. A.: LMM Auger spectra of Cu, Zn, Ga, and Ge, II. Relationship with the L<sub>23</sub> photoelectron spectra via the L<sub>2</sub>L<sub>3</sub>M<sub>45</sub> Coster-Kronig process. *Physical Review B* 15, 4596 (1977).
- [13] Wagner C. D., and Joshi A.: The Auger Parameter, Its Utility and Advantages - a Review. *J. Electron. Spectrosc.* 47, 283-313 (1988).
- [14] Gaskell K. J., Asunskis A. L., and Sherwood P. M. A.: Sodium polyphosphate (Na<sub>4</sub>P<sub>4</sub>O<sub>12</sub>) by XPS. *Surface Science Spectra* 9, 151-158 (2002).
- [15] Eglin M., Development of a combinatorial approach to lubricant additive characterization, PhD Thesis No. 15054, ETH Zurich, Zürich, 2003, pp. 226.
- [16] Mangolini F., Reactivity of Environmentally Compatible Lubricant Additives: an In Situ and Ex Situ Investigation, PhD Thesis No. 19677, ETH Zürich, Zürich, 2011.
- [17] Olla N., Elsener and Rossi: Nondestructive in-depth composition profile of oxyhydroxide nanolayers on iron surfaces from ARXPS measurement. *Surf. Interface Anal.* 38, 964-974 (2006).
- [18] Fantauzzi M., Pacella A., Atzei D., Gianfagna A., Andreozzi G. B., and Rossi A.: Combined use of X-ray photoelectron and Mossbauer spectroscopic techniques in the analytical characterization of iron oxidation state in amphibole asbestos. *Analytical and Bioanalytical Chemistry* 396, 2889-2898 (2010).
- [19] Brow R. K., and Arens C. M.: An XPS study of iron phosphate glasses. *Phys. Chem. Glasses* 35, 132-199 (1993).

- [20] Marasinghe G. K., Karabulut M., Ray C. S., Day D. E., Shumsky M. G., Yelon W. B., Booth C. H., Allen P. G., and Shuh D. K.: Structural features of iron phosphate glasses. *J. Non-Cryst. Solids* 222, 144-152 (1997).
- [21] Brow R. K., Tallant D. R., Myers S. T., and Phifer C. C.: The Short-Range Structure of Zinc Polyphosphate Glass. *J. Non-Cryst. Solids* 191, 45-55 (1995).
- [22] Van Wazer J. R.: Phosphorus and its compounds, New York (1958).
- [23] Martin S. W.: Review of the structures of phosphate glasses. *European Journal of Solid State and Inorganic Chemistry*, 163-205 (1991).
- [24] Gresch R., Müller-Warmuth W., and Dutz H.: X-ray photoelectron spectroscopy of sodium phosphate glasses. *J. Non-Cryst. Solids* 34, 127-136 (1979).
- [25] Beletskii I. P., and Yatsimirskii K. B.: Electronic structure of polyphosphate ions. *Theoretical and Experimental Chemistry* 23, 621-627 (1988).
- [26] Moretti G.: Auger parameter and Wagner plot in the characterization of chemical states: initial and final state effects. *J. Electron. Spectrosc.*, 365-370 (1995).
- [27] Moretti G.: Auger parameter and Wagner plot in the characterization of chemical states by X-ray photoelectron spectroscopy: a review. *J. Electron. Spectrosc.*, 95-144 (1998).
- [28] Satta M., and Moretti G.: Auger parameters and Wagner plots. *J. Electron. Spectrosc.* 178-179, 123-127 (2010).
- [29] Reis S. T., Karabulut M., and Day D. E.: Chemical durability and structure of zinc-iron phosphate glasses. *J. Non-Cryst. Solids* 292, 150-157 (2001).
- [30] Armelao L., Bettinelli M., Rizzi G. A., and Russo U.: X-Ray photoelectron and Mossbauer spectroscopies of a binary iron phosphate glass. *J. Materials Chem.* 1, 805-808 (1991).
- [31] Concas G., Congiu F., Manca E., Muntoni C., and Pinna G.: Mössbauer spectroscopic investigation of some iron-containing sodium phosphate glasses. *J. Non-Cryst. Solids*, 175-178 (1995).
- [32] Süess M., The influence of the phosphorus to zinc ration on chemical and mechanical properties of zinc phosphate glasses, Master project - ETH Zürich, 2009.
- [33] Mura E., Polifosfati di calcio e zinco: caratterizzazione chimica e proprietà meccaniche, Master Thesis, Università degli Studi di Cagliari, 17 Dec 2010.
- [34] Shirley D. A.: High-Resolution X-Ray Photoemission Spectrum of Valence Bands of Gold. *Physical Review B* 5, 4709-& (1972).
- [35] Pauly N., and Tougaard S.: Surface and core hole effects in X-ray photoelectron spectroscopy. *Surf. Sci.* 604, 1193-1196 (2010).
- [36] Scofield J. H.: Hartree-Slater Subshell Photoionization Cross-Sections at 1254 and 1487ev. *J. Electron. Spectrosc.* 8, 129-137 (1976).
- [37] Seah M. P., and Gilmore I. S.: Quantitative x-ray photoelectron spectroscopy: Quadrupole effects, shake-up, Shirley background, and relative sensitivity factors from a database of true x-ray photoelectron spectra. *Physical Review B* 73, (2006).
- [38] Lee J. L. S., Gilmore I. S., and Seah M. P.: Quantification and methodology issues in multivariate analysis of ToF-SIMS data for mixed organic systems. *Surf. Interface Anal.* 40, 1-14 (2008).
- [39] Wagner M. S., Graham D. J., and Castner D. G.: Simplifying the interpretation of ToF-SIMS spectra and images using careful application of multivariate analysis. *Appl. Surf. Sci.* 252, 6575-6581 (2006).
- [40] Hagenhoff B., Pfitzer K., Tallarek E., Kock R., and Kersting R.: Polyatomic primary ion bombardment of organic materials: experiences in routine analysis. *Appl. Surf. Sci.* 231-232, 196-200 (2004).

## 6 Chain-length-identification strategy in polyphosphate glasses by means of XPS and ToF-SIMS

The aim of this chapter is to design an analytical strategy that can serve as a basis for an accurate interpretation of complex spectra such as those of the polyphosphates glasses formed by lubricant additives under extremely high pressures and at high temperatures. All the experimental data that appear in this chapter have been already presented and discussed in Chapter 5. In the first part of the chapter (Section 6.1), a strategy to determine the chain-length of the samples by means of XPS will be proposed. In the second part (Section 6.1), principal-component analysis will be used, in order to i) discriminate between the different zinc/iron oxides and the different composition polyphosphates, ii) recognize the most significant peaks for the identification of the chain-length of the samples in the ToF-SIMS spectra of zinc and iron polyphosphates. Finally (Paragraph 6.1.2), the possibility to correlate the information obtained by XPS and ToF-SIMS will be discussed.

The part concerning the XPS analysis of zinc polyphosphates has been published in [1].

### 6.1 Chain-length-identification strategy in polyphosphate glasses by means of XPS

The identification of the chain length in polyphosphate glasses, on the basis of the BO-to-NBO ratio has been extensively reported in the literature [2-12] and will be also discussed here in Section 6.1.1. The following Section (6.1.2) will deal with all the other information available in a XPS spectrum for the chain-length identification of polyphosphate.

#### 6.1.1 *The bridging/non bridging (BO/NBO) ratio*

The determination of the chain length of phosphate glasses has been based on magic-angle spinning ( $^{31}\text{P}$  MAS) NMR spectroscopy in the solid state [13-16] and in solution [17-21], by HPLC chromatography of dissolved glasses [22] and by titration [23]. These techniques are providing average bulk information and require the dissolution of the sample. Besides the BO/NBO ratio from the curve-fitting of the O1s XPS signals [7; 11; 24; 25] not many other surface analytical methods have been used with this aim, except for XANES both in FY and TEY mode [12; 26; 27].

The average chain-length predicted from the molar fraction  $x$  of the ZnO glass modifier according to Equation 2.2 is shown in Figure 6.1. The decrease of the chain-length from metaphosphate (infinite chain-length) to the polyphosphate glasses and finally to pyrophosphate (chain-length = 2) and orthophosphate (chain-length = 1) is clearly observed. The experimental data obtained using HPLC chromatography [22] are in accord with the theoretical values, and therefore the ZnO content is directly correlated with the chain-length. Changing the ZnO content, the number of  $Q_2$ ,  $Q_1$  and  $Q_0$  units in the glass changes, as well as the number of oxygen atoms in the bridging (BO) and in the non-bridging positions (NBO) (see Figure 2.10) [28]. The theoretical curve relating the BO/NBO ratio to the chain-length is plotted in Figure 6.2.

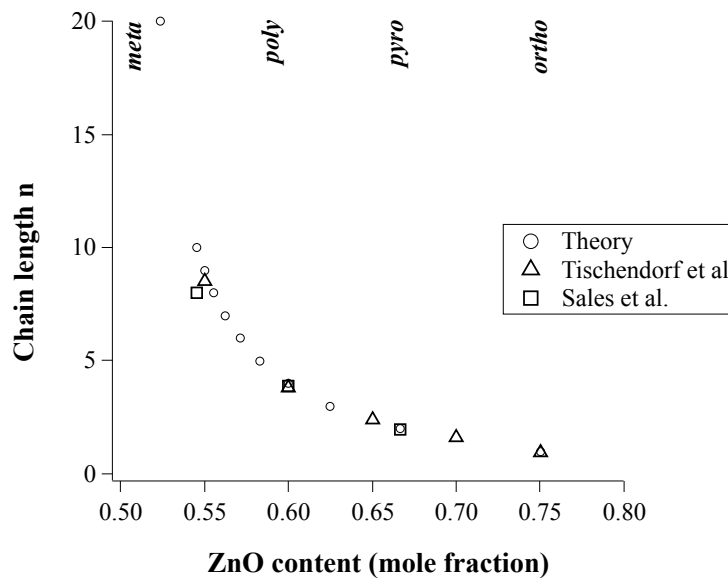


**Figure 6.1:** Calculated average chain-length  $n$  versus the composition of the phosphate glasses (circles). Experimental data from HPLC chromatograms of Tischendorf et al. [5] (squares) and Sales et al. [6] (triangles) are also included

It can be observed that the BO/NBO ratio is strongly affected at short chain-length (from ortho- to poly-phosphates). However, upon reaching the range of polyphosphate to meta-phosphate (chain-length longer than 10) the BO/NBO ratio asymptotically approaches the limiting value of 0.5.

It is instructive to examine several specific examples concerning chain-length identification in unknown phosphate glassy films based on experimentally determined BO/NBO ratio, taking into account the experimental error (Figure 6.2). For a BO/NBO ratio  $< 0.05$  (ortho in Figure 6.2) the average chain-length is 1, corresponding to orthophosphate. For the experimental value of  $BO/NBO = 0.20 \pm 0.05$  (pyro), the average chain-length is 1.8 – 2.5, in good agreement with pyrophosphate. For the experimental value  $BO/NBO = 0.37 \pm 0.05$  (poly) the chain-length can lie between 5 and 15 and for the BO/NBO ratio  $0.48 \pm 0.02$  (meta) the chain-length can be anything between 30 and infinity (Figure 6.2). Thus, one can



conclude that the determination of chain-length is more accurate at low values of the BO/NBO ratio.

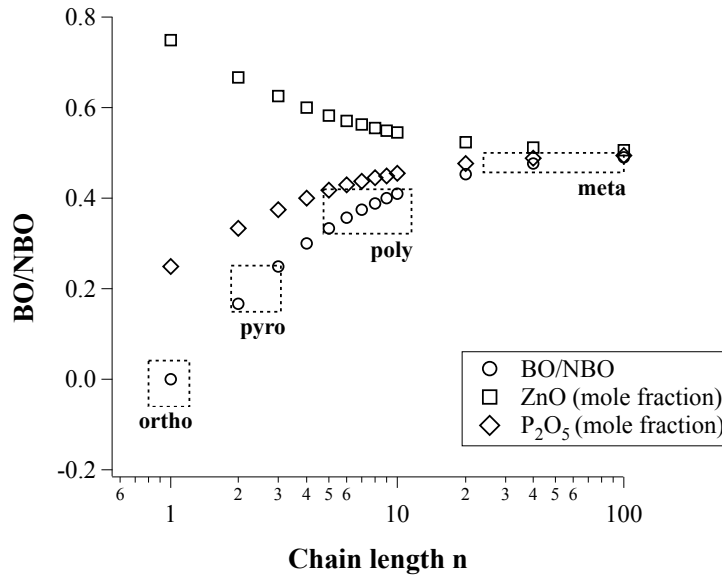


**Figure 6.2:** Calculated BO/NBO ratio vs the chain-length  $n$  of the phosphate glasses (open circles). Included are the experimental BO/NBO ratio values determined for the four phosphate glasses studied in this work. Y height of the dashed boxes correspond to the standard deviations of the BO/NBO value (Table 2), X-length is the associated variation in chain-length

The discussion above concerned only zinc polyphosphates, for simplicity, but the same conclusions are still valid when zinc is substituted by an other modifying oxide. All the experimentally derived BO/NBO presented in Chapter 5 are summarized in Figure 6.3. Given that iron is present in polyphosphates as iron (II) and iron (III) while zinc is always present as zinc (II), the total metal oxide content would not be adequate to describe the structural effect of the presence of zinc and/or iron in the network as in Figure 6.1. An increase in the ratio iron(III)/iron(II), in fact, will result in a decrease of the BO/NBO, even if the total iron content remains constant. This effect can be taken into account if the ratio between the metal oxide content and the phosphorus content is corrected by the average oxidation state of the metallic components in the glass. The corrected ratio  $R_c$  has been defined as follows:

**Equation 6.1**

$$R_c = \frac{V_{Fe}^{av}[Fe] + V_{Zn}[Zn]}{[Fe] + [Zn]} \cdot \frac{[Fe] + [Zn]}{[P]}$$

where  $V_{Fe}^{av}$  is the average oxidation state of iron (calculated using the XPS results in Chapter 5) and  $V_{Zn}$  the oxidation state of zinc. The graph shows how an increase in the value of  $R_c$  corresponds to a decrease of the measured BO/NBO for all polyphosphates under investigation.

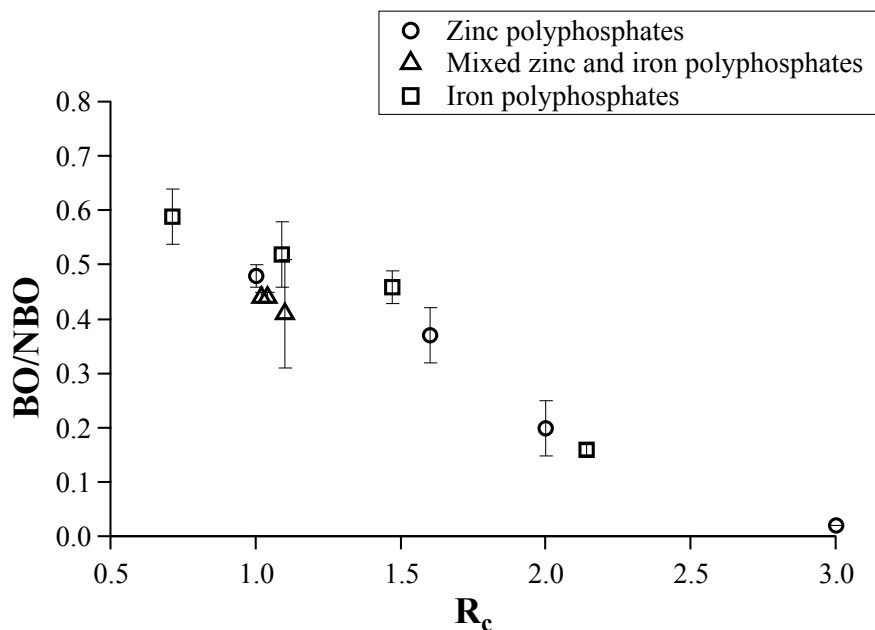


**Figure 6.3:** Experimental BO/NBO values for zinc, iron and mixed zinc and iron polyphosphates as a function of  $R_c$  (ratio between the metal oxide content and the phosphorus content corrected by the average oxidation state of the metallic components in the glass, calculated according to Equation 6.1)

All the experimental results discussed above have been acquired on homogeneous and clean samples. Complex systems such as tribological surfaces are particularly challenging analytical problems. A typical tribological experiment involves two sliding surfaces in the presence of a lubricant oil that can contain one or more lubricant additives. Prior to the XPS analysis, the lubricant oil used during the test has to be rinsed from the sample using one or more organic solvents. Residuals from the lubricant oil used and the rinsing solvents used will add up to an already complex surface film, heterogeneous in the three dimensions. In the XPS, O 1s spectrum peaks originating from a contaminant or from species other than phosphate will be often present and not easily resolved. In these cases, calculating the average chain-length relying only on the BO/NBO intensity ratio might be misleading.

### 6.1.2 Other parameters for the chain-length identification by means of XPS

Another experimental value that is strongly dependent on chain length in the XPS spectra is the binding energy of the P 2p<sub>3/2</sub>. It is useful to first discuss the case of zinc polyphosphates and then extend the discussion to iron and mixed zinc and iron polyphosphates.

In the XPS spectra of zinc polyphosphates the P 2p signal is acquired in the same BE range with the Zn 3s, but while the phosphorus P2p<sub>3/2</sub> binding energy is shifting with the chain-length, the binding energy of the Zn 3s remains unchanged (Table 5.1). When comparing the absolute BE values obtained from different samples,

uncertainties due to calibration of the spectra (necessary when using charge compensation) might arise. The amount of carbon present on the sample was very low and using this very small peak as a reference for the binding energy scale might have introduced some scatter into the data. However, the difference between the BEs of the characteristic signals appearing in the XP-spectra is not affected by the charge compensation and for this reason in Figure 6.4 the distance between the position of the Zn 3s signal, whose BE remains constant with composition, and the P2p<sub>3/2</sub> signal has been plotted ( $\Delta BE = \text{Zn } 3s - \text{P}2p_{3/2}$ ).

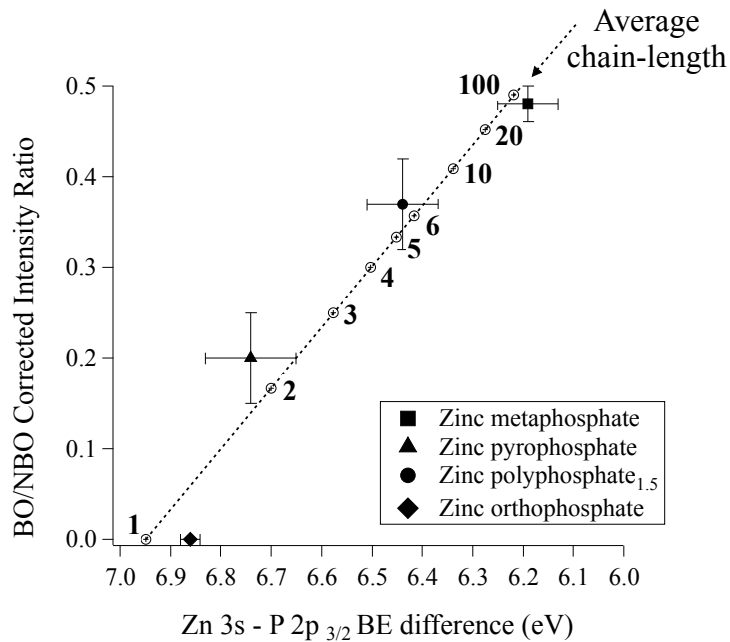


**Figure 6.4:** BO/NBO versus Zn3s BE - P 2p<sub>3/2</sub> BE difference for different chain-length zinc polyphosphate glasses. The dotted line is the result of the correlation between the BO/NBO and Zn3s BE - P 2p<sub>3/2</sub> BE difference experimental data. The average chain-length n (open circles) has been calculated using Equation 5.1

The use of the  $\Delta BE$  (Zn3s-P2p<sub>3/2</sub>) together with the BO/NBO intensity ratio could also be an effective and diagnostic analytical tool. This graph allows the identification of the chain-length on the surface of zinc polyphosphate glasses. In Chapter 7 this method will be used in order to interpret the effects of the mechanical tests on zinc polyphosphate glasses. Auger parameter and valence band are also changing with chain length (Paragraph 5.3.1) and they can be used to further confirm the interpretation made on the basis of the graph in Figure 6.4.

When extending the discussion to iron-containing polyphosphates, the same trends can be observed. In Figure 6.5 the binding energy of the P 2p<sub>3/2</sub> signal for zinc, iron, and mixed-zinc-and-iron polyphosphates are plotted as a function of R<sub>c</sub>.

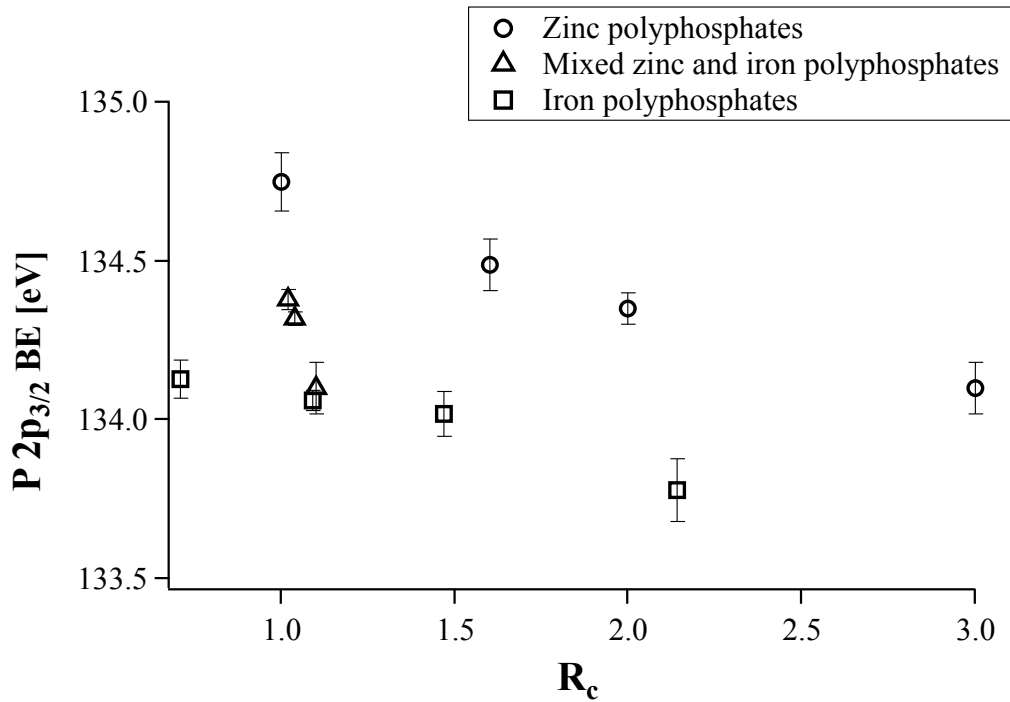


**Figure 6.5: Experimental P 2p<sub>3/2</sub> BEs for zinc, iron and mixed-zinc-and-iron polyphosphates as a function of R<sub>c</sub>**

Also in the case of iron polyphosphates the P 2p<sub>3/2</sub> BE value is decreasing with decreasing R<sub>c</sub>. It can also be observed that the BEs of iron polyphosphates are lower than those of zinc polyphosphates with similar R<sub>c</sub> values. The experimental values for BO/NBO and the P 2p<sub>3/2</sub> of zinc, iron and calcium polyphosphates are reported in Figure 6.6.

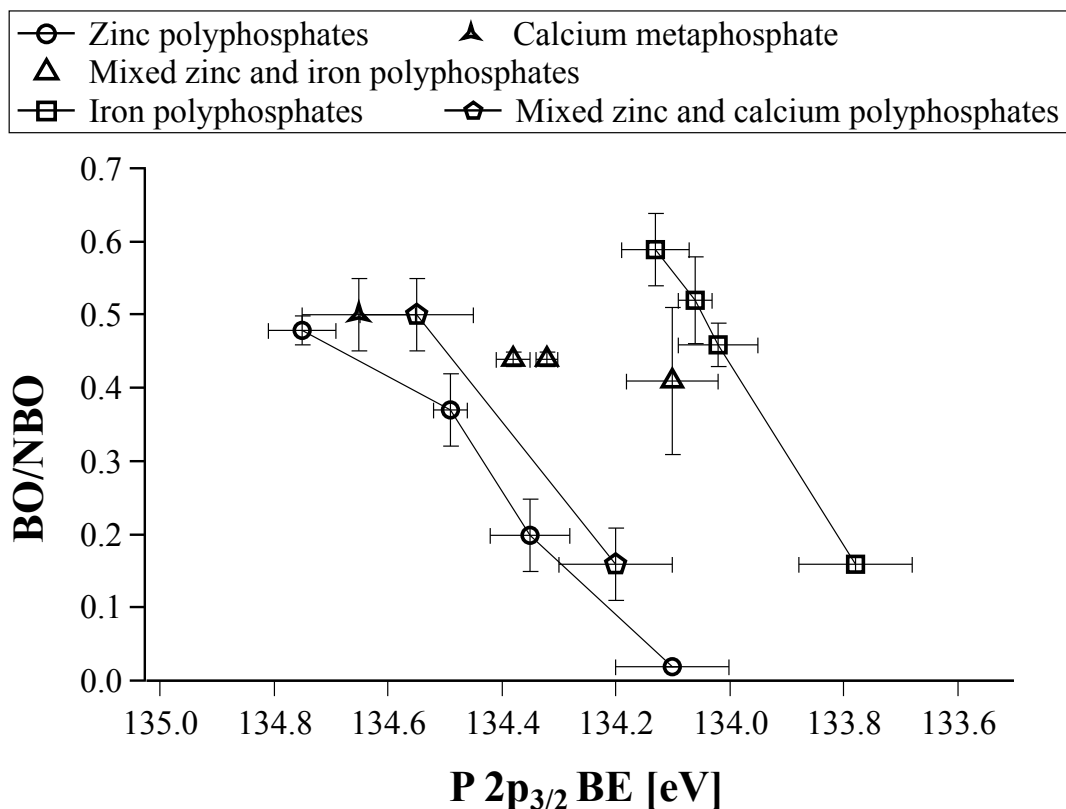


**Figure 6.6:** Experimental BO/NBO values for zinc, iron, calcium, mixed-zinc-and-iron and mixed-zinc-and-calcium polyphosphates as a function of P 2p<sub>3/2</sub> BE. The calcium-containing polyphosphates have been characterized by Mura in [29]

Zinc and calcium have formal oxidation state II and a very similar short-range order with an average cation coordination number of 4 [19; 30-34]. Conversely, iron has an average oxidation state higher than 2 and the iron atoms (or ions ?) occupy octahedral coordination sites [35; 36]. The shifts correlated with the change of cation are in the same order of magnitude as those correlated with the chain-length. Therefore we can expect that the kind of cation will influence the chain-length as well as the properties of the glass (see also Chapter 4). The mixed polyphosphates P 2p<sub>3/2</sub> BE are affected by the influence of both effects and they can be found at intermediate values according to their composition, as shown in Figure 6.5 and in Figure 6.6.

Chain-length-identification graphs such as Figure 6.4 can only be used for binary polyphosphates. When more than one modifying oxide is present in the network, a change in the chain-length will always be followed by a shift in the BE of the P 2p<sub>3/2</sub>. In this case, the shift can still be used as analytical tool to identify the chain-length, but only if the ratio between the modifying oxides present in the glass is constant. In this case the use of the valence band can be a valuable help. As can be seen in Figure 6.7, the P 3s signal shifts about 2.5 eV towards higher BE values upon going from short chain length to long chain length for both zinc and iron polyphosphates.

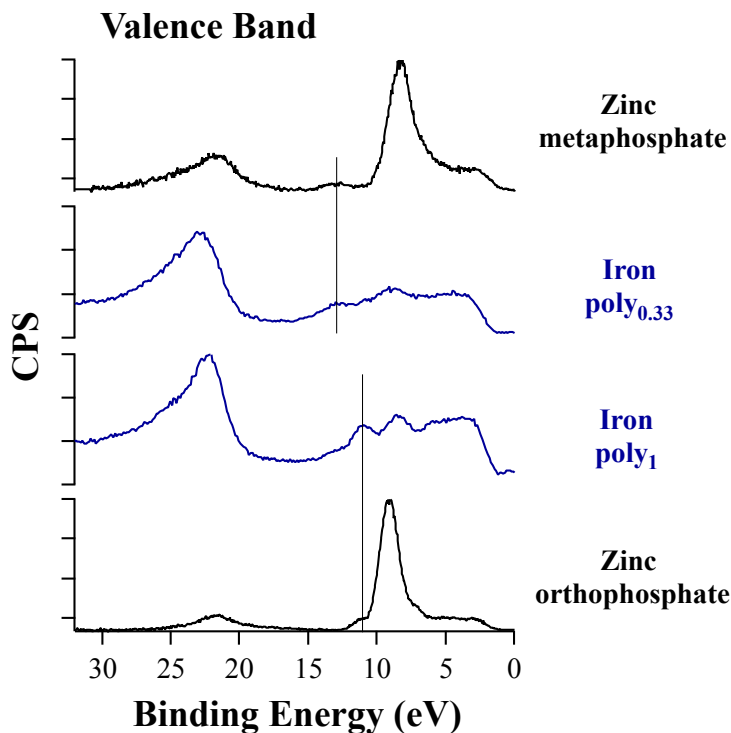


**Figure 6.7:** Comparison of the valence band XP-spectrum for zinc and iron polyphosphate of different chain-lengths

### 6.1 ToF SIMS

In Chapter 5 it was observed that the relative intensities of the phosphate peaks were dependent on the chain length. The phosphate fingerprint was found to consist of a peak list of about 100 different fragments. Principal-component analysis (PCA) was used, in order to reliably recognize the series of peaks that contain the information necessary to discriminate between different composition polyphosphates. The aim of the following section is to define a method to reliably interpret complex tribological spectra, where mixtures of these compounds can be found in the first monolayer of the two counterparts.

#### 6.1.1 Chain-length identification by ToF-SIMS: PCA analysis

The intensities of the selected peaks were normalized by the total intensities and mean-centered prior to the PCA analysis. In the pre-processing phase the fragments that were interfering, because of peak overlap between zinc and iron samples or between phosphate peaks and contaminants, were excluded. PCA analysis was first performed on smaller groups of samples: zinc polyphosphates, iron polyphosphates and only at the final stage extended to all compositions. The peak list can be found in Appendix C.1, while scores and loadings plots have been reported in Figure 6.8 and Figure 6.9.

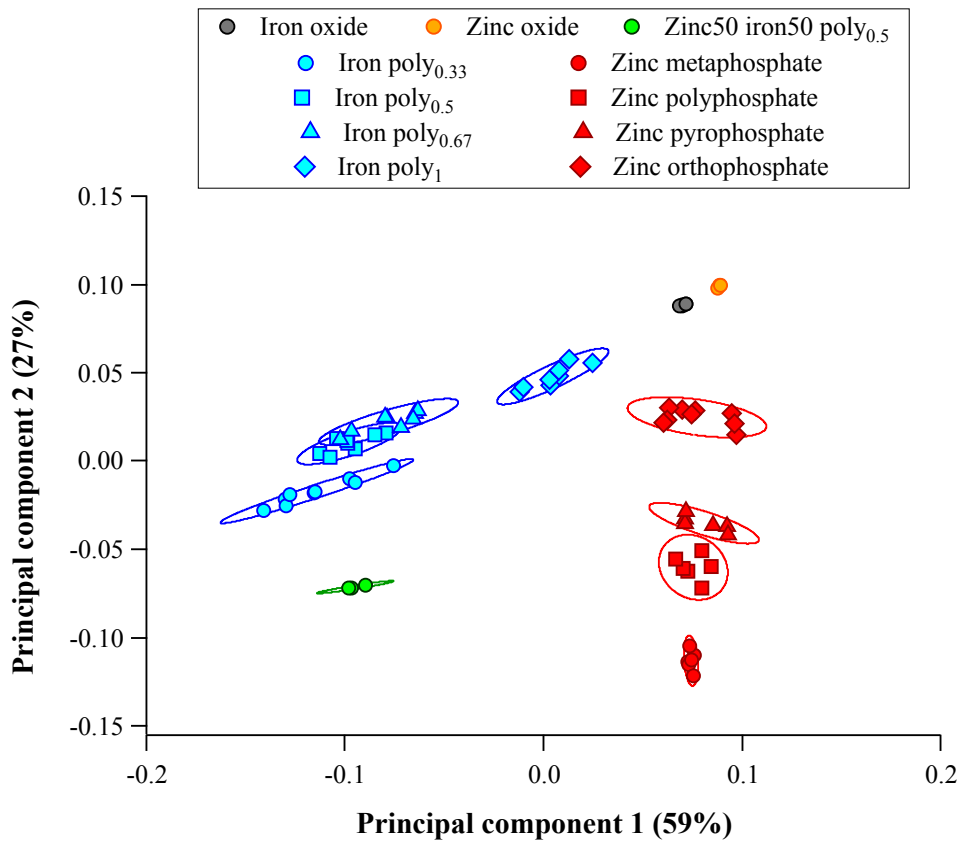


**Figure 6.8: Scores plot obtained from the PCA analysis of the ToF-SIMS spectra acquired on different composition polyphosphates and on zinc and iron oxide**

At least three independent measurements per sample were included in the analysis. Zinc and iron oxide spectra were also acquired and included in this analysis not only as reference and comparison, but also because they are often found, together with polyphosphate glasses, in tribological systems (positive and negative mode spectra can be found in Appendix C.1). The first two components, Principal Component 1 (PC1) and Principal Component 2 (PC2) in Figure 6.8, describe 86 % of the variation in the data. The samples appear in the graph as separated points and samples with the same composition are found in the same region of the graph forming a point cluster. For each cluster, a confidence ellipse has been obtained based on the *t* distribution and with a confidence limit of 95% [37]. The analysis is able to clearly differentiate not only between oxides and polyphosphates, but also between different chain-length zinc and iron polyphosphates. It can also be observed that the PC1 describes the variation between zinc compounds, on the positive part of the x-axis, and iron compounds, on the negative side. In contrast, most of the information on the chain-length of the samples is contained in principal component 2: the two oxides show the most positive values while the polyphosphates are found at lower values with the short chain lengths still on the positive side of the y-axis and the long chain-length samples on the negative side.

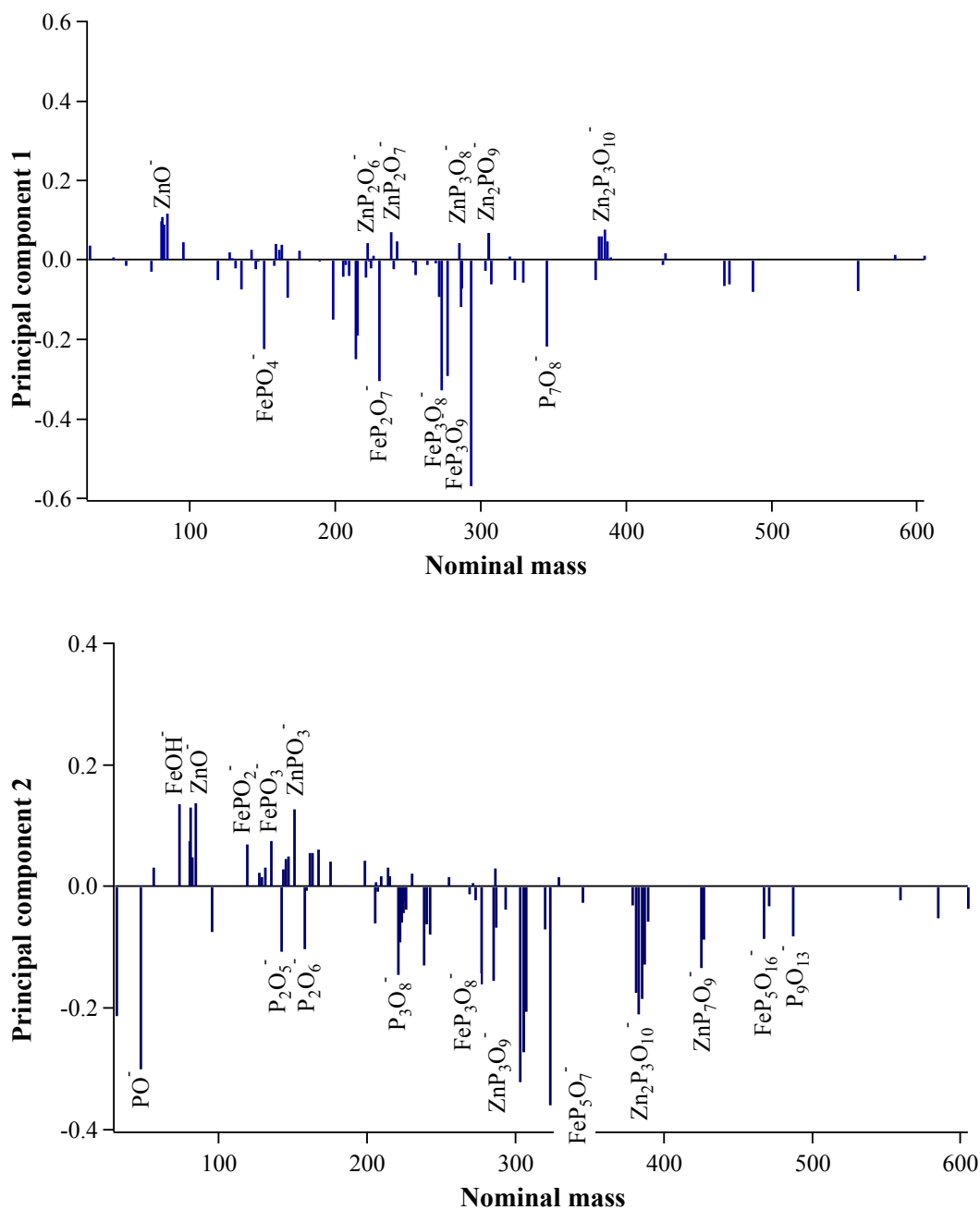


**Figure 6.9:** Loadings plots obtained from the PCA analysis of the ToF-SIMS spectra acquired on different composition polyphosphates

The loadings plots (Figure 6.9) show that the peaks with highest intensities are those carrying the best discrimination ability. Therefore we would expect, for PC1, positive scores for zinc fragments, and negative scores for iron fragments. Indeed zinc oxide and other zinc-containing fragments show the most positive coefficients, while equivalent iron-containing fragments obtained the most negative coefficients. PC1 is also already discriminating between the different chain length iron polyphosphates, but not between zinc polyphosphates. A fragment without iron or zinc,  $P_7O_8^-$ , is also present with a high negative score carrying some information on chain-length.



Finally, the key peaks for discriminating the different chain-length polyphosphates are those that show the highest coefficient in PC2. It is immediately evident that most of low-mass fragments (below  $m/z \approx 150$ ) show positive coefficients, while high-mass fragments always exhibit a negative coefficient.  $\text{Zn/FeO}^-$ ,  $\text{Zn/FeOH}^-$ ,  $\text{Zn/FePO}_3^-$  are the fragments with higher intensity in short chain-length polyphosphates.  $\text{PO}^-$ ,  $\text{P}_2\text{O}_5^-$ ,  $\text{P}_2\text{O}_6^-$ ,  $\text{P}_3\text{O}_8^-$ ,  $\text{P}_9\text{O}_{13}^-$ ,  $\text{Zn/FeP}_3\text{O}_8^-$ ,  $\text{Zn/FeP}_3\text{O}_9^-$ ,  $\text{FeP}_5\text{O}_9^-$ ,  $\text{FeP}_5\text{O}_{16}^-$ ,  $\text{Zn}_2\text{P}_3\text{O}_{10}^-$  and  $\text{Zn}_2\text{P}_7\text{O}_9^-$  are the peaks whose intensity becomes higher with increasing chain-length. Also mixed zinc and iron polyphosphates are described by the same fragments: the zinc50 iron50 poly<sub>0.5</sub> can be found with a negative y values (the long chain-lengths part of the graph) in between iron and zinc in the x axis. It is interesting to note that most of these peaks contain 2 or more P atoms and only even numbers of P atoms appear in the fragments with more than 2 of them. This phenomenon is most likely related to the fragmentation mechanism of polyphosphates, whose understanding is beyond the scope of this work.

### 6.1.2 Determining the polyphosphate chain length from ToF-SIMS data

The PCA analysis was able to discriminate between the different composition polyphosphates and to identify the key fragments for chain-length identification. If possible, it would be useful to have a method to calculate the polyphosphate chain-length from the ToF-SIMS data. Partial-least-squares regression is a multivariate analysis method that involves the analysis of the relationship between two or more measurements on the same entities using a two-block predictive model to model the relationship between the two matrices, X (predictor variables) and Y (response variables) [38; 39]. In this case we wanted to correlate the ToF-SIMS spectra (predictor variables) with the BO/NBO ratios measured by XPS (response variables). PLS provides a quantitative model by using a calibration dataset where both series of variables are known [38; 39]. PLS is a well established tool of chemometrics [38] and, like PCA, is included in most common commercial chemometric softwares. The PLS toolbox 6.5 (Eigenvector Research, Inc., 3905 West Eaglerock Drive, Wenatchee, WA 98801) was used for this analysis.

All the data used for the PCA analysis (excluding the oxides) were used for building the predictive model, which was validated using a random subset of samples. In Figure 6.10 the predicted BO/NBO values (from the ToF-SIMS spectra) have been plotted as a function of the measured ones (by XPS).

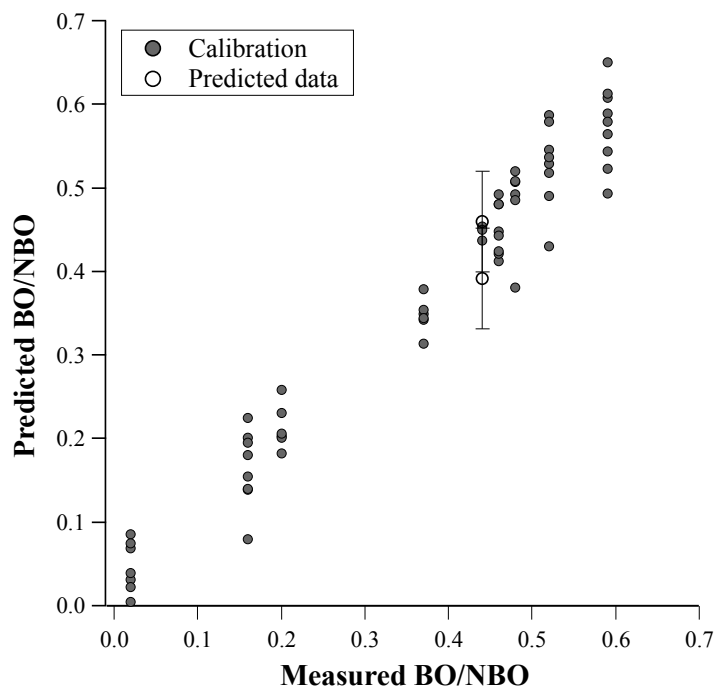


**Figure 6.10: Predicted BO/NBO (from ToF-SIMS data) vs. measured BO/NBO (for XPS data) resulting from the PLS regression**

The closed circles in the figure are the data points used as calibration to build the predictive model, while in the open circles are the outcomes of the predictive model applied to the zinc75 iron25 poly<sub>0.5</sub> ToF-SIMS spectra. The XPS BO/NBO values used for building this model were the average ones reported in Chapter 5 and plotted together in Figure 6.3: it was then necessary to make the assumption that the errors in the XPS measurements are significantly smaller than those involved in the prediction. The error in the prediction was found to be about  $\pm 0.1$  compared to a value included between  $\pm 0.01$  and  $\pm 0.05$  for the XPS analysis. In an ideal situation the correlation would have been performed with results from the two techniques on each sample acquired within a very small timeframe (to avoid changes in the surface chemistry). This was not possible in this work, where the XPS data were acquired on independent samples and a different surface treatment was used prior to the ToF-SIMS analysis. Despite that, the results show a good correlation of the ToF-SIMS results with the XPS ones and the model obtained is able to predict the BO/NBO for samples with different composition than those used in the model.

The coefficients of the regression are plotted in Figure 6.11.

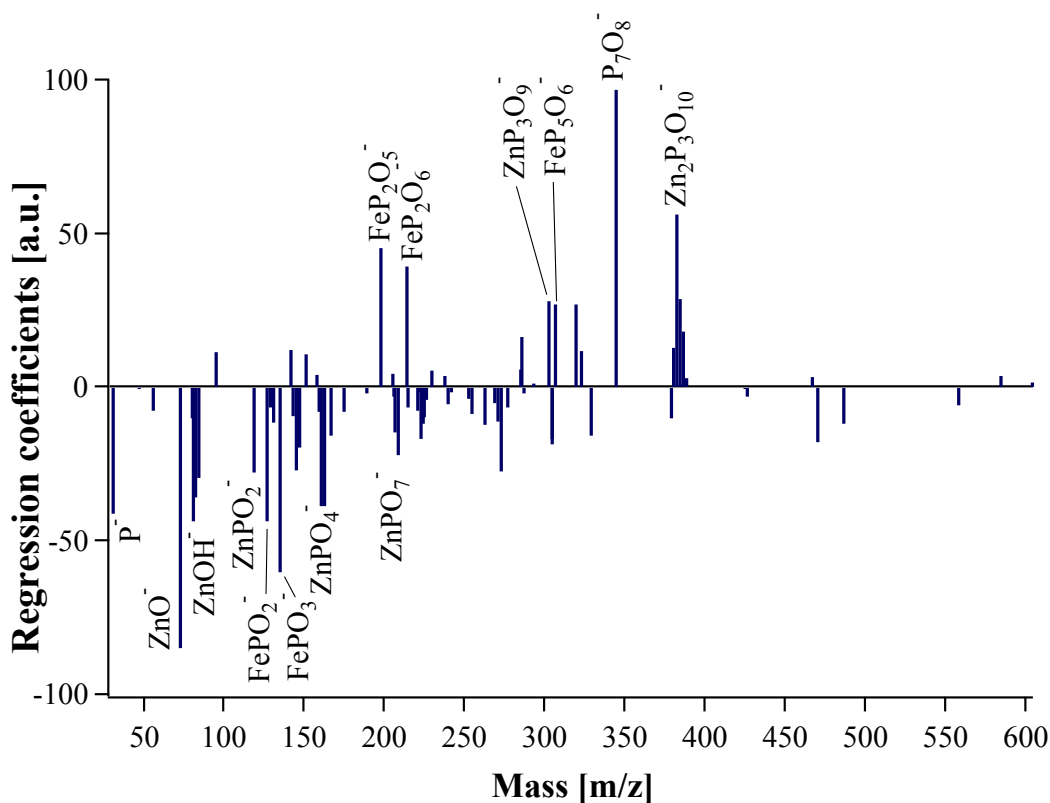


Figure 6.11: Coefficients of the PLS regression

The fragments with the highest coefficients are those having the most influence on the predicted value of the BO/NBO. Most of the fragments shown in Figure 6.11 have been already highlighted by the PCA in the previous paragraph. It is interesting to note that, as in the PCA analysis, the fragments contributing to a high BO/NBO ratio, i.e. long chain-length, are those containing two or more phosphorus atoms. But, unlike the PCA loadings, the PLS coefficient does not exhibit high values for the fragments without a metal atom, apart from  $P_7O_8^-$ . Moreover the model seems to take into account a lower number of peaks compared to the PCA analysis. This could be an advantage in simplicity but could result in poor stability if applied to samples with contamination and/or to more noisy spectra like those obtained from imaging-mode spectra.

## 6.2 Summary

In this chapter, a method for the discrimination of polyphosphate glasses of different chain-lengths by means of surface-analytical tools has been described. A solid foundation of systematic studies on the pure compounds is essential when applying these same techniques to more complex systems. ToF-SIMS, as well as XPS, appear to be well suited for the investigation of such systems:

In the case of zinc polyphosphates, the combined use of the BO/NBO intensity ratio, the Zn3s-P 2p<sub>3/2</sub> difference energy and the modified Auger parameter allow unambiguous differentiation between four samples with composition ranging from zinc orthophosphate, formed by PO<sub>4</sub> monomers, to zinc metaphosphate, which is characterized by a long-chain structure.

A similar method can be used also for iron and mixed zinc and iron polyphosphates, where the chain-length identification can be done using the BO/NBO ratio and the P 2p binding energy. In case of mixed samples a shift of the P 2p binding energy due to the presence of two different cations has to be taken into account. In this case the valence band, where the Zn 3s peak is shifting with the chain-length, is of immense help in validating the interpretation of the data.

PCA was used to successfully discriminate between the different composition polyphosphates. From the loading coefficients it was also possible to determine the key fragments for the chain-length identification. Zn/FeO<sup>-</sup>, Zn/FeOH<sup>-</sup>, Zn/FePO<sub>3</sub><sup>-</sup> are the fragments with higher intensity in short chain-length polyphosphates, while PO<sup>-</sup>, P<sub>2</sub>O<sub>5</sub><sup>-</sup>, P<sub>2</sub>O<sub>6</sub><sup>-</sup>, P<sub>3</sub>O<sub>8</sub><sup>-</sup>, P<sub>9</sub>O<sub>13</sub><sup>-</sup>, Zn/FeP<sub>3</sub>O<sub>8</sub><sup>-</sup>, Zn/FeP<sub>3</sub>O<sub>9</sub><sup>-</sup>, FeP<sub>5</sub>O<sub>9</sub><sup>-</sup>, FeP<sub>5</sub>O<sub>16</sub><sup>-</sup>, Zn<sub>2</sub>P<sub>3</sub>O<sub>10</sub><sup>-</sup> and Zn<sub>2</sub>P<sub>7</sub>O<sub>9</sub><sup>-</sup> are the peaks whose intensity becomes higher with increasing chain-length.

Using PLS regression it was possible to correlate the ToF-SIMS results with those from XPS. The developed predicted model was able to predict the BO/NBO ratio on the basis of the ToF-SIMS spectra.

In conclusion, these surface-analytical methods, alone or in combination with each other, can thus provide a powerful tool for basic research in fields, such as tribology, where the surface chemistry of polyphosphates can play a key role.

## References

- [1] Crobu M., Rossi A., Mangolini F., and Spencer N. D.: Chain-length identification in zinc polyphosphate glasses using Time of flight secondary ion mass spectroscopy and X-ray photoelectron spectroscopy. *Analytical and Bioanalytical Chemistry*, (2011).
- [2] Chowdary B. V. R., Tan K. L., Chia W. T., and Gopalakrishnan R.: X-ray photoelectron spectroscopic studies of molibdenum phosphate glassy sistem. *J. Non-Cryst. Solids*, 95-102 (1990).
- [3] Smets B. M. J., and Krol D. M.: Group III ions in sodium silicate glass. Part 1. X-ray photoelectron spectroscopy study *Phys. Chem. Glasses* 25, 113-118 (1984).
- [4] Brow R. K., and Arens C. M.: An XPS study of iron phosphate glasses. *Phys. Chem. Glasses* 35, 132-199 (1993).
- [5] Liu H. S., Chin T. S., and Yung S. W.: FTIR and XPS studies of low-melting PbO-ZnO- P<sub>2</sub>O<sub>5</sub> glasses. *Mater. Chem. Phys.* 50, 1-10 (1997).

- [6] Shih P. Y., Yung S. W., and Chin T. S.: FTIR and XPS studies of  $P_2O_5$ - $Na_2O$ - $CuO$  glasses. *J. Non-Cryst. Solids* 244, 211-222 (1999).
- [7] Heuberger R., Rossi A., and Spencer N. D.: Pressure Dependence of ZnDTP Tribochemical Film Formation: A Combinatorial Approach. *Tribol. Lett.* 28, 209-222 (2007).
- [8] Heuberger R., Rossi A., and Spencer N. D.: XPS study of the influence of temperature on ZnDTP tribofilm composition. *Tribol. Lett.* 25, 185-196 (2007).
- [9] Eglin M., Rossi A., and Spencer N. D.: X-ray photoelectron spectroscopy analysis of tribostressed samples in the presence of ZnDTP: a combinatorial approach. *Tribol. Lett.* 15, 199-209 (2003).
- [10] Piras F. M., Rossi A., and Spencer N. D.: Combined in situ (ATR FT-IR) and ex situ (XPS) study of the ZnDTP-iron surface interaction. *Tribol. Lett.* 15, 181-191 (2003).
- [11] Rossi A., Piras F. M., Kim D., Gellman A. J., and Spencer N. D.: Surface reactivity of tributyl thiophosphate: effects of temperature and mechanical stress. *Tribol. Lett.* 23, 197-208 (2006).
- [12] Kasrai M., Fuller M., Scaini M., Yin Z., Brunner R. W., Bancroft G. M., Fleet M. E., Fyfe K., and Tan K. H.: Study of tribochemical film formation using x-ray absorption and photoelectron spectroscopies. *Tribol. Ser.* 30, 659-669 (1995).
- [13] Le Saout G., Simon P., Fayon F., Blin A., and Vaills Y.: Raman and infrared study of  $(PbO)_x(P_2O_5)_{(1-x)}$  glasses. *J. Raman Spectrosc.* 33, 740-746 (2002).
- [14] Le Saout G., Fayon F., Bessada C., Simon P., Blin A., and Vaills Y.: A multispectroscopic study of  $PbO_xZnO_{0.6-x}(P_2O_5)_{(0.4)}$  glasses. *J. Non-Cryst. Solids* 293, 657-662 (2001).
- [15] Qiu D., Guerry P., Ahmed I., Pickup D. M., Carta D., Knowles J. C., Smith M. E., and Newport R. J.: A high-energy X-ray diffraction,  $^{31}P$  and  $^{11}B$  solid-state NMR study of the structure of aged sodium borophosphate glasses. *Mater. Chem. Phys.* 111, 455-462 (2008).
- [16] Sales B. C., Otaigbe J. U., Beall G. H., Boatner L. A., and Ramey J. O.: Structure of zinc polyphosphate glasses. *J. Non-Cryst. Solids* 226, 287-293 (1998).
- [17] Brow R. K., Tallant D. R., Myers S. T., and Phifer C. C.: The Short-Range Structure of Zinc Polyphosphate Glass. *J. Non-Cryst. Solids* 191, 45-55 (1995).
- [18] Flambar A., Videau J. J., Delevoye L., Cardinal T., Labrugere C., Rivero C. A., Couzi M., and Montagne L.: Structure and nonlinear optical properties of sodium-niobium phosphate glasses. *J. Non-Cryst. Solids* 354, 3540-3547 (2008).
- [19] Lai A., Musinu A., Piccaluga G., and Puligheddu S.: Structural evolution in zinc and lead phosphate glasses by x-ray diffraction and P MAS NMR spectroscopy. *Phys. Chem. Glasses* 38, 173-178 (1997).
- [20] Meyer K.: Characterization of the structure of binary zinc ultraphosphate glasses by infrared and Raman spectroscopy. *J. Non-Cryst. Solids* 209, 227-239 (1997).
- [21] Wiench J. W., Tischendorf B., Otaigbe J. U., and Pruski M.: Structure of zinc polyphosphate glasses studied by two-dimensional solid and liquid state NMR. *J. Mol. Struct.* 602, 145-157 (2002).
- [22] Tischendorf B., Otaigbe J. U., Wiench J. W., Pruski M., and Sales B. C.: A study of short and intermediate range order in zinc phosphate glasses. *J. Non-Cryst. Solids* 282, 147-158 (2001).
- [23] Baluyot E. S., and Hartford C. G.: Comparison of polyphosphate analysis by ion chromatography and by modified end-group titration. *Journal of Chromatography A* 739, 217-222 (1996).
- [24] Crobu M., Rossi A., Mangolini F., and Spencer N. D.: Tribochemistry of Bulk Zinc Metaphosphate Glasses. *Tribol. Lett.* 39, 121-134 (2010).

- [25] Martin J. M., Grossiord C., Le Mogne T., Bec S., and Tonck A.: The two-layer structure of ZnTP tribofilms: Part I: AES, XPS and XANES analyses. *Tribol. Int.* 34, 523-530 (2001).
- [26] Huang L. J., Lau W. M., Tang H. T., Lennard W. N., Mitchell I. V., Schultz P. J., and Kasrai M.: Near-Surface Structure of Low-Energy-Argon-Bombarded Si(100). *Physical Review B* 50, 18453-18468 (1994).
- [27] Yin Z. F., Kasrai M., Bancroft G. M., Tan K. H., and Feng X. H.: X-Ray-Absorption Spectroscopic Studies of Sodium Polyphosphate Glasses. *Physical Review B* 51, 742-750 (1995).
- [28] Brow R. K.: Review: the structure of simple phosphate glasses. *J. Non-Cryst. Solids* 263-264, 1-28 (2000).
- [29] Mura E., Polifosfati di calcio e zinco: caratterizzazione chimica e proprietà meccaniche, Master Thesis, Università degli Studi di Cagliari, 17 Dec 2010.
- [30] Musinu A., Piccaluga G., Pinna G., Narducci D., and Pizzini S.: Short-range order of Zn and Cu in metaphosphate glasses by X-ray diffraction. *J. Non-Cryst. Solids* 111, 221-227 (1989).
- [31] Musinu A., and Piccaluga G.: An X-ray diffraction study of the short-range order around Ni(II), Zn(II) and Cu(II) in pyrophosphate glasses. *J. Non-Cryst. Solids* 192-193, 32-35 (1995).
- [32] Hoppe U., Walter G., Carl G., Neufeind J., and Hannon A. C.: Structure of zinc phosphate glasses probed by neutron and X-ray diffraction of high resolving power and by reverse Monte Carlo simulations. *J. Non-Cryst. Solids* 351, 1020-1031 (2005).
- [33] Bionducci M., Licheri G., Musinu A., Navarra G., Piccaluga G., and Pinna G.: The structure of a Zn(II) metaphosphate glass .1. The cation coordination by a combination of X-ray and neutron diffraction, EXAFS and X-ray anomalous scattering. *J. Phys. Sci.* 51, 1209-1215 (1996).
- [34] Walter G., Hoppe U., Vogel J., Carl G., and Hartmann P.: The structure of zinc polyphosphate glass studied by diffraction methods and <sup>31</sup>P NMR. *J. Non-Cryst. Solids*, 252-262 (2004).
- [35] Concas G., Congiu F., Manca E., Muntoni C., and Pinna G.: Mössbauer spectroscopic investigation of some iron-containing sodium phosphate glasses. *J. Non-Cryst. Solids*, 175-178 (1995).
- [36] Marasinghe G. K., Karabulut M., Ray C. S., Day D. E., Shumsky M. G., Yelon W. B., Booth C. H., Allen P. G., and Shuh D. K.: Structural features of iron phosphate glasses. *J. Non-Cryst. Solids* 222, 144-152 (1997).
- [37] Wagner M. S., and Castner D. G.: Characterization of Adsorbed Protein Films by Time-of-Flight Secondary Ion Mass Spectrometry with Principal Component Analysis. *Langmuir* 17, 4649-4660 (2001).
- [38] Wold S., Sjöström M., and Eriksson L.: PLS-regression: a basic tool of chemometrics. *Chemometrics and Intelligent Laboratory Systems* 58, 109-130 (2001).
- [39] Vickerman J. C.: Multivariate Data Analysis Techniques in Surface Analysis. in: Vickerman, J. C., (Ed.), *Surface Analysis - the Principal Techniques*, 1997, pp. 564-612.

## 7 Tribochemical properties of zinc polyphosphate glasses

In this chapter the results obtained exploring the tribochemical properties of zinc polyphosphate are presented and discussed.

In the first section (7.1), a sample-preparation protocol that allows the reproducible synthesis of zinc metaphosphate glasses for tribological testing is outlined. The tribological tests were performed by sliding steel balls on the metaphosphate discs, while the composition of the contact area in the wear track and on the balls has been monitored by small-area and imaging X-ray photoelectron spectroscopy (i-XPS).

The same approach was then applied in the following sections in order to investigate the effect of composition on the tribochemical behavior of bulk zinc polyphosphate glasses by considering two important variables:

- The effect of chain-length (Section 7.2)
- The effect of the counterpart material (Section 7.3)

The XPS analyses on the tribostressed zinc polyphosphates showed that the long-chain-length polyphosphates are depolymerized in the wear track as a consequence of a tribochemical reaction, while the composition of the short-chain-length polyphosphates remained unchanged after the tribological stress (Section 7.4). Comparing the results obtained changing the counterpart material (quartz instead of steel balls) it was observed that while the reaction of iron oxide with the polyphosphates certainly takes place and plays a role in the depolymerization of the samples under sliding conditions, on the other hand pressure and shear stress are also able to depolymerize the glass when a non-bearing iron-material (e.g. quartz) is used as counterpart. The composition of the wear track, in this case, is dependent on the applied load (Section 7.5).

All the glasses, independent of chain-length, were able to form analogous adhesive glassy transfer films on both steel and quartz balls, while lower friction coefficients and wear rates (Section 7.5) were measured when using the discs made of short-chain-length polyphosphates.

The results presented in section 7.1 have been published in [1].

## 7.1 Steel-versus-zinc metaphosphate tribopair: the establishment of a protocol for the assessment of the tribochemical properties of polyphosphate glasses

Steel ball versus zinc metaphosphate disc was the first tribopair investigated at the beginning of this work. Using this tribopair, a protocol for the tribological tests and the surface analysis of the mechanically stressed discs and balls was established (see also Section 3.4.2).

### 7.1.1 Tribological tests

The first tests were performed using one single ball (previously flattened during a running-in experiment on a steel disc) and moving it from one radius to the other on the same sample. A decrease in the friction with the order of the test, and independent of the applied load, was observed (Figure 7.1).

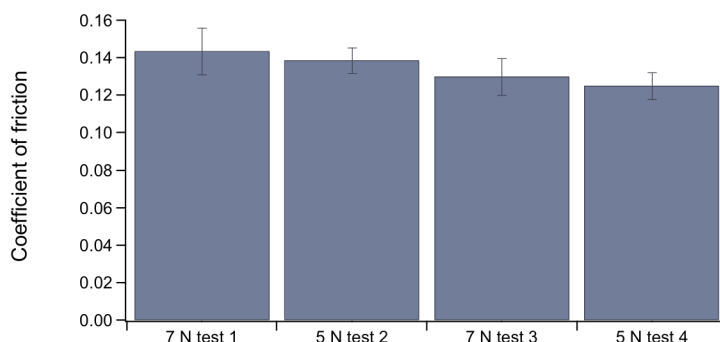


**Figure 7.1: Coefficient of friction (COF) measured during the sliding of a steel ball (after running-in on steel) on a bulk zinc metaphosphate glass disc in a pure PAO bath at room temperature with sliding speed of 0.5 mm/s and applying a normal load of 5 and 7N from reference [1]**

These findings suggest that during sliding the chemistry on the surface ball is changing. This change is able to affect both friction and wear. This is the reason why, in order to obtain reproducible data, a new ball was used for every test. The tests shown in Figure 7.2, Figure 7.4 and in all the results that will follow in both this chapter and the following one (Chapter 7 and Chapter 8) were run using a new ball for each new test on the different annuli. Also the comparison tests on the steel-versus-steel tribopair were carried out using the same protocol.

### 7.1.2 Steel-versus-zinc metaphosphate tribopair: friction and wear

In Figure 7.2 the values of the coefficient of friction at two different loads for steel-versus-steel and steel-versus-zinc metaphosphate tribopairs are shown (no



running-in in either case). No significant changes of friction were observed during a two-hour test. A small running-in effect was only observed in the first 500 mm. For this reason the average coefficient of friction has been calculated considering only the last 2000 mm of the test. The mean values and their standard deviations are reported in Figure 7.2.

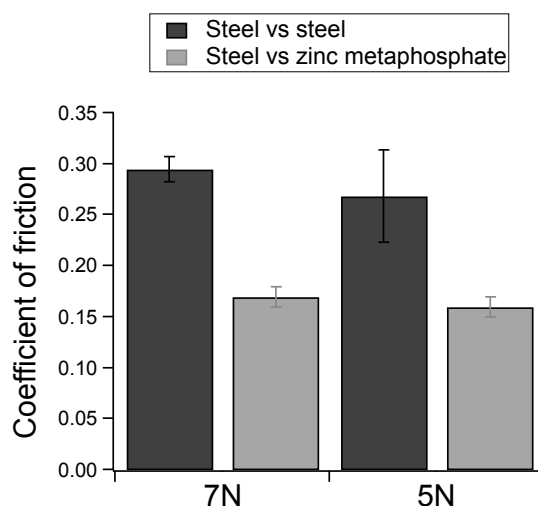


**Figure 7.2: Tribological results - comparison between steel-versus-steel and steel-versus-zinc-metaphosphate tribopairs**

The coefficient of friction was always lower in the case of the steel-versus-zinc-metaphosphate tribopair.

The 3D-topography of the flattened area on a steel ball after a tribological test with a zinc metaphosphate disc is reported in Figure 7.3 as an example.

A circular flattened area is formed on the ball as a consequence of wear. The wear rate of the balls was calculated from the flattened area on top of the balls, which was measured by means of optical microscopy. The wear rate was then calculated as worn volume divided by sliding distance (Figure 7.4).

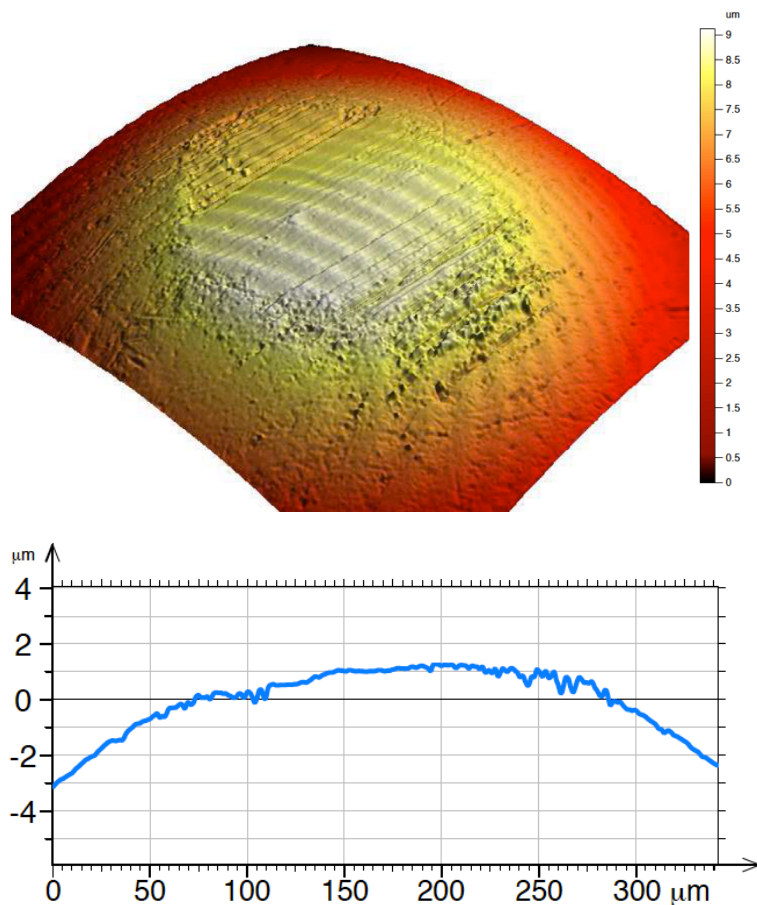


**Figure 7.3: 3D-Topography and profile of a steel ball after a tribological test (7N load) with a zinc metaphosphate disc obtained by white-light profilometry**

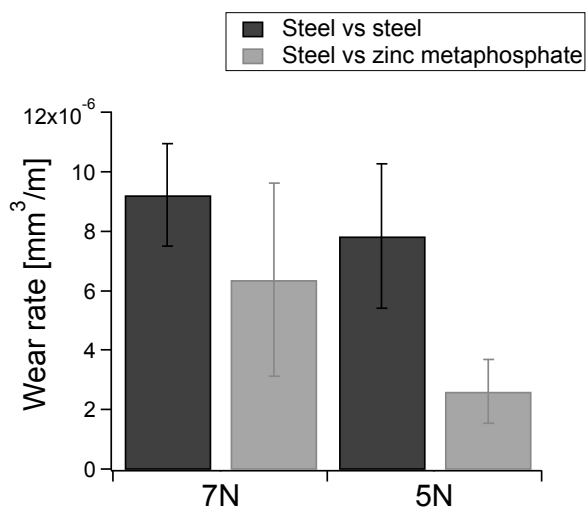


**Figure 7.4: Wear rate of the ball; comparison between steel-versus-steel and steel-versus-zinc-metaphosphate tribopairs**

The contact pressures (based on the area measured by the light microscope) were calculated and found to be around 200 MPa for the steel-versus-steel and 300 MPa for the steel-versus-metaphosphate tribopair. Compared to the steel-versus-steel tribopair, which exhibits only a slight dependence of the wear rate with the applied load within the experimental uncertainty, lower values were obtained for the steel-versus-metaphosphate tribopair with the lowest value measured for the experiment performed at 5 N.

The tribotacks on the discs were investigated with the light microscope (Figure 7.5): both the metallic samples appear drastically damaged while, on the other hand, on the zinc metaphosphate samples the damage is very limited for both the investigated loads. The dark large spots visible in Figure 7.5 b and c can be attributed to the debris originating from the ball and transferred to the disc.

The 3D-topography of a wear track on a zinc metaphosphate disc is also reported in Figure 7.6 as an example. The wear on the disc is very low and difficult to quantify because the presence of debris and transfer material can be observed on the wear track. For this reasons it was decided not to report the values of the wear rate on the discs.

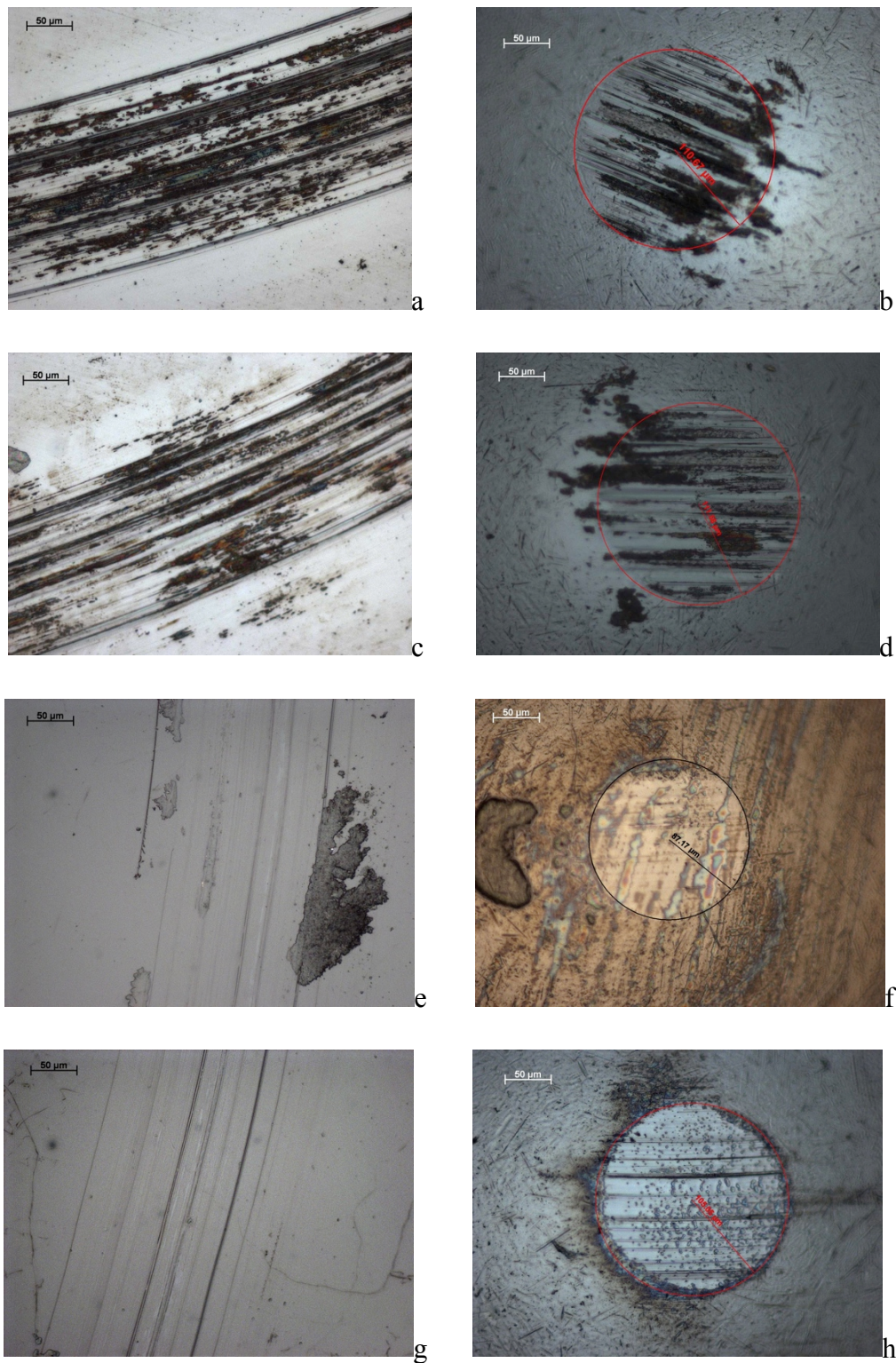


**Figure 7.5: Light microscopy image of the wear track on the disc and the contact area on the ball for the steel-versus-steel tribopair at 5 N(a, b) and 7N (c, d). Wear tracks on the disc and the contact area on the ball for the steel-versus-zinc-metaphosphate tribopair at 5 N(e, f) and 7N (g, h) from reference [1]**

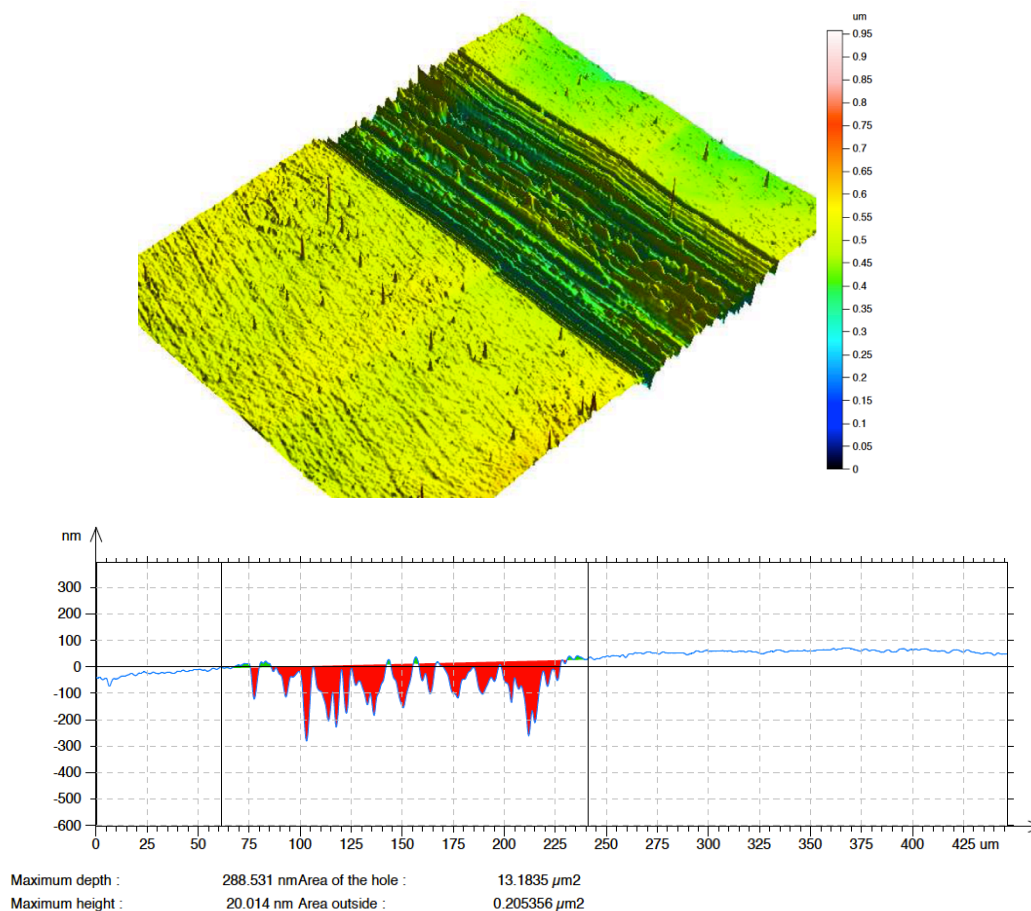


**Figure 7.6: 3D-Topography and profile of a wear track on a zinc metaphosphate disc after a tribological test at 7N normal load obtained by white-light profilometry**

### 7.1.3 Steel-versus-zinc-metaphosphate tribopair: XPS analysis of the balls

Small-area XPS and i-XPS were used in order to characterize the balls after the tribological tests. The maps in Figure 7.7 show the spatial distribution of the intensity of each element.

For each pixel a complete spectrum was acquired, the calculated intensity of each spectrum corresponding to the color in the map. The oxygen O1s signal was fitted using three different Gaussian-Lorentzian functions, one corresponding to the oxygen of the iron oxide (from the substrate) at 530.0 eV, one to the NBO at 532.3 eV (this component may also include iron oxides and hydroxides), and one to the BO at a BE 1.6 eV higher than the NBO peak. Three maps, corresponding to the three chemical states, were reconstructed using a linear-least-squares routine. The images show the presence of a uniform layer on the contact area, where zinc, phosphorus, bridging and non-bridging oxygen are present, while the signal of iron oxide is not detected. On the other hand, in the non-contact region only the oxide and NBO signal are present. The diameter of the contact area in the chemical maps, around 150 $\mu\text{m}$  for

the 5N test as shown in Figure 7.5, was comparable to that observed with the light microscope.

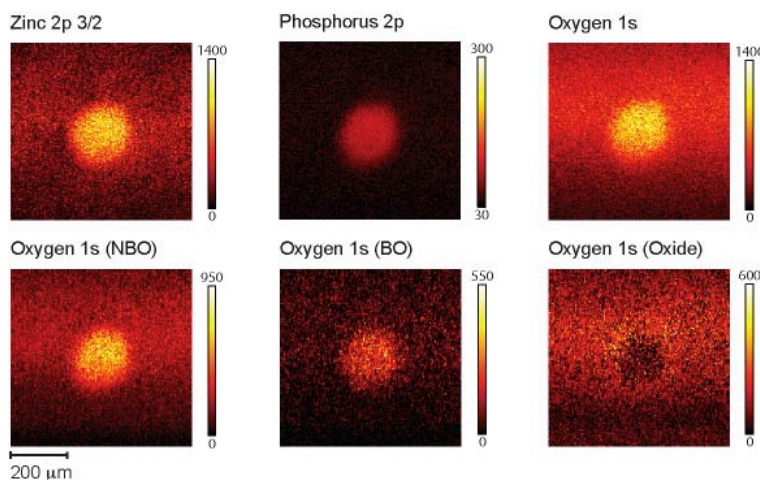


**Figure 7.7: i-XPS on the steel ball following the tribotests on zinc metaphosphate disc (load 5N). Each pixel on the map corresponds to a complete spectrum: the color is proportional to the intensity of the spectrum calculated as the area under the peak**

Small-area XPS was performed in three different locations (shown by a circle in in the SXI): inside, outside and at the border of the contact area (Figure 7.8). Also in this case the O1s spectra were curve fitted with three components, i.e. oxide, NBO and BO. In the oxygen 1s spectra of the contact area only the BO and NBO components are present, while the oxide component is not detected. Inside the contact area the iron 2p signal (Figure 7.8) is completely attenuated: the tribological films is so thick that it masks the underlying iron oxy-hydroxide. Considering that the information depth is estimated to be equal to  $3\lambda \cos(\theta)$ , where  $\lambda$  is the inelastic mean free path [calculated according with the parameters reported in Appendix A] equal to 2nm, and  $\theta$  is the emission angle equal to  $45^\circ$  in this experiment, the glassy layer is calculated to be at least thicker than 5 nm. One may assume that the hydroxides do not contribute to the oxygen signal and thus the component at 532.3 eV can only be assigned to the NBO signal. In this case the spectra can be used for calculating the composition of the transfer film. The value of the BO/NBO intensity ratio is found to be equal to 0.3, and thus the polyphosphate chain-length is calculated to be intermediate between a zinc pyrophosphate (BO/NBO of 0.2) and a zinc poly<sub>0.67</sub> (BO/NBO of 0.37, see also Table 5.1).

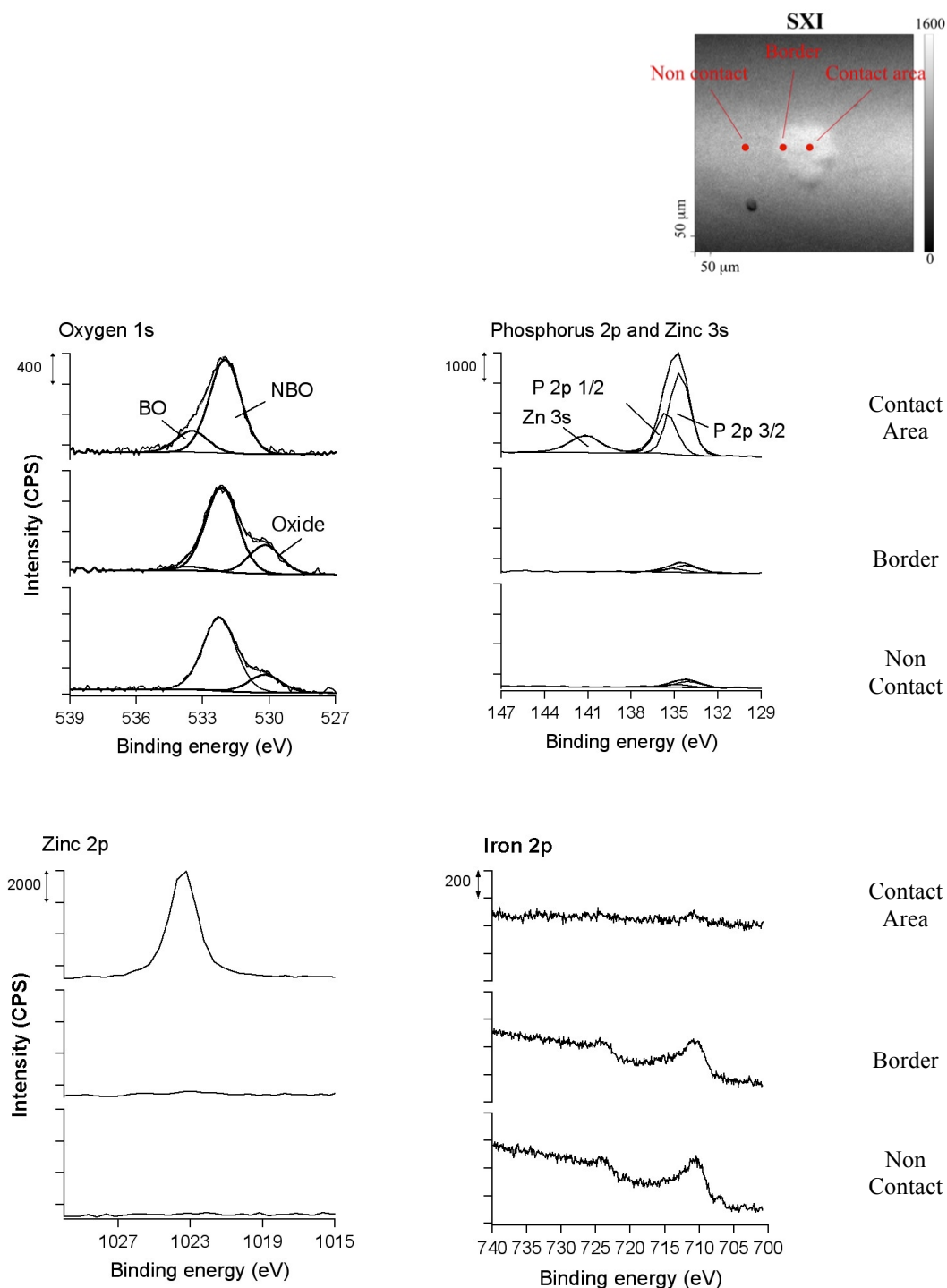


**Figure 7.8: Small-area XPS on the contact area of the ball after the tribotest**

The O1s spectrum acquired at the border of the contact area shows the presence of the iron oxide signal at lower BEs, together with the BO and NBO signals. In this position the phosphorus peak is present with lower intensity, while neither the Zn 2p nor the Zn 3p signals could be detected. In the non-contact region, the BO signal could no longer be detected.

The P2p signal is intense in the contact area (P 2p 3/2 was found at  $134.6 \pm 0.2$  eV). At the border and out-of-contact regions, however, this signal was very weak. The peak maximum of P2p<sub>3/2</sub> is shifted towards lower BEs:  $134.2 \pm 0.2$  eV at the border and at  $134.0 \pm 0.2$  eV in the non-contact region.

#### 7.1.4 Steel-versus-zinc metaphosphate tribopair: XPS analysis of the discs

The wear tracks on the discs were characterized by i-XPS, and small-area XPS spectra were acquired both inside and outside the tribotracks. The O 1s intensity map is shown in Figure 7.9.

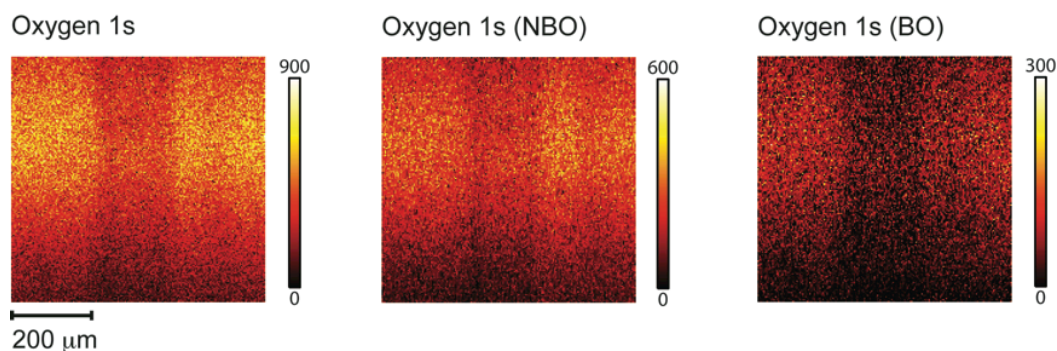


**Figure 7.9: i-XPS of the tribotrack on the zinc metaphosphate disc after tribological test (load 7N)**

As described in the previous section, the O 1s signal was curve fitted with the two characteristic signals of the polyphosphate glass: NBO at 532.3 eV and BO at 533.9 eV. The intensity of the total oxygen is lower inside the tribotrack, with the BO/NBO ratio being lower in the entire contact area.

From the quantitative analysis of the small-area XPS results (Figure 7.10), a BO/NBO ratio of  $0.33 \pm 0.05$  was obtained in the contact area compared to the  $0.41 \pm 0.05$  obtained in the non-contact area (same value obtained for the mechanically polished samples). The NBO signal is shifted from  $532.4 \pm 0.1$  to  $532.1 \pm 0.1$  eV. Also the P 2p signal is shifted towards lower BEs: the signal was found at  $134.7 \pm 0.1$  eV for the non-contact region and  $134.3 \pm 0.2$  eV inside the tribotrack. These results suggest that the glass is depolymerized within the contact area as a consequence of the tribological test (see also Table 7.1).

The Fe 2p peak is detected within the tribotrack, indicating a transfer of iron from the ball to the disc. The chemical state of iron is a mixture of oxides, hydroxides and, possibly, phosphates.



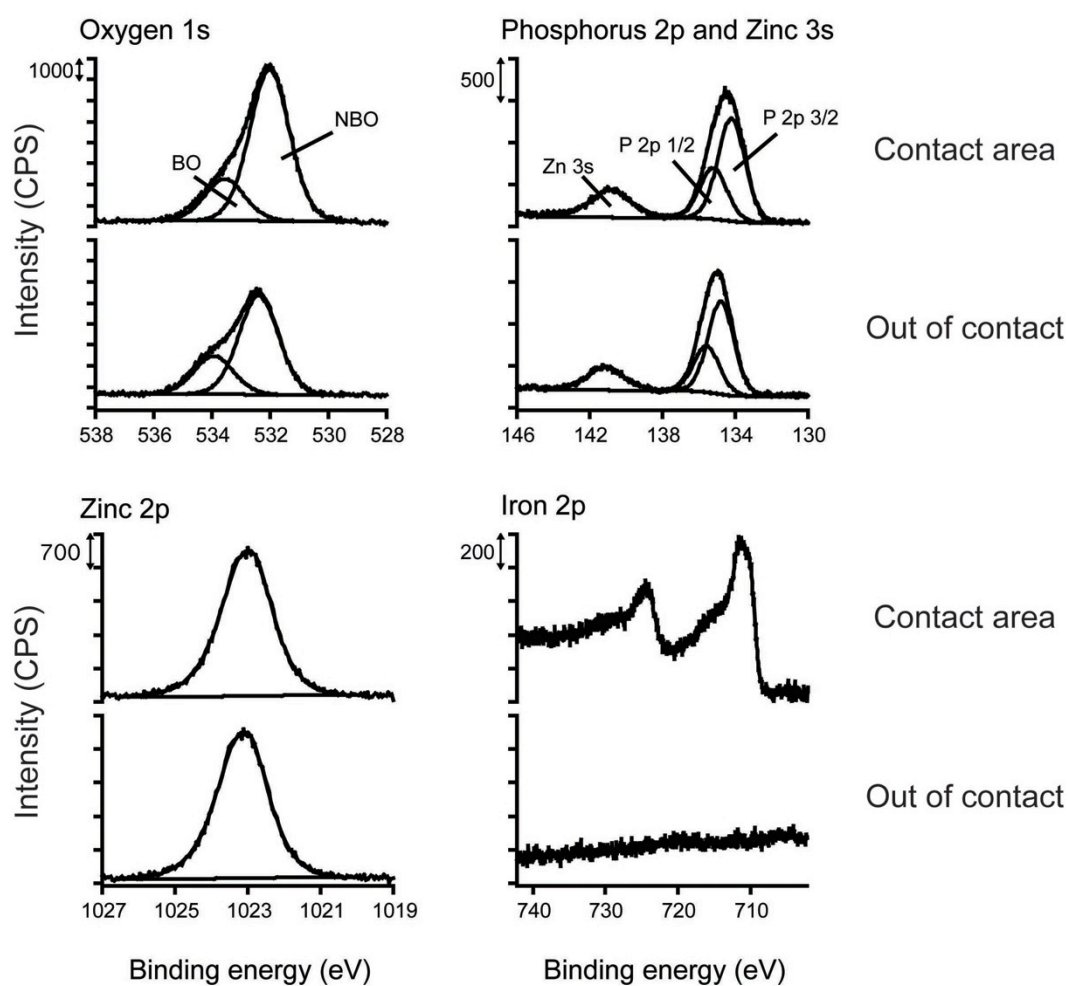


**Figure 7.10: High-resolution spectra on the zinc metaphosphate disc after tribological test (load 7N)**

## 7.2 Effect of the chain-length and of the counterpart material on the tribochemistry of bulk zinc polyphosphate glasses.

The protocol described in the previous section for the steel-versus-zinc-metaphosphate tribopair was applied to different chain-length zinc polyphosphate glasses and the results are reported in the following.

### 7.2.1 Steel-versus-zinc-polyphosphate tribopair: tribological tests

The synthesis and characterization of the glasses has been already reported and discussed in Chapter 4 and 5. Three different chain-length zinc polyphosphates have been investigated: zinc metaphosphate ( $[O]/[P] = 3$ ), already presented in the previous section), zinc poly<sub>0.67</sub> ( $[O]/[P] = 3.167$ ) and zinc pyrophosphate ( $[O]/[P] = 3.5$ ). The zinc orthophosphate composition ( $[O]/[P] = 4$ ) does not appear in this chapter because

only small and brittle glassy samples could be obtained, not suitable to be used for the tribological tests (see also Section 4.2).

The results of the tribological tests carried out sliding a steel ball against the zinc polyphosphates discs with different compositions are shown in Figure 7.11. The coefficient of friction appears to be constant with the sliding distance. A small running-in effect was observed in the first 500 mm. As already described in the previous section, the average coefficient of friction has been calculated considering only the last 2000 mm of the test thus assuming that after this period the ball reached a conformal shape with the disk. The coefficient of friction does not depend on the applied load (5N and 7N, see Figure 7.11), while its value changes with the chain-length of the polyphosphate sample.

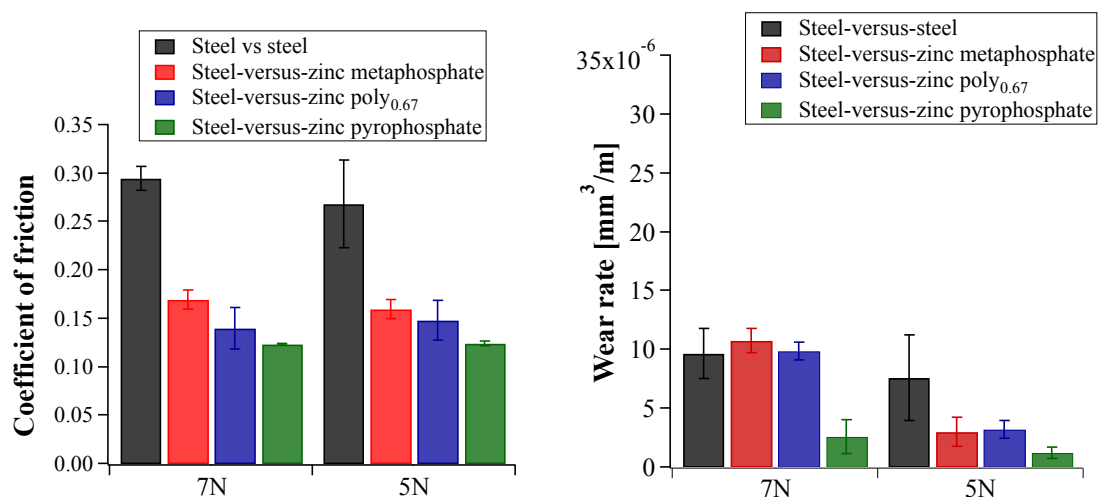


**Figure 7.11: Coefficient of friction (COF) and wear rate measured on the steel ball after sliding on bulk zinc polyphosphate disc with different chain-lengths in a pure PAO bath at room temperature; sliding speed of 0.5 mm/s and normal load of 5 and 7N**

The coefficient of friction was found to be  $0.16 \pm 0.1$  for the steel-versus-zinc metaphosphate,  $0.13 \pm 0.1$  for the steel-versus-zinc poly<sub>0.67</sub>, and  $0.12 \pm 0.1$  for the steel-versus-zinc-pyrophosphate tribopair.

The flattened areas on the balls were measured by means of light microscopy (see Figure 7.12) and using the average values it was possible to calculate the worn volume for each test. The average values of the wear rates for the steel balls, calculated as worn volume per sliding distance, are reported in Figure 7.11. The wear rate is lower in the case of shorter-chain-length polyphosphates and increases with increasing normal load for all compositions.

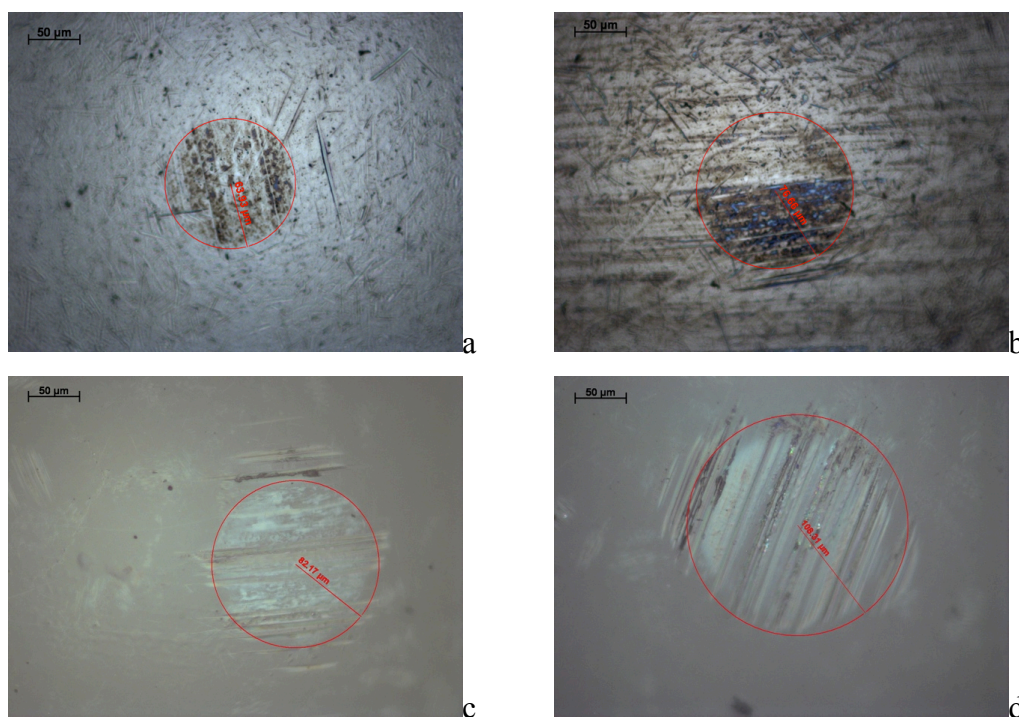


**Figure 7.12:** Light-microscope image of the contact area on the ball for the steel versus zinc pyrophosphate (a, b) and the quartz versus zinc pyrophosphate (c, d) at 5N (a, c) and 7N (b, d) normal load

### 7.2.2 Steel-versus-polyphosphate tribopair: XPS analysis of the polyphosphate disc

The tribostressed polyphosphate discs were analyzed by XPS; high-resolution spectra were acquired in both wear tracks and non-contact areas for comparison. An example of XPS spectra for a zinc pyrophosphate disc after a mechanical test applying a 5N load is presented in Figure 7.13, in which the spectra acquired inside and outside the contact area are directly compared.

The averaged BO/NBO intensity ratios for all the tests and compositions are listed in Table 7.1. The composition in the wear tracks at 5N and 7N loads was the same, and therefore the results in the table are the average of all tests. All quantitative results reported in Table 7.1 have been calculated using the experimental sensitivity factors calculated in Chapter 5, Table 5.6. The BO/NBO values are lower in the wear track compared to the values obtained in the non-contact area and this trend is common for the three compositions: from  $0.41 \pm 0.05$  in the non-contact region to  $0.33 \pm 0.05$  in the wear track for zinc metaphosphate, from  $0.29 \pm 0.04$  to  $0.24 \pm 0.05$  for zinc poly<sub>0.67</sub> and from  $0.18 \pm 0.04$  to  $0.14 \pm 0.05$  for zinc pyrophosphate.

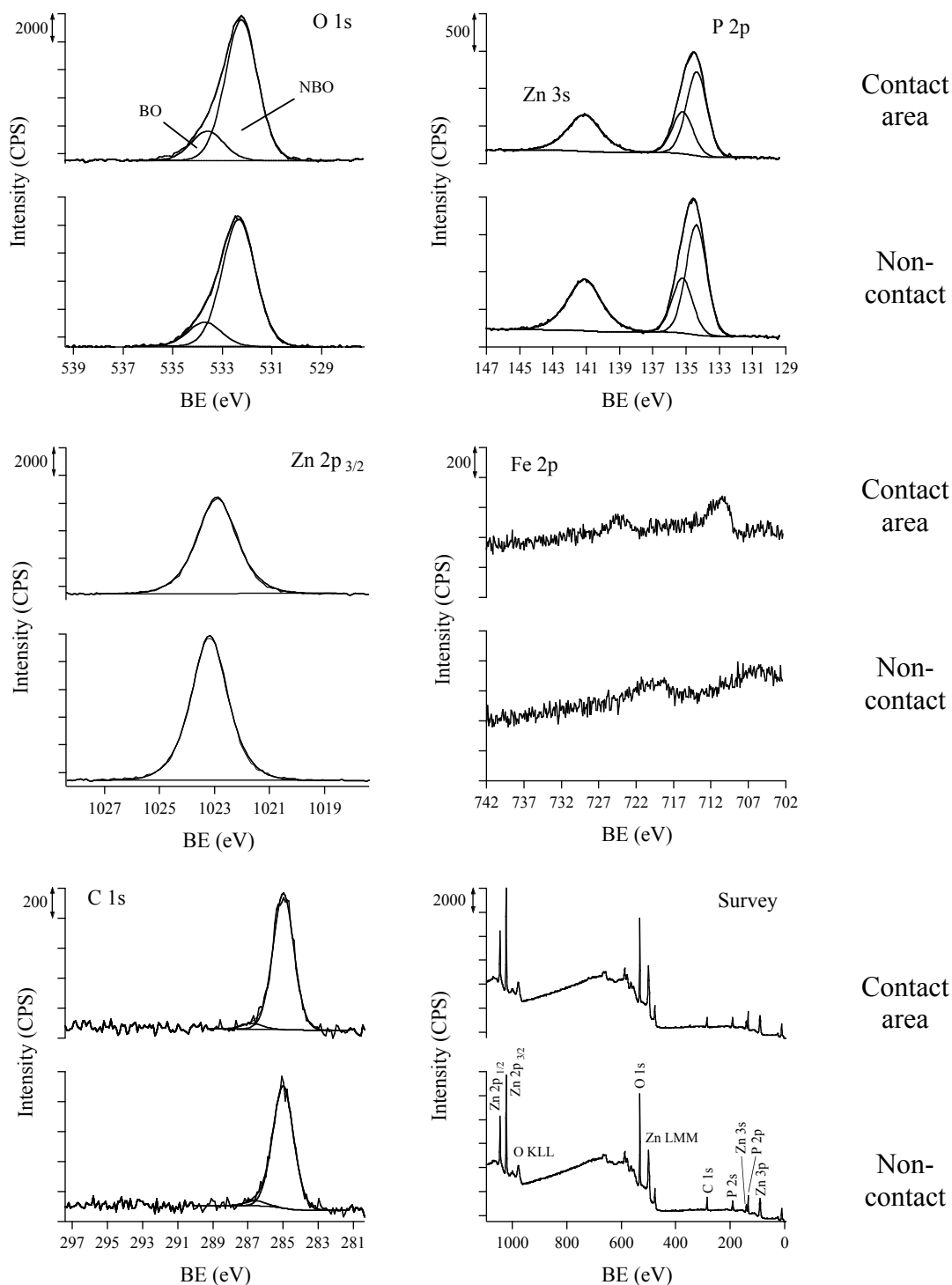


**Figure 7.13: High-resolution XPS spectra outside and inside of the tribotrack on the zinc pyrophosphate disc after the tribological test with a steel ball at 5N normal load**

The Zn 3s BE value, 141.0 eV, was found to be constant with composition while the P 2p<sub>3/2</sub> peak position shifts (Table 7.1) [2]. In order to minimize possible uncertainties due to the fact that the method here used for referencing all signals was based on the contamination layer, also when the C1s was very small, and under the assumption that the steady-state static charge exhibited by the specimen surface was

reached (no differential charging), the difference between the position of the Zn 3s signal and the P 2p<sub>3/2</sub> has been calculated for all tests (Table 7.1). For all samples this parameter is higher in the contact region than outside the contact: Zn 3s - P 2p BE difference increases from 6.32±0.04 eV in the non-contact region to 6.48±0.09 eV in the wear track for the case of zinc metaphosphate, from 6.51±0.04 eV to 6.65±0.05 eV for the zinc poly<sub>0.67</sub>, and from 6.73±0.01 eV to 6.80±0.03 eV for zinc pyrophosphate.

**Table 7.1: XPS analysis of discs with different chain-length polyphosphates after tribological tests with steel balls. For each composition the table shows the values obtained analyzing inside the wear track (in contact) and outside the wear track (non-contact). The calculated values (from stoichiometry) for the [P]/[Zn] and [O]/[P] intensity ratios are respectively 2 and 3 for metaphosphate, 1.5 and 3.2 for poly<sub>0.67</sub>, 1 and 3.5 for pyrophosphate**

	<i>Zinc metaphosphate</i>		<i>Zinc poly<sub>0.67</sub></i>		<i>Zinc pyrophosphate</i>	
	<i>Non-contact</i>	<i>Wear track</i>	<i>Non-contact</i>	<i>Wear track</i>	<i>Non-contact</i>	<i>Wear track</i>
<b><i>BO/NBO</i></b> <b><i>Intensity ratio</i></b>	0.41±0.05	0.33±0.05	0.29±0.04	0.24±0.05	0.18±0.04	0.14±0.05
<b><i>Zn 3s - P 2p</i></b> <b><i>BE difference</i></b> <b><i>(eV)</i></b>	6.32±0.04	6.48±0.09	6.51±0.04	6.65±0.05	6.73±0.01	6.80±0.03
<b><i>[P]/[Zn]</i></b> <b><i>Intensity ratio</i></b>	2.1±0.2	2.0±0.2	1.6±0.1	1.5±0.1	1.1±0.1	1.1±0.1
<b><i>[O]/[P]</i></b> <b><i>Intensity ratio</i></b>	3.0±0.3	3.5±0.3	3.2±0.2	3.6±0.4	3.4±0.2	3.8±0.2
<b><i>Modified</i></b> <b><i>Auger</i></b> <b><i>parameter</i></b>	2008.90 ±0.07	2009.1 <sub>1</sub> ±0.1 <sub>4</sub>	2008.9 <sub>4</sub> ±0.1 <sub>2</sub>	2009.0 <sub>9</sub> ±0.1 <sub>2</sub>	2009.15 ±0.09	2009.27 ±0.09

The Auger Zn LMM signal has been also acquired and the values of the modified Auger parameter,  $\alpha'$ , seems to exhibit a trend towards higher values inside the tribotracks (see Table 7.1).

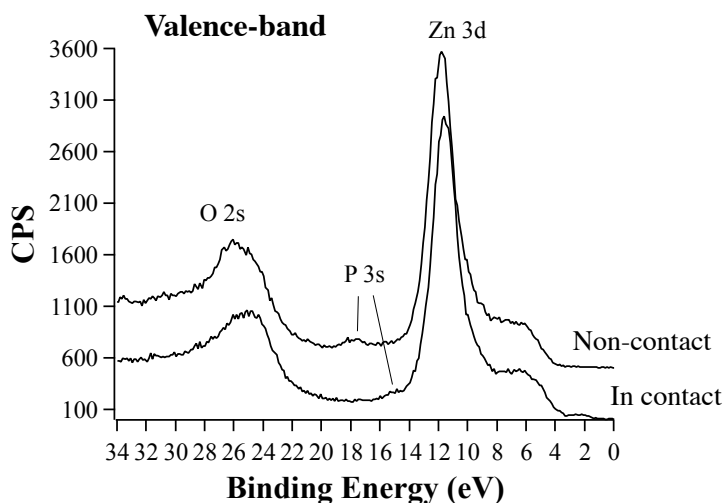


**Figure 7.14: High-resolution XPS spectra of the valence band outside and inside the tribotrack on the zinc metaphosphate disc after the tribological test with a steel ball at 7N normal load**

In agreement with the previous results, the valence band region also shows the depolymerization of the glass inside the tribotrack: going from long towards shorter chain lengths, the position of the P 3s peak shifts towards higher BEs [2]. The zinc metaphosphate exhibited the largest shift, 2.5 eV, and a spectrum has been reported in Figure 7.14.

The iron peak was detected in the wear track as a result of transfer of material from the steel ball to the disc. The position and line shape of the carbon peak does not change in the wear track and, as shown in Figure 7.13, there are no additional elements in the survey spectrum.

The values of the [O]/[P] intensity ratio (Table 7.1) are also higher in the contact region: [O]/[P] increases from  $3.00 \pm 0.03$  in the non-contact region to  $3.50 \pm 0.03$  in the wear track for the case of zinc metaphosphate, from  $3.2 \pm 0.2$  to  $3.6 \pm 0.4$  for zinc poly<sub>0.67</sub>, from  $3.4 \pm 0.2$  to  $3.8 \pm 0.2$  for zinc pyrophosphate. The Zn 2p<sub>3/2</sub> signal, at 1022.9 eV, was also curve fitted and used to calculate the [P]/[Zn] intensity ratio; this parameter did not show any relevant change in the tribostressed areas for any of the samples (Table 7.1).

### 7.2.3 Steel-versus-zinc-polyphosphate tribopair: XPS analysis of the steel ball

The high-resolution spectra and chemical-state maps for a steel ball after a tribological test with a pyrophosphate disc at the normal load of 5N are shown in Figure 7.15 and Figure 7.16, while the corresponding optical image is reported in Figure 7.12a. The spectra were acquired in three different areas (shown by a circle in the SXI), in the center of the contact, at the border and in the non-contact area.

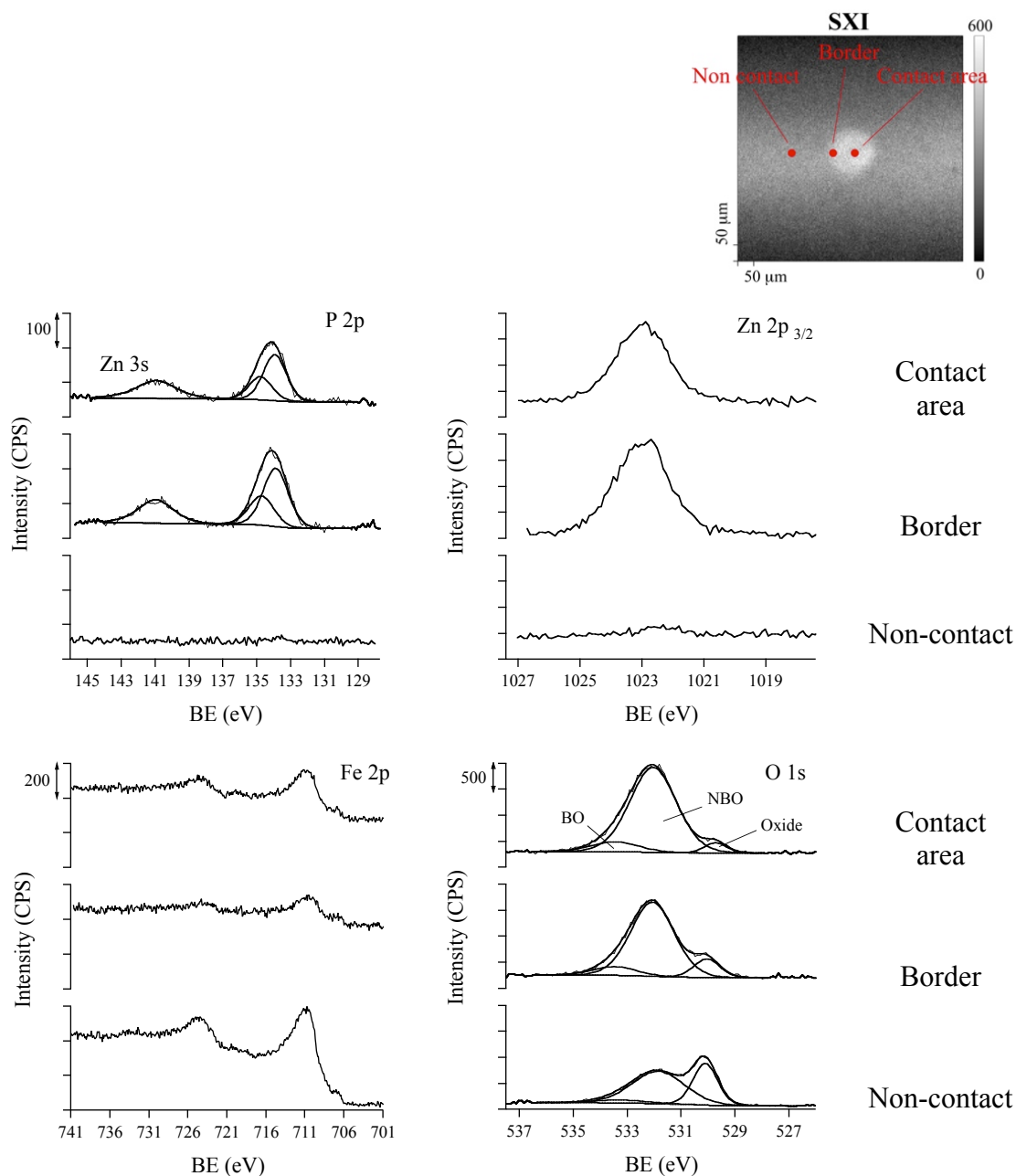


**Figure 7.15: Small-area XPS on the contact, border and non-contact area of the steel ball after the tribological test (at 5N normal load) on a zinc polyphosphate disc**

Phosphorus, P2p, zinc, Zn3s and Zn2p<sub>3/2</sub> signals were present in the contact area, indicating the presence of zinc polyphosphate inside the contact area. Looking at the maps in Figure 7.16 the transfer-film area appears in a round shape with a radius of about 60 μm. This value is consistent with the 64 μm measured on the optical image. The high-resolution spectra show that the intensity of the phosphorus and zinc signals is higher at the border than in the center of the area. Moreover, the iron peak is more attenuated at the border than in the center of the area, suggesting that the thickness of the transfer film is thicker in that area.

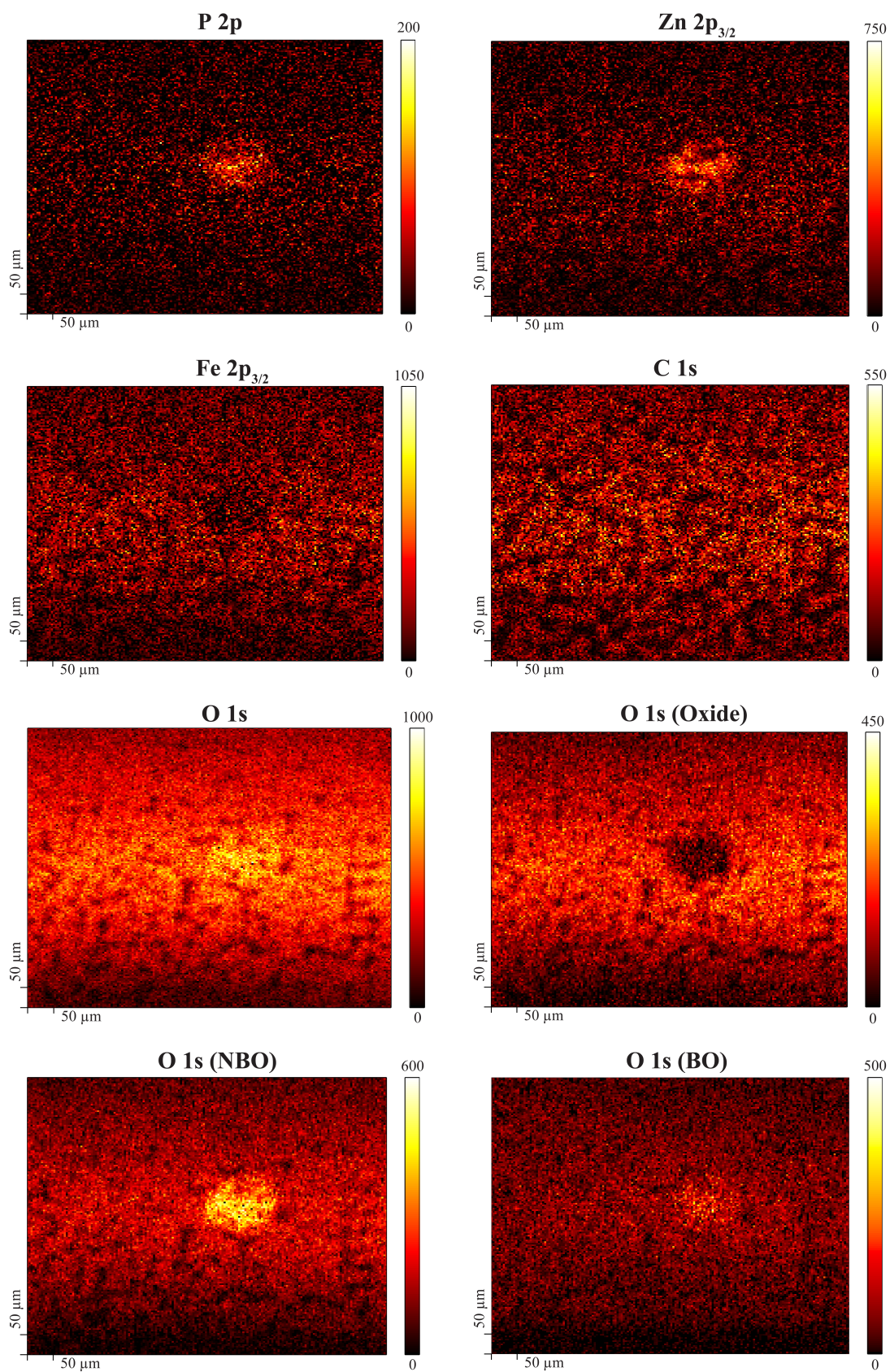


**Figure 7.16:** i-XPS on the contact area of the steel ball after the tribological test (at 5N normal load) on a zinc pyrophosphate disc



The oxygen 1s signal presented three components: a first one at 530.0 eV assigned to oxide species; a second one at 532.2 eV assigned to the NBO in the polyphosphate glass and the hydroxides (these two chemical states are overlapping in the BE scale and cannot be resolved in the spectra); a third and last one at 534.0 eV assigned to the BO of the polyphosphate. Using a linear-least-squares routine the O 1s map was converted into three maps corresponding to the three chemical states described above (Figure 7.16). Further confirming the previous results, the maps show that the BO signal from the polyphosphate glass is present only in the contact area, while the oxide signal is detected only outside.

The map of the carbon 1s signal was acquired to show that there are no areas of preferential charging on the map. The spectra extracted from the transfer film area were compared with the spectra extracted from the outer area (not shown): the position and line shape of the C 1s signal were unchanged.

### 7.3 Quartz-versus-zinc polyphosphate tribopair

In order to investigate the effect of the presence of iron on the depolymerization of the polyphosphate glasses under mechanical stress, quartz was chosen as counterpart material in the experiments presented in this section.

#### 7.3.1 *Quartz-versus-zinc polyphosphate tribopair: tribological tests*

Quartz was chosen for its chemical stability but its brittleness turned out to be a problem for the tribological tests. Often some quartz particles detached from the ball as a consequence of brittle rupture and were lost in the contact area (see Figure 7.17). This led to different final values for the contact areas with irregular geometries that explain the non-reproducibility of the tests. As in the case of steel-versus-polyphosphates tribopairs, a running-in effect is observed in the first 500 mm, after which the coefficient of friction reaches a plateau value. Only one contact area corresponding to one of the tests performed on sample 1 (in red at the bottom in Figure 7.18) shows a flat contact area. The friction coefficient measured in this test is comparable to that of steel-versus-zinc pyrophosphate.

Given the difficulty to obtain reproducible results, the wear and friction behavior of these tribopairs will not be compared with the previous results.

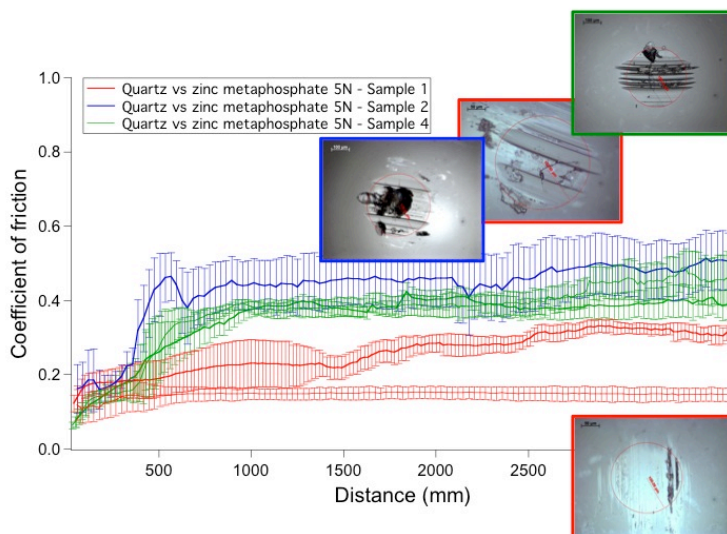


**Figure 7.17: Coefficient of friction (COF) obtained for the quartz-versus-metaphosphate tribopair and light microscope images of the contact area on the balls (for samples 1 and 4 the test was repeated on two different annuli with the same conditions and are reported in the graph as two different curves with the same color)**

### 7.3.2 Quartz-versus-zinc polyphosphate tribo-pair: XPS analysis of the polyphosphate disc

The data concerning zinc metaphosphate and zinc pyrophosphate discs after the tribological tests with quartz balls are summarized in Table 7.2.

For the case of zinc metaphosphate the BO/NBO values were lower in the wear track compared to the values obtained in the non-contact area and this time, in contrast to the steel-versus-polyphosphate tribopairs, the value at 5N,  $0.37 \pm 0.05$ , was different than the value at 7N normal load,  $0.30 \pm 0.05$ . The value of the BO/NBO intensity ratio in the case of pyrophosphate, on the other hand, did not exhibit any significant change. Also the Zn 3s – P 2p BE difference, which does not change in the case of zinc pyrophosphates, increases from  $6.30 \pm 0.01$  eV in the non-contact region, to  $6.35 \pm 0.1$  eV in the 5 N wear track and to  $6.42 \pm 0.08$  eV in the 7N wear track for the case of zinc metaphosphate. The same trend was exhibited by the modified Auger parameter,  $\alpha'$ , which was found to shift towards higher values inside the tribotracks for zinc metaphosphate (see Table 7.2).

A low-intensity Si 2p peak revealed the presence of a transfer of quartz from the ball to the wear track. The values of the BO/NBO and the [O]/[P] intensity ratios (Table 7.2) might be influenced by the presence of a small O 1s peak ( $533.3 \pm 0.1$  eV on sputtered clean quartz, not shown), not easy to discriminate from the NBO and BO peaks. As in the case of the steel-versus-polyphosphates tribopairs, the [P]/[Zn] intensity ratio did not show any relevant change in the tribostressed areas (Table 7.2).

The reference spectra of the sputtered cleaned quartz ball can be found in Appendix C.

	<i>Zinc metaphosphate</i>			<i>Zinc pyrophosphate</i>		
	<i>non-contact</i>	<i>5N</i>	<i>7N</i>	<i>non-contact</i>	<i>5N</i>	<i>7N</i>
<b><i>BO/NBO</i></b> <i>Intensity ratio</i>	0.45±0.03	0.37±0.05	0.30±0.05	0.20±0.01	0.21±0.03	0.24±0.01
<b><i>Zn 3s – P 2p</i></b> <i>BE difference (eV)</i>	6.30±0.01	6.3 <sub>5</sub> ±0.1	6.42±0.08	6.75±0.01	6.76±0.03	6.78±0.03
<b><i>[P]/[Zn]</i></b> <i>Intensity ratio</i>	1.8±0.1	1.8±0.1	1.9±0.1	1.1±0.1	1.1±0.2	1.1±0.1
<b><i>[O]/[P]</i></b> <i>Intensity ratio</i>	3.5±0.1	3.4±0.1	3.7±0.2	3.7±0.2	3.6±0.4	4.0±0.1
<b><i>Modified Auger</i></b> <i>parameter</i>	2008.71 ±0.06	2008.8 <sub>6</sub> ±0.16	2009.18 ±0.06	2009.19 ±0.07	2009.11 ±0.06	2009.17 ±0.09

**Table 7.2: XPS analysis of discs with different chain-length polyphosphates after tribological test using quartz balls. For each composition the table shows the values obtained analyzing inside the 5N wear track (5N), inside the 7N wear track (7N) and outside the wear track (non- contact)**

### 7.3.3 Quartz-versus-zinc-polyphosphate tribo-pair: XPS analysis of the quartz balls

The high-resolution spectra for the quartz ball after a tribological test against a zinc pyrophosphate disc at 7N are shown in Figure 7.18 and the corresponding chemical state maps and optical image can be found respectively in Figure 7.19 and Figure 7.12d. As described before for the steel balls, the spectra were acquired in the center, at the border and outside of the contact area (shown as a circle in the SXI).

Also on the quartz balls, the phosphorus, P2p, zinc, Zn3s and Zn2p<sub>3/2</sub> signals were present inside the contact area, indicating the presence of a glassy transfer film. The Si 2p peak, found at 103.9±0.1 eV, was almost completely attenuated by the presence of the transfer film. The O 1s peak, present in the non- contact spectrum, can be assigned to quartz (see Figure 7.18). Conversely, in the first two points, where the polyphosphate transfer film is present, the O 1s peak was curve-fitted with two components, BO and NBO, at 533.7 eV and 532.2 eV, respectively, although a superimposition with a low-intensity quartz peak cannot be excluded.

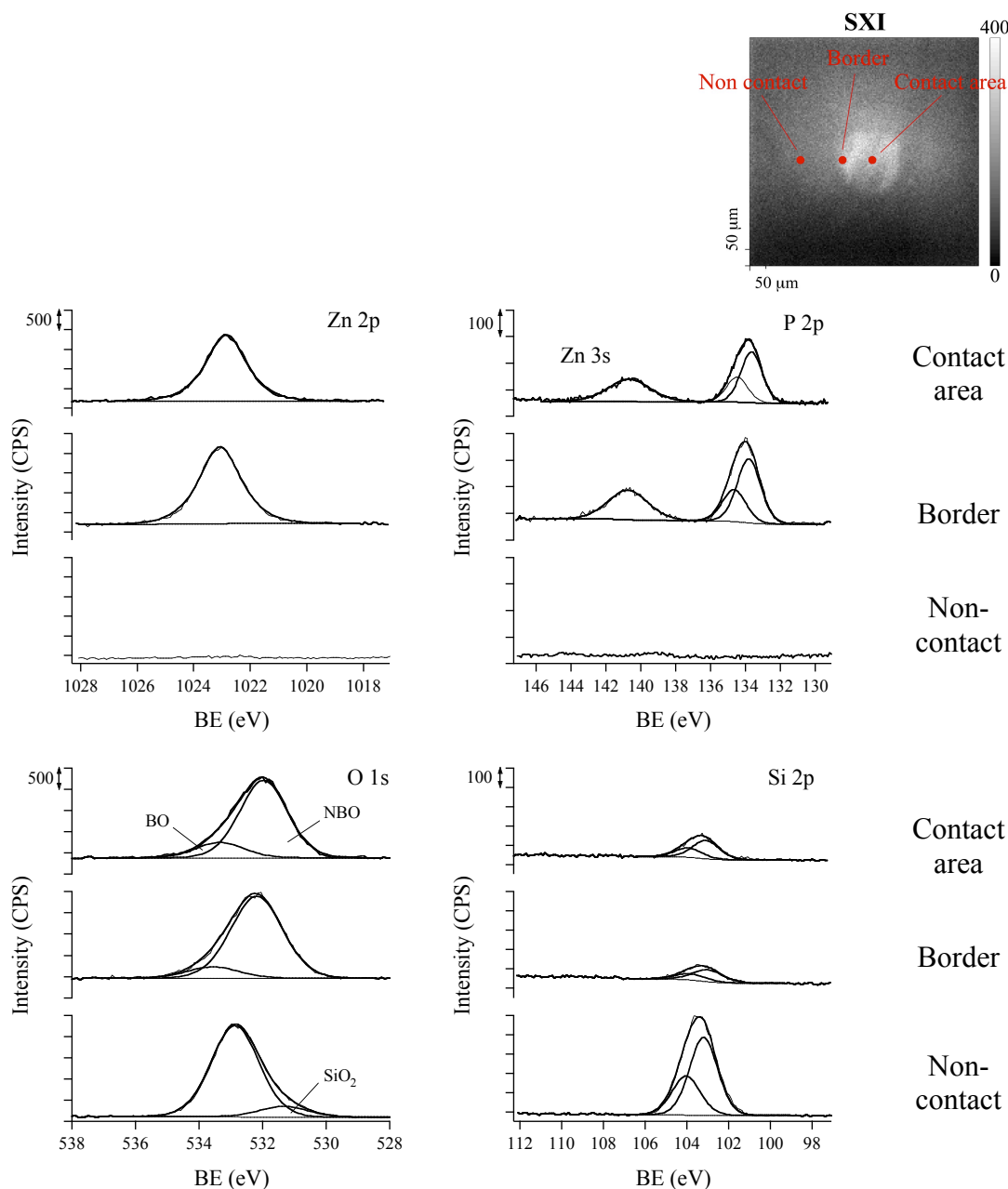


**Figure 7.18: Small area XPS on the contact, border and non-contact area of the quartz ball after the tribological test with a zinc pyrophosphate disc at 7N normal load.**

For this reason it was not possible to convert the O 1s map into a chemical-state map, as for the steel balls. However the P 2p, Zn 2p<sub>3/2</sub>, and Si 2p maps in Figure 7.19, together with the high-resolution spectra described above, are showing the presence of an adhesive polyphosphate transfer film over the entire contact area. As in the case of steel, the films appear to be thicker at the border than in the center of the contact area because the Si 2p peak is less attenuated in the central region.

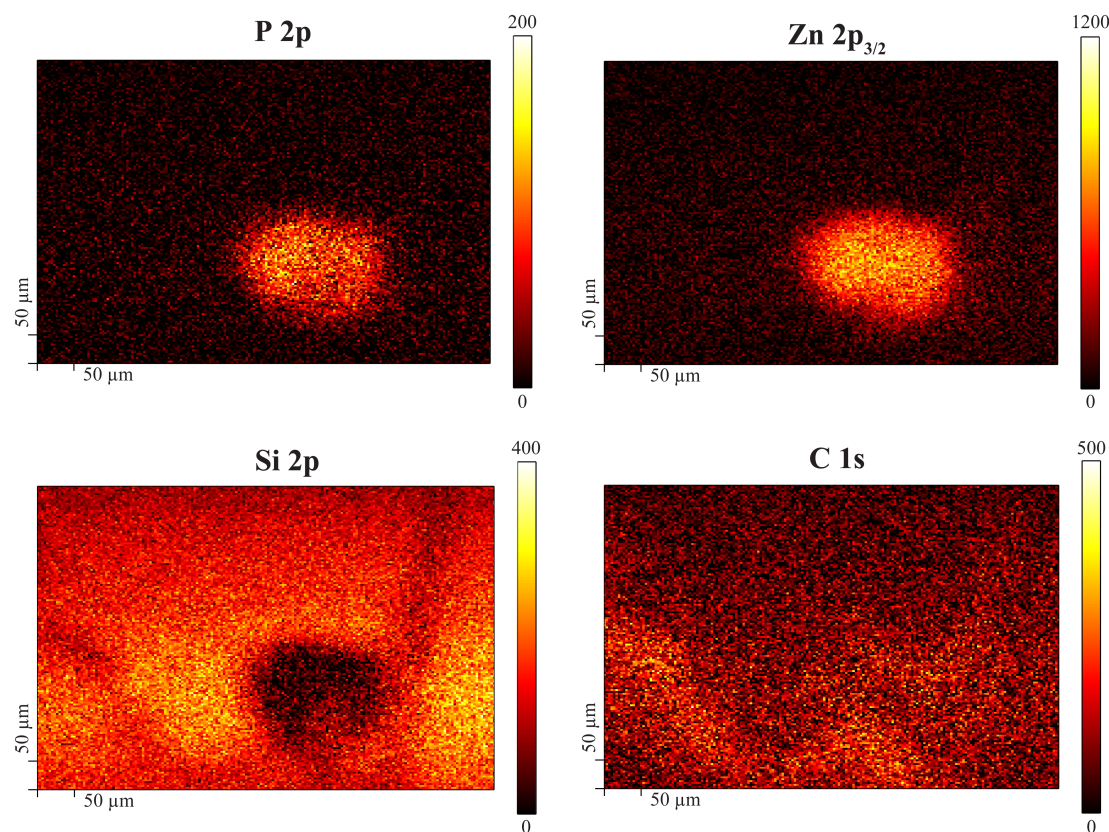


**Figure 7.19: i-XPS on the contact area of the quartz ball after the tribological test against a zinc pyrophosphate disc (Load = 5N)**

#### **7.4 The tribochemical reaction of depolymerization at the steel-versus-zinc-metaphosphate interface**

The depolymerization reaction of zinc polyphosphates in the presence of iron oxide was first described by Martin [3]. The presence of shorter chain lengths inside the tribotracks compared to the non-contact regions of ZnDTP tribofilms was also previously observed [4; 5], but in such complex analytical systems it is very challenging to identify the tribochemical reactions involved. In the first section of this chapter, bulk amorphous zinc metaphosphate glasses have been tested and, by means of a surface-sensitive analytical tool, XPS, it was possible to directly investigate the tribochemical reactions taking place under sliding conditions. Those results will be discussed in the following.

##### *7.4.1 Steel-versus-zinc-metaphosphate tribopair: composition of the transfer film*

The imaging-XPS of the ball (figure 7.7) shows a very clear contrast between the contact area and the non-contact area: a transfer film is present in the contact area of the ball and it is mainly composed of zinc polyphosphates. The diameter of the area showing the transfer film, around 150 μm, is approximately the same as that of the flattened area on the ball (figure 7.4). The detailed spectra acquired in the center of

the contact area (figure 7.8) show the absence of an iron signal. Therefore, at this point the transfer film is thick enough to completely attenuate the iron (the layer is therefore thicker than 6 nm). At this point the signal of the O1s spectrum at 530.0 eV, assigned to iron oxide, is absent too; the two components used for the curve fitting correspond to the characteristic signals of polyphosphates, i.e. the BO and NBO peaks (figure 7.8). The BO/NBO ratio was found to be 0.3 within the contact area (table 7.1). The average chain-length is thus shorter than the metaphosphate composition of the disc before the tribological test. In the non-contact area, the zinc signal and the BO signal are not detected: iron oxide is mainly present together with a very low-intensity phosphorus peak (figure 7.8). At the border of the contact area, a small peak assigned to the BO was detected together with the oxide peak, which means that a thinner layer of glass is present. However neither zinc signals, Zn 2p and Zn 3s, could be detected. The only possible cation in this case is iron, i.e. the presence of iron phosphate is indicated. Moreover the phosphorus peak is shifted towards lower BE values suggesting the presence of shorter chain lengths at the border of the area and, therefore, of a lateral compositional gradient in the transfer film.

#### *7.4.2 Steel-versus-zinc-metaphosphate tribopair: composition of the wear track on the disc*

The tribostressed area is clearly visible in the O 1s map (Figure 7.9). Qualitatively it is already possible to observe in the chemical-state maps that the intensity of the BO signal is lower inside the contact area. Comparing the high-resolution spectra inside and outside the contact (figure 7.10), the presence of a shorter-chain-length polyphosphate inside the tribotrack is supported by the lower BO/NBO value and the chemical shift of the phosphorus peak (table 7.1). In Figure 7.20 these results are compared with the data obtained from reference zinc polyphosphate glasses of different chain lengths. The observed depolymerization was very reproducible, despite the inhomogeneous appearance of the tribotrack in the optical microscope, where it was possible to observe islands of material transferred from the ball to the disc. The iron signal due to this transfer film was detected inside the tribotrack and suggests the presence of a mixture of iron oxides and phosphates.

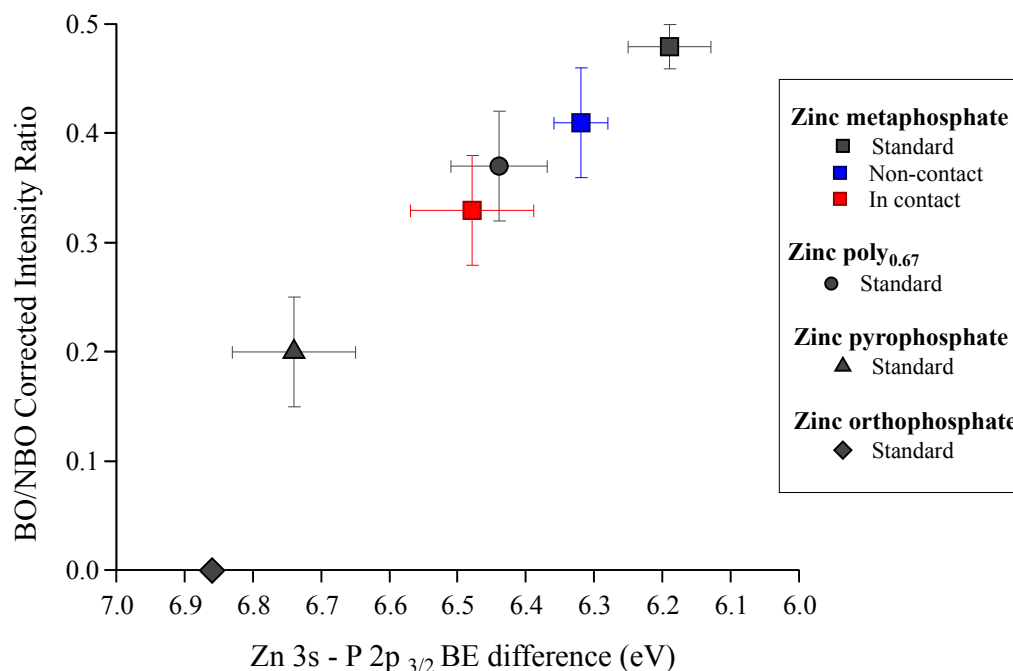
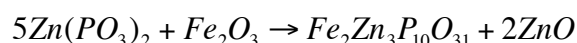


**Figure 7.20: BO/NBO versus Zn 3s - P 2p BE difference: comparison between reference and disc after tribological tests**

#### 7.4.3 Proposed reaction at the ball/disc interface

A reaction mechanism for the tribochemical reaction between iron oxide and zinc polyphosphates was first proposed by Martin [3]. According to the HSAB (hard-and soft-acid-base) principle, a hard base reacts preferentially with a hard acid and a soft base with a soft acid [6]. The formation of mixed zinc and iron glass is therefore the result of the reaction between the hard-base  $\text{PO}_4^{3-}$  with the hard-acid  $\text{Fe}^{3+}$ . As an example, the reaction between metaphosphate and iron(III)oxide is reported.

#### Equation 7.1



This reaction could be activated by high shear stress and would explain the shortening of the polyphosphate chain and the formation of iron phosphate. This reaction normally takes place only at high temperatures (above 1300 K). This means that enough energy has to be available for the reaction in the tribological system.

### 7.5 Effect of chain-length and role of iron on the tribochemical reaction of depolymerization of zinc polyphosphate glasses

In the previous section, it was demonstrated that zinc metaphosphate under sliding conditions against steel is depolymerized. In section 7.2, two more compositions with shorter chain-lengths were examined and compared to the case of zinc metaphosphate. A full characterization of these samples and a method for discriminating different chain-lengths polyphosphates by XPS can be found in

Chapters 5 and 6. It has been shown that the combined use of the BO/NBO intensity ratio, the Zn 3s-P 2p<sub>3/2</sub> difference, the modified Auger parameter and the valence-band region, when available, allows the determination of the sample average chain-length. For this reason, in the following discussion not only the BO/NBO intensity ratio and the Zn 3s-P 2p<sub>3/2</sub> difference, but also the modified Auger parameter (Table 7.1 and Table 7.2) and the valence-band region (Figure 7.14) will be examined.

### 7.5.1 Reaction of depolymerization: effect of chain-length

The change in average chain-length,  $n$ , of the samples before and after the tribological tests against steel balls can be monitored on the BO/NBO versus Zn 3s-P 2p<sub>3/2</sub> graph in Figure 7.21. The Zn 3s-P 2p<sub>3/2</sub> difference has been used to calculate the average “ $n$ ” because it is less affected by the presence of contamination than the BO/NBO ratio and therefore more suitable to tribological samples (Chapter 6).

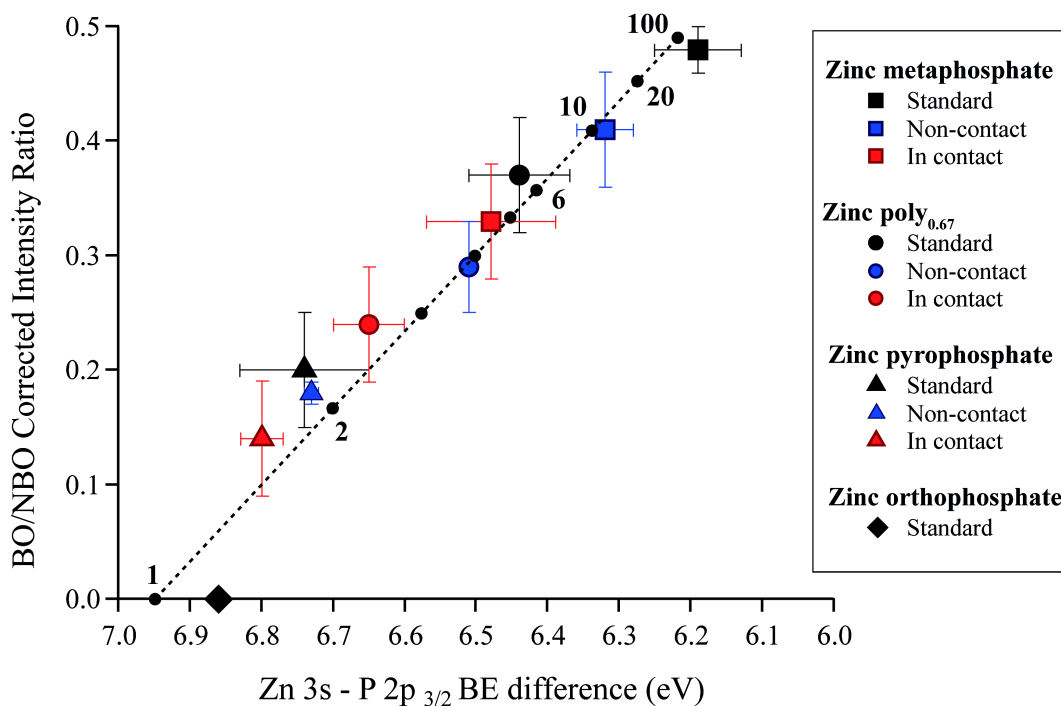


**Figure 7.21: BO/NBO ratio versus Zn 3s – P2p<sub>3/2</sub> BE difference of zinc meta-, poly-, and pyrophosphate discs after tribotest using steel balls**

For the case of metaphosphate,  $n$  is reduced from ca. 13 to 5 after the tribological stress, from 3.9 to 2.4 in the case of poly<sub>0.67</sub>, and stays almost constant in the case of pyrophosphate (from 2.0 to 1.9). Uncertainties in the use of this method are strongly dependent upon the composition, because the correlation between the Zn 3s-P 2p<sub>3/2</sub> and the BO/NBO is exponential: for a Zn 3s-P 2p<sub>3/2</sub> of 6.32±0.04 (zinc metaphosphate in the non-contact region)  $n$  can lie in between 19 and 8 while for a Zn 3s-P 2p<sub>3/2</sub> of 6.8±0.1 (zinc pyrophosphate after tribological stress)  $n$  is included between 1.1 and 2.0 (see also section 6.1.2).



The trend is confirmed by the values of the modified Auger parameter (table 7.1, 7.2), which shift towards higher values in the tribostressed area. The observed shifts are more pronounced for the metaphosphates and small for zinc pyrophosphates. A further proof of the tribochemical reaction is the shift of the P 3s peak in the valence band. In Figure 7.14, the case of metaphosphate, which shifts by 2.5 eV, is shown as an example.

The activation energy for the depolymerization reaction is provided by the tribological stress. The longer phosphate chain-lengths are stabilized by a delocalization of the electrons involved in the covalent bond. The bond length increases with increasing chain-length and, as a result, the P-O-P bond can be more easily broken by the effect of shear stress. In fact the average chain length of metaphosphate is halved by the tribological stress, while in the case of the pyrophosphate n remains almost unchanged.

#### *7.5.2 Role of iron in the tribochemical reaction of zinc polyphosphate glasses*

It has been shown that iron oxide can react at low temperatures with zinc polyphosphates in the presence of high pressure and shear stress. Using a different material, in this case quartz, as a counterpart in the tribological tests can clarify the effect of pressure and shear stress alone on the tribochemistry of zinc polyphosphates.

The BO/NBO versus Zn 3s-P 2p<sub>3/2</sub> graph in Figure 7.22 shows that in the tribologically stressed regions, the calculated BO/NBO ratios are affected by the presence of the quartz transferred from the ball. The O1s signal of SiO<sub>2</sub> is at 533.4±0.1 eV and thus cannot be resolved in the O 1s spectrum: the data points measured inside the tribotracks, in fact, are not lying on the line that describes the variation of the average chain-length n for zinc polyphosphates (Section 6.1.2).

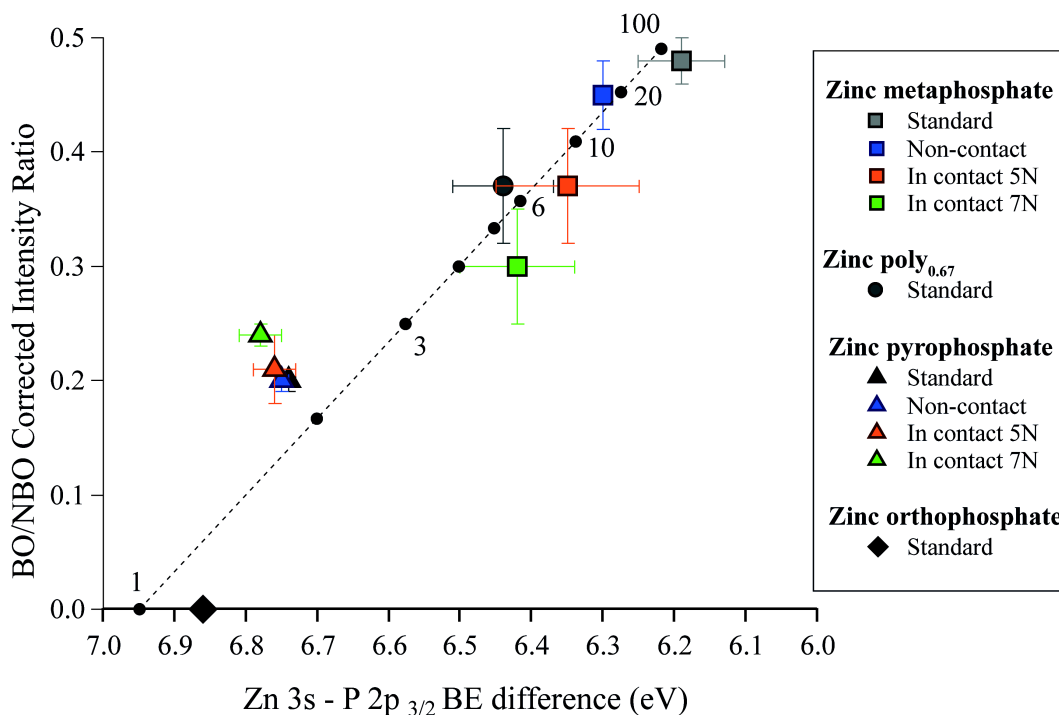


**Figure 7.22: BO/NBO ratio versus Zn 3s – P2p<sub>3/2</sub> BE difference of zinc meta-, poly-, and pyrophosphate discs after tribotest using quartz balls**

Therefore, also in this case, the only Zn 3s-P 2p<sub>3/2</sub> difference was used to estimate  $n$ . While in the test with the steel balls the composition in the tribotracks was not dependent upon the applied load, in the tests with the quartz balls the applied load influenced the composition of the tribofilm. In the case of zinc metaphosphate the average chain-length varies from 14 in the non-contact region to 9 for the 5N wear track and ca. 6 in the 7N wear track. This is confirmed by the values of the modified Auger parameter, which is increasing by 0.15 eV from the non-contact region to the 5N tracks and by 0.47 eV from the non-contact region to the 7N tribotrack (table 7.2). The zinc pyrophosphate sample, however, does not show any significant change in composition.  $n$  is 2 for both the non-contact region and the 5N wear track, and 1.9 in the 7N wear track. It is evident that pressure and shear stress are causing the depolymerization of the long polyphosphate chains.

### 7.5.3 Formation and functionality of the transfer film

The formation of a glassy transfer film on the steel ball contact area is able to reduce friction and prevent wear (Section 7.1). The tribological tests showed that the friction coefficient, for all the steel-versus-zinc-polyphosphate tribopairs, was always lower than in the case of their steel-versus-steel counterparts. The friction coefficient shows a trend towards smaller values for the shorter chain-lengths (Figure 7.11). Also the wear rate on the ball exhibits the same trend with the composition. A transfer film was found after each test, regardless of the phosphate chain-length. The steel-versus-

zinc-pyrophosphate tribopair shows the lowest wear rate value and an example of the corresponding transfer film is given in figure 7.6. The ex-situ analysis of the transfer film of pyrophosphate resembled those formed by the other polyphosphates: the only difference being the size of the flattened area because the worn volume was lower.

The interpretation of these findings has to take into account that the process that leads to the transfer film formation is a dynamic one and that in this investigation, part of the transfer film might have been lost during the rinsing steps, necessary prior the XPS analyses. *In situ* approaches in tribology are still at a pioneering stage, but very interesting results on dry friction have been published by Singer et al. [7]. Monitoring the transfer film of diamond-like nanocomposites on sapphire, many third-body processes have been identified: thickening, thinning, and loss of transfer film [7]. It has also been observed that the wear of the center of the transfer film is the beginning of the thinning process [7]. In this work, both the images and the small-area XP spectra provided evidence that the transfer film was thinner in the center than in the rest of the contact area. This suggests that a similar dynamic behavior can be assigned to the transfer film of polyphosphate glasses on steel. The reasons for the different behavior with the different polyphosphate chain-lengths could be related to the different mechanical and rheological properties of the transfer film material. In this work hardness and Young modulus of bulk zinc polyphosphates have been found to be dependent upon the chain-length. The highest values of hardness and reduced modulus (Section 4.2, Figure 4.7 and Figure 4.9) were measured for the short-chain-length polyphosphates, which are also showing the lowest wear-rate values. The transfer film is formed by very small wear particles, which are detached from the polyphosphate disc, and their properties could be very different from those of the bulk materials. Size, shape, structure of the particles will influence their rheological behavior. For example, the ability of the particles to form a 'compact' layer under the effect of normal load and shear stress, also called 'cohesion' [8; 9], will determine if the behavior of the transfer film will be solid- or fluid-like [10]. In fact, all the attempts to use phosphate powders as antiwear additives failed to reproduce the antiwear behavior of ZnDTPs [11; 12]. The same transfer film could also show a completely different behavior depending on the geometry of the contact for example, or simply at different loads or temperatures. A satisfactory method for the determination of such properties has not been developed yet. Even the use of techniques such as nanoindentation would already disturb the investigated layer [8]. It is now commonly accepted that the third body behavior is governing friction and wear in dry contacts [8; 9; 13], and it can be proposed that the same phenomena also plays an important role in boundary lubrication. For these reasons, the development of new techniques for *in situ* tribological measurements is necessary, to shed a light into the boundary lubrication wear mechanisms.

Many previous publications about ZnDTP hypothesize that the formation of mixed iron and zinc polyphosphate, as a consequence of the reaction of iron oxide with zinc polyphosphates, can promote the formation and adhesion of the polyphosphate tribofilm on the steel surface [14-16]. The quartz balls after the tribotests have been analyzed, in order to ascertain the ability of zinc polyphosphates to form adhesive transfer films on a different substrate. A transfer film was found on the quartz balls for all the chain-length polyphosphates, suggesting that the adhesion of the transfer film can take place also on materials not containing iron. The formation of phosphosilicate compounds has been documented at high temperature by Massiot et al [17]. The Si 2p signal in Si-O-P bond was detected in the XPS spectrum at 1 eV distance towards lower BEs from the Si-O-Si signal found at 104.7 eV [17]. A typical Si 2p spectrum measured in a zinc metaphosphate wear track after sliding against quartz is reported in Figure 7.23, in comparison with the same region acquired on the clean ball before the tribotest. The two spectra are similar and no evidence of the formation of Si-O-P bonds can be found.

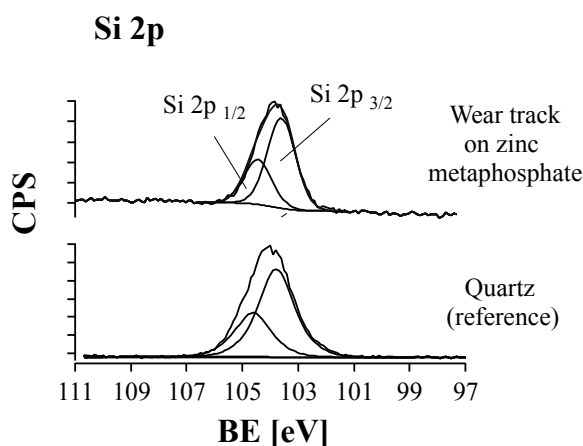


**Figure 7.23: High-resolution XP-Si 2p spectra acquired on a clean quartz ball in comparison with the Si 2p spectrum acquired inside of the wear track on the zinc metaphosphate disc after the tribological test with a quartz ball at 7N normal load**

Quartz detached as a consequence of wear and brittle rupture on the ball is transferred and embedded in the polyphosphate discs but does not react with the substrate.

The role played by tribochemical reactions, by the presence of iron oxide and by the transfer film formation in the antiwear mechanism of polyphosphate glasses and of antiwear tribofilms will be discussed in detail in Chapter 9.

## 7.6 Summary

A protocol for tribological tests on different chain-length polyphosphate samples has been established.

When sliding a steel ball onto a zinc metaphosphate disc, a glassy transfer film is formed on the ball. This film turned out to be able to reduce friction and prevent further wear on the ball.

A depolymerization of the polyphosphate glass was observed in the tribotracks present on the zinc metaphosphate discs. The material transfer from the ball to the disc resulted in the presence of iron in the tribostressed area on the discs. A tribochemical reaction between zinc metaphosphate and iron oxide at the ball/disc interface has been proposed. This leads to the formation of iron phosphate and causes the depolymerization of the glass

Extending the investigation to shorter-chain-length polyphosphates, it was observed that the tribochemical reaction of depolymerization takes place on the long-chain-length polyphosphate (zinc metaphosphate and poly<sub>0.67</sub>) wear tracks, while the composition of the short-chain-length samples remains almost unchanged after sliding. When an inert counter-face (quartz balls) is sliding against the long-chain length glasses the final composition in the wear track is dependent upon the applied load: the higher the applied load, the shorter the chain-length in the wear track. The composition of the short chain-length samples remains unchanged. These results proved that the depolymerization of the glass can also occur as a consequence of high pressure and shear stress without the presence of iron.

The shorter-chain-length polyphosphates exhibit lower friction coefficients and wear rates compared to the long chain-length samples and the formation of a glassy adhesive transfer film on the steel contact area suggests a third-body mechanism with the polyphosphates acting as a solid lubricant.

## References

- [1] Crobu M., Rossi A., Mangolini F., and Spencer N. D.: Tribology of Bulk Zinc Metaphosphate Glasses. *Tribol. Lett.* 39, 121-134 (2010).
- [2] Crobu M., Rossi A., Mangolini F., and Spencer N. D.: Chain-length identification in zinc polyphosphate glasses using Time of flight secondary ion mass spectroscopy and X-ray photoelectron spectroscopy. *Analytical and Bioanalytical Chemistry*, (2011).
- [3] Martin J.: Antiwear mechanisms of zinc dithiophosphate: a chemical hardness approach. *Tribol. Lett.* 6, 1-8 (1999).
- [4] Heuberger R., Rossi A., and Spencer N. D.: Pressure Dependence of ZnDTP Tribological Film Formation: A Combinatorial Approach. *Tribol. Lett.* 28, 209-222 (2007).
- [5] Canning G. W., Suominen Fuller M. L., Bancroft G. M., Kasrai M., Cutler J. N., De Stasio G., and Gilbert B.: Spectromicroscopy of tribological films from engine oil additives. Part I. Films from ZDDP's. *Tribol. Lett.* 6, 159-169 (1999).
- [6] Pearson R. G.: *Chemical hardness* Wiley, New York (1997).
- [7] Scharf T. W., and Singer I. L.: Monitoring Transfer Films and Friction Instabilities with In Situ Raman Tribometry. *Tribol. Lett.* 14, 3-8 (2003).
- [8] Descartes S., and Berthier Y.: Rheology and flows of solid third bodies: background and application to an MoS<sub>1.6</sub> coating. *Wear* 252, 546-556 (2002).
- [9] Iordanoff I., Berthier Y., Descartes S., and Heshmat H.: A Review of Recent Approaches for Modeling Solid Third Bodies. *Journal of Tribology* 124, 725-735 (2002).
- [10] Hou K., Kalousek J., and Magel E.: Rheological model of solid layer in rolling contact. *Wear* 211, 134-140 (1997).
- [11] Gauvin M., Dassenoy F., Belin M., Minfray C., Guerret-Piecourt C., Bec S., Martin J. M., Montagnac G., and Reynard B.: Boundary lubrication by pure crystalline zinc orthophosphate powder in oil. *Tribol. Lett.* 31, 139-148 (2008).
- [12] Pawlak Z., Yarlagadda P. K. D. V., Frost R., and Hargreaves D.: The mechanical characteristics of phosphate glasses under high temperature and friction-induced cross-linking processes. *Journal of Achievements in Materials and Manufacturing Engineering* 37, 458-465 (2009).
- [13] Singer I. L.: Mechanics and chemistry of solids in sliding contact. *Langmuir* 12, 4486-4491 (1996).
- [14] Spikes H.: The History and Mechanisms of ZDDP. *Tribol. Lett.* 17, 469-489 (2004).
- [15] Gellman A., and Spencer N.: Surface chemistry in tribology. *Proceedings of the Institution of Mechanical Engineers, Part J: Journal of Engineering Tribology* 216, 443-461 (2002).
- [16] Nicholls M. A., Norton P. R., Bancroft G. M., Kasrai M., Do T., Frazer B. H., and De Stasio G.: Nanometer scale chemomechanical characterization of antiwear films. *Tribol. Lett.* 17, 205-216 (2004).
- [17] Massiot P., Centeno M. A., Carrizosa I., and Odriozola J. A.: Thermal evolution of sol-gel-obtained phosphosilicate solids (SiPO). *J. Non-Cryst. Solids* 292, 158-166 (2001).

## 8 Tribochemistry of iron and mixed zinc and iron polyphosphate glasses

In this chapter the tribochemical properties of iron and mixed zinc-iron-polyphosphates are investigated and discussed.

High friction and wear are observed in the case of iron polyphosphate. I-XPS carried out on the tribologically stressed balls showed that some phosphate was transferred from the disc to the ball and deposited outside the contact area. However, with the addition of zinc to the composition of the glasses, the friction and wear behavior is similar to that of zinc polyphosphates (Section 8.2) and a glassy transfer film is found in the contact area of the balls.

The effect of the counter-ion on the tribochemical properties of polyphosphates is discussed in Section 8.3.

### 8.1 Steel-versus-iron-polyphosphate tribopair

The iron-containing polyphosphate glasses turned out to be very brittle and difficult to polish. The polishing process itself introduced macroscopic (up to 1 mm) defects on the surface. Those samples were not suitable for tribological testing. This effect was more pronounced with increasing iron content. For this reason it was possible to only test the iron poly<sub>0.33</sub> samples.

#### 8.1.1 Steel-versus-iron-poly<sub>0.33</sub> tribopair: friction and wear

In Figure 8.1 it can be observed that the coefficient of friction (COF) measured upon sliding a steel ball on the iron poly<sub>0.33</sub> disc does not change as a function of sliding distance, excluding some running-in effects in the first 500 mm.

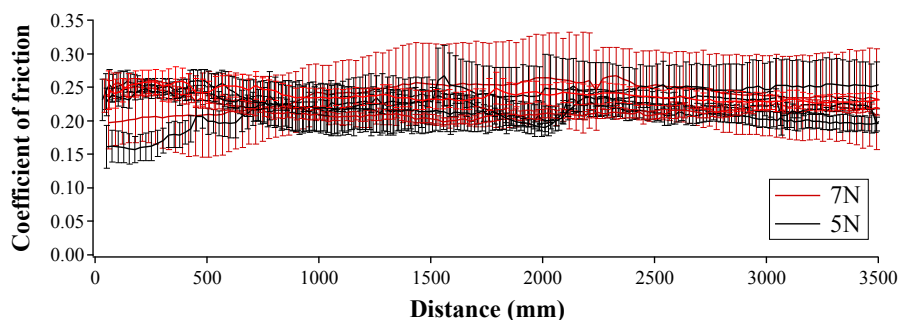


**Figure 8.1: COF (averaged on every turn and reported with its experimental error) versus sliding distance for the steel-versus-iron poly<sub>0.33</sub> tribopair at 5 and 7N of normal load and 30 mm/min of sliding speed**

The average coefficients of friction for the steel-versus-iron poly<sub>0.33</sub> are reported in Figure 8.2 in comparison with the steel-versus-steel and the steel-versus-zinc metaphosphate tribopairs. While the COF measured on the iron poly<sub>0.33</sub> disc is higher than that on zinc metaphosphate and lower than steel, the wear rate measured on the steel ball (see Figure 8.2 and Figure 8.3) is much higher for the iron poly<sub>0.33</sub> than for either zinc metaphosphate or steel discs.

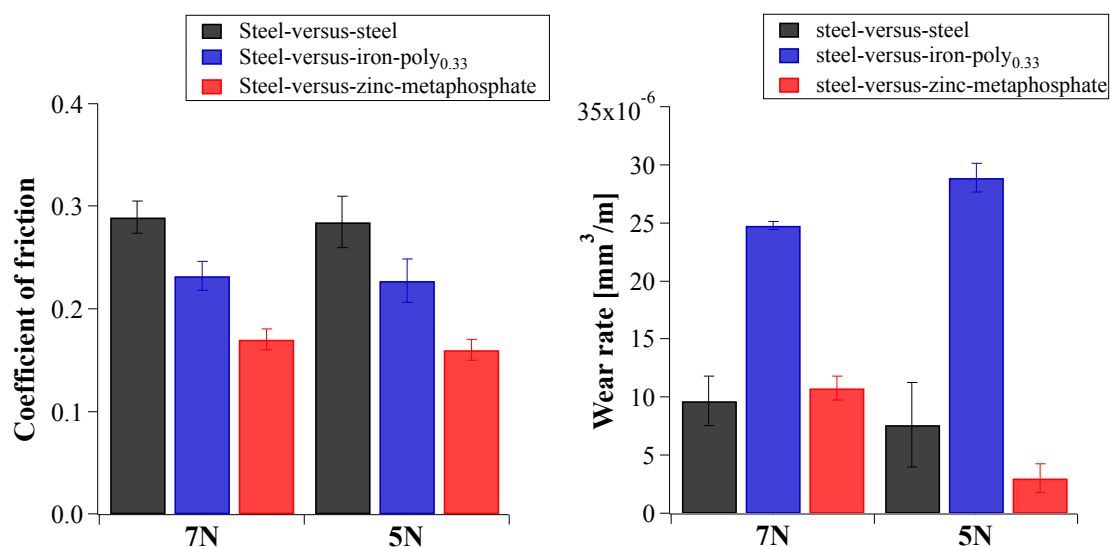


**Figure 8.2: Tribological results: comparison between steel-versus-steel, steel-versus-zinc-metaphosphate and steel-versus-iron-poly<sub>0.33</sub> tribopairs**

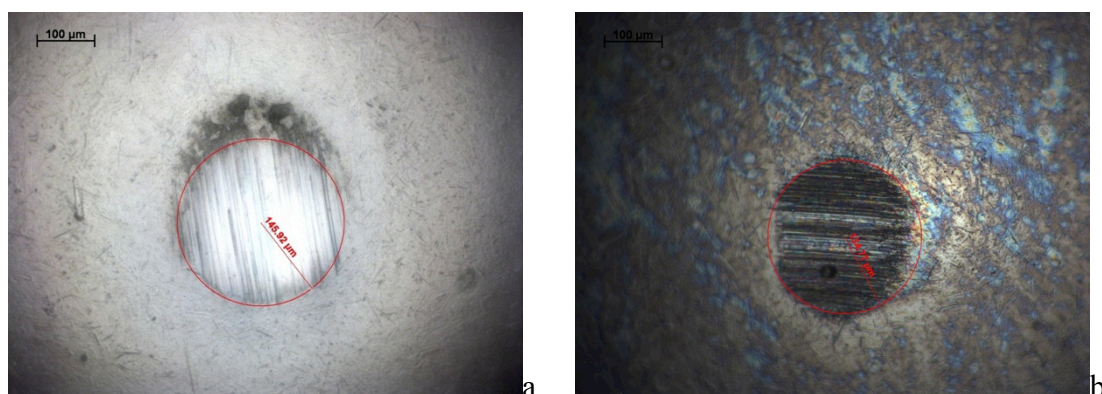


**Figure 8.3: Light-microscope images of the contact area on the ball for the steel-versus-iron poly<sub>0.33</sub> at 5N (a) and 7N (b) normal load**

### 8.1.2 Steel-versus-iron poly<sub>0.33</sub> tribopair: XPS analysis of the steel ball

The tribostressed balls were investigated by i-XPS (Figure 8.4) and small-area XPS (Figure 8.5). As in the case of zinc polyphosphates, a transfer of material from the disc to the ball is revealed, but this time it does not appear as a homogeneous transfer film. The phosphate is instead deposited along the border of the ball's contact



area, as it appears from the chemical state maps obtained for the O1s region (Figures 8.4 and 8.5)

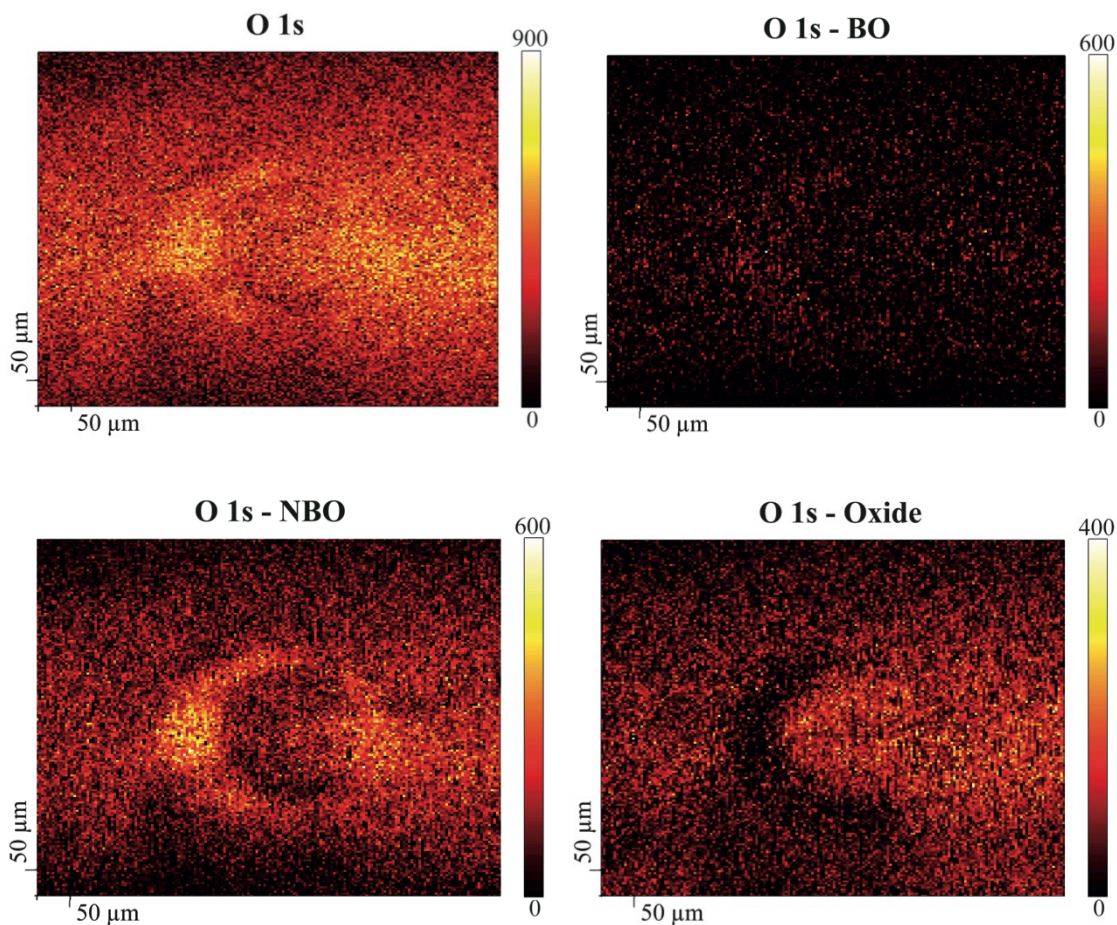


**Figure 8.4:** i-XPS on the contact area of the steel ball after the tribological test (at 7N normal load) on an iron poly<sub>0.33</sub> disc

The high-resolution spectra in Figure 8.5 were collected in the points indicated in the x-ray induced image (SXI). The high-resolution spectra (Figure 8.5) in the non-contact region show the presence of iron oxides, hydroxides and carbonates/carboxylates, typical of steel surfaces after a mechanical test in the presence of PAO. These results are in agreement with previous results obtained in our research group [1; 2]. Iron oxide is also present at the surface of the contact area. Moreover, as a consequence of sliding, some iron oxide has been worn away exposing the metallic iron: its signal at 707 eV is very intense in the Fe 2p region acquired in the contact area. The presence of the phosphorus signal indicates that some phosphates are present, but not as a continuous film because the oxide peak (530.0 eV) in the O1s region is not attenuated. Therefore, there was transfer of material from the disc to the ball, even though it did not adhere to form a homogeneous film.

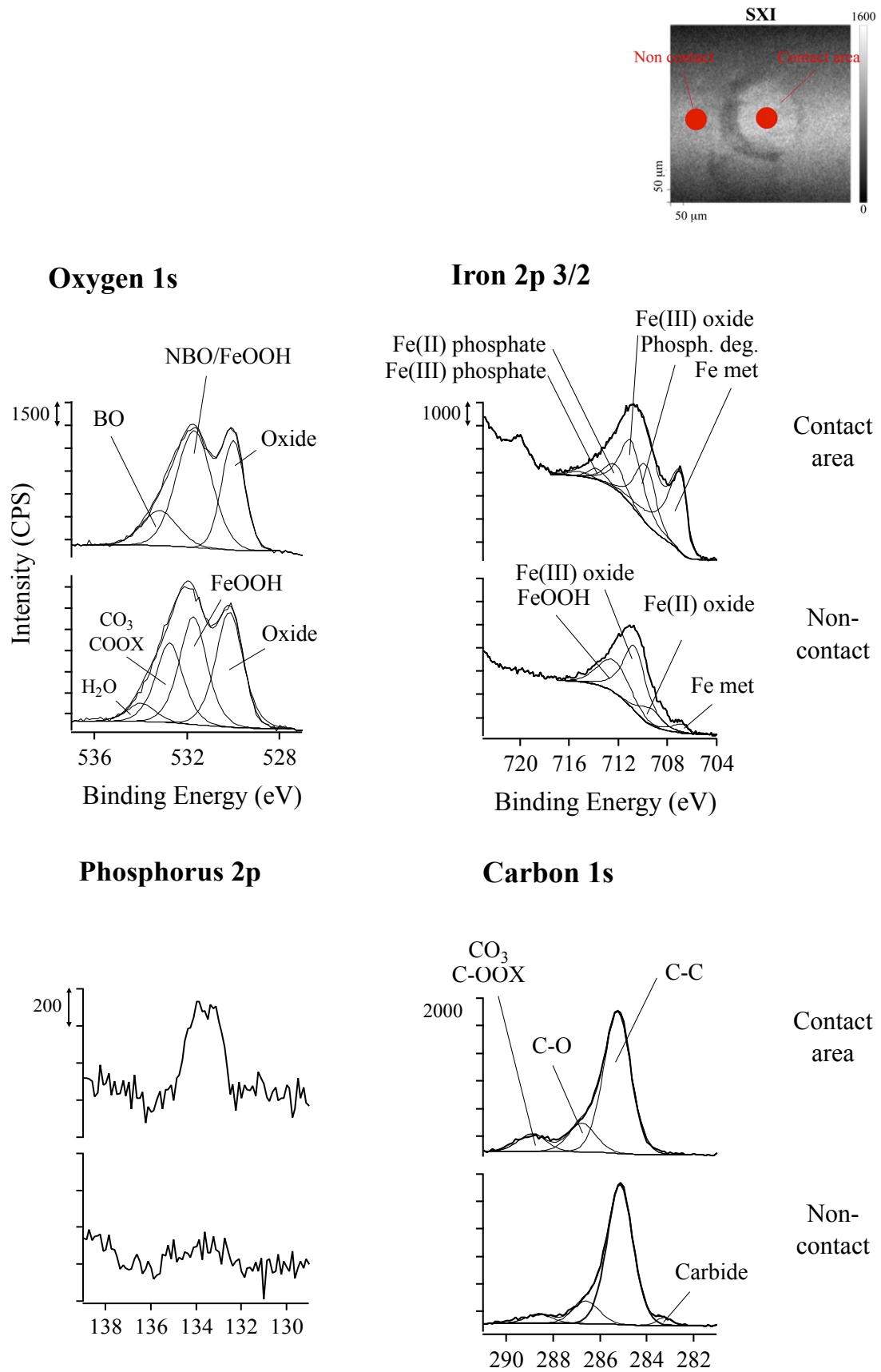


**Figure 8.5:** Small area XPS on the contact and non-contact area of the steel ball after the tribological test (at 7N normal load) on an iron poly<sub>0.33</sub> disc

In the O 1s region, the signal due to the presence of carbonate and/or carboxylates (532.8 eV) and the hydroxide signals (531.7 eV) are contributing to the BO (533.2 eV) and NBO signal (531.7 eV). In the Fe 2p region, the hydroxide signal (712.4 eV) contributes to the phosphate peak intensities, while the carbonate (710.0 eV) overlaps with the peak assigned to the x-ray degradation of the phosphate peaks (710.0 eV). In this situation the BO/NBO ratio cannot be used to estimate the chain-length of the phosphate layer. The P 2p<sub>3/2</sub> was found at 133.4 eV, 0.7 eV lower than the iron poly<sub>0.33</sub> before the tribological test (Table 5.2), indicating a short-chain-length polyphosphate (Figures 6.5 and 6.6).

### 8.1.3 *Steel-versus-iron-poly<sub>0.33</sub> tribopair: XPS analysis of the glass discs*

The tribostressed polyphosphate discs were also analyzed by XPS. High-resolution spectra were acquired in both wear tracks produced by applying 5 and 7N load and in the non-contact areas; examples are provided in Figure 8.6.

In the oxygen 1s region, only the peaks due to oxygen in the bridging /non-bridging bonds can be resolved, while no iron oxide peaks at 530.0 eV could be detected. The same is true for the iron 2p signal, which has been curve fitted with only components assigned to the iron phosphates. However, it can be observed that the signal at low BEs (710.0 eV) assigned to the phosphate degradation is higher if compared to the samples before the tribological stress (Figure 5.5). The presence of iron carbonate, usually found at the same BE, could be the reason for this difference. The component at high BEs in the C 1s region can be assigned to CO<sub>3</sub> confirming this hypothesis. The phosphorus peak, P2p<sub>3/2</sub>, slightly shifts towards lower binding energies, going from the non-contact to the contact region, as reported in Table 8.1. More enhanced is the change in the BO/NBO ratio, suggesting a possible depolymerization inside the tribotrack.

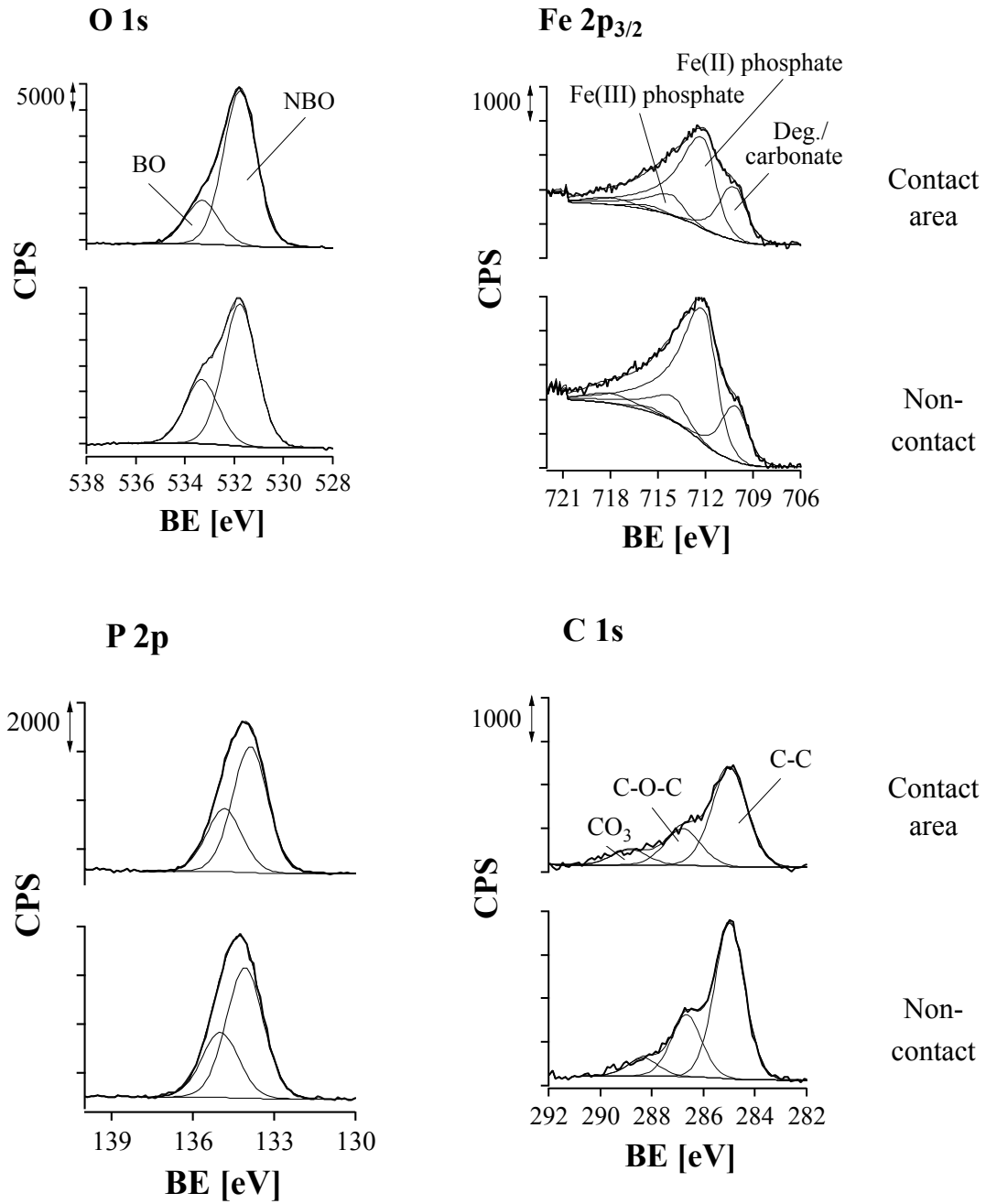


**Figure 8.6:** High-resolution XP-spectra outside and inside of the tribotrack on the iron poly<sub>0.33</sub> disc after the tribological test using a steel ball at 7N normal load

**Table 8.1: XPS analysis of iron poly<sub>0.33</sub> discs after tribological tests with steel balls. The table shows the values obtained by analyzing inside the wear track (in contact) and outside the wear track (non-contact)**

	<i>Iron poly<sub>0.33</sub></i> <i>Contact area</i>	<i>Iron poly<sub>0.33</sub></i> <i>Non-contact</i>
<i>O 1s - NBO [eV]</i>	531.84±0.04	531.85±0.05
<i>O 1s - BO [eV]</i>	533.38±0.03	533.42±0.05
<i>P 2p<sub>3/2</sub> [eV]</i>	134.02±0.06	134.17±0.04
<i>Fe(II) 2p<sub>3/2</sub> [eV]</i>	712.11±0.06	712.10±0.03
<i>Fe(III) 2p<sub>3/2</sub> [eV]</i>	714.11±0.09	714.25±0.1
<b><i>BO/NBO</i></b> <b><i>Intensity ratio</i></b>	0.33±0.05	0.41±0.04
<b><i>Fe(III)/Fe(II)</i></b> <b><i>Intensity ratio</i></b>	0.25±0.04	0.28±0.03

## 8.2 Steel-versus-mixed-zinc-and-iron polyphosphates

The addition of zinc, even in small percentages, to the iron polyphosphates improved the properties of the glasses so that they could be polished and tribologically tested; the results are reported in the following.

### 8.2.1 *Steel-versus-mixed-zinc-and-iron-polyphosphates tribopair: friction and wear*

The coefficient of friction as a function of sliding distance is shown in Figure 8.7 for three different mixed polyphosphates. The curves remained unchanged with sliding time. Few exceptions can be found for the polyphosphates containing 50 at.% and 75 at.% iron; some curves show a sudden increase in the coefficient of friction without any apparent external cause. In particular, an experiment at 5N normal load in the zinc 25 iron 75 poly<sub>0.5</sub> shows a sudden increase of the coefficient of friction to a value similar to that of the steel-versus-iron poly<sub>0.33</sub> tribopair.

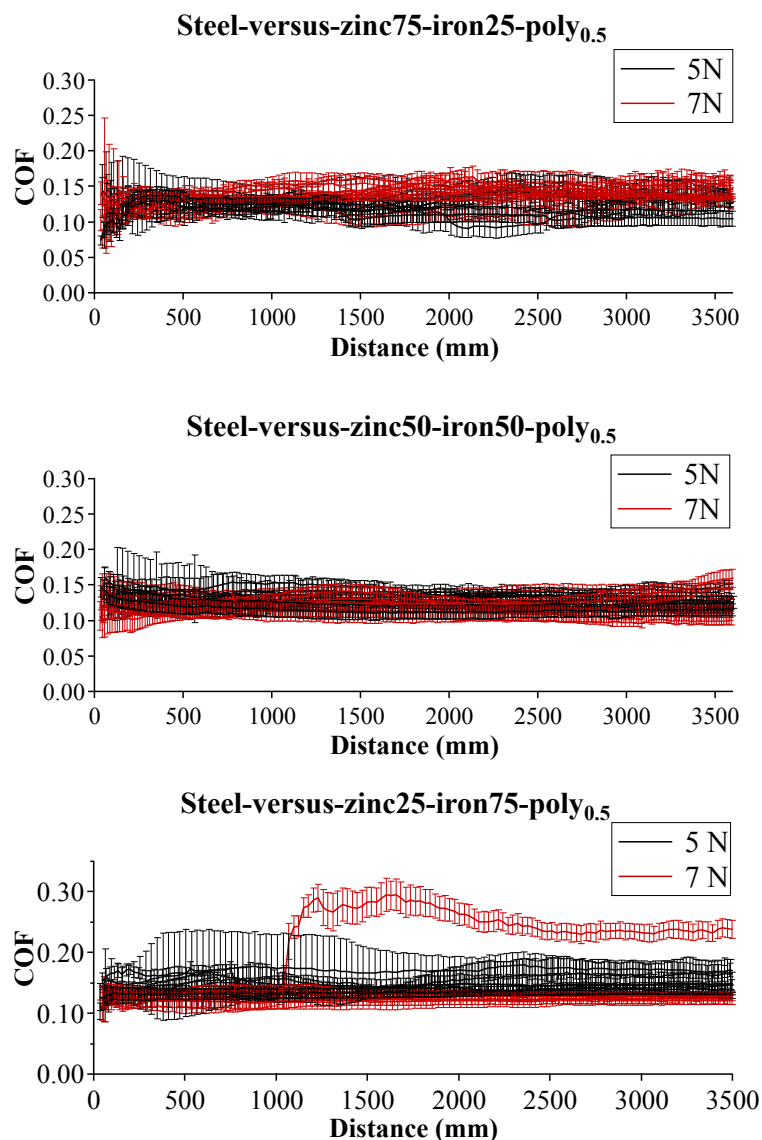


**Figure 8.7** COF (averaged on every turn and reported with its experimental error) versus sliding distance for the steel-versus-zinc75-iron25-poly<sub>0.5</sub>, steel-versus-zinc50-iron50-poly<sub>0.5</sub> tribopairs and steel-versus-zinc25-iron75-poly<sub>0.5</sub> at 5 and 7N of normal load and 30 mm/min of sliding speed

The average coefficients of friction for the mixed polyphosphates are compared to all the other tribopairs investigated in this work in Figure 8.8. The addition of zinc to the iron polyphosphates, even in low amounts, has the effect of reducing the coefficient of friction to values comparable to those measured for the zinc polyphosphates.

The same is true for the wear rates measured on the ball, that are as low as those measured for zinc pyrophosphate—the one exhibiting the best wear behavior among all zinc polyphosphates.

The light microscope images of the balls are shown in Figure 8.10.

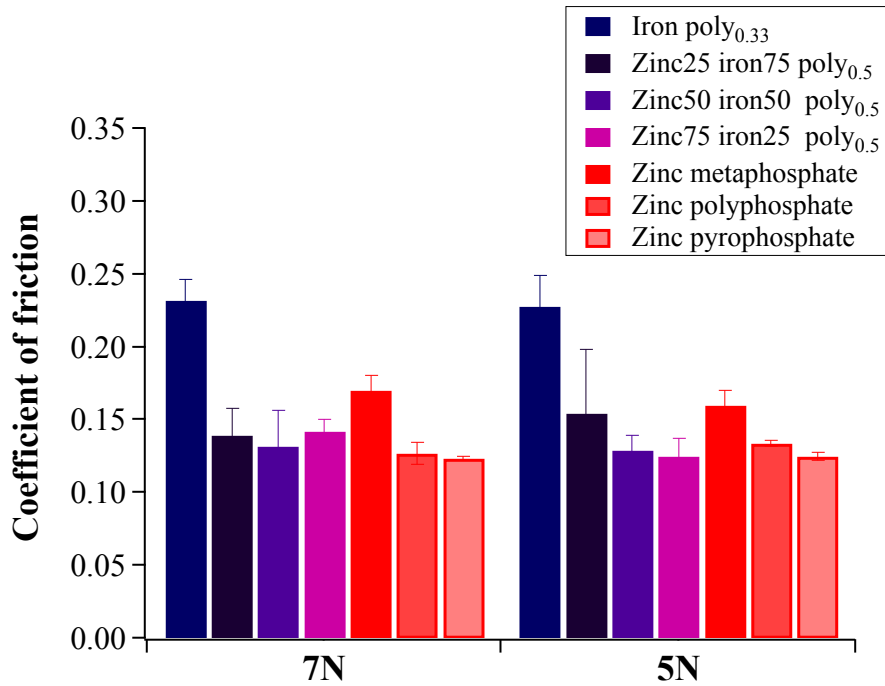


Figure 8.8: Tribological results: comparison between the COF obtained using steel-versus-zinc polyphosphate, steel-versus-iron poly<sub>0.33</sub> and steel-versus-mixed zinc and iron polyphosphate tribopairs

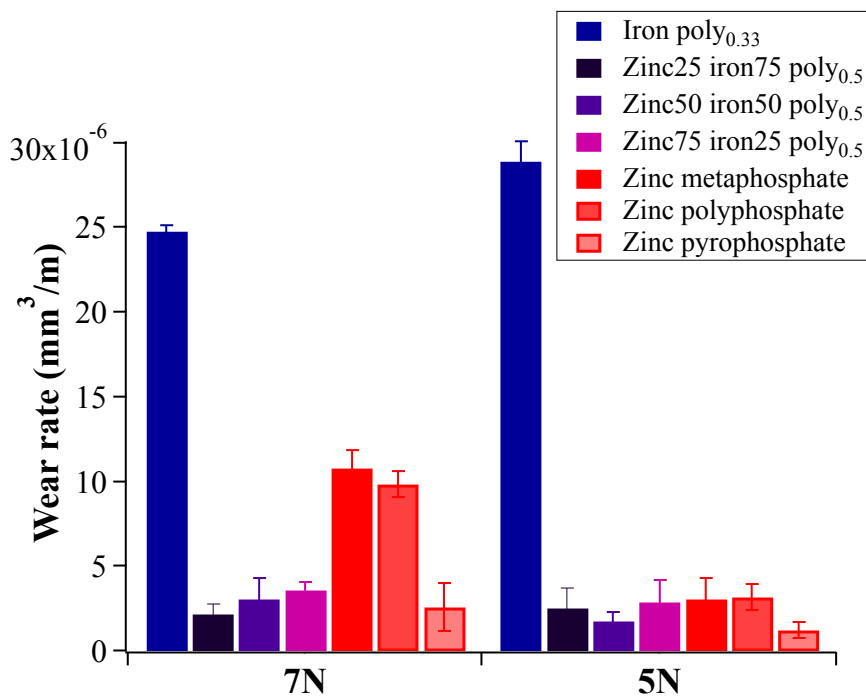
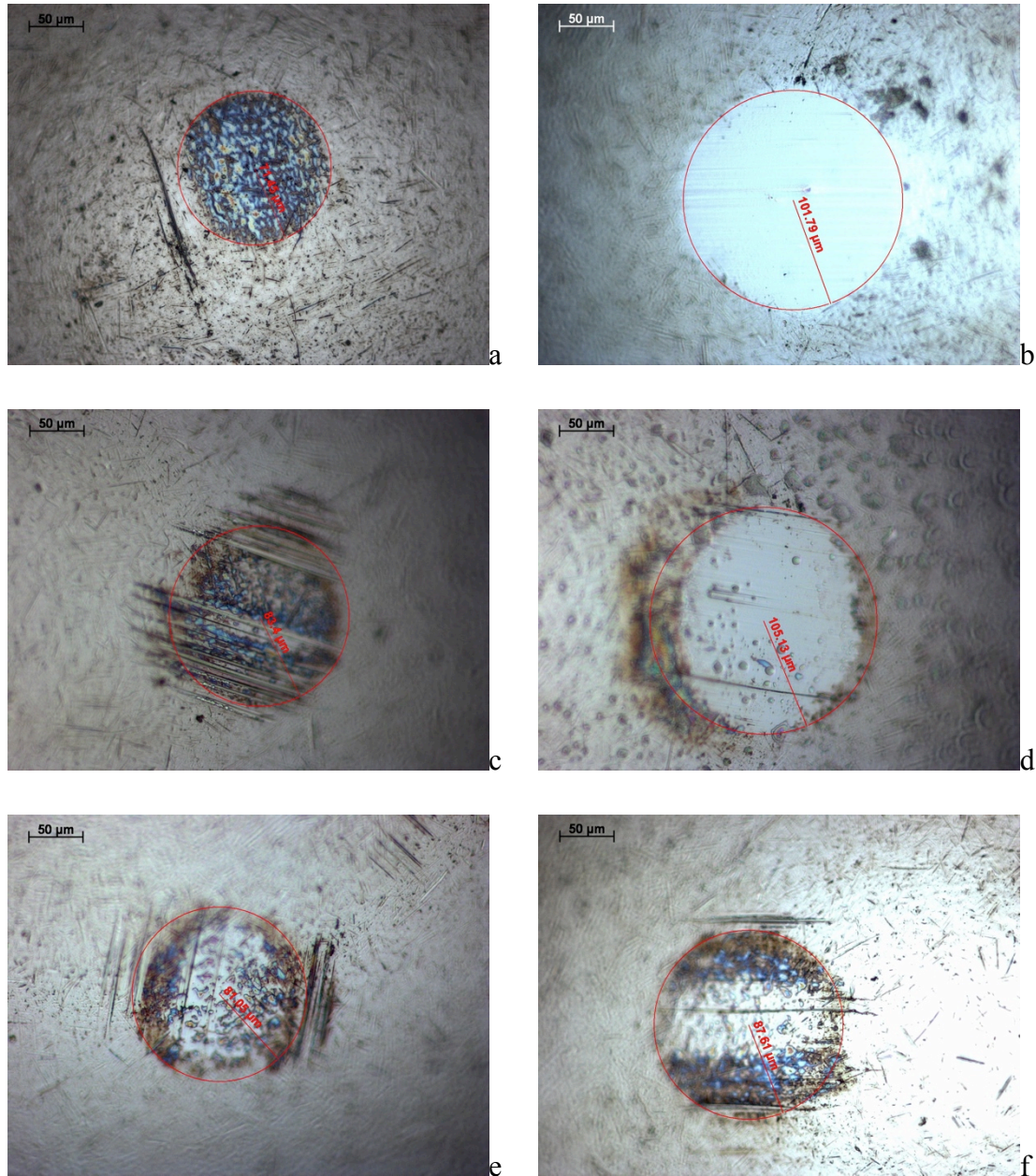


Figure 8.9: Tribological results: comparison between the wear coefficients obtained using steel-versus-zinc polyphosphate, steel-versus-iron poly<sub>0.33</sub> and steel-versus-mixed zinc- and iron-polyphosphates tribopairs



**Figure 8.10:** Light-microscope images of the contact area on the ball for the steel-versus-zinc75 iron25 poly<sub>0.5</sub> at 5N (a) and 7N (b) normal load, the steel-versus-zinc50 iron50 poly<sub>0.5</sub> at 5N (c) and 7N (d) and the steel-versus-zinc25 iron75 poly<sub>0.5</sub> at 5N (e) and 7N (f)

### 8.2.2 Steel-versus-mixed zinc and iron polyphosphates tribopair: XPS analysis of the steel ball

I-XPS results from a steel ball following tribotesting on a zinc75 iron25 poly<sub>0.5</sub> disc at 5 N normal load are shown in Figure 8.11. The coefficient of friction as a function of sliding distance is reported as well, together with the XPS images, in Figure 8.11a, in order to ascertain if any correlation between the coefficient of friction and the maps could be established. The i-XPS results were collected on the ball used for the test highlighted in green. The correspondent micrograph is in figure 8.10a. The



coefficient of friction and the wear rate (Figure 8.10a) are the lowest within the series of tested samples and they correlate with the presence of a polyphosphate glassy film, as is clearly demonstrated by the P2p map (Figure 8.11b). The O1s map shows that the iron oxide signal from the steel substrate is completely attenuated by the phosphate layer (figure 8.11d).

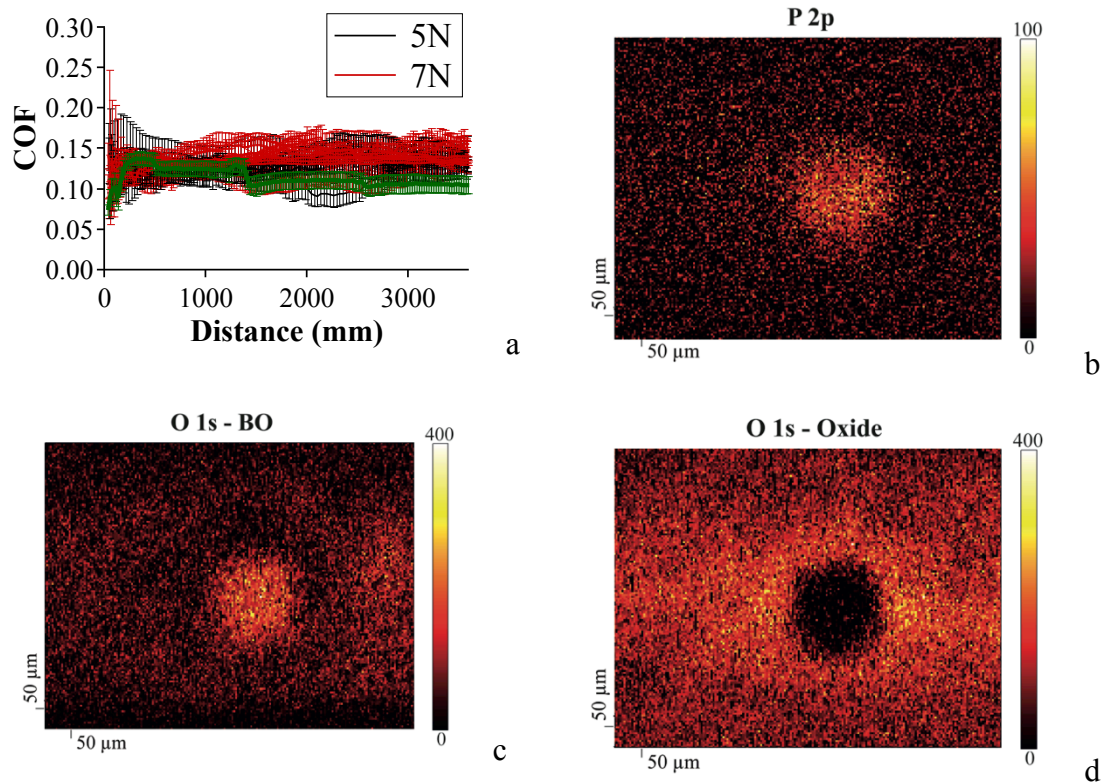


**Figure 8.11: (a) COF-versus-sliding distance for the steel-versus-zinc75-iron25-poly<sub>0.5</sub> tribopair at 5 and 7N normal loads. The ball used for the tribological test highlighted in green (7N) has been analyzed by i-XPS and the P2p (b), O1s BO (c) and oxide (d) maps are reported here**

The results of the small area XPS shown in Figure 8.12 were acquired on a different ball after a tribotest at 7N normal load (Figure 8.10b). The attenuation of the oxide peak in the contact area and the appearance of the P2p<sub>3/2</sub> peak at 133.8 eV and Zn 2p<sub>3/2</sub> at 1022.7 eV are both evidence of the presence of a phosphate film. Since the oxide signal is not totally attenuated, the oxide, hydroxide and carbonate signals from the substrate could overlap with the phosphate signals in the contact region. The BO/NBO ratio cannot be used to identify the chain-length, but the position of the P 2p<sub>3/2</sub> signal at 133.8 indicates the presence of short-chain-lengths (Figures 6.5 and 6.6).

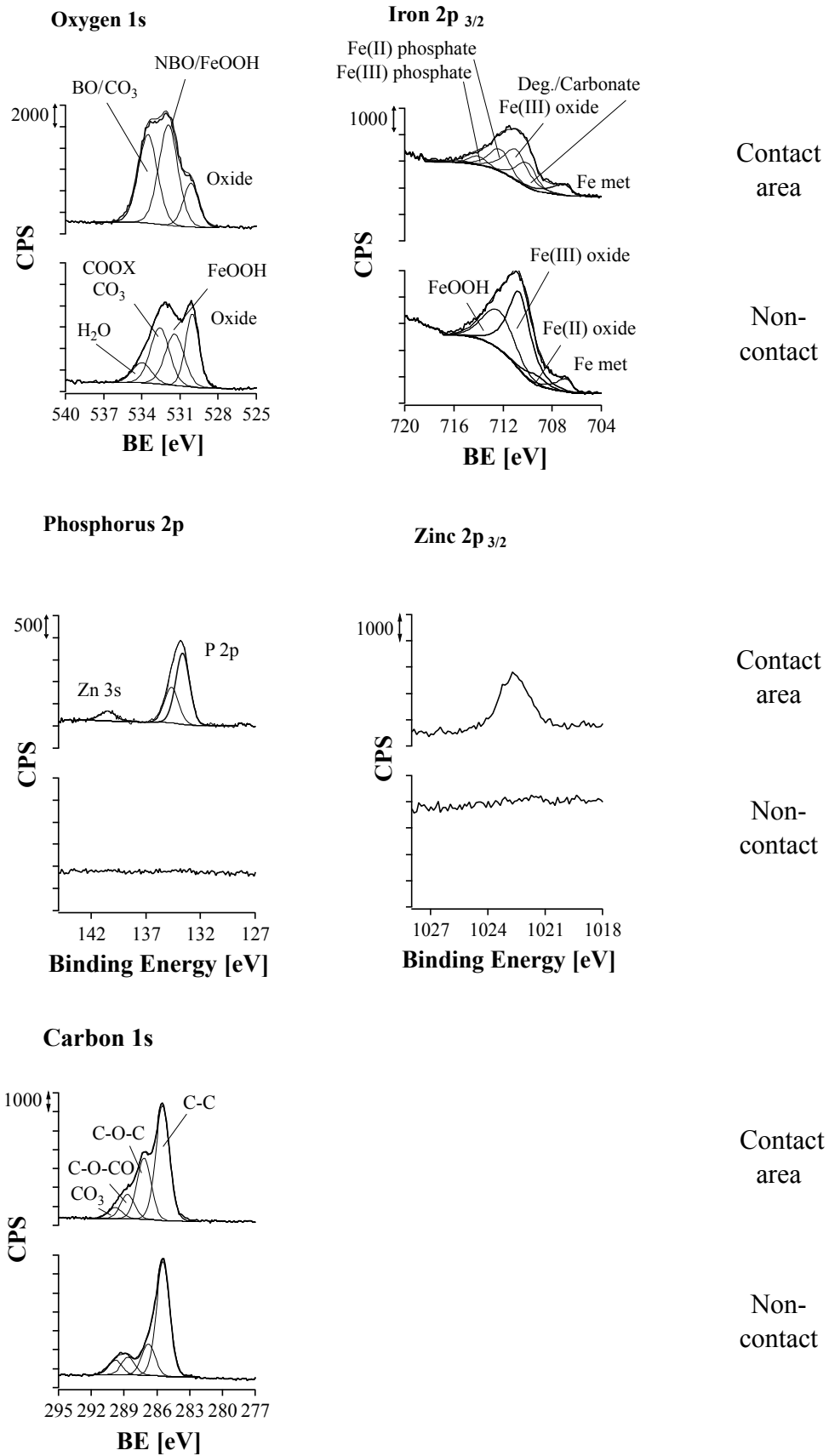
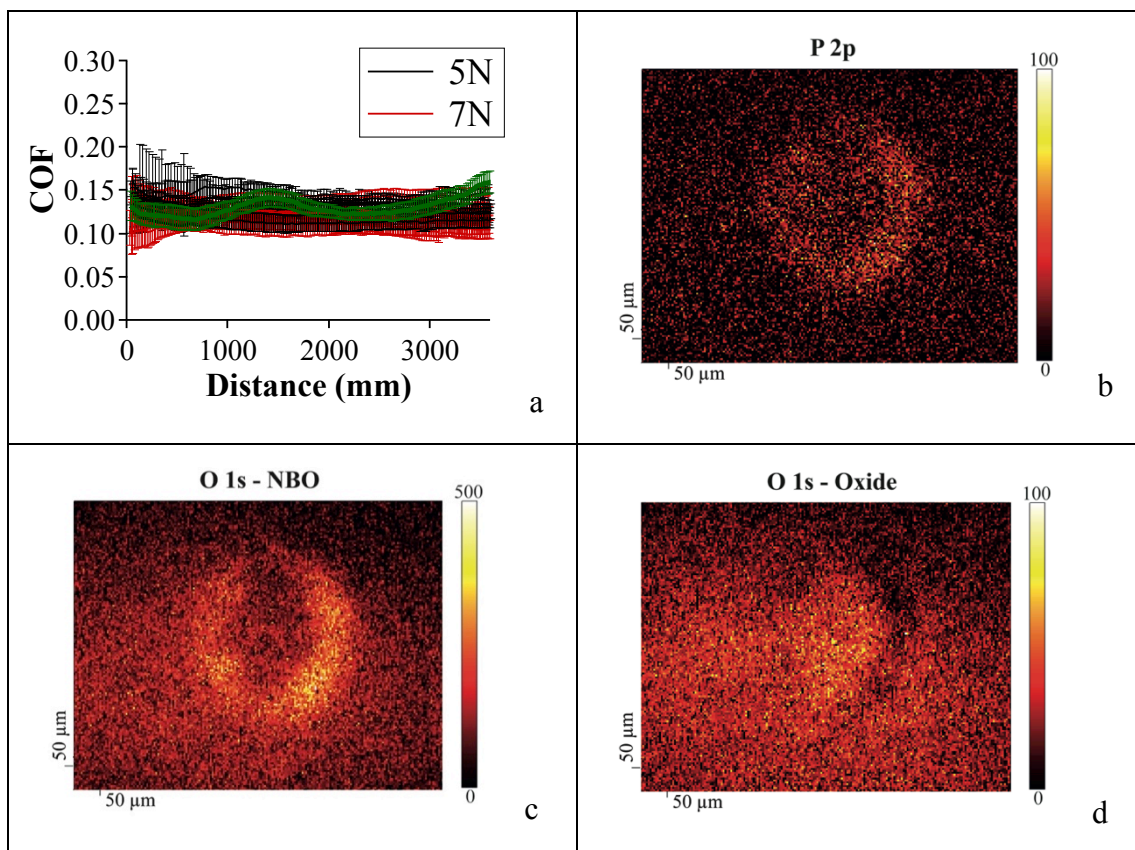


Figure 8.12: High-resolution XP-spectra outside and inside of the tribotrack on the zinc<sub>75</sub> iron<sub>25</sub> poly<sub>0.5</sub> disc after the tribological test using a steel ball at 7N normal load

The results of the tribological test using the steel-versus-zinc50-iron50-poly<sub>0.5</sub> tribopair are shown in Figure 8.13a. The coefficient of friction versus sliding distance remains unchanged with only one exception that is highlighted in green. This case of instability in the coefficient of friction was also investigated by XPS and the corresponding maps are shown in Figure 8.13b (P2p) 8.13c (O1s, BO) and 8.13d (O1s, oxide). The oxygen and phosphorus maps clearly show that no transfer film is present in the contact area but some phosphate material is detected at its borders. The maps in Figure 8.13 may be considered a snapshot of the chemical distribution of the elements when the friction was higher.



**Figure 8.13: (a) COF-versus-sliding distance for the steel-versus-zinc50-iron50-poly<sub>0.5</sub> tribopair at 5 and 7N normal loads. The ball used for the tribological test highlighted in green (7N) has been analyzed by i-XPS and the P2p (b), O1s BO (c) and oxide (d) maps are reported here**

In Figure 8.14 the small-area XPS results corresponding to another steel ball used for a test on zinc50 iron25 poly<sub>0.5</sub> case can be found. Phosphorus and zinc peaks are detected in the contact area at the BE of 133.7 eV and 1022.6 eV respectively. In analogy with the previous zinc75 iron25 poly<sub>0.5</sub> case, the spectra show the presence of a glassy transfer film.

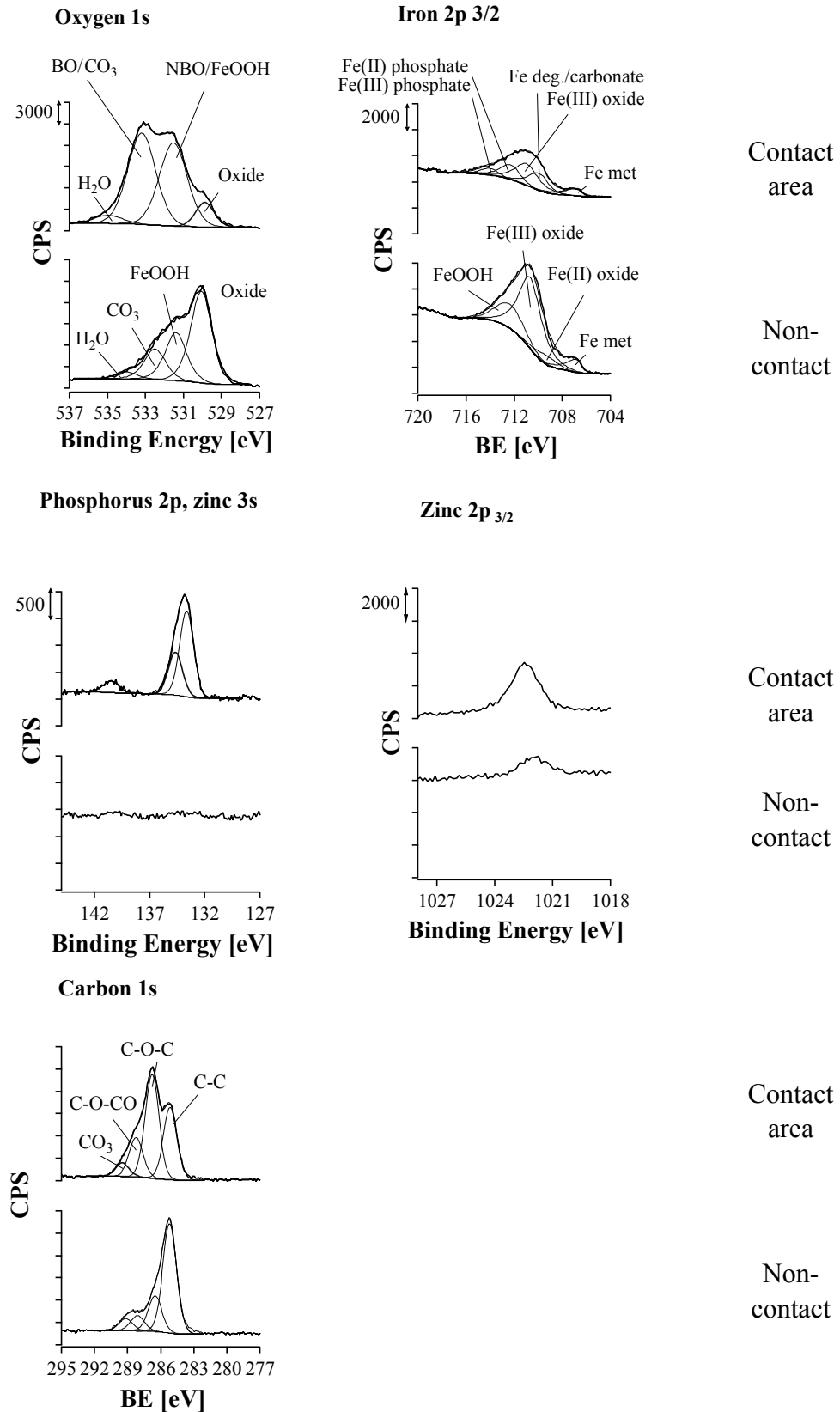


**Figure 8.14: High-resolution XP-spectra outside and inside of the tribotrack on the zinc50 iron50 poly<sub>0.5</sub> disc after the tribological test using a steel ball at 7N normal load (see Figure 8.10c). To the BO – O1s signal also contribute the oxidized species following the oil oxidation**

Finally, in Figure 8.15 the zinc<sub>25</sub> iron<sub>75</sub> poly<sub>0.5</sub> composition it is examined. The ball used for a test that shows constant and low friction, highlighted in green in Figure 8.15a, was analyzed. The corresponding maps of P2p (Figure 8.15b) and O 1s BO (Figure 8.15c) exhibit a discontinuity in the center of the area that correlates with the component assigned to iron oxide (Figure 8.15d). This peculiar topography is visible in both oxygen and phosphorus maps and was observed very often also for the other compositions. Also in this case the XPS maps demonstrate the formation of a polyphosphate transfer film.

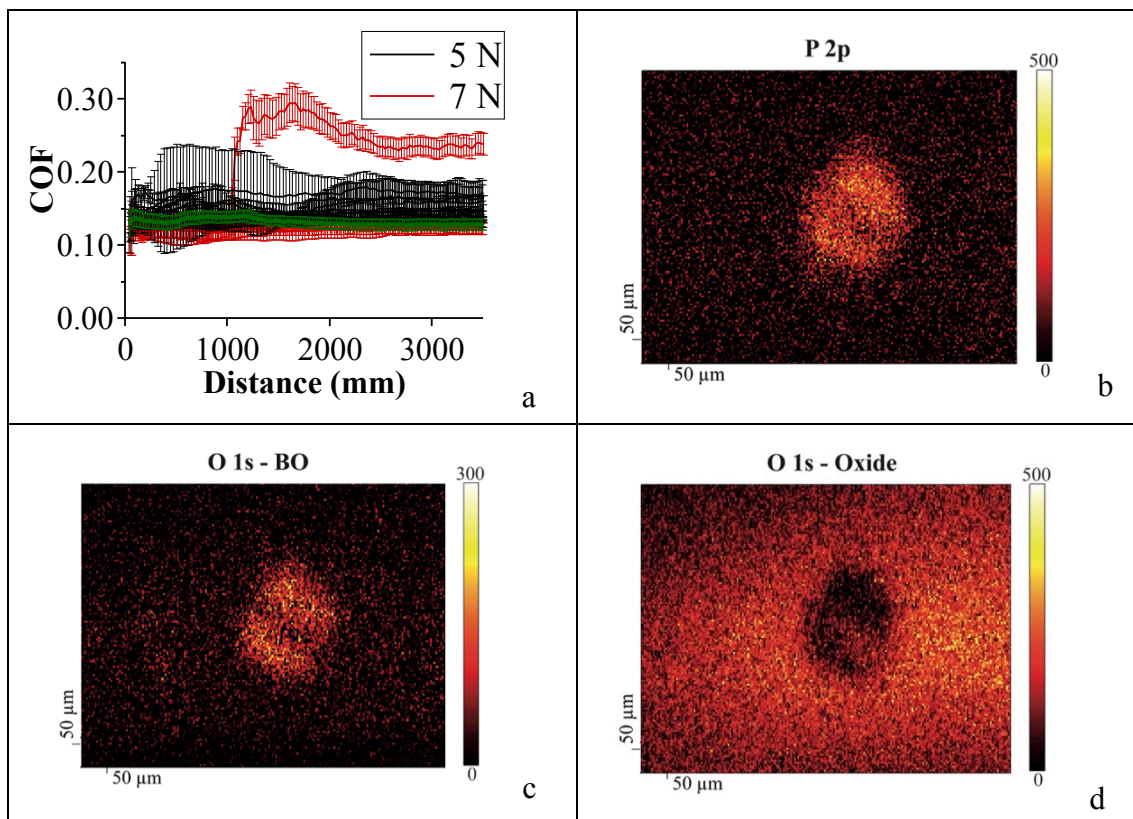


**Figure 8.15:** (a) COF-versus-sliding distance for the steel-versus-zinc<sub>25</sub>-iron<sub>75</sub>-poly<sub>0.5</sub> tribopair at 5 and 7N normal loads. The ball used for the tribological test highlighted in green (7N) has been analyzed by i-XPS and the P2p (b), O1s BO (c) and oxide (d) maps are reported here

### 8.2.3 Steel-versus-mixed-zinc-and-iron-polyphosphates tribopair: XPS analysis of the glass discs

An example of the small-area XPS spectra acquired inside and outside the tribotrack on the zinc<sub>75</sub> iron<sub>25</sub> poly<sub>0.5</sub> disc is shown in Figure 8.16. The results obtained were similar for all three compositions examined. The spectra have been curve fitted with the same parameters used for the polyphosphates after the synthesis but the presence of some iron oxide in traces, not possible to resolve, cannot be excluded. All corresponding curve fitting parameters can be found in Table 8.2.

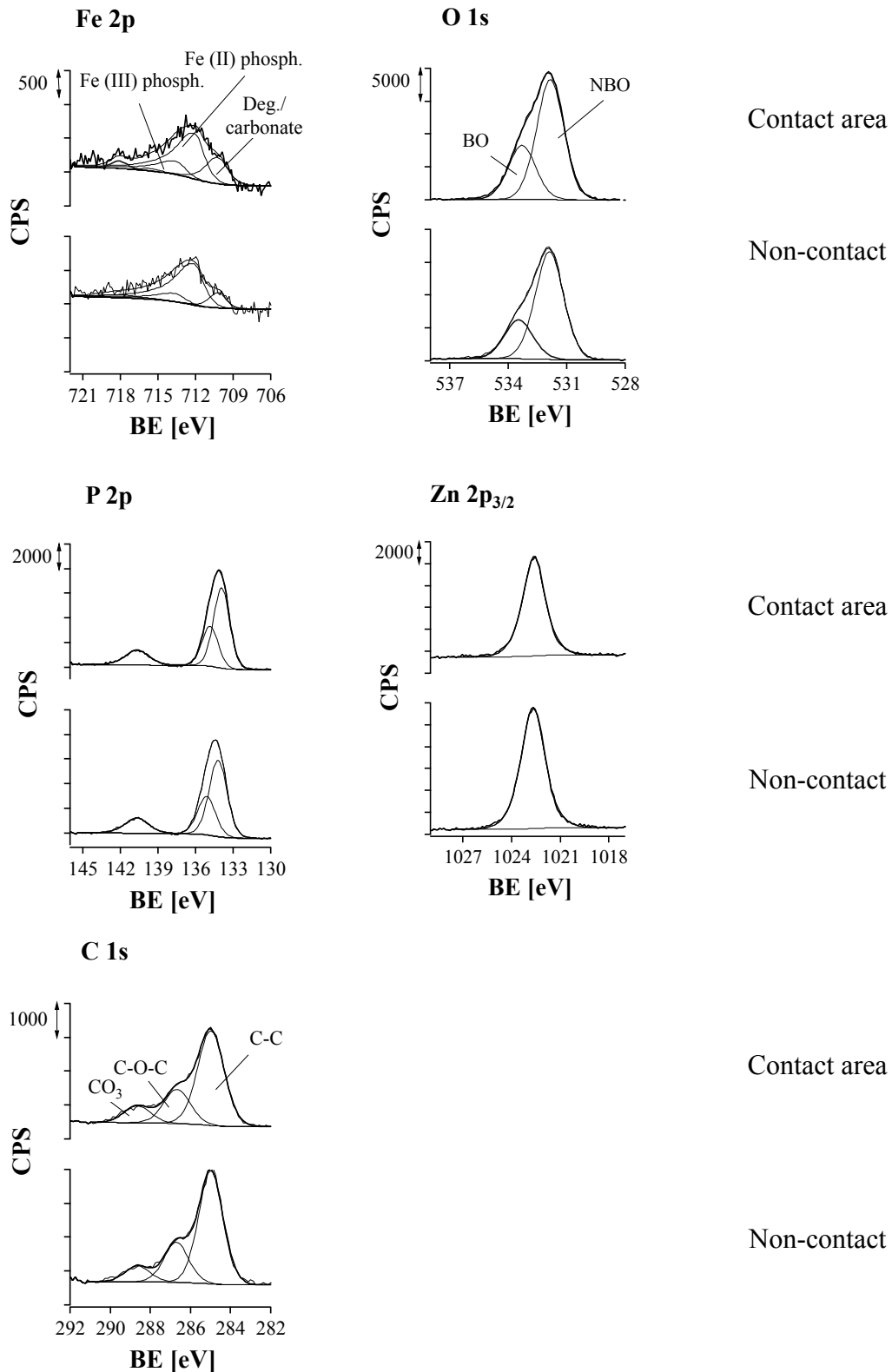


**Figure 8.16: High-resolution XPS spectra outside and inside of the tribotrack on the mixed zinc<sub>75</sub> iron<sub>25</sub> poly<sub>0.5</sub> disc after the tribological test with a steel ball at 7N normal load**

In the iron  $2p_{3/2}$  signal, as already observed on the spectra acquired on the balls, the peak attributed to the degradation is high because of the overlap with the iron carbonate peak at 710.0 eV.

The phosphorus  $2p_{3/2}$  peak shows a shift towards lower binding energies going from the non-contact to the contact region for the compositions investigated (Table 8.2). Also the BE differences ( $Zn\ 3s - P2p_{3/2}$ ) (Table 8.2) increase going from the non-contact to the contact area thus substantiating a depolymerization of the polyphosphates in the contact area.

Only in the case of zinc75iron25 poly05 is a change in the BO/NBO ratio detected; in the other two cases this parameter remains unchanged. The presence of iron oxides and carbonates cannot be excluded and this makes it challenging to resolve the BO contribution to the O 1s signal (Table 8.2 and Figure 8.16). It has to be emphasized that the calculations performed without excluding the interferences just mentioned would lead to an ultraphosphate.

**Table 8.2: XPS analysis of mixed zinc75 iron25 poly<sub>0.5</sub>, zinc50 iron50 poly<sub>0.5</sub> and zinc25 iron75 poly<sub>0.5</sub> discs after tribological test with steel balls. For each composition the table shows the values obtained analyzing inside the wear track (contact area) and outside the wear track (non contact)**

<i>[eV]</i>	<i>Zinc75 iron25 poly<sub>0.5</sub></i>		<i>Zinc50 iron50 poly<sub>0.5</sub></i>		<i>Zinc25 iron75 poly<sub>0.5</sub></i>	
	<i>Contact area</i>	<i>Non-contact</i>	<i>Contact area</i>	<i>Non-contact</i>	<i>Contact area</i>	<i>Non-contact</i>
<b><i>O 1s - NBO</i></b>	531.83 ±0.08	531.91 ±0.06	531.75 ±0.08	531.86 ±0.04	531.61 ±0.06	531.67 ±0.04
<b><i>O 1s - BO</i></b>	533.2 <sub>6</sub> ±0.1 <sub>2</sub>	533.48 ±0.06	533.2 <sub>6</sub> ±0.1 <sub>2</sub>	533.45 ±0.05	533.18 ±0.08	533.27 ±0.04
<b><i>P 2p<sub>3/2</sub></i></b>	133.9 <sub>5</sub> ±0.1 <sub>2</sub>	134.20 ±0.06	133.9 <sub>2</sub> ±0.1 <sub>3</sub>	134.18 ±0.03	133.7 <sub>2</sub> ±0.1 <sub>3</sub>	133.96 ±0.05
<b><i>Fe(II) 2p<sub>3/2</sub></i></b>	712.09 ±0.01	712.09 ±0.01	712.09 ±0.01	712.10 ±0.02	712.3 <sub>0</sub> ±0.2 <sub>2</sub>	712.3 <sub>4</sub> ±0.3 <sub>1</sub>
<b><i>Fe(III) 2p<sub>3/2</sub></i></b>	714.5 <sub>1</sub> ±0.2 <sub>8</sub>	714.8 <sub>4</sub> ±0.5 <sub>3</sub>	713.59 ±0.01	713.60 ±0.02	713.8 <sub>0</sub> ±0.2 <sub>2</sub>	713.8 <sub>4</sub> ± 0.3 <sub>1</sub>
<b><i>Zn 3s</i></b>	140.66 ±0.08	140.74 ± 0.06	140.4 <sub>6</sub> ±0.1 <sub>1</sub>	140.62 ±0.09	140.35 ±0.08	140.40 ±0.07
<b><i>Zn 2p<sub>3/2</sub></i></b>	1022.63 ±0.05	1022.70 ±0.06	1022.54 ±0.08	1022.64 ±0.05	1022.49 ±0.05	1022.52 ±0.03
<b><i>BO/NBO</i></b>	0.5 <sub>1</sub> ±0.1 <sub>8</sub>	0.35±0.02	0.40±0.09	0.40±0.04	0.3 <sub>6</sub> ±0.1 <sub>5</sub>	0.36±0.05
<b><i>Zn 3s - P 2p BE difference (eV)</i></b>	6.71±0.07	6.54±0.03	6.54±0.6	6.43±0.06	6.63±0.08	6.44±0.04

### 8.3 Effect of the counter-ion on the friction, wear and tribochemical behavior of polyphosphate glasses

Due to their complexity, the XPS spectra of the tribologically stressed iron polyphosphate in the presence of iron oxide were more difficult to interpret than in the case of zinc polyphosphates. Nonetheless, very useful information could be obtained from imaging-XPS data.

High friction and very high wear on the steel ball is observed when iron poly<sub>0.33</sub> were used as discs. The i-XPS on the tribologically stressed balls showed that the iron polyphosphate transferred from the disc to the ball was not adhering on the contact area as happened for the steel and quartz-versus-zinc polyphosphates tribopairs. The iron poly<sub>0.33</sub> is probably forming a non-cohesive third body, unable to withstand the load and protect the ball from wear. In fact, the coefficient of wear was higher than that measured for the steel-versus-steel tribopairs (figure 8.2).

When adding zinc to the batch composition, the properties of the glasses change again and the measured friction and wear were in the same order of those measured for zinc polyphosphate glasses already, even the addition of 25% of zinc (figures 8.8. and 8.9). The wear rate at 7 N is lower for the mixed polyphosphates than for the zinc ones. This change in the tribological properties corresponds again to the formation of a glassy transfer film on the contact area of the tribologically stressed balls. Interestingly, in some cases, the transfer film breaks down (Figure 8.13) with a sudden increase in the coefficient of friction and wear. This phenomenon has the characteristic of a stochastic process and it is presumably caused by some wear particles or by some defect on the surface of the disc or the ball. Similar cases seem to be more frequent in the samples with higher iron content (Figure 8.7).

These findings confirm the hypothesis, formulated previously in Chapter 7, that wear and friction in phosphate glasses are governed by a third-body mechanism. A consequence of this process is the formation of the transfer film that is observed in the ex-situ i-XPS analysis.

The shift of the (Zn3s-P2p<sub>3/2</sub>) binding energy difference towards lower values was used to estimate changes in the chain-length of the glasses, since the BO and NBO signals could overlap with iron oxide and carbonate species. Both iron and mixed polyphosphates discs are depolymerized as a consequence of the tribological stress, despite the fact that the addition of iron has shown to improve the chemical durability of zinc polyphosphates [3]. The P2p<sub>3/2</sub> BEs measured on the ball contact areas were at least 0.5 eV lower than those measured on the discs. Only short chain-lengths are present on the transfer film.



#### 8.4 Summary

In this chapter the results on the tribochemical properties of iron- and mixed zinc-and iron-polyphosphates have been presented. The replacement of the counter-ion in polyphosphates has been found to influence the wear mechanism. Mixed zinc and iron polyphosphates are characterized by low friction and low wear rate and by the formation of a transfer film on the steel ball. Iron poly<sub>0.33</sub>, in contrast, was not able of forming an adhesive transfer film on the ball with consequent high friction and wear.

XPS and i-XPS were proven to be useful tools for correlating the composition of the tribostressed surfaces with the friction and wear behavior. The P 2p<sub>3/2</sub> chemical shift allowed the identification of changes in the polyphosphate chain-length to be made when the BO/NBO ratio could not be used.

***References***

- [1] Mangolini F., Reactivity of Environmentally Compatible Lubricant Additives: an In Situ and Ex Situ Investigation, PhD Thesis No. 19677, ETH Zürich, Zürich, 2011.
- [2] Heuberger R. C., Combinatorial Study of the Tribiochemistry of Anti-Wear Lubricant Additives LSST, ETH, Zürich, 2007, pp. 226.
- [3] Reis S. T., Karabulut M., and Day D. E.: Chemical durability and structure of zinc-iron phosphate glasses. *J. Non-Cryst. Solids* 292, 150-157 (2001).

## **9 Polyphosphate glasses as model compounds for tribofilms**

The aim of this chapter is to correlate tribological and surface-analytical results reported and discussed in this thesis, in order to shed light on some of the many open issues in the tribochemistry of ZnDTP and ashless thiophosphates.

First of all it is critically considered to which extent the use of bulk polyphosphate glasses is a valid model of tribofilms (Section 9.1).

In the following section, the influence that the tribochemical reactions observed in the model system could have on the tribofilms' formation and composition is discussed. Section 9.3 concerns the antiwear mechanism of tribofilms: the role played by the tribochemical reactions, the effect of the presence of long- or short-chain-length polyphosphates and the functionality of the transfer film. The effect of different cations on the tribochemical properties of the glasses and the relevance of this on the performance of ashless thiophosphates can be found in Section 9.4.

Finally in Section 9.5 the characteristics of a functional antiwear film are also discussed in comparison with another relevant system in this field: diamond-like-carbon coatings.

### **9.1 Bulk polyphosphate glasses as models for ZnDTP tribofilms: advantages and disadvantages**

In this work, bulk polyphosphate glasses have been proposed and used as model compounds for ZnDTP tribofilms. Using a model to simplify a more complex system involves advantages and disadvantages that have to be carefully discussed.

The typical experiment used for investigating ZnDTP tribofilms consists of two steel surfaces rubbing onto each other in the presence of an oil solution of ZnDTP (or other additive). This is also a simulation of real operating conditions in an engine, which is a very complex system, but it is accepted as a procedure for investigating friction, wear and lubrication. The properties of the resulting tribofilm are then correlated with its tribological performance. Different physical-chemical parameters are usually exploited, ranging from the nature of the additives and their concentrations, to the temperature of the lubricant, and the pressure and sliding velocity applied during the tests.

The model system studied in this work consisted of a steel ball sliding against a phosphate glass disc of known composition in presence of pure oil. Different zinc-, iron-, mixed zinc-and iron-polyphosphate compositions and chain-lengths were investigated under different loads.

Working in pure oil instead of ZnDTP oil solution is an advantage for the model system because all the changes in composition observed will be attributed without any doubt to a reaction between the two rubbing surfaces activated by the sliding process, excluding the influence of other reactions such as decomposition or rearrangements of ZnDTP in the solution. On the other hand, starting from an already formed polyphosphate will exclude the possibility to investigate the film formation process, which still has some open issues.

Tribofilms have a heterogeneous composition; they contain, for example, sulfides [1] that are believed to play a role in EP regime by preventing adhesion between the metal surfaces when the phosphate layer is worn away [2]. Polythiophosphates could also be present in the tribofilms and act as precursors for the formation of long-chain polyphosphates [3]. Investigating polyphosphates in absence of sulfur is an advantage because it allows isolating and studying the properties of pure polyphosphates. It would be very interesting, as a further research topic, to investigate also polythiophosphates and mixtures of polyphosphates and polythiophosphates.

Real tribofilms can contain mixtures of different-chain-length zinc and iron polyphosphates, which depend on the experimental conditions and vary dramatically with the topography in the microscopic scale [4-7]. Tuning the composition of the discs in this study it was possible to investigate the effect of composition and chain-length, an impossible task using the classical experimental setup.

The structure of the polyphosphates present in the tribofilms is reported to be amorphous [7]. The samples investigated in this thesis were also amorphous, thanks to rapid quenching, but it is unlikely that they possess the same structure of a film which has been formed under high load and shear stress [8]. This is an unavoidable limitation of the model system, and has to be taken into account especially when confronting mechanical properties.

The poly(thio)phosphate tribofilm is typically formed on both sliding surfaces, while in this model system one counterpart is bare steel. This can also be regarded as a disadvantage in the comparison between the two systems. However, since it was observed that a transfer film was always formed on the steel surface after a certain running-in time, the sliding was actually taking place between two polyphosphate surfaces. On the other hand, the presence of iron and iron oxide in the contact allowed the investigation of the reactions between iron oxide and polyphosphates.

## 9.2 Influence of tribochemical reaction on the tribofilm formation and composition

The composition of the tribological films formed in the presence of ZnDTP is heterogeneous, with longer polyphosphate chain-lengths being present in the outermost layer, at the bottom a layer of shorter-chain-length polyphosphates, which also contains zinc, iron and some sulfur, and unreacted, or partially reacted, additive adsorbed on the surface [5; 9-11]. Temperature, pressure, composition and degree of degradation of the additive also influence the chain-length of the polyphosphate in the tribofilms.

As described in Chapter 2, Section 2.3 two different mechanisms have been proposed for the formation of the layered structure of tribofilms: some researchers think that first short chain-length polyphosphates are formed that then polymerize under the effect of pressure [12; 13]; others believe that the long chain-lengths are formed first and depolymerized subsequently. The second argument is supported by the fact that there would be a lack of counter-ions to form short chain-lengths directly from the decomposition of ZnDTP [7], while the depolymerization could take place in a second step, when the phosphate comes into contact with iron oxide as a consequence of wear or by hydrolysis with the water potentially present in the oil [10; 14; 15].

In order to investigate the effect of water, zinc metaphosphate was exposed to different relative humidity (RH) and its surface chemistry was followed by XPS as a function of time (Figure 9.1). The sample is depolymerized already after few days of exposure to humid air as a consequence of the hydrolysis of the P-O-P bonds.

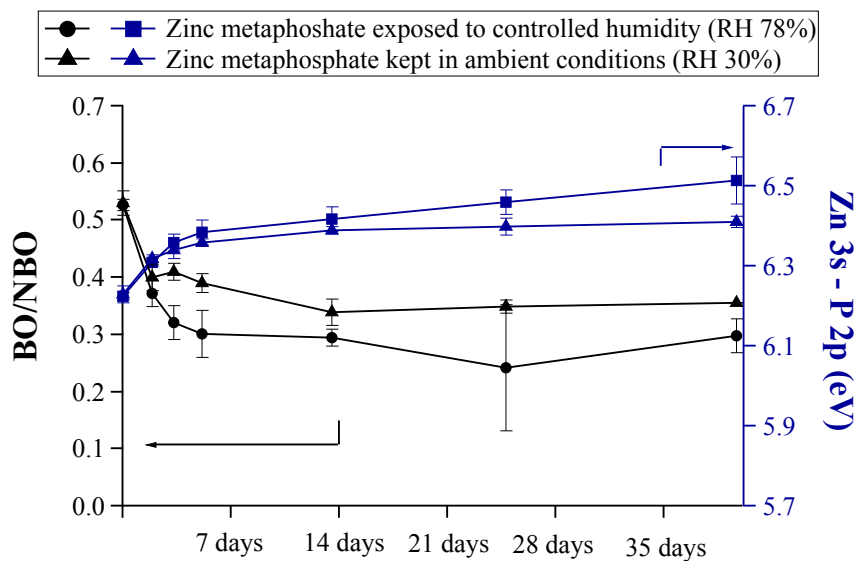


Figure 9.1: BO/NBO ratio and Zn 3s-P 2p BE difference for zinc metaphosphate after different exposure times to different relative humidity (RH) conditions

The tribochemical reaction between iron oxide and long chain-length polyphosphates was first predicted by Martin [2] according to the principles of hard and soft bases [16; 17]. It has been very difficult to obtain any experimental evidence for these tribological reactions: starting from fully formed ZnDTP tribofilms, Canning [18] has observed that long-chain polyphosphates convert to short-chain polyphosphates upon rubbing in base oil. Given the inhomogeneous nature of the tribofilm, this could be due to a depolymerization reaction or to the removal of the outermost layer, richer in long chain polyphosphates, through wear. It has also been shown that an increased contact pressure leads to the formation of tribofilms characterized by shorter-chain lengths [4; 18].

In this work, it has been demonstrated that a long-chain phosphate glass is depolymerized as a consequence of sliding against steel (Chapter 7). The experiments using a quartz ball instead of steel demonstrated that the depolymerization takes place also in absence of iron oxide, as a consequence of high pressure and shear stress. These results demonstrate that it is mainly the tribological stress that is causing the depolymerization of the chains: therefore the long chain-lengths observed in the external part of the tribological film should be regarded as the products of the thermo-oxidative degradation of ZnDTP deposited on the surface from the solution. The gradient in the composition within the depth can be interpreted as a consequence of the fact that the kinetics of film formation is sufficiently high to be able to compete with the combined effects of the reaction with the steel substrate and the hydrolysis—both activated by tribological stress.

The reaction between iron oxide and polyphosphates normally takes place only at high temperatures (above 1300 K). This means that enough energy has to be available for the reaction in the tribological system. The dissipation of energy caused by friction causes a temperature rise that is not uniform but reaches maximum values locally where there contact between the asperities takes place [19]. This temperature spike, known as flash temperature, is believed to play a role in the formation of tribological films [20]. There is no agreement in the literature on the estimate of the flash temperature [20] but it is now believed that temperature alone cannot explain the reactions caused by the tribological stress. Explaining the mechanism of how friction is able to promote the reaction is not the goal of the present thesis, but other groups have done a lot of work in this direction. Nakayama, for example, proposed a model for a tribo-electromagnetic phenomenon, involving tribocharging, triboplasma generation, triboemission of electrons, ions, photons and radicals in oil lubricated sliding conditions [21]. Some of those phenomena, such as the generation of plasma, have been proven by experimental results [21]. Certainly, friction can provide sufficient activation energy for reactions that would not kinetically be possible at room temperature.

### 9.3 Antiwear mechanism of polyphosphate tribofilms

The tribofilms are, therefore, not only the result of a thermal degradation of the additive but also of tribochemical reactions occurring at the interface between the lubricant and the steel surface, activated only by the sliding process. In the previous section the effect of the tribochemical reaction on the composition of the tribofilms was discussed, and the next two questions to be addressed are:

- Is the tribochemical reaction of depolymerization of polyphosphates playing a role in the antiwear action of tribofilms?
- Does the tribofilm antiwear efficiency benefit of the presence of short- or long-chain-length polyphosphates?

One mechanism by which the reaction of polyphosphates with iron oxide could contribute to the antiwear action of polyphosphates is by transforming the abrasive iron oxide particles into ‘softer’ phosphates [2; 22; 23]. In Chapter 7 it has been determined that short-chain-length polyphosphates show lower coefficients of friction and wear rates than the long chain-length ones, while the depolymerization reaction is taking place only on the long-chain length polyphosphates. The experimental data (paragraph 7.4.3) prove that indeed the hypothesized reaction is taking place and is certainly contributing to the friction and wear reduction. However, this reaction cannot explain the low wear rates of short-chain-length polyphosphates, which do not react with iron oxide. Therefore, in this system the “digestion” of iron oxide cannot be considered as the main mechanism of wear reduction.

In the tribofilms formed in the presence of ZnDTP, the depolymerization reaction is also taking place, influencing the composition of the tribofilm and, as a consequence, its antiwear properties: where the shear stress and pressure are high, the polyphosphates are depolymerized, even in absence of iron oxide, giving rise to a harder and tougher film of short-chain-length polyphosphates with a higher wear resistance. These results support the hypothesis that the tribochemical reactions in the film are indeed contributing to the antiwear performance of the tribofilm.

Short-chain-length polyphosphate exhibited higher hardness and Young’s modulus, according to the experimental results on bulk polyphosphates reported in Chapter 4. Unfortunately, as already mentioned in the previous section, the presence of high load and shear stress will dramatically change the structure of the polyphosphates and, as a consequence, their mechanical properties [24]. In fact, the comparison between synthesized polyphosphates and ZnDTP tribofilms with the same chain-length showed an enhancement of the Young’s modulus by a factor of 3 for the tribological samples [24]. In this comparison it has also to be considered that polyphosphate glasses are only a model for the actual tribofilm, which presents a much more heterogeneous composition (it might contain e.g. iron oxide, sulfides,

sulfates and organic phosphates) that could further influence its mechanical and tribochemical properties. According to Baikova et al [25], the Young's modulus of polyphosphate glasses is directly proportional to the total bonding energy per unit volume,  $U_m$  (Paragraph 2.4.3). We can hypothesize an increase in the atomic packing density of the glasses formed under a high load [26] that would result in an increase of  $U_m$  and, most probably, of the Young's modulus. The reversed indentation size effect (RISE) in the microindentation tests (Chapter 4, Paragraph 4.2.1) suggests that polyphosphate glasses are releasing the indentation stress, thereby densifying their structure. The correlation between atomic packing densities and the mechanical properties is well known also for other categories of glasses [27]. Silica glasses and even sand are known to change dramatically their mechanical properties through high-pressure densification [28; 29]. Glasses with low atomic packing densities are found to deform mainly through densification [29].

It has been found that the hardness of the tribofilms formed is comparable to the mean applied pressure in the rubbing contact [30]. The ability of polyphosphates to change composition and structure under high load and shear stress is certainly contributing to the capability of ZnDTP tribofilms to respond to a wide range of conditions.

The most widely accepted model for the antiwear action of ZnDTP is that the polyphosphates act as sacrificial film (Chapter 2, section 2.2). This model is in contrast with the experimental evidence that very little wear is observed on the fully formed tribofilms even when the ZnDTP solution is removed and they are rubbed for long time in pure base oil [7]. The tribological results in Chapters 7 and 8 have shown that the polyphosphate transfer film formed on the steel ball during sliding is able to reduce friction and prevent wear. The ability to form transfer films on bare steel surfaces has been observed before also on ZnDTP tribofilms. The following hypothesis can be formulated: once the tribofilm is formed, most of the wear particles formed do not leave the contact (Chapter 2, Figures 2.3 and 2.4) but participate in withstanding the load and accommodating the velocity difference, thereby minimizing any further wear of the film.

Finally, another mechanism by which the tribochemical reactions could participate in the wear mechanism is by providing a strong adhesion to the substrate through the compositional gradient that is formed at the interface with the steel substrate. The phosphate layer seems to be inter-grown with the oxide layer on steel and the composition varies gradually from iron containing to zinc containing phosphates. The experiments in chapter 7 show that an adhesive zinc phosphate transfer film can also be formed in the absence of iron, on a quartz ball. On the other hand, a chemical interaction through the formation of Si-O-P bonds, at the interface between quartz and the polyphosphate transfer film cannot be completely ruled out



[31]. When investigating the interaction of lubricant additives with diamond-like carbon (DLC) coatings, Equey reported that ZnDTP tribofilms formed on DLC showed significantly lower adhesion to the substrate in comparison with those formed on steel [32]. The capability of ZnDTP to form adhesive tribofilms is clearly dependent on the nature of the substrate.

#### **9.4 Effect of the cation in the tribochemistry of polyphosphate glasses; ashless thiophosphates and interaction of ZnDTP with other additives**

There are many differences between the performance of ZnDTP and of ashless thiophosphates, not only related to the composition of the tribofilm that they form during a mechanical test. Ashless thiophosphates, for example, do not behave as good antioxidants at high temperatures [33]—a capability which is believed to play a role in the antiwear mechanism of ZnDTP by preventing a corrosive attack to the steel that could interact synergistically with wear. Moreover, the oxidation of the base oil causes the formation of carbonate and carboxylate species that can have a detrimental effect on the antiwear efficiency. When using this class of additives, an antioxidant has to be added to the oil formulation.

A fundamental problem in tribofilm formation in the absence of zinc is the lack of cations suitable for the formation of polyphosphate networks. The only cation available is the iron in steel; and therefore, the tribofilm formation requires the wear of a certain amount of steel. This will inevitably limit the kinetics of formation of the film and the final film thickness, while, in the case of ZnDTP, the availability of steel is not rate limiting and the kinetics of film formation seem to be controlled mainly by the activation energy (temperature and pressure) [20]. Even if it has been observed that an increase in film thickness is not corresponding to an increase in antiwear efficiency, a minimum film thickness is anyway necessary to guarantee a good protection of the substrate.

A topic to which usually literature pays little attention is the interaction of the antiwear additives with other additives present in the oil formulation. In particular, detergents and dispersants containing a high percentage of calcium are used to minimize the formation of deposits and engine dust at high temperature. Calcium could provide a source of cations for the tribofilms formed in presence of ashless additives. In the case of ZnDTP the formation of mixed Ca and Zn polyphosphates has been already observed in correlation with a deterioration of ZnDTP antiwear properties [34; 35]. Calcium phosphates and mixed zinc and calcium phosphates have been investigated by Mura [36]. A transfer film was found on the balls after the tribological tests against calcium and mixed zinc and calcium polyphosphates. While the friction coefficients were comparable to the case of zinc, the wear coefficients

measured on the balls were higher in the case of calcium metaphosphate. The addition of zinc led to a decrease of the wear rate (Figure 9.1).

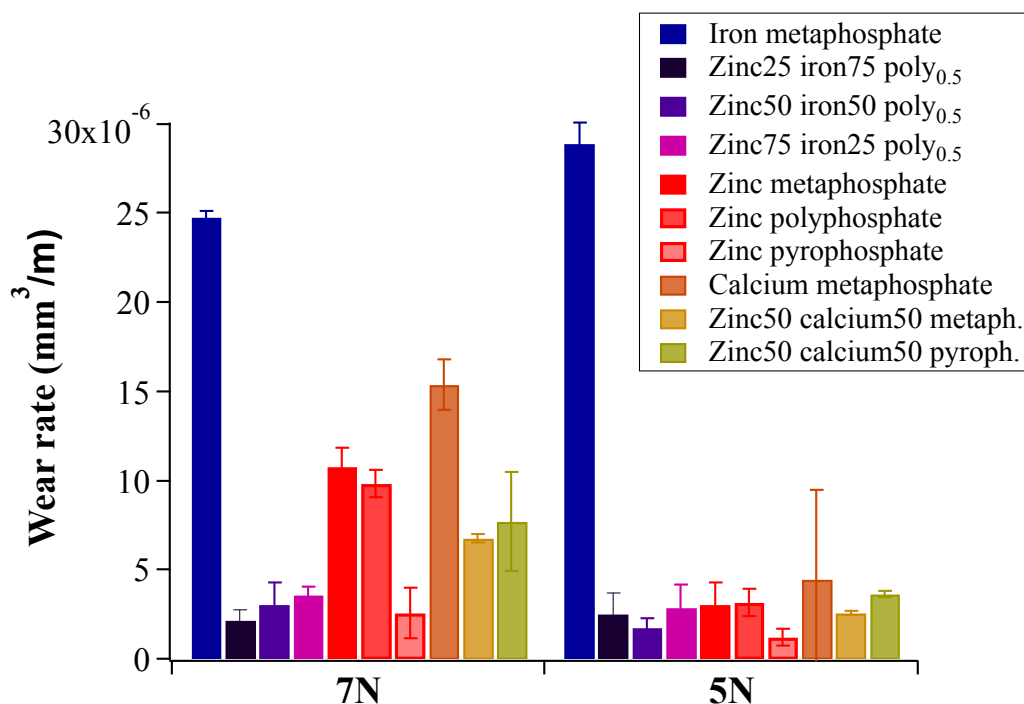


**Figure 9.2: Comparison between the wear rates obtained with steel-versus-zinc polyphosphates, steel-versus-iron poly<sub>0.33</sub>, steel-versus-mixed zinc and iron polyphosphates, steel-versus-calcium meta-phosphate and steel-versus-mixed zinc50 calcium50 polyphosphates tribopairs**

Keeping in mind these findings, one can also wonder if the different tribological behavior of ZnDTPs and ashless thiophosphates could be the result of a difference between the tribological properties of zinc and iron polyphosphates. In fact, a reduction of the wear rate is measured at 7N when iron is added to zinc polyphosphates (Figure 9.2). This is not the case at 5N: at this load the differences are within the experimental uncertainty. This behavior might be ascribed to the fact the applied pressure could induce a rearrangement of the local structure, thus contributing to the mechanical performance of the glass under the applied pressure. In contrast, very high friction and wear are measured for the steel-versus-iron-poly<sub>0.33</sub> tribopair. The iron-poly<sub>0.33</sub> is also not able to form an adhesive transfer film on the steel ball, as opposed to all zinc-containing polyphosphates. As already discussed in the previous sections (Sections 9.3, 8.3 and 7.5), the ability to form an adhesive transfer film is correlated with low friction and wear.

It can be now stated that the key difference between ZnDTP and ashless thiophosphates tribofilms is not the polyphosphate chain-length, but, more likely, the

presence of zinc in the tribofilm. In fact, the addition of zinc to both iron and calcium polyphosphates resulted in an improvement of their tribological properties.

These findings are in agreement with the observations made on the tribofilms formed in presence of mixtures of ZnDTP and DTPs [9; 37], which possess antiwear properties comparable to those formed with pure ZnDTP. In fact DDPs are already partially substituting ZnDTP in commercial oil formulations, in order to reduce their Zn content, as required by modern regulations.

### 9.5 Characteristics of a functional tribofilm

At this point, the main issue to address is what makes Zn polyphosphates so special. The results in Chapter 4 show that the mechanical properties are changing with composition and chain-length. Hardness and Young's modulus have been used to characterize both tribofilm and polyphosphates; in Figure 9.3 the properties of the polyphosphates of different composition investigated in this thesis are plotted as a function of the ratio between the metal oxide content and the phosphorus content corrected by the average oxidation state,  $R_c$  (Chapter 6, Equation 6.1). Higher values of  $R_c$  correspond to shorter chain-lengths (Chapter 6, Figure 6.1).

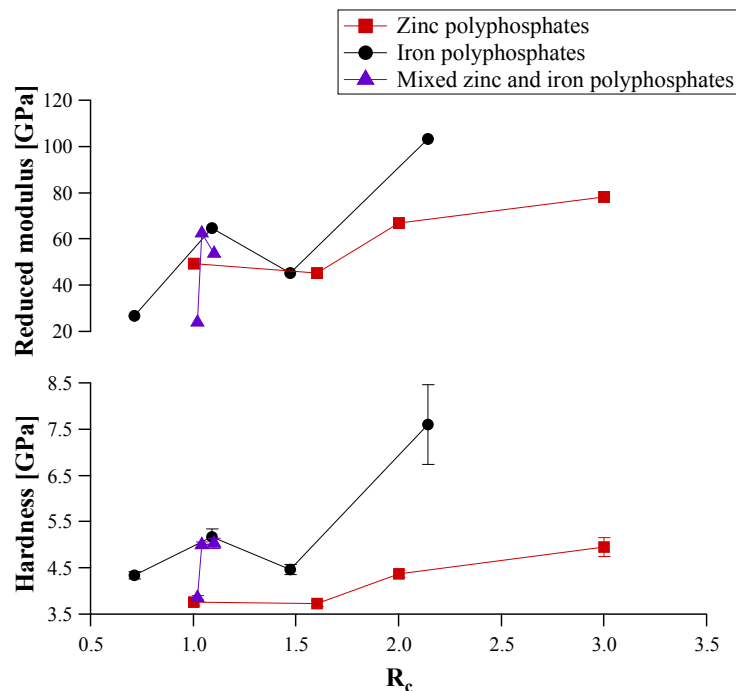


**Figure 9.3: Hardness and reduced modulus of different composition polyphosphates measured by nano-indentation, and plotted as a function of the ratio between the metal oxide content and the phosphorus content, divided by the average oxidation state,  $R_c$  (Chapter 6, equation 6.1)**

Hardness and reduced modulus are both increasing upon decreasing the chain-lengths and with the addition of iron to the polyphosphate composition. Higher

hardness and Young's modulus seems to correlate well with the wear behavior of zinc and mixed zinc and iron polyphosphates (Figure 9.2). Short chain-length zinc polyphosphates show lower wear rates compared to the long-chain ones, but the lowest wear rates are measured for the mixed zinc and iron polyphosphate glasses. On the other hand, the dramatic increase in the wear rate measured for iron poly<sub>0.33</sub> does not correspond to significant change in hardness or reduced modulus. These findings are strongly supporting the idea that the surface chemistry plays a very important role in tribology.

Other mechanical properties could also play an important role in this case. Toughness, for example, which describes the material's resistance to fracture, and is usually mutually exclusive with hardness, has been found to be important for wear-resistant materials [38; 39]. Strong (hard) and tough materials can be obtained by tuning the structure of the material on different length-scales [39]. For these reasons it would be necessary to investigate the tribofilm and transfer-film mechanical properties, which are certainly different from those of the bulk materials investigated here. However, it has to be admitted that the analytical tools available in this regard are still inadequate [19].

A correlation between transfer-film formation and wear protection has been found in this work. In this regard it is also worth examining the case of diamond-like-carbon (DLC) coatings—a completely different system that is currently considered as a way to circumvent ZnDTP in technical applications. DLC coatings are characterized by a very high hardness (20 to 80 GPa), and very low friction and wear coefficients. When DLC slides against a metal, the formation of a DLC transfer film on the metallic counterpart protects the metal from further wear [40]. The mechanism of transfer-film formation for DLC coatings has also been monitored and studied using *in situ* techniques that provided direct evidence that third-body processes control friction and wear processes [41]. The formation and adhesion of the transfer layer was found to depend on the chemistry of the substrate and on the experimental conditions [40], and therefore chemistry (or tribochemistry) can be considered to be part of the third-body mechanism for DLC coatings. As described in the previous section, tribochemistry is also likely to promote the adhesion of the transfer layer in the case of zinc polyphosphates. In conclusion, a functional tribofilm should be characterized by high hardness and Young's modulus, adhere strongly to the substrate and, at the same time, it should be able to form a cohesive low-shear-modulus third body.

More fundamental work in this direction is needed in order to find a reliable method to predict the antiwear properties of a tribopair.

## References

- [1] Eglin M., Rossi A., and Spencer N. D.: X-ray photoelectron spectroscopy analysis of tribostressed samples in the presence of ZnDTP: a combinatorial approach. *Tribol. Lett.* 15, 199-209 (2003).
- [2] Martin J.: Antiwear mechanisms of zinc dithiophosphate: a chemical hardness approach. *Tribol. Lett.* 6, 1-8 (1999).
- [3] Spedding H., and Watkins R. C.: The antiwear mechanism of zddp's. Part I. *Tribol. Int.* 15, 9-12 (1982).
- [4] Heuberger R., Rossi A., and Spencer N. D.: Pressure Dependence of ZnDTP Tribochemical Film Formation: A Combinatorial Approach. *Tribol. Lett.* 28, 209-222 (2007).
- [5] Heuberger R., Rossi A., and Spencer N. D.: XPS study of the influence of temperature on ZnDTP tribofilm composition. *Tribol. Lett.* 25, 185-196 (2007).
- [6] Nicholls M. A., Norton P. R., Bancroft G. M., Kasrai M., Do T., Frazer B. H., and De Stasio G.: Nanometer scale chemomechanical characterization of antiwear films. *Tribol. Lett.* 17, 205-216 (2004).
- [7] Spikes H.: The History and Mechanisms of ZDDP. *Tribol. Lett.* 17, 469-489 (2004).
- [8] Martin J. M., Belin M., Mansot J. L., Dexpert H., and Lagarde P.: Friction-Induced Amorphization with ZDDP, an EXAFS Study. *A S L E Transactions* 29, 523-531 (1986).
- [9] Zhang Z., Yamaguchi E. S., Kasrai M., Bancroft G. M., Liu X., and Fleet M. E.: Tribofilms generated from ZDDP and DDP on steel surfaces: Part 2, chemistry. *Tribol. Lett.* 19, 221-229 (2005).
- [10] Yin Z., Kasrai M., Fuller M., Bancroft G. M., Fyfe K., and Tan K. H.: Application of soft X-ray absorption spectroscopy in chemical characterization of antiwear films generated by ZDDP Part I: the effects of physical parameters. *Wear* 202, 172-191 (1997).
- [11] Martin J. M., Grossiord C., Le Mogne T., Bec S., and Tonck A.: The two-layer structure of Zndtp tribofilms: Part I: AES, XPS and XANES analyses. *Tribol. Int.* 34, 523-530 (2001).
- [12] Mosey N. J., Woo T. K., Kasrai M., Norton P. R., Bancroft G. M., and Müser M. H.: Interpretation of experiments on ZDDP anti-wear films through pressure-induced cross-linking. *Tribol. Lett.* 24, 105-114 (2006).
- [13] Willermet P. A., Dailey D. P., Carter R. O., Schmitz P. J., and Zhu W.: Mechanism of Formation of Antiwear Films from Zinc Dialkyldithiophosphates. *Tribol. Int.* 28, 177-187 (1995).
- [14] Fuller M., Yin Z., Kasrai M., Bancroft G. M., Yamaguchi E. S., Ryason P. R., Willermet P. A., and Tan K. H.: Chemical characterization of tribochemical and thermal films generated from neutral and basic ZDDPs using X-ray absorption spectroscopy. *Tribol. Int.* 30, 305-315 (1997).
- [15] Nedelcu I., Piras E., Rossi A., and Pasaribu H. R.: XPS analysis on the influence of water on the evolution of zinc dialkyldithiophosphate-derived reaction layer in lubricated rolling contacts. *Surf. Interface Anal.* Published online, (2011).
- [16] Pearson R. G.: *Chemical hardness* Wiley, New York (1997).
- [17] Martin J. M., Minfray C., Miyamoto A., Kubo M., and Onodera T.: Acid-base tribochemical reactions under boundary lubrication. *Abstracts of Papers of the American Chemical Society* 231, - (2006).

- [18] Canning G. W., Suominen Fuller M. L., Bancroft G. M., Kasrai M., Cutler J. N., De Stasio G., and Gilbert B.: Spectromicroscopy of tribological films from engine oil additives. Part I. Films from ZDDP's. *Tribol. Lett.* 6, 159-169 (1999).
- [19] Stachowiak G. W., and Batchelor A. W.: *Engineering tribology*, Elsevier, Amsterdam (1993).
- [20] Fujita H., and Spikes H. A.: The formation of zinc dithiophosphate antiwear films. *PROC. INST. MECH. ENG. J.* 218, 265-277 (2004).
- [21] Nakayama K.: The plasma generated and photons emitted in an oil-lubricated sliding contact. *Journal of Physics D-Applied Physics* 40, 1103-1107 (2006).
- [22] Minfray C., Le Mogne T., Martin J.-M., Onodera T., Nara S., Takahashi S., Tsuboi H., Koyama M., Endou A., Takaba H., Kubo M., Del Carpio C. A., and Miyamoto A.: Experimental and Molecular Dynamics Simulations of Tribochemical Reactions with ZDDP: Zinc Phosphate-Iron Oxide Reaction. *Tribol. Trans.* 51, 589 - 601 (2008).
- [23] Minfray C., Le Mogne T., Lubrecht A. A., and Martin J. M.: Experimental simulation of chemical reactions between ZDDP tribofilms and steel surfaces during friction processes. *Tribol. Lett.* 21, 67-78 (2006).
- [24] Pawlak Z., Yarlagadda P. K. D. V., Frost R., and Hargreaves D.: The mechanical characteristics of phosphate glasses under high temperature and friction-induced cross-linking processes. *Journal of Achievements in Materials and Manufacturing Engineering* 37, 458-465 (2009).
- [25] Baikova L. G., Pukh V. P., Fedorov Y. K., Sinani A. B., Tikhonova L. V., and Kireenko M. F.: Mechanical properties of phosphate glasses as a function of the total bonding energy per unit volume of glass. *Glass Phys. Chem.* 34, 126-131 (2008).
- [26] Mackenzie J. D.: High-pressure Effects on Oxide Glasses: I, Densification in Rigid State. *Journal of the American Ceramic Society* 46, 461-470 (1963).
- [27] Greaves G. N., Greer A. L., Lakes R. S., and Rouxel T.: Poisson's ratio and modern materials. *Nature Materials* 10, 823-837 (2011).
- [28] Rouxel T., Ji H., Hammouda T., and Moreac A.: Poisson's ratio and the densification of glass under high pressure. *Physical Review Letters* 100, (2008).
- [29] Rouxel T., Ji H., Guin J. P., Augereau F., and Ruffle B.: Indentation deformation mechanism in glass: Densification versus shear flow. *Journal of Applied Physics* 107, 094903-094905 (2010).
- [30] Bec S., Tonck A., Georges J. M., Coy R. C., Bell J. C., and Roper G. W.: Relationship between mechanical properties and structures of zinc dithiophosphate anti-wear films. *Proc. R. Soc. London A* 455, 4181-4203 (1999).
- [31] Massiot P., Centeno M. A., Carrizosa I., and Odriozola J. A.: Thermal evolution of sol-gel-obtained phosphosilicate solids (SiPO). *J. Non-Cryst. Solids* 292, 158-166 (2001).
- [32] Equey S., Investigation on the interaction of lubricant additives with diamond-like carbon coatings, ETH Zurich, Zurich, 2008.
- [33] Mangolini F., Reactivity of Environmentally Compatible Lubricant Additives: an In Situ and Ex Situ Investigation, PhD Thesis No. 19677, ETH Zürich, Zürich, 2011.
- [34] Wan Y., Suominen Fuller M. L., Kasrai M., Bancroft G. M., Fyfe K., Torkelson J. R., Hu Y. F., Tan K. H., Dowson D., Priest M., Dalmaz G., and Lubrecht A. A.: Effects of detergent on the chemistry of tribofilms from ZDDP: studied by X-ray absorption spectroscopy and XPS, *Tribology Series*, Elsevier, 2002, pp. 155-166.
- [35] Willermet P. A., Dailey D. P., Carter R. O., Schmitz P. J., Zhu W., Bell J. C., and Park D.: The composition of lubricant-derived surface layers formed in a lubricated cam/tappet contact II. Effects of adding overbased detergent and dispersant to a simple ZDTP solution. *Tribol. Int.* 28, 163-175 (1995).

- [36] Mura E., Polifosfati di calcio e zinco: caratterizzazione chimica e proprietà meccaniche, Master Thesis, Università degli Studi di Cagliari, 17 Dec 2010.
- [37] Zhang Z., Yamaguchi E. S., Kasrai M., and Bancroft G. M.: Tribofilms generated from ZDDP and DDP on steel surfaces: Part 1, growth, wear and morphology. *Tribol. Lett.* 19, 211-220 (2005).
- [38] Falvo M. R., and Superfine R.: Mechanics and Friction at the Nanometer Scale. *Journal of Nanoparticle Research* 2, 237-248 (2000).
- [39] Ritchie R. O.: The conflicts between strength and toughness. *Nature Materials* 10, 817-822 (2011).
- [40] Hauert R.: An overview on the tribological behavior of diamond-like carbon in technical and medical applications. *Tribol. Int.* 37, 991-1003 (2004).
- [41] Singer I. L., Dvorak S. D., Wahl K. J., and Scharf T. W.: Role of third bodies in friction and wear of protective coatings. *J Vac Sci Technol A* 21, S232-S240 (2003).





## 10 Conclusions and Outlook

### 10.1 Conclusions

The good anti-wear properties of phosphorus-based engine-oil additives are due to the formation of glass-like poly(thio)phosphates under tribological conditions. These polyphosphate glasses act as “smart materials”, their mechanical properties and, as a consequence, the wear resistance adapting to the tribostress applied. A key parameter is considered to be the chain-length of the polyphosphate glasses, but no analytical technique could so far clearly identify this quantity. The new approach of this thesis was to synthesize zinc-, iron- and mixed zinc/iron bulk phosphate glasses with controlled chain lengths and to use these materials as model compounds for tribological tests in pure PAO.

Chain-lengths of these well-characterized model compounds were determined by means of two independent surface-analytical methods. XPS analysis showed that the combined use (two-dimensional plot) of the BO/NBO intensity ratio and the P2p<sub>3/2</sub> chemical shift allows the unambiguous differentiation and identification of the chain length of polyphosphate glasses. Supporting information can be obtained from the modified Auger parameter and the binding energy of the P 3s peak in the valence band. Principal-component analysis was used to identify, in the ToF-SIMS spectra, those high-mass peaks whose intensities were sensitive to chain-length. It can be concluded that the analytical method for chain-length determination of polyphosphate glasses is now successfully established and can be applied to tribostressed samples.

Tribological tests on the model compound polyphosphate discs were carried out using steel and quartz balls as counterparts in a poly- $\alpha$ -olefin (PAO) bath at room temperature. The coefficient of friction and the wear rate measured in the case of zinc polyphosphates were found to be lower compared to iron polyphosphates and were found to decrease with increasing initial chain-length. With the established analytical method, small-area XPS analysis of the discs showed that the composition of the short-chain-length polyphosphates remained unchanged after the tribological stress. The long-chain-length polyphosphates are depolymerized in the wear track as a consequence of a tribochemical reaction. Comparing the results with steel and quartz balls it can be concluded that pressure and shear stress control the depolymerization of the phosphate glass, but the counterpart material also influenced this reaction: iron

oxide from the steel balls reacts with the polyphosphates and promotes their depolymerization.

Imaging-XPS analyses of the steel balls following tribological tests on polyphosphate discs showed the formation of a glassy, phosphorus-containing transfer film in the contact area, reducing friction and wear of the steel ball. For zinc polyphosphates the transfer film is well adherent and compact, in the case of iron phosphates the glass transferred from the disc to the ball during the test is found to accumulate towards the border rather than adhering to the contact area. This corresponds to a higher wear on the ball. It can be concluded that the formation of an adhesive transfer film leads to lower friction and wear on the steel ball, with best results for mixed zinc and iron polyphosphates. Thus, a third body mechanism is governing wear in the steel-versus-polyphosphate tribopair.

Vickers' hardness and the reduced Young's modulus of the polyphosphate model compounds, as measured by micro- and nano-indentation, were found to decrease with increasing chain-length for both zinc- and iron- polyphosphates. Iron polyphosphates were found to be harder than zinc polyphosphates with the same chain-length. Comparing the mechanical with tribological properties it can be concluded that higher hardness correlates well with the better wear behavior of mixed zinc and iron polyphosphates. However, the dramatic increase of the wear rate for the iron poly<sub>0.33</sub> indicates that the chemistry, i.e. essentially the presence of zinc, plays an important role.

In conclusion, these results have led to a better understanding of the anti-wear efficiency of ZnDTP additives. The tribological stress leads to depolymerization reactions and the formation of short-chain polyphosphates that are harder and, thus, more wear-resistant. The presence of iron oxide (steel ball) promotes this depolymerization and might assist good adhesion of the tribofilm on the steel substrate. Ashless P-based additives (without zinc) provide less effective anti-wear resistance because their tribofilms contain only iron polyphosphates, which do not form adhesive transfer films on the steel ball, in contrast to zinc-containing glasses. The presence of zinc in the polyphosphate network thus appears crucial for the antiwear efficiency of the tribofilms.

## 10.2 Outlook

The use of well-characterized polyphosphate model compounds with different iron- and zinc content and controlled chain-lengths turned out to be effective in establishing an unambiguous analytical method for chain-length determination of tribofilms. Additionally, it allows us to gain new insights into the complex interaction between polyphosphate chain-length and tribological stress. This work opens the door to new approaches for following polyphosphate film formation during tribological experiments *in-situ* and for the characterization of the tribofilm *post-mortem*.

The third-body mechanism has been proposed for tribofilm formation in this and other works. This dynamic process is better characterized with the use of *in-situ* techniques. It is possible, for example, to observe the formation and evolution of a third-body compound as a function of time when one of the two sliding counterparts is optically transparent, using *in-situ* monitoring via video analysis [1]. As zinc polyphosphate discs are fully transparent they would be suitable, after optimization of the synthesis and polishing process, for this kind of investigation. The dynamics of transfer-film formation, its growth and eventually its rupture could be observed in real time and related to tribological data.

The method developed to determine the chain length of polyphosphates is in principle ready to be extended, with the help of multivariate analysis, to the processing of ToF-SIMS images. Thanks to the high lateral resolution of ToF-SIMS it will become possible to correlate changes in composition with the topography of the tribofilms. Moreover, the use of the new polyatomic primary ion sources allows sputtering of the sample with minimal damage. Thus the primary ion source can be used to cut a “slice” of the sample with a similar procedure as used in focussed ion beam (FIB) devices. The surface of this cross-section through the tribofilm obtained in this way should show minimal roughness and damage and could be analyzed with ToF-SIMS (or other laterally high-resolution surface analytical technique) after tilting the sample. This would allow an in-depth profile of composition and chain-length identification through the tribofilm from the surface to the substrate.

Furthermore, computational-chemistry methods might be used to investigate relationships between material morphology, adhesion, and sliding friction in polyphosphate at the nanoscale.

Regarding the model compounds themselves and tribotests, several parameters that might influence tribofilm formation have not been investigated in this work, among them the presence of humidity (polyphosphate glasses are easily

depolymerized in the presence of humidity), the influence of sulfur, and the influence of temperature (temperature influences the reaction rate and probably the mechanical properties). Last but not least also the analytical method presented to determine the chain-length can be improved, especially when iron oxide, hydroxides and carbonates are present in the tribofilms together with phosphates. Here shorter-chain-length mixed polyphosphates should be synthesized and analyzed.

### References

- [1] Scharf T. W., and Singer I. L.: Monitoring Transfer Films and Friction Instabilities with In Situ Raman Tribometry. *Tribol. Lett.* 14, 3-8 (2003).

## Appendix

In this chapter, guidance for calibrating the X-ray photoelectron spectrometers (Appendix A.1), for the determination of the parameters used for the quantitative analysis of the polyphosphate glasses (Appendix A.2), is provided, together with the XP-survey spectra of all glasses (Appendix A.3) and the spectra of calcium- and ammonium phosphates that have been taken as reference phosphate materials for the quantitative surface analysis (Appendix A.4). Appendix B follows, in which the routines used for processing the tribological data are reported. Appendix C is dedicated to ToF – SIMS: the spectra of iron and zinc pure oxides are shown together with the spectra obtained using the  $\text{Bi}_1^+$  ion source and the peak-list of the fragments used for the PCA and PLS regression.

## Appendix A XPS

### A.1 Linearity of the binding energy scale of the XP-spectrometers

The XP-spectrometers, PHI Quantera SXM<sup>TM</sup> and Theta Probe, were calibrated weekly according to the international standard ISO 15472:2001, prepared by the Technical Committee ISO/TC 201 (Surface Chemical Analysis), subcommittee 7 (X-ray photoelectron spectroscopy). Sputter-cleaned gold, silver, and copper foils (Purity > 99.99 %, Goodfellow Cambridge Limited, Huntingdon, UK) were used as reference samples. The binding-energy values of the Au 4f<sub>7/2</sub>, Ag 3d<sub>5/2</sub> and Cu 2p<sub>3/2</sub> signals were acquired as a function of pass energy and beam size. The measured values were compared to the expected values to check for any offset or non-linearity of the BE scale. A typical example of calibration of the PHI Quantera SXM<sup>TM</sup> is reported in Table A.1 and Table A.2.

**Table A.1: Binding-energy values (eV) of the Au 4f<sub>7/2</sub>, Ag 3d<sub>5/2</sub> and Cu 2p<sub>3/2</sub> signals and difference,  $\Delta$ , from the corresponding expected values as a function of pass energy, measured for the calibration of the PHI Quantera SXM<sup>TM</sup> with a beam size of 20  $\mu\text{m}$**

<i>Pass Energy (eV)</i>	<i>Au 4f<sub>5/2</sub></i>		<i>Ag 3d<sub>7/2</sub></i>		<i>Cu 2p<sub>3/2</sub></i>	
	<i>BE (eV)</i>	<i><math>\Delta</math> (ISO BE:83.96 eV)</i>	<i>BE (eV)</i>	<i><math>\Delta</math> (ISO BE:368.21 eV)</i>	<i>BE (eV)</i>	<i><math>\Delta</math> (ISO BE:932.62 eV)</i>
<b>6.5</b>	83.97	0.01	368.22	0.01	932.72	0.1
<b>13</b>	83.98	0.02	368.23	0.02	932.73	0.11
<b>26</b>	83.96	0	368.21	0	932.71	0.09
<b>55</b>	83.91	-0.05	368.17	-0.04	932.69	0.07
<b>69</b>	83.95	-0.01	368.21	0	932.70	0.09
<b>112</b>	83.90	-0.06	368.16	-0.05	932.66	0.04
<b>140</b>	83.85	-0.1	368.14	-0.07	932.63	0.01
<b>224</b>	83.92	-0.04	368.18	-0.03	932.65	0.02
<b>280</b>	83.97	0.01	368.22	0.01	932.68	0.06

**Table A.2: Binding-energy values (eV) of the Au 4f<sub>7/2</sub>, Ag 3d<sub>5/2</sub> and Cu 2p<sub>3/2</sub> signals and difference,  $\Delta$ , from the corresponding expected values as a function of pass energy, measured for the calibration of the PHI Quantera SXM<sup>TM</sup> with a beam size of 100  $\mu\text{m}$**

<i>Pass Energy (eV)</i>	<i>Au 4f<sub>5/2</sub></i>		<i>Ag 3d<sub>7/2</sub></i>		<i>Cu 2p<sub>3/2</sub></i>	
	<i>BE (eV)</i>	<i><math>\Delta</math> (ISO BE:83.96 eV)</i>	<i>BE (eV)</i>	<i><math>\Delta</math> (ISO BE:368.21 eV)</i>	<i>BE (eV)</i>	<i><math>\Delta</math> (ISO BE:932.62 eV)</i>
<b>6.5</b>	83.95	-0.01	368.21	0	932.72	0.1
<b>13</b>	83.97	0.01	368.23	0.02	932.72	0.1
<b>26</b>	83.96	0	368.22	0.01	932.70	0.08
<b>55</b>	83.92	-0.04	368.18	-0.03	932.67	0.05
<b>69</b>	83.94	-0.02	368.20	-0.01	932.69	0.07
<b>112</b>	83.89	-0.07	368.16	-0.06	932.64	0.02
<b>140</b>	83.85	-0.11	368.12	-0.09	932.61	-0.01
<b>224</b>	83.90	-0.06	368.16	-0.05	932.62	0
<b>280</b>	83.96	0	368.20	0	932.66	0.04

These BEs were also monitored as a function of time on control charts (Figure A.1). An accuracy of  $\pm 0.1$  eV on the BE scale was obtained.

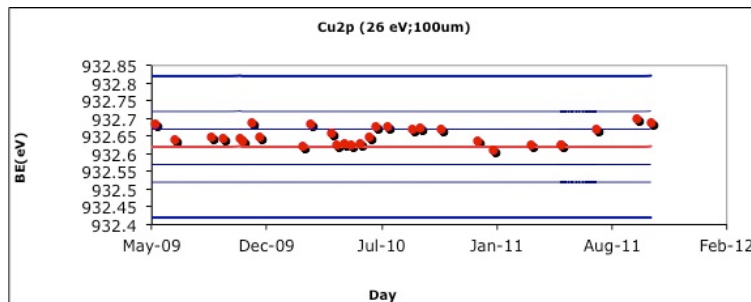


**Figure A.1: Example of control chart: BE of the Cu 2p<sub>3/2</sub> signal as a function of time (PHI Quantera SXM<sup>TM</sup>)**

### A.2 Sensitivity factors

In this Appendix, the parameters used in this thesis for calculating the concentration of the elements constituting the polyphosphate glasses from the peak areas of the XP-spectra are reported.

Table A.3 lists the values used for the calculation of the inelastic mean free path using the Tanuma, Powell and Penn approach [1]:

Equation A.1

$$\lambda = \frac{E}{\left\{ E_p^2 \left[ \beta \ln(\gamma E) - \left( \frac{C}{E} \right) + \left( \frac{D}{E^2} \right) \right] \right\}}$$

$$\beta = -0.10 + \frac{0.944}{(E_p^2 + E_g^2)^{0.5}} + 0.069 \cdot \rho^{0.1}$$

$$\gamma = 0.191 \cdot \rho^{-0.5}$$

$$C = 1.97 - 0.91 \cdot U$$

$$D = 53.4 - 20.8 \cdot U$$

$$U = \frac{N_v \cdot \rho}{M} = \frac{E_p^2}{829.4}$$

where  $\rho$  is the density,  $N_v$  is the number of valence electrons and  $E_g$  the band gap energy.

The energy band gap for the zinc polyphosphates was measured using a Cary 1E instrument (Varian, Australia). The UV – visible spectra are shown in Figure A.2. For the iron and mixed-iron polyphosphates  $E_g$  was assumed to be constant at the values of zinc orthophosphate reported in [2]:

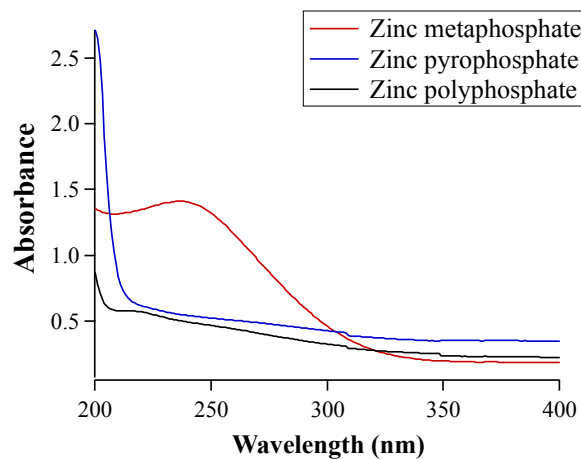


Figure A.2: UV-visible spectra of zinc metaphosphate, zinc poly<sub>0.67</sub> and zinc pyrophosphate



**Table A.3: Parameters used for the calculation of  $\lambda$  with the TPP-2M formula  
(Paragraph 3.5.4)**

<i>Compound</i>	<i>Formula</i>	<i>Density <math>\rho</math> [g/cm<sup>3</sup>]</i>	<i>Number of valence electrons <math>N_v</math></i>	<i>Energy Band gap <math>E_g</math> [eV]</i>
<i>Zinc metaphosphate</i>	Zn(PO <sub>3</sub> ) <sub>2</sub>	2.9	58	3.6
<i>Zinc poly<sub>0.67</sub></i>	Zn <sub>4</sub> P <sub>6</sub> O <sub>19</sub>	3.1	192	6.1
<i>Zinc pyrophosphate</i>	Zn <sub>2</sub> P <sub>2</sub> O <sub>7</sub>	3.4	76	5.9
<i>Zinc orthophosphate</i>	Zn <sub>3</sub> (PO <sub>4</sub> ) <sub>2</sub>	4.0	94	3.4
<i>Iron poly<sub>0.33</sub></i>	Fe <sub>2</sub> O <sub>3</sub> 3(P <sub>2</sub> O <sub>5</sub> )	2.8	154	3.4
<i>Iron poly<sub>0.5</sub></i>	Fe <sub>2</sub> O <sub>3</sub> 2(P <sub>2</sub> O <sub>5</sub> )	2.8	114	3.4
<i>Iron poly<sub>0.67</sub></i>	Fe <sub>4</sub> P <sub>6</sub> O <sub>21</sub>	2.9	188	3.4
<i>Iron poly<sub>1</sub></i>	Fe(PO <sub>4</sub> )	3.2	37	3.4
<i>Zinc75 iron25 poly<sub>0.5</sub></i>	FeZn <sub>3</sub> (PO <sub>3</sub> ) <sub>8</sub>	2.9	251	3.4
<i>Zinc50 iron50 poly<sub>0.5</sub></i>	Fe <sub>2</sub> Zn <sub>2</sub> P <sub>6</sub> O <sub>19</sub>	2.9	184	3.4
<i>Zinc25 iron75 poly<sub>0.5</sub></i>	Fe <sub>3</sub> Zn(PO <sub>3</sub> ) <sub>8</sub>	2.9	220	3.4

**Table A.4: Values of cross section  $\sigma_A$ , asymmetry factor  $L_A(\gamma)$  and sensitivity factors  $S_A$  (valid for the PHI Quantera SXM<sup>TM</sup> spectrometer) as a function of the signal A for all polyphosphates investigated in this thesis. The sensitivity factors are calculated as reported in Paragraph 3.5.4**

<i>Zinc polyphosphates</i>						
<i>Signal A</i>	$\sigma_A$ <i>Barns</i>	$L_A(\gamma)$	$S_A$ ( <i>Zinc metaphosphate</i> )	$S_A$ ( <i>Zinc poly<sub>0.67</sub></i> )	$S_A$ ( <i>Zinc pyrophosphate</i> )	$S_A$ ( <i>Zinc orthophosphate</i> )
<i>P 2p</i>	1.192	0.86	1.9	1.8	1.9	1.7
<i>Zn 3s</i>	1.04	0.75	1.4	1.4	1.6	1.3
<i>Zn 2p<sub>3/2</sub></i>	18.92	0.82	14.8	14.4	14.9	13.8
<i>O1s</i>	2.93	0.75	3.3	3.2	3.3	3.1
<i>Cl1s</i>	1	0.75	1.3	1.2	1.3	1.2
<i>Iron polyphosphates</i>						
<i>Signal A</i>	$\sigma_A$ <i>Barns</i>	$L_A(\gamma)$	$S_A$ ( <i>Iron poly<sub>0.33</sub></i> )	$S_A$ ( <i>Iron poly<sub>0.5</sub></i> )	$S_A$ ( <i>Iron poly<sub>0.67</sub></i> )	$S_A$ ( <i>Iron poly<sub>1</sub></i> )
<i>P 2p</i>	1.192	0.86	2.18	2.11	2.70	2.64
<i>Fe 2p<sub>3/2</sub></i>	10.82	0.82	12.5	12.1	12.3	12.1
<i>O1s</i>	2.93	0.75	3.6	3.5	3.6	3.5
<i>Cl1s</i>	1	0.75	1.5	1.4	1.4	1.4
<i>Mixed zinc and iron polyphosphates</i>						
<i>Signal A</i>	$\sigma_A$ <i>Barns</i>	$L_A(\gamma)$	$S_A$ ( <i>Iron poly<sub>0.33</sub></i> )	$S_A$ ( <i>Iron poly<sub>0.5</sub></i> )	$S_A$ ( <i>Zinc25 iron75 poly<sub>0.5</sub></i> )	
<i>P 2p</i>	1.192	0.86	2.2	2.1	2.2	
<i>Zn 3s</i>	1.04	0.75	1.6	1.6	1.6	
<i>Zn 2p<sub>3/2</sub></i>	18.92	0.82	15.0	15.0	15.0	
<i>Fe 2p<sub>3/2</sub></i>	10.82	0.82	12.3	12.3	12.3	
<i>O1s</i>	2.93	0.75	3.6	3.6	3.6	
<i>Cl1s</i>	1	0.75	1.4	1.4	1.4	

### A.3 Survey spectra

The survey spectra for all polyphosphates under investigation in Chapter 5 are reported in the following.

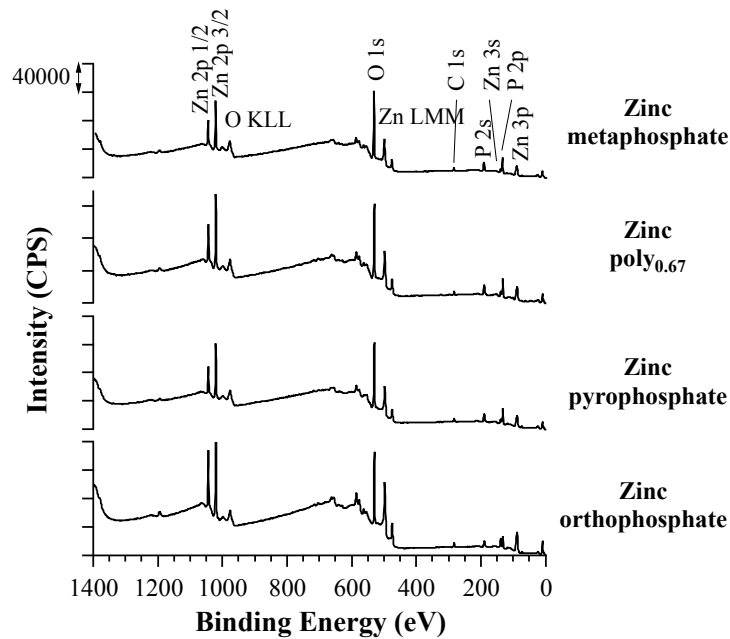


**Figure A.3: Survey XP-spectra of zinc metaphosphate, zinc poly<sub>0.67</sub>, zinc pyrophosphate and zinc orthophosphate**

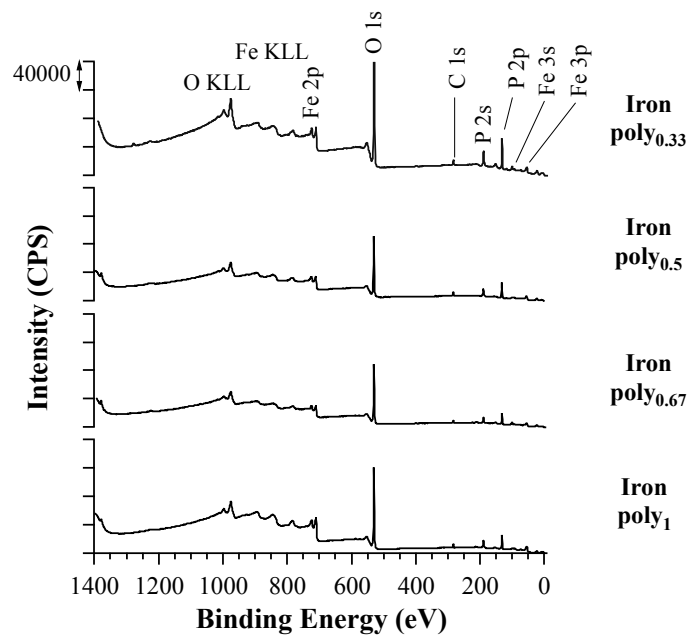


**Figure A.4: Survey XP-spectra of iron poly<sub>0.67</sub>, iron poly<sub>0.5</sub>, iron poly<sub>0.33</sub> and iron poly<sub>1</sub>**

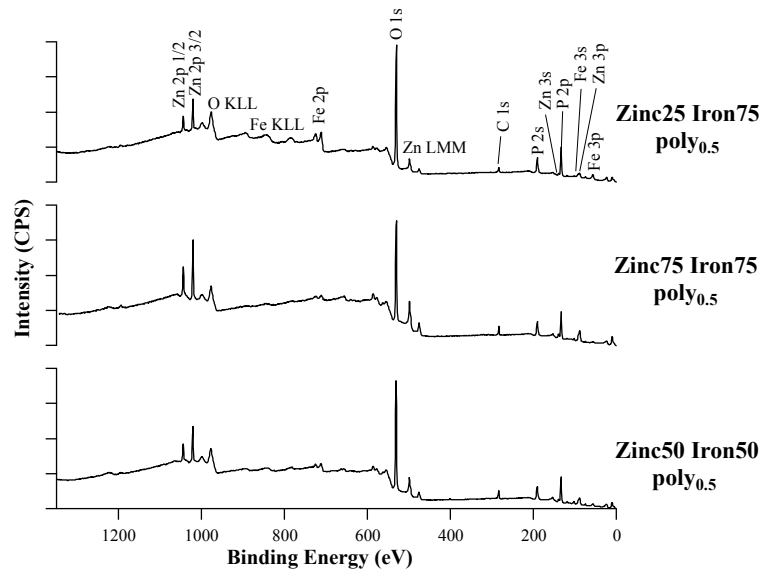


**Figure A.5: Survey XP-spectra of zinc25 iron75 poly<sub>0.5</sub>, zinc50 iron50 poly<sub>0.5</sub> and zinc75 iron25 poly<sub>0.5</sub>**

#### A.4 Reference Phosphate compounds

##### *Calcium phosphate*

Calcium phosphate,  $\text{Ca}_3\text{P}_2\text{O}_8$  in crystalline powder, has been pressed into a pellet and analyzed by XPS as reference compound.

In Figure A.7, the high-resolution spectra for the P 2p, P 2s, O 1s and Ca 2p signals are reported.

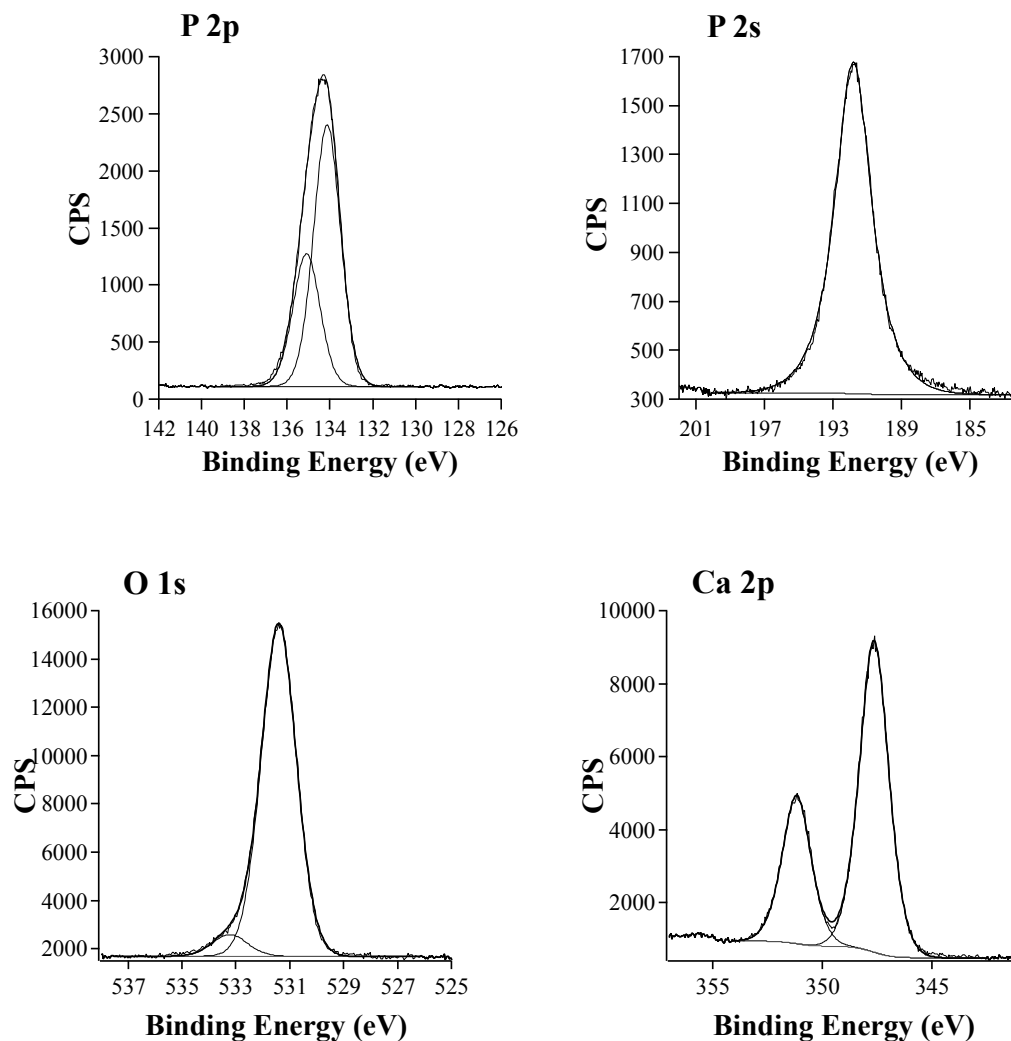


**Figure A.6: Phosphorus, P2p, phosphorus, P3s, oxygen, O1s, calcium, Ca2p, high-resolution spectra for calcium phosphate (data acquired with the PHI Quantera SXM™)**

The P2p was curve-fitted with two components: the  $\text{P}2\text{p}_{3/2}$  was found at  $133.2 \pm 0.1$  eV while the  $\text{P}2\text{p}_{1/2}$  at  $134.2 \pm 0.1$  eV. The P 2s was curve fitted with a single component and its maximum has a binding energy value of  $190.0 \pm 0.1$  eV. The component assigned to the NBO for the O 1s spectrum was found  $531.4 \pm 0.1$  eV while the BO component at  $533.2 \pm 0.1$  eV. Finally the  $\text{Ca } 2\text{p}_{3/2}$  was found at  $347.6 \pm 0.1$  eV

while the Ca  $2p_{1/2}$  at  $351.2 \pm 0.1$  eV. The results of the quantitative analysis are reported in Table A.6 and compared with the stoichiometric composition. As already observed for the zinc phosphate samples, the phosphorus content has been overestimated by the XPS analysis and this is also the element that shows the largest relative error ( $\sim 16\%$  calculated as the difference from the expected value).

**Table A.5: Composition of calcium phosphate**

	<i>[P]</i>	<i>[Ca]</i>	<i>[O]</i>
<i>Stoichiometric</i>	15.4 at. %	23.1 at. %	61.5 at. %
<i>XPS</i>	18 at. %	25 at. %	57 at. %

*Ammonium dihydrogen phosphate*

Ammonium dihydrogen phosphate,  $\text{NH}_4\text{H}_2\text{PO}_4$  in crystalline powder, has been pressed into a pellet and analyzed by XPS as reference compound.

In Figure A.7, the high-resolution spectra for the P 2p, P 2s, O 1s and N 1s signals are reported. The P2p<sub>3/2</sub> was found at  $133.9 \pm 0.1$  eV, while the P2p<sub>1/2</sub> was at  $134.8 \pm 0.1$  eV. The P2s signal has a binding energy value of  $191.6 \pm 0.1$  eV. The component assigned to the NBO for the O 1s spectrum was found at  $531.7 \pm 0.1$  eV while the BO component at  $533.2 \pm 0.1$  eV. Finally the N 1s was found at  $402.0 \pm 0.1$  eV.

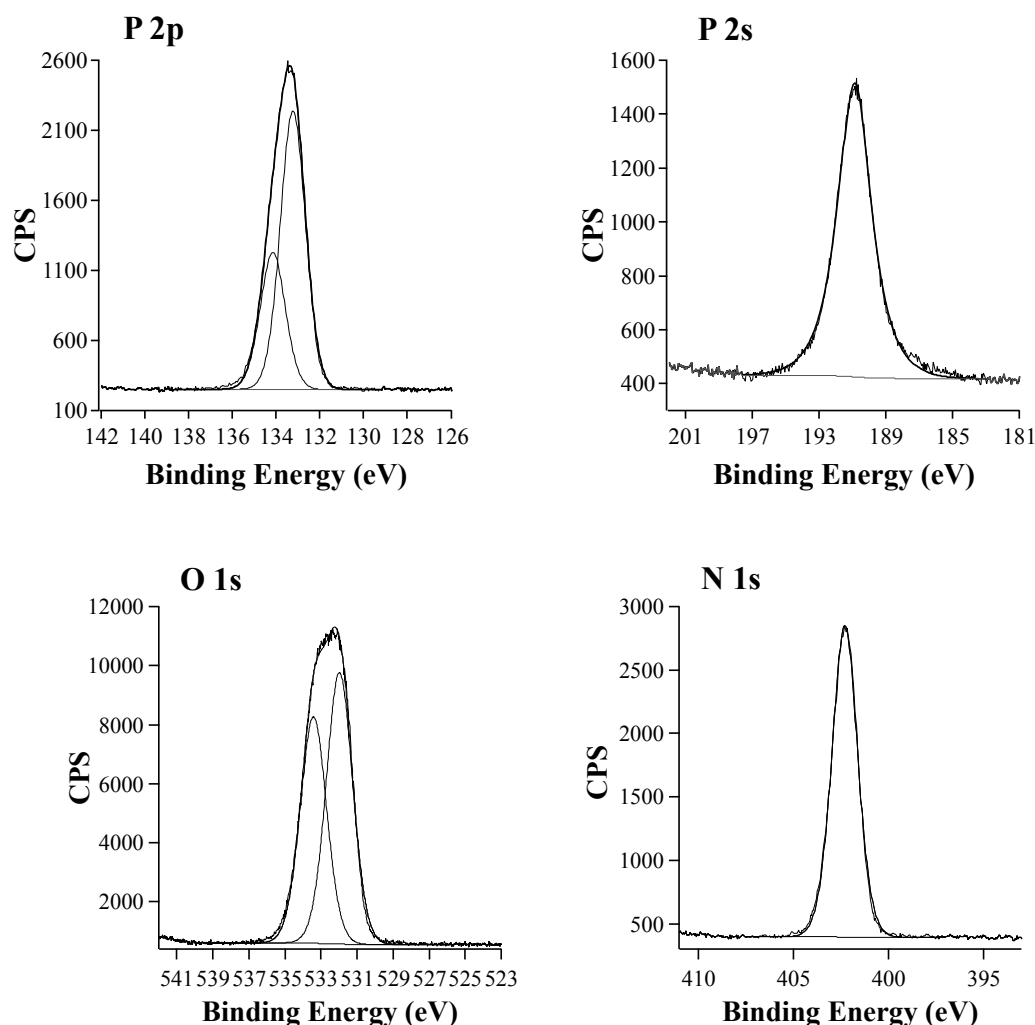


**Figure A.7: Phosphorus, P2p, phosphorus, P3s, oxygen, O1s, nitrogen, N1s, high-resolution spectra for ammonium dihydrogen phosphate (data acquired with the PHI Quantera SXM™)**

The results of the quantitative analysis in comparison with the stoichiometric composition are reported in Table A.6. As already observed for the zinc

polyphosphates, and calcium phosphate the phosphorus content is overestimated by the XPS analysis.

**Table A.6: Composition of calcium phosphate**

	<i>[P]</i>	<i>[N]</i>	<i>[O]</i>
<i>Stoichiometric</i>	16.7 at.%	16.7 at.%	66.6 at.%
<i>XPS</i>	20.4 at.%	13.1 at.%	66.5 at.%



## Appendix B Processing of tribological data

An example of the Matlab R20011a software (The MathWorks, Inc., Natick, MA, USA) routine used to process the tribological data obtained with the CETR tribometer is reported in the following:

```

%LOAD DATA
%
clear all
close all
[filename, pathname] = uigetfile('*.txt', 'Pick an M-file');cd(pathname);
[Fx Fz Time Distance Turns
Diameter]=textread(filename, '%f%f%f%f%f', 'headerlines', 13);
% COF calculation
mu=abs(Fx./Fz);
Muav=mean(mu)
muerr=std(mu)
%
radius=input('radius in mm = ');
%
Turns=abs(Turns-fix(Turns(1))); Turn=floor(Turns);T=Turn-Turns;
%
l=max(Turn)-1;
c=zeros(l,1);
b=0;
a=1;
for i=1:(max(Turn)-1)
    b=a+length(find(Turn==i));
    A=mu(a:b);
    a=b;
    k=i+1;
    c(k,1)=mean(A);d(k,1)=std(A);d(k,2)=k*radius*2*3.14;
end
plot(c)
c=[c,d];
raw=[mu,T];
save filename.txt c -ASCII
save filename.txt raw -ASCII

```

**Appendix C TOF-SIMS***C.1 Reference compounds*

The positive and negative mode ToF-SIMS spectra of zinc and iron oxide are depicted in Figure C.1 and Figure C.2. The compounds, in powder form, were pressed into a pellet for analysis.

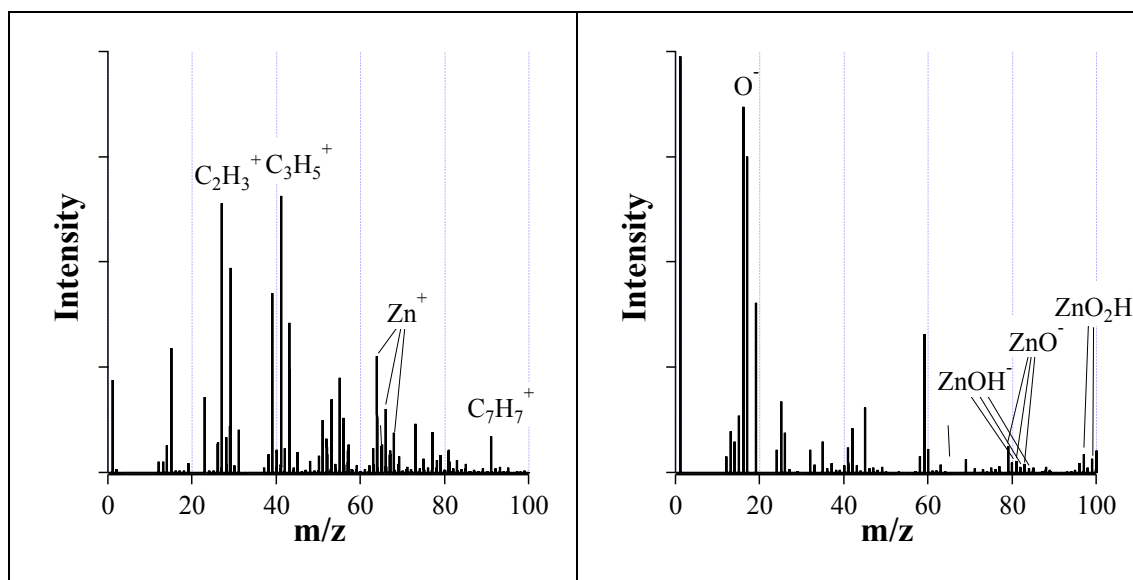


**Figure C.1: Positive (left side) and negative (right side) ToF-SIMS spectra in the mass range 0-100 amu of zinc oxide**

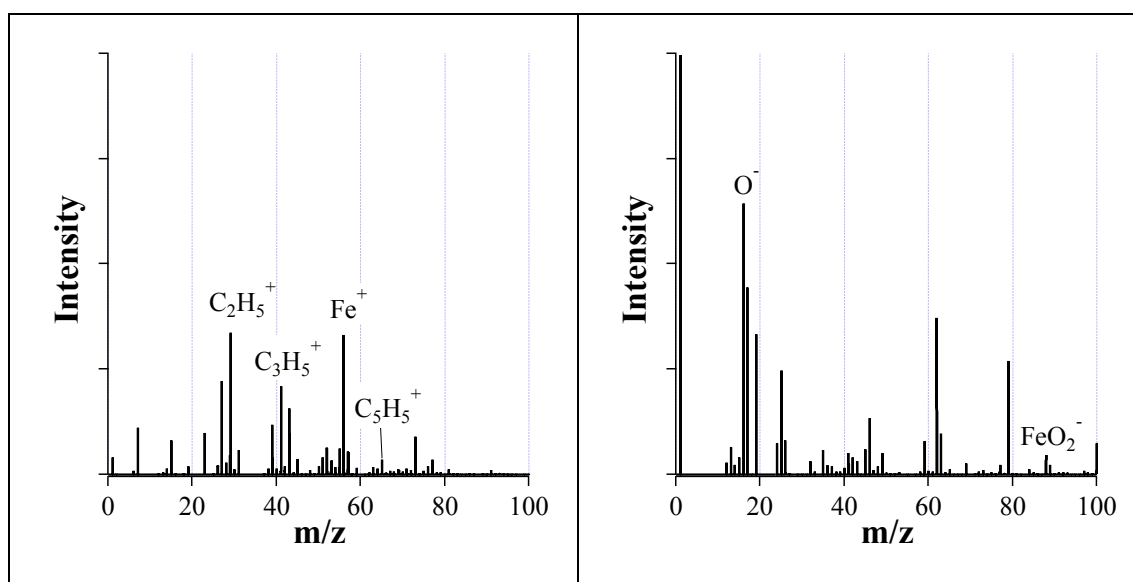


**Figure C.2: Positive (left side) and negative (right side) ToF-SIMS spectra in the mass range 0-100 amu of iron oxide**

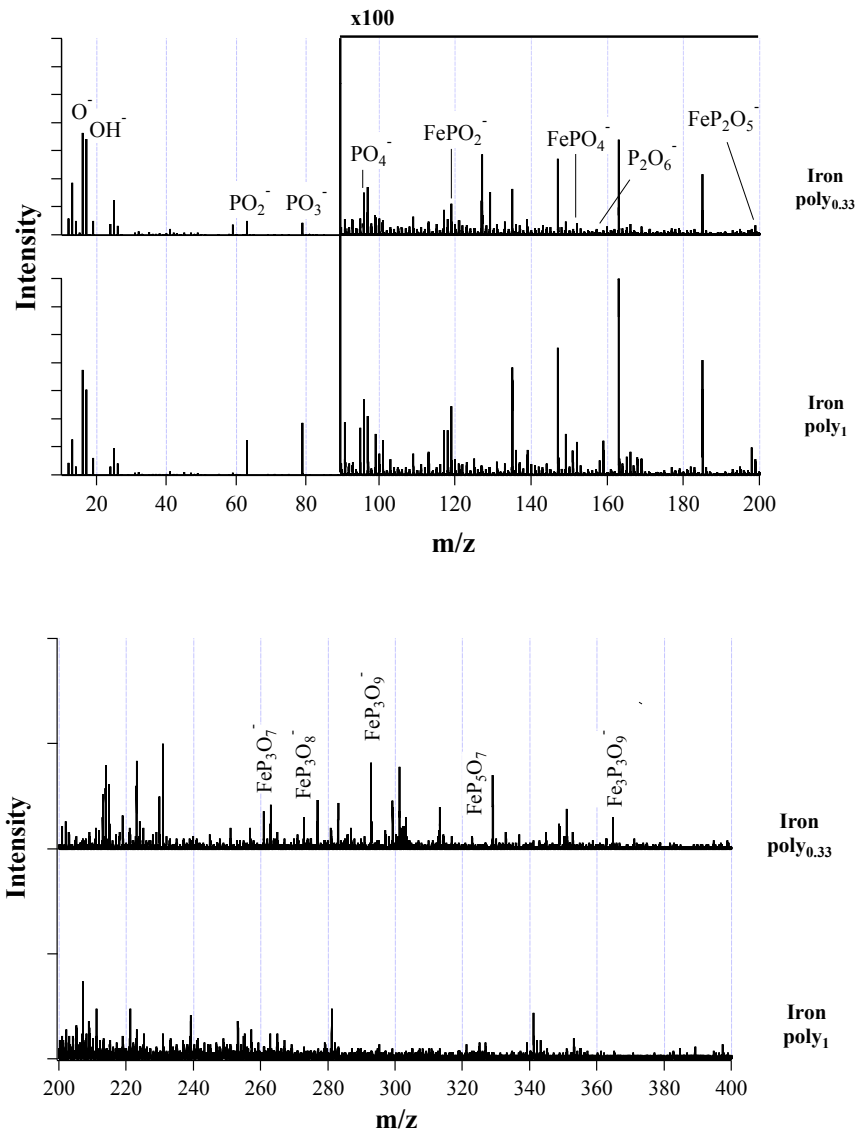
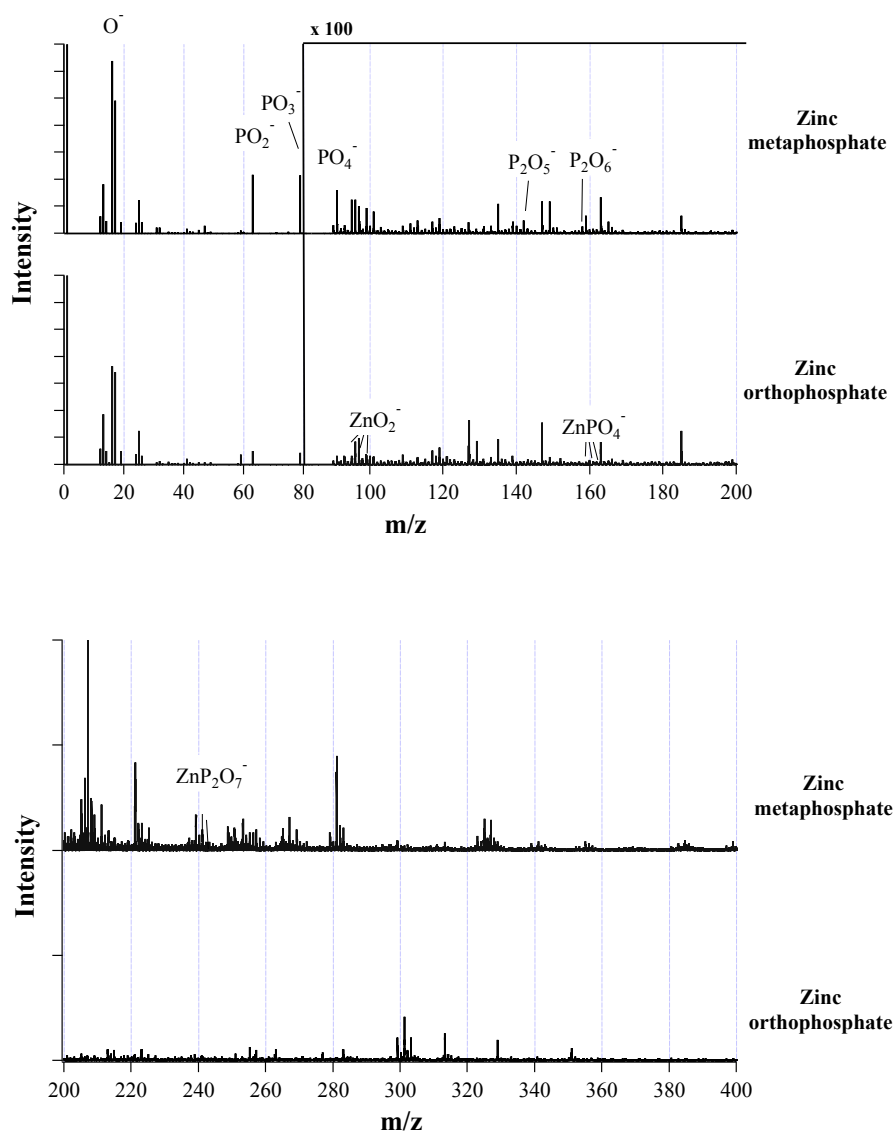
C.2 Spectra acquired with  $\text{Bi}_1^+$  primary ions

Figure C.3: Negative ToF-SIMS spectra in the mass range 0-400 amu of iron poly<sub>0.33</sub> and iron poly<sub>1</sub> acquired with  $\text{Bi}_1^+$  primary ions



**Figure C.4: Negative ToF-SIMS spectra in the mass range 0-400 amu of zinc metaphosphate and zinc orthophosphate acquired with  $Bi_1^+$  primary ions**

C.1 Comparison between normalization methods

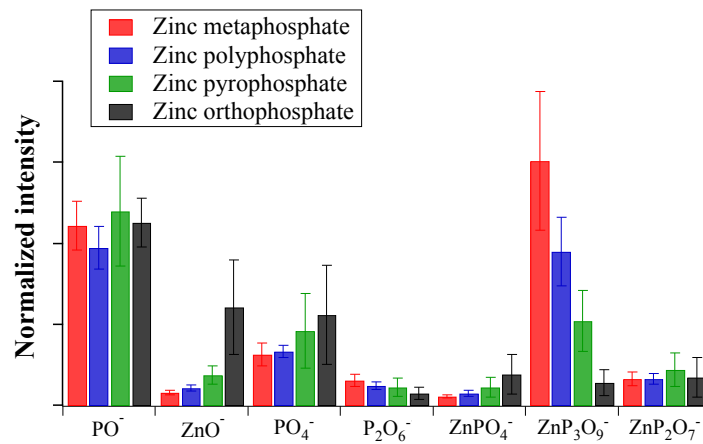


Figure C.5: Comparison between ToF-SIMS peak intensities normalized by the intensity of the P<sup>-</sup> peak corrected by the stoichiometry

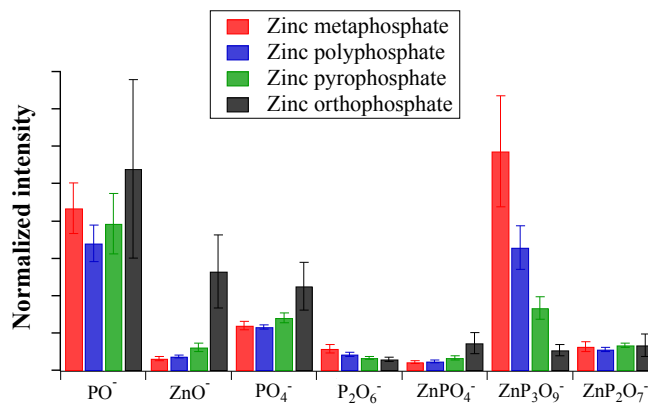


Figure C.6: Comparison between ToF-SIMS intensities normalized by the sum of the selected peak (peak list in Table C.1)

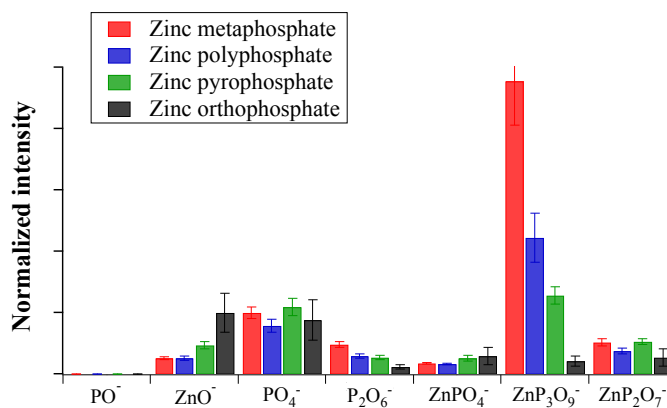


Figure C.7: Comparison between ToF-SIMS intensities normalized by total intensity

C.2 *Peak list*

In Table C.1 is reported the complete peak list of the fragments used for the PCA and PLS regression in chapter 6.

**Table C.1: List of ToF-SIMS relevant fragments identified and used for the multivariate analysis**

Ion	Mass
P <sup>-</sup>	30.97
PO <sup>-</sup>	46.97
Fe <sup>-</sup>	55.93
FeO <sup>-</sup>	71.93
FeOH <sup>-</sup>	72.94
ZnO <sup>-</sup>	79.92
ZnOH <sup>-</sup>	80.93
<sup>66</sup> ZnO <sup>-</sup>	81.93
<sup>68</sup> ZnO <sup>-</sup>	83.93
PO <sub>4</sub> <sup>-</sup>	94.95
FePO <sub>2</sub> <sup>-</sup>	118.89
ZnPO <sub>2</sub> <sup>-</sup>	126.90
<sup>66</sup> ZnPO <sub>2</sub> <sup>-</sup>	128.89
<sup>68</sup> ZnPO <sub>2</sub> <sup>-</sup>	130.89
FePO <sub>3</sub> <sup>-</sup>	134.89
P <sub>2</sub> O <sub>5</sub> <sup>-</sup>	141.92
ZnPO <sub>3</sub> <sup>-</sup>	142.89
<sup>66</sup> ZnPO <sub>3</sub> <sup>-</sup>	144.89
<sup>68</sup> ZnPO <sub>3</sub> <sup>-</sup>	146.89
FePO <sub>4</sub> <sup>-</sup>	150.88
P <sub>2</sub> O <sub>6</sub> <sup>-</sup>	157.91
ZnPO <sub>4</sub> <sup>-</sup>	158.89
<sup>66</sup> ZnPO <sub>4</sub> <sup>-</sup>	160.89
<sup>68</sup> ZnPO <sub>4</sub> <sup>-</sup>	162.90
FePO <sub>5</sub> <sup>-</sup>	166.88
ZnPO <sub>5</sub> <sup>-</sup>	174.88
<sup>66</sup> ZnPO <sub>5</sub> <sup>-</sup>	176.89
<sup>68</sup> ZnPO <sub>5</sub> <sup>-</sup>	178.89
P <sub>3</sub> O <sub>6</sub> <sup>-</sup>	188.89
FeP <sub>2</sub> O <sub>5</sub> <sup>-</sup>	197.85
FePO <sub>7</sub> <sup>-</sup>	198.86
P <sub>3</sub> O <sub>7</sub> <sup>-</sup>	204.89
ZnP <sub>2</sub> O <sub>5</sub> <sup>-</sup>	205.87
ZnPO <sub>7</sub> <sup>-</sup>	206.84
<sup>66</sup> ZnPO <sub>7</sub> <sup>-</sup>	208.86
<sup>68</sup> ZnPO <sub>7</sub> <sup>-</sup>	210.86
FeP <sub>2</sub> O <sub>6</sub> <sup>-</sup>	213.85
FePO <sub>8</sub> <sup>-</sup>	214.86
P <sub>3</sub> O <sub>8</sub> <sup>-</sup>	220.88
ZnP <sub>2</sub> O <sub>6</sub> <sup>-</sup>	221.85
ZnPO <sub>8</sub> <sup>-</sup>	222.85
<sup>66</sup> ZnP <sub>2</sub> O <sub>6</sub> <sup>-</sup>	223.86
<sup>66</sup> ZnPO <sub>8</sub> <sup>-</sup>	224.86
<sup>68</sup> ZnP <sub>2</sub> O <sub>6</sub> <sup>-</sup>	225.85
<sup>68</sup> ZnPO <sub>8</sub> <sup>-</sup>	226.86
FeP <sub>2</sub> O <sub>7</sub> <sup>-</sup>	229.84
ZnP <sub>2</sub> O <sub>7</sub> <sup>-</sup>	237.85
<sup>66</sup> ZnP <sub>2</sub> O <sub>7</sub> <sup>-</sup>	239.85
<sup>68</sup> ZnP <sub>2</sub> O <sub>7</sub> <sup>-</sup>	241.85
ZnP <sub>3</sub> O <sub>6</sub> <sup>-</sup>	252.83
Fe <sub>2</sub> P <sub>2</sub> O <sub>5</sub> <sup>-</sup>	253.79
<sup>66</sup> ZnP <sub>3</sub> O <sub>6</sub> <sup>-</sup>	254.82
FeP <sub>3</sub> O <sub>7</sub> <sup>-</sup>	260.86
FePO <sub>11</sub> <sup>-</sup>	262.86
ZnP <sub>3</sub> O <sub>7</sub> <sup>-</sup>	268.82
Fe <sub>2</sub> P <sub>2</sub> O <sub>6</sub> <sup>-</sup>	269.79
<sup>66</sup> ZnP <sub>3</sub> O <sub>7</sub> <sup>-</sup>	270.82
ZnPO <sub>11</sub> <sup>-</sup>	270.82

$^{68}\text{ZnP}_3\text{O}_7^-$	272.82
$\text{FeP}_3\text{O}_8^-$	276.83
$\text{ZnP}_3\text{O}_8^-$	284.81
$\text{Fe}_2\text{P}_2\text{O}_7^-$	285.78
$\text{Fe}_2\text{PO}_6^-$	286.79
$^{66}\text{ZnP}_3\text{O}_8^-$	286.79
$^{68}\text{ZnP}_3\text{O}_8^-$	288.82
$\text{FeP}_3\text{O}_9^-$	292.81
$\text{ZnP}_3\text{O}_9^-$	300.80
$\text{Fe}_2\text{P}_2\text{O}_8^-$	301.77
$^{66}\text{ZnP}_3\text{O}_9^-$	302.78
$^{66}\text{ZnZnPO}_9^-$	304.81
$^{68}\text{ZnP}_3\text{O}_9^-$	304.81
$\text{FeP}_3\text{O}_6^-$	306.83
$\text{P}_7\text{O}_6^-$	312.79
$\text{Fe}_2\text{P}_3\text{O}_7^-$	316.79
$\text{Zn}_2\text{P}_2\text{O}_8^-$	317.78
$\text{Zn}_2\text{PO}_{10}^-$	318.79
$^{66}\text{ZnZnP}_2\text{O}_8^-$	319.77
$^{66}\text{ZnZnPO}_{10}^-$	320.79
$^{68}\text{ZnZnP}_2\text{O}_8^-$	321.78
$^{66}\text{Zn}_2\text{PO}_{10}^-$	322.77
$\text{FeP}_3\text{O}_7^-$	322.82
$^{68}\text{Zn}^{66}\text{ZnP}_2\text{O}_8^-$	323.77
$\text{P}_7\text{O}_7^-$	328.76
$\text{ZnP}_3\text{O}_7^-$	330.77
$\text{Fe}_2\text{P}_3\text{O}_8^-$	332.75
$\text{P}_7\text{O}_8^-$	344.76
$\text{Zn}_2\text{P}_3\text{O}_8^-$	348.75
$\text{Fe}_2\text{P}_3\text{O}_9^-$	348.75
$\text{Fe}_3\text{P}_2\text{O}_8^-$	357.71
$\text{P}_7\text{O}_9^-$	360.76
$\text{ZnP}_3\text{O}_9^-$	362.73
$\text{Fe}_2\text{P}_3\text{O}_6^-$	362.74
$\text{Zn}_3\text{P}_2\text{O}_7^-$	365.74
$^{68}\text{ZnP}_3\text{O}_6^-$	366.75
$^{66}\text{ZnZnP}_3\text{O}_9^-$	366.75
$^{68}\text{ZnZnP}_3\text{O}_9^-$	368.74
$\text{Fe}_3\text{P}_2\text{O}_9^-$	373.77
$\text{Fe}_2\text{P}_3\text{O}_7^-$	378.76
$\text{Zn}_2\text{P}_3\text{O}_{10}^-$	380.74
$^{66}\text{ZnZnP}_3\text{O}_{10}^-$	382.76
$^{66}\text{Zn}_2\text{P}_3\text{O}_{10}^-$	384.72
$^{68}\text{Zn}^{66}\text{ZnP}_3\text{O}_{10}^-$	386.77
$^{68}\text{Zn}_2\text{P}_3\text{O}_{10}^-$	388.73
$\text{P}_3\text{O}_{15}^-$	394.75
$\text{Fe}_3\text{P}_3\text{O}_9^-$	404.71
$\text{FeP}_7\text{O}_9^-$	416.67
$\text{Fe}_3\text{P}_3\text{O}_{10}^-$	420.67
$\text{P}_9\text{O}_9^-$	422.73
$\text{ZnP}_7\text{O}_9^-$	424.73
$^{66}\text{ZnP}_7\text{O}_9^-$	426.72
$\text{Zn}_3\text{P}_3\text{O}_9^-$	428.75
$\text{Fe}_3\text{P}_3\text{O}_7^-$	434.67
$\text{Fe}_3\text{P}_3\text{O}_{11}^-$	436.66
$\text{P}_8\text{O}_1^{2-}$	439.69
$\text{ZnP}_7\text{O}_{10}^-$	440.69
$^{66}\text{ZnP}_7\text{O}_{10}^-$	442.70
$\text{Zn}_3\text{P}_3\text{O}_6^-$	442.70
$^{66}\text{ZnZnP}_5\text{O}_{10}^-$	444.66
$\text{Zn}_3\text{P}_3\text{O}_{10}^-$	444.67
$^{67}\text{Zn}^{66}\text{ZnP}_6\text{O}_8^-$	446.67
$^{68}\text{Zn}^{66}\text{ZnP}_5\text{O}_{10}^-$	448.66
$\text{FeP}_5\text{O}_{15}^-$	450.69
$\text{P}_9\text{O}_{11}^-$	454.70
$\text{Zn}_3\text{P}_3\text{O}_{11}^-$	460.66
$^{68}\text{ZnZn}_2\text{P}_3\text{O}_{11}^-$	464.65
$^{68}\text{Zn}^{66}\text{ZnZnP}_3\text{O}_{11}^-$	466.67
$\text{FeP}_5\text{O}_{16}^-$	466.68
$^{68}\text{Zn}_2\text{ZnP}_3\text{O}_{11}^-$	468.67

---

$P_9O_{12}^-$	470.70
$P_9O_{13}^-$	486.66
$Fe_4P_3O_{12}^-$	508.58
$Zn_4P_3O_{10}^-$	508.60
$FeP_9O_{14}^-$	558.59
$ZnP_7O_{19}^-$	584.62
$Zn_3P_3O_{12}^-$	604.56
$Fe_2P_9O_{15}^-$	630.51

### *References*

- [1] Tanuma S., Powell C. J., and Penn D. R.: Calculations of electron inelastic mean free paths. *Surf. Interface Anal.* 37, 1-14 (2005).
- [2] Altaf M., Chaudhry M. A., Bilal M. S., and M. Ashfaq Ahmad J.: *Journal of Scientific Research* 19, (2002).



# Curriculum Vitae

## Maura Crobu

### Personal information

Date of Birth August 2, 1982  
Nationality Italian  
Address Wehntalerstrasse 418,  
CH-8046 Zürich  
Switzerland

### Education and training

July 2007 – **Doctoral student** at the Laboratory for Surface Science and Technology (LSST), Department of Materials, ETH Zurich, Zurich, Switzerland.  
to date

March 2007 – **Research assistant** at the Department of Analytical Chemistry, Università degli Studi di Cagliari, Cagliari, Italy.  
June 2007

September 2004 **Master Degree in Chemical Engineering** (110/110 *summa cum laude*),  
– February 2007 Università degli Studi di Cagliari, Cagliari, Italy.

September 2001 **Bachelor Degree in Chemical Engineering** (108/110), Università degli  
– July 2004 Studi di Cagliari, Cagliari, Italy.

February 2002 – Internship at Progetto 2000, Oristano, Italy.  
March 2002

Academic year Diploma in classical studies (100/100), E. Piga College, Villacidro, Italy.  
2000/01

### Teaching and Supervising Experience

2008-2012 **Teaching assistant** in the course “Quantitative surface analysis” with Prof. A. Rossi, ETH Zürich.

2010 **Undergraduate student project supervisor**  
“Zinc and Calcium polyphosphates: chemical characterization and mechanical properties.” E. Mura, Master Thesis.

2009 “The influence of the phosphorus to zinc ratio on chemical and mechanical properties of zinc phosphate glasses.” M. Süess, Semester project.

2008 “XPS Study of Zinc Phosphate Glasses.” P. Lewdeni, Semester project.

## Language skills

Italian	Native speaker
English	Fluent (Certificate of Advanced English, Grade A)
German	Basic knowledge
French	Basic knowledge

## Publications

- 2012 M. Crobu, A. Rossi, N. D. Spencer: "Effect of the chain-length and of the counterpart material on the tribochemistry of bulk zinc polyphosphate glasses." (in preparation).
- 2012 M. Crobu, A. Rossi, N. D. Spencer: "ToF-SIMS of polyphosphate glasses." *Surface and Interface Analysis* (submitted).
- 2012 M. Crobu, A. Rossi, F. Mangolini, N. D. Spencer: "Chain-length identification in zinc polyphosphate glasses using Time of flight secondary ion mass spectroscopy and X-ray photoelectron spectroscopy." *Analytical and Bioanalytical Chemistry* (2012).
- 2011 P. Fesser, C. Iacovita, C. Waeckerlin, S. Vijayaraghavan, N. Ballav, K. Howes, J. P. Gisselbrecht, M. Crobu, C. Boudon, M. Stohr, T. A. Jung, F. Diederich: "Visualizing the Product of a Formal Cycloaddition of 7,7,8,8-Tetracyano-*p*-quinodimethane (TCNQ) to an Acetylene-Appended Porphyrin by Scanning Tunneling Microscopy on Au(111)". *Chemistry-A European Journal* 17, 5246-5250 (2011).
- 2010 M. Crobu, A. Rossi, F. Mangolini, N. D. Spencer: "Tribochemistry of Bulk Zinc Metaphosphate Glasses." *Tribology Letters* 39, 121-134 (2010).
- 2008 B. Elsener, M. Crobu, M. Scorciapino, A. Rossi: "Electroless deposited Ni-P alloys: corrosion resistance mechanism." *Journal of Applied Electrochemistry* 38, 1053-1060 (2008).
- 2008 M. Crobu, M. Scorciapino, B. Elsener, A. Rossi: "The corrosion resistance of electroless deposited nano-crystalline Ni-P alloys." *Electrochimica Acta* 53, 3364-3370 (2008).
- 2009 A. Rossi, B. Elsener, D. Addari, D. Atzei, M. Crobu, M. Fantauzzi, A. Rigoldi, M. A. Scorciapino "Analisi XPS di strati sottili." *La chimica e l'industria*, 77-92 (2009)

## Oral Presentations

- 2011 ToF-SIMS of Polyphosphate Glasses  
M. Crobu, A. Rossi, N. D. Spencer  
*SIMS XVIII - International conference on Secondary Ion Mass Spectroscopy* (Riva del Garda; Italy)
- 2011 Tribological Behavior of Zinc and Iron Bulk Polyphosphate Glasses  
M. Crobu, A. Rossi, N. D. Spencer  
*Material Science Colloquium* (ETH Zürich, Zürich, Switzerland)

- 2010 Tribological Behavior of Zinc and Iron Bulk Polyphosphate Glasses  
M. Crobu, A. Rossi, N. D. Spencer  
*Asiatrib* (Perth, Australia)
- 2010 Zinc and Iron Bulk Polyphosphate Glasses: Mechanical Properties and Tribological Behavior  
M. Crobu, A. Rossi, N. D. Spencer  
*SAOG Annual Meeting of the Swiss Working Group on Surface and Interface Science* (Fribourg, Switzerland)
- 2009 Chemical and Tribological Characterization of Different Chain Length Zinc Polyphosphate Glasses: an XPS Study  
M. Crobu, A. Rossi, N. D. Spencer  
*Advances in Boundary Lubrication and Boundary Surface Films* (Seville, Spain)
- 2011 Surface Chemistry of Glassy Polyphosphates Investigated by ToF-SIMS  
A. Rossi, M. Crobu, E. Mura and N. D. Spencer  
*International Tribology Conference* (Hiroshima, Japan)
- 2011 Progressi nella Caratterizzazione di Superfici di Materiali Morfologicamente Complessi e di Nanostrutture  
D. Addari, D. Atzei, M. Crobu, B. Elsener, M. Fantauzzi, M. Pisu, A. Rigoldi e A. Rossi  
*La Chimica in Sardegna* (Sassari, Italy)
- 2007 Nano-Crystalline Ni-P Alloys: Mechanism of the Outstanding Corrosion Resistance  
M. Crobu, A. Scorciapino, B. Elsener, A. Rossi  
*GEI-ERA* (Cagliari, Italy)

### Poster Presentations

- 2011 ToF-SIMS and XPS Study of Amorphous Polyphosphates  
M. Crobu, A. Rossi, N. D. Spencer  
*SIMS Europe* (Münster, Germany)
- 2009 Tribochemistry of Zinc and Iron Bulk Polyphosphate Glasses  
M. Crobu, A. Rossi, N. D. Spencer  
*Tribochemistry 2009, satellite forum of the World Tribology Congress WTC 2009* (Kyoto, Japan)
- 2009 Mechanical Properties of Zinc and Iron Phosphate Glasses  
M. Crobu, A. Rossi, N. D. Spencer  
*World Tribology Congress WTC 2009* (Kyoto, Japan)
- 2009 Environmentally Compatible, Energy-Efficient Lubricants: an Analytical Study of the Tribochemistry of Antiwear Additives  
M. Crobu, F. Mangolini, A. Rossi, N. D. Spencer  
*Materials Day – ETH Zürich* (Zürich, Switzerland)
- 2008 Analysis of the effect of mechanical stress and tribological testing on the composition of zinc polyphosphate glasses  
M. Crobu, A. Rossi, N. D. Spencer  
*Gordon Research Conference –Tribology* (Waterville, USA).

- 2008 XPS Analysis of Zinc Polyphosphates to Investigate the Effect of the Mechanical Stress on their Composition  
M. Crobu, A. Rossi, N. D. Spencer  
*ISA 2008* (Ferrara, Italy)
- 2011 Surface chemistry of glassy polyphosphates investigated by ToF-SIMS  
A. Rossi, M. Crobu, N. D. Spencer  
*Tribochemistry Forum* (Hagy, Japan)

# Acknowledgments

During these last years, many people contributed with their help and encouragement to the successful achievement of these project goals. I would like to take this opportunity to express my warmest gratitude to:

Prof. Nicholas D. Spencer for giving me the great opportunity to work in his research lab and supervising me during my PhD.

Prof. Antonella Rossi for believing in my capabilities, sometimes more than myself, for strongly supporting my scientific and personal growth and for the correction of this thesis.

Prof. Richard K. Brow and Prof. Markus Niederberger, for their interest in my work.

Prof. L. Gauckler for helping me with the synthesis protocol of my samples.

Dr. Beat Keller, Dr. Karl-Emanuel Mayerhofer and Dr. Peggy Roszbach for training me on ToF-SIMS and for the useful discussions.

Dr. Diana Courty for performing the nanoindentation measurements.

Dr. Sina Saxer for her help with the UV-visible measurements.

Prabath Lewdeni, Martin Süess, and Emanuele Mura for collaborating with me on this project and enriching it with their personal contributions.

Filippo Mangolini for his scientific and personal support, especially in the first year of my PhD, and for the numerous scientific discussions.

Giovanni Cossu for his precious technical help, his friendship and his wise encouragements when things looked tough.

Josephine Baer for being able to solve any kind of trouble you could encounter and for her cheerful company.

Prathima C. Nalam for her friendship, for her company during some of the most memorable trips of my life, for introducing me to the delight of Indian food and culture, and for the scientific discussions about tribology.

Eva Beurer, Doris Spori, and Whitney Hartung for their help with language issues, for sharing my passion for cooking, and for the countless joyful moments we spent together.

Marcella Roba for being a nice flat-mate, a loyal friend and a patient confidante.

Jarred and Lucy Clasohm for making me feel always at home in their company and for being so generous with their hospitality.

Cristoph Mayer and Torben Gillich for being my “supervisors” in the chemistry lab and for being such great party guys.

Shivaprakash Narve Ramakrishna for appreciating so much my cooking abilities, and for sharing my dreams of entrepreneurship in the restaurant industry.

Karthik Kumar for showing to me a new philosophical point of view on science and on life.

Bidhari Pidhatikha for being a kind friend, a pleasant roommate on many occasions and for her contagious spontaneity.

Lucio Isa for giving me the opportunity to organize with him an unforgettable off-site group meeting in the breath taking landscape of lake Como.

Christian Zink and Erich Schurtenberger for the many fun moments shared together and for bringing me to new horizons in one of the most memorable pictures ever taken during a LSST off-site group meeting.

Raphael Heeb, Fabian Anderegg, Chiara Perrino, Mathias (Ciccio) Rodenstein, Stefan Kaufmann, Robert Bielecki, Tomoko Hirayama, Andrea Penna, Ana Bela Ferreira Faia Torres, Tolga Goren, Jia Pei, Ang Li, Cathrein Hückstädt, Sara Morgenthaler Akshata Rao, Edmondo Benetti for being pleasant office-mates.

Olof Sterner, Angela Serrano, Barbora Malisova, Adrienne Nelson, Rachel Knowler, Canet Acikgoz, Deepak Kumar, Vikrant Naik, Nicolas Fernandez, Ganna Gorodyska, Vincent Zoulalian, Maria Håkanson, Seunghwan Lee, Rosa Espinosa Marzal, Manjesh Kumar Singh for the many lunch- and coffee breaks we shared and all the LSST members for the friendly working atmosphere.

A special thanks goes to Clément Cremmel who has been my closest friend from the moment he arrived at LSST. I am most grateful for his loving support in the difficult moments as well as for the happy and joyful moments that we shared in this last year.

Finally I would like to thank my parents for giving me life and for teaching me the most important lessons of my life: the power of integrity, humbleness and commitment enables one to achieve any goal in life. Thanks to them also for the efforts they made to give me the opportunity to study and for their warm support in all these years.